Stony Brook University

Performance Evaluation and Characterization of Metallic Bipolar Plates in a Proton Exchange Membrane (PEM) Fuel Cell

A Dissertation Presented

by

Yue Hung

to

The Graduate School

in Partial Fulfillment of the

Requirements

for the Degree of

Doctor of Philosophy

in

Materials Science and Engineering

Stony Brook University

December 2010

Stony Brook University

The Graduate School

Yue Hung

We, the dissertation committee for the above candidate for the
Doctor of Philosophy degree, hereby recommend
acceptance of this dissertation.

Dr. Devinder Mahajan - Dissertation Advisor
Professor, Department of Materials Science and Engineering

Dr. Hazem Tawfik - Dissertation Co-Advisor
Professor, Institute for Technology Transfer (IRTT), Farmingdale State College

Dr. Charles Fortmann - Chairperson of Defense
Professor, Department of Materials Science and Engineering

Dr. Mahmoud Abd Elhamid - External Member
Staff Research Engineer, General Motors

This dissertation is accepted by the Graduate School

Lawrence Martin
Dean of the Graduate School

Abstract of the Dissertation

Performance Evaluation and Characterization of Metallic Bipolar Plates in a Proton Exchange Membrane (PEM) Fuel Cell

by

Yue Hung

Doctor of Philosophy

in

Materials Science and Engineering

Stony Brook University

2010

Bipolar plate and membrane electrode assembly (MEA) are the two most repeated components of a proton exchange membrane (PEM) fuel cell stack. Bipolar plates comprise more than 60% of the weight and account for 30% of the total cost of a fuel cell stack. The bipolar plates perform as current conductors between cells, provide conduits for reactant gases, facilitate water and thermal management through the cell, and constitute the backbone of a power stack. In addition, bipolar plates must have excellent corrosion resistance to withstand the highly corrosive environment inside the fuel cell, and they must maintain low interfacial contact resistance throughout the operation to achieve optimum power density output. Currently, commercial bipolar plates are made of graphite composites because of their relatively low interfacial contact resistance (ICR) and high corrosion resistance. However, graphite composite's manufacturability,

permeability, and durability for shock and vibration are unfavorable in comparison to metals. Therefore, metals have been considered as a replacement material for graphite composite bipolar plates. Since bipolar plates must possess the combined advantages of both metals and graphite composites in the fuel cell technology, various methods and techniques are being developed to combat metallic corrosion and eliminate the passive layer formed on the metal surface that causes unacceptable power reduction and possible fouling of the catalyst and the electrolyte.

The main objective of this study was to explore the possibility of producing efficient, cost-effective and durable metallic bipolar plates that were capable of functioning in the highly corrosive fuel cell environment. Bulk materials such as Poco graphite, graphite composite, SS310, SS316, incoloy 800, titanium carbide and zirconium carbide were investigated as potential bipolar plate materials. In this work, different alloys and compositions of chromium carbide coatings on aluminum and SS316 substrates were also tested for suitability in performing as PEM fuel cell bipolar plates. Interfacial contact resistance and accelerated corrosion resistance tests were carried out for various bulk materials and chromium carbide coatings. Results of the study showed that chromium carbide protective coatings had relatively low interfacial contact resistance and moderate corrosion resistance in comparison to other metals.

Single fuel cells with 6.45cm^2 and 50cm^2 active areas were fabricated and tested for performance and lifetime durability using chromium carbide coated aluminum bipolar plates and graphite composite bipolar plates as a control reference. Polarization curves and power curves were recorded from these single cells under various load conditions. The results showed that coated aluminum bipolar plates had an advantage of anchoring

the terminals directly into the plates resulting in higher power density of the fuel cell. This was due to the elimination of additional ICR to the power stack caused by the need for extra terminal plates. However, this study also revealed that direct terminal anchoring was efficient and useable only with metallic bipolar plates but was inapplicable to graphite composite plates due to the poor mechanical strength and brittleness of the graphite composite material. In addition, the 1000 hour lifetime testing of coated aluminum single cells conducted at 70°C cell temperature under cyclic loading condition showed minimal power degradation (<5%) due to metal corrosion. Surface characterization was also conducted on the bipolar plates and MEAs to identify possible chemical change to their surfaces during the fuel cell operation and the electrochemical reaction.

The single cell performance evaluation was complemented by an extended study on the fuel cell stack level. For the latter, a ten-cell graphite composite stack with a 40 cm^2 active area was fabricated and evaluated for the effect of humidity and operating temperature on the stack performance. Graphite plates were selected for this study to eliminate any possible metal corrosion. A finite element analysis (FEA) model of a bipolar plate was developed to evaluate the effect of air cooling system design parameters and different bipolar plate materials on maintaining the PEM power stack at a safe operating temperature of 80°C or less. In the final stage of this work, a three-cell metallic stack with a 50 cm^2 active area and coated aluminum bipolar plates was fabricated based on the positive results that were obtained from earlier studies. The three-cell stack was successfully operated and tested for 750 hours at different temperatures and power densities. This laboratory testing coupled with characterization studies showed that small

amounts of aluminum oxide were observed on the coating surface due to localized imperfections in the coating and a lack of protection in the uncoated areas, such as internal manifolds and mounting plates. However, the scanning electron microscopy (SEM) and the energy dispersive x-ray spectroscopy (EDX) showed that coating thickness, chemistry, and surface morphology remained consistent after 750 hours of operation.

Table of Contents

List of Tables

List of Figures

List of Abbreviations

IEO	International Energy Outlook
EIA	Energy Information Administration
kWh	kilowatt hour
USDOE	United States Department of Energy
ICE	Internal Combustion Engine
AFC	Alkaline Fuel Cell
PAFC	Phosphoric Acid Fuel Cell
MCFC	Molten Carbonate Fuel Cell
SOFC	Solid Oxide Fuel Cell
PEMFC	Proton Exchange Membrane Fuel Cell
DMFC	Direct Methanol Fuel Cell
MEA	Membrane Electrode Assembly
ICR	Interfacial Contact Resistance
SEM	Scanning Electron Microscopy
EDX/EDS	Energy Dispersive X-ray
XRD	X-ray Diffraction
XPS	X-ray Photoelectron Spectroscopy
XRF	X-ray Fluorescence
CTE	Coefficient of Thermal Expansion
HVOF	High Velocity Oxygen Fuel
PANI	Polymers Polyaniline
PPY	Polypyrrole
PVD	Physical Vapor Deposition
SLPM/SLM	Standard Liters per Minute
SCCM	Standard Cubic Centimeter per Minute
GDL	Gas Diffusion Layer
SCE	Saturated Calomel Electrode
OCP	Open Circuit Potential
ICP	Inductively coupled plasma

CHAPTER 1

Introduction

Since the early part of the twentieth century, fossil fuels are the main conventional source of energy in the global economy. Thermal systems such as turbines and internal combustion engines that burn fossil fuels are the traditional way to generate electrical and mechanical energy. However, thermal systems emit heat and carbon dioxide as byproduct and these systems are inefficient due to a large amount of waste heat energy rejected to the environment. In addition, the byproduct, carbon dioxide, directly contributes to increased atmospheric CO_2 levels.

The diminishing global reserves of fossil fuels have been causing the price of oil and natural gas to increase, reaching levels that threaten our economy and national security. Therefore, alternative energy sources and systems are sought to reduce our dependence on fossil fuels. Renewable sources of energy such as wind and solar can provide clean electricity but these are still considered economically unviable due to the relatively low power density and high manufacturing cost per kilowatt with the presently available technology. Wind and solar technologies are widely used as stationary power station but they are highly location dependant. In addition, they are not suitable in automobile application due to their low power density. Nuclear energy has the potential to offer relatively low cost and high density energy but it is impractical to install a reactor in every vehicle. Also, the major challenges for nuclear energy are: 1) maintaining safe operation of reactors with no risk and 2) managing nuclear waste. Fuel cell is another system choice that offers relatively clean, high efficiency, high power density and safe operation for automobile industry.

1.1 World energy consumption

According to the recently published International Energy Outlook 2009 (IEO2009) by the Energy Information Administration (EIA) [1], the proven world oil reserves are estimated at 1,342 billion barrels. The IEO2009 has also projected that the total world energy use will rise from 472 quadrillion British thermal units (Btu) in 2006 to 552

quadrillion Btu in 2015 and then to 678 quadrillion Btu in 2030 due to economic growth in all countries, an increase of 44 percent over the projection period (Figure 1.1). The report assumes that fossil fuels will continue to be the primary source of fuel and supply to meet the projected increase in energy consumption worldwide. In particular, Figure 1.2 projects that liquid fuels are expected to continue to provide the largest share of world energy over the projection period.

On global basis, energy use is expected to grow in all sectors but the major growth is expected to be in the transportation sector where it will account for 79% of the total projected increase in liquid fuel use between 2006 and 2030 [1]. As the world continues to experience strong economic growth, transportation around the world increases. The world liquid fuels consumption therefore is projected to increase to 107 million barrels per day (216 quadrillion Btu) in 2030 due to the increase in transportation. Currently, liquid fuel is still considered as the main energy source for transportation sector due to the relatively flexible storage requirements, ease of fuel transportation and relatively high power density for the end users. In the International Energy Outlook 2009, it was mentioned that more than half of the world liquid fuel consumption is projected for use just in the transportation sector alone where there are few competitive alternatives to petroleum (Figure 1.3).

In the United States, the use of passenger vehicles is expected to grow in the foreseeable future. The transportation oil gap: the difference between U.S. petroleum production and the transportation sector demand was 6.1 million barrels per day in 2009. According to the Department of Energy projections, this gap will continue to get wider in spite of increasing U.S. petroleum production and in 2030, it could reach 6.7 million barrels per day as depicted in Figure 1.4 [2]. Renewable sources of energy and more efficient systems such as fuel cells that utilize fossil and renewable energy sources are being researched and developed to reduce the transportation oil gap. If the fuel cell technology is successfully developed, it could eventually offset the projected petroleum demand due to sheer efficiency.

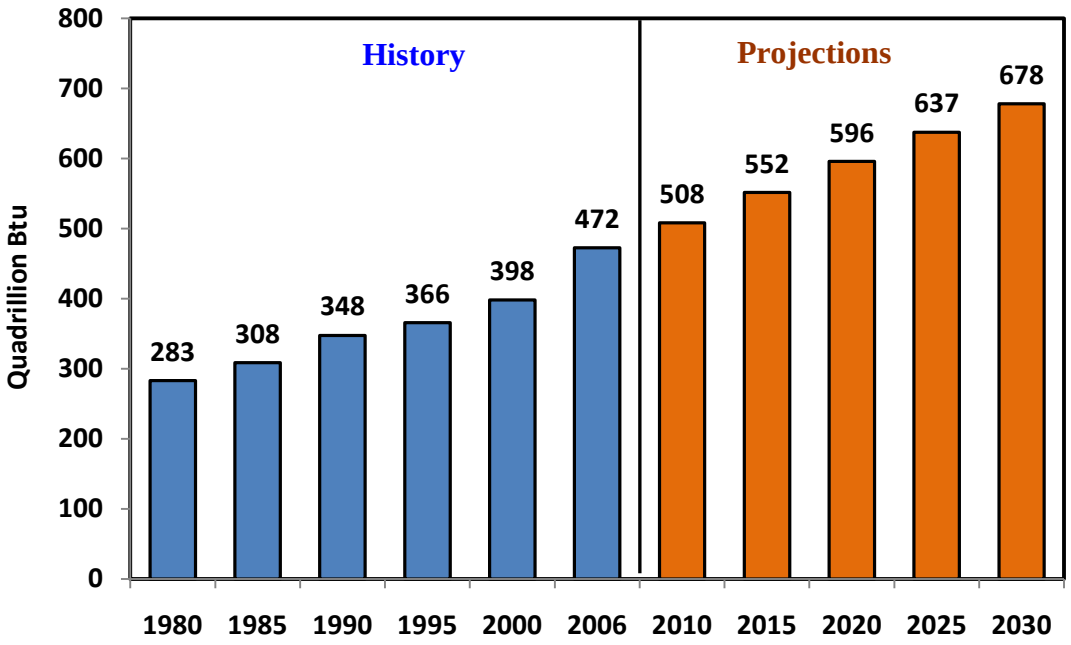

Figure 1.1: World marketed energy consumption, 1980-2030.

Sources: Energy Information Administration (EIA), International Energy outlook 2009 (May 2009)

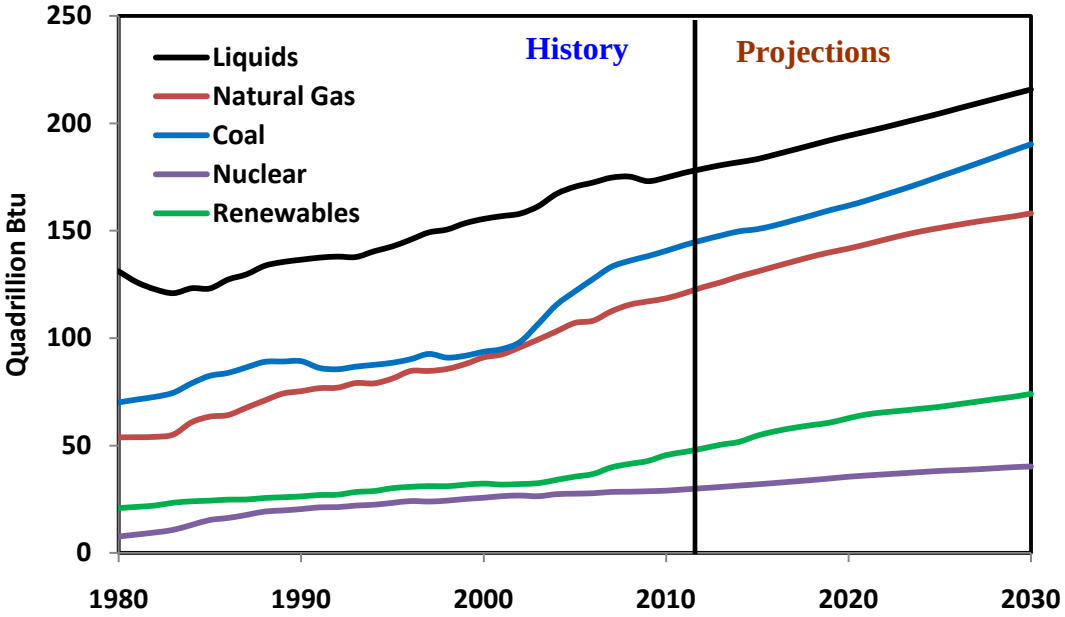

Figure 1.2: World marketed energy use by fuel type, 1980-2030

Sources: Energy Information Administration (EIA), International Energy outlook 2009 (May 2009)

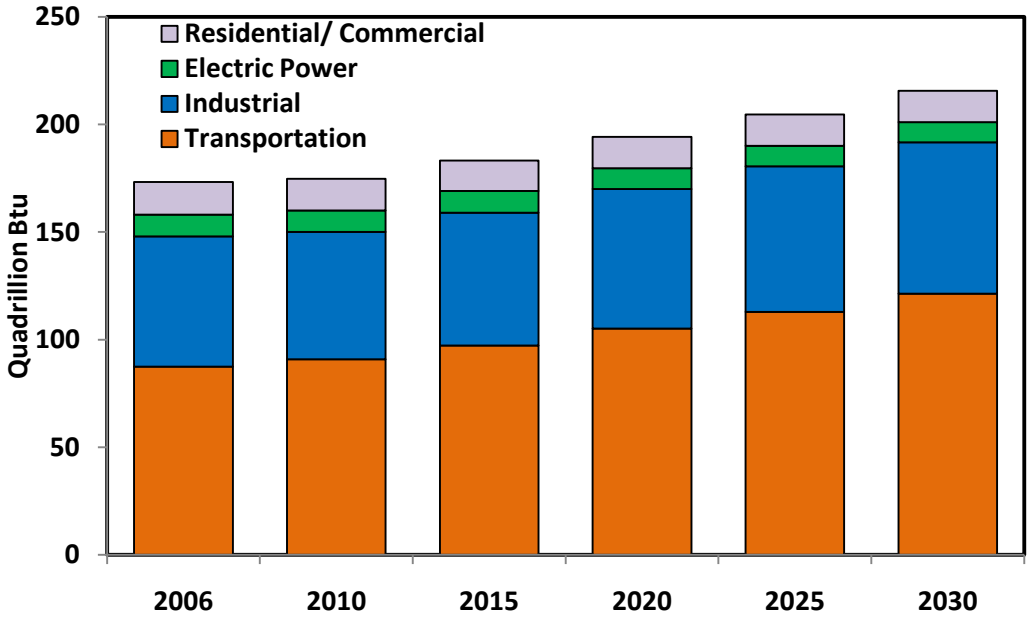

Figure 1.3: World liquids consumption by sector, 2006-2030

Sources: Energy Information Administration (EIA), International Energy outlook 2009 (May 2009)

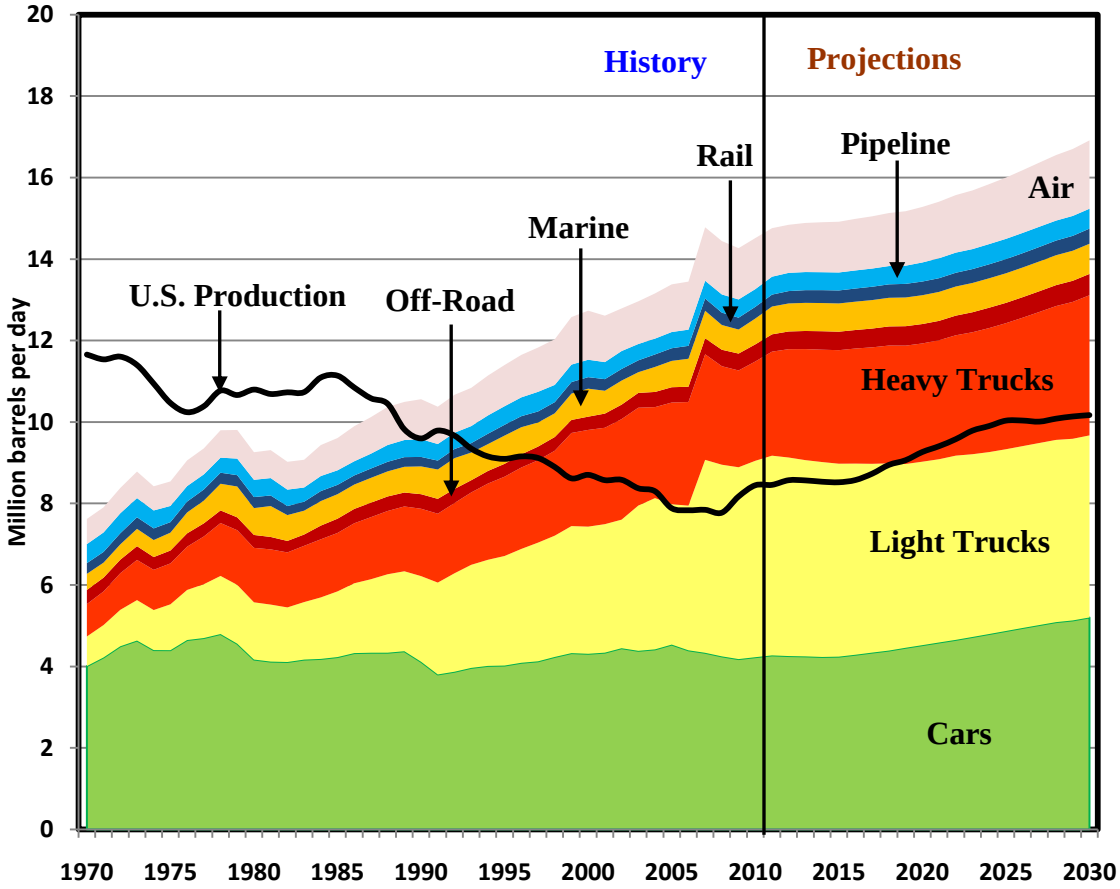

Figure 1.4: United States petroleum production and consumption, 1970–2030

Sources: U.S. Department of Energy (DOE),
Transportation Energy Data Book: Edition 28 (2009)

1.2 Fuel cells and their types.

Fuel cells generate power in a fundamentally different way compared to internal combustion engines (ICEs) and storage batteries. ICEs operate by burning fuel to create heat that is converted into mechanical energy and then motive power, or electric power by turning an electric generator. The efficiency of this conversion process is greatly affected by the loss of waste heat and friction. On the other hand, batteries are energy storage devices; they can only produce power intermittently as they must be recharged. The recharging process is lengthy and inconvenient. The advantages of fuel cells are: 1) they have no moving parts and 2) they operate by the electrochemical reaction between hydrogen from fuel and oxygen from air to produce electric power directly. Heat and non-polluted water vapor are the only by-products of these systems [3-5]. The schematic in Figure 1.5 demonstrates different energy conversion pathways. Fuel cells produce electricity using fuel from an external tank. They operate continuously as long as fuel is supplied and the tank can be quickly refueled, avoiding the time-consuming recharging process that is associated with batteries. Fuel cells rely on electrochemical reaction with no combustion. Emissions from this type of system would be much smaller than those from the cleanest fuel combustion processes.

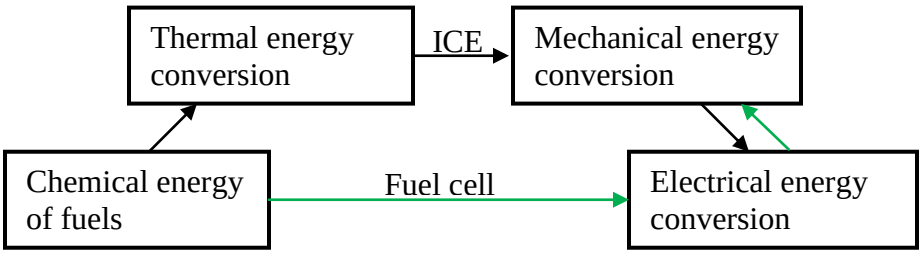

Figure 1.5: A comparison of energy conversion pathways between a fuel cell and an internal combustion engine (ICE)

Theoretically, a fuel cell can convert more than 80% of the energy contained in the fuel into usable electric power and heat [4-6]. In comparison, the efficiencies of most mechanical and electrical energy sources used today range from 15% to 30%. Therefore, fuel cells have the potential of providing advantages in efficiency, reliability, economy, cleanliness, low fossil fuel dependence and unique operation characteristics. In particular,

polymer electrolyte membrane fuel cells (PEMFC) operate at relatively low temperature of 80^{o}C or less, have high power density, can vary their power output quickly to meet the shifting power demand, and are suited for automobiles, where quick startup is required [4,6-8]. PEM fuel cell stacks operating on hydrogen can produce over 53% electrical efficiency and with system heat recovery, the overall efficiency can exceed 80%. The size of a PEM fuel cell system can vary from less than 100W for most portable power applications to few kW (stationary-residential or small transport vehicles), 50–75kW for cars and 200–250kW for buses and trucks. A key requirement for power application used in automotive industry is the production of compact and lightweight PEMFC power system, which may be achieved by proper selection of materials.

According to the U.S. Department of Energy, "Fuel cells are primary candidates for light-duty vehicles, for buildings, and potentially for much smaller applications such as replacements for rechargeable batteries." However, high cost and poor reliability are the main factors hindering environmentally friendly fuel cell technology from commercialization and mass production. DOE has also set the target price for a fuel cell stack at $35/kW in 2010 in order to be cost effective and competitive in the transportation market.

1.2.1 Alkaline fuel cells (AFC)

Alkaline fuel cells, long used by NASA on space missions, can achieve electrical power generating efficiencies of up to 60% [4,9,10]. Until recently these systems were too costly for commercial applications, but several companies are now examining ways to reduce costs and improve operating flexibility. The cells use alkaline potassium hydroxide as the electrolyte. The concentration of the electrolyte varies from 30-45% by weight for lower temperature operation (< 120°C) and 85% by weight for high temperature operation (~250°C). One of the advantages is that non-precious metals can be used as electrodes and no particular materials are needed.

Pure H_2 and O_2 are preferred reactant gases that simply produce water during electric power generation and eliminate generation of CO_2. It is due to small amount of CO_2 in air can react with the hydroxide ion during the reaction. This results in forming carbonate that could block the pores of the electrodes and reduces the performance of the fuel cell.

1.2.2 Phosphoric acid fuel cells (PAFC)

These are the most commercially developed type of fuel cells and they are already in use in hospitals, nursing homes, hotels, office buildings, schools, utility power plants, and/or airport terminals. Phosphoric acid fuel cells generate electricity at more than 40% efficiency and nearly 85% of the steam produced from these fuel cells is used for cogeneration. Their performance is remarkable when compared to less than 30% efficiency of the most efficient internal combustion engine. The operation principle of a phosphoric acid fuel cell is similar to a proton exchange membrane fuel cell. Platinum is used in the electrodes and the electrolyte is a colorless viscous phosphoric acid liquid. These cells operate around 205°C.

1.2.3 Molten carbonate fuel cells (MCFC)

Molten carbonate fuel cells promise high fuel efficiencies and the ability to consume coal-based fuels. These cells operate between 600°C and 700°C and the electrolyte is highly conductive molten carbonate salt, with carbonate ions providing ionic conduction. The first full-scale molten carbonate stacks were tested in demonstration units in California in 1996. Molten carbonate fuel cells generate electricity with up to 47% efficiency. When wasted heat is captured and recycled in the system, the efficiency can be as high as 80% [3-5].

1.2.4 Solid oxide fuel cells (SOFC)

The SOFC is another highly promising fuel cell that is suitable for high power applications, including industrial and large-scale central electricity generating stations. Solid oxide fuel cells have a good potential to power motor vehicles.

Many test cells are developed and tested around the world, including Europe and Japan. A solid oxide system usually uses a hard ceramic material instead of a liquid electrolyte, allowing operating temperatures to reach 1,000°C. Because of the high operating temperatures, precious metal catalysis is not needed. Electrical power generating efficiencies could reach up to 43%. One type of SOFC uses an array of tubes that is about a meter in length. Other variations include a compressed disc that resembles the top of a soup can [3-5].

1.2.5 Proton exchange membrane fuel cells (PEMFC)

These cells operate at relatively low temperatures (60-80°C), have high power density, and can vary their output quickly to meet shifting power demands. These are suitable for automobile applications, where quick startup is required. This type of fuel cell is sensitive to fuel impurities because noble-metal (typically platinum) is used as a catalyst. Therefore, pure H_2 is the preferred fuel. The cell output generally ranges from 50 watts to 75 kW [3,4,8,10].

The proton exchange membrane is a thin membrane that allows hydrogen ions to pass through. Since the electrolyte is made of solid polymer, it does not require corrosive fluids like some other types of fuel cells

1.2.6 Direct methanol fuel cells (DMFC)

Direct methanol fuel cells (DMFC) are similar to the PEM cells in that they both use a polymer membrane as the electrolyte. However, in the DMFC, the anode catalyst draws hydrogen from liquid methanol, eliminating the need for a fuel reformer. The efficiency of about 40% is expected with this type of fuel cell at an operating temperature between 50°-120°C. Higher efficiencies are possible at higher operating temperature.

Figure 1.6 shows the summary of different fuel cells with respect to their electrical efficiency, reactant gases, electro chemical reaction and operating temperature [3-5,10,11].

1.3 History and description of PEM fuel cell

The idea of producing electric current from hydrogen and oxygen was first demonstrated by William Grove in 1839. He discovered that by reversing the electrolysis of water, recombining hydrogen and oxygen, usable electric current can be produced. Grove created an experimental device that could be used for such process and named this device as fuel cell or the “gaseous voltaic battery”. This discovery is significant in introducing alternative sources of energy, especially in the 20^{th} century when energy use was expanding. Though the idea of fuel cell had been known for over 100 years, it was not utilized until General Electric developed the first practical fuel cell called “solid

polymer fuel cell" for use by NASA in the U.S. Space Program in the early 1960's [4,5,10].

In principle, a PEM fuel cell operates like a battery. However, a fuel cell does not run down or require recharging as long as the fuel is supplied. It directly converts chemical energy in the form of electricity and heat. The basic component of a PEM fuel cell consists of two channeled plates and two electrodes sandwiched around an electrolyte. Hydrogen fuel is channeled through flow-field plates to the anode side of the fuel cell while oxygen (or air) is channeled to the cathode side of the fuel cell. A catalyst splits the hydrogen atom into a proton and an electron. The function of the electrolyte is to transport the hydrogen ion from the anode to the cathode. The electron takes external paths to the cathode meeting the oxygen atom and the hydrogen ion (Figure 1.7). This electron produced from hydrogen can be utilized as an electric current before it returns to the cathode, and the electron will be reunited with the hydrogen ion and the oxygen atom to form water [3,4,10,11].

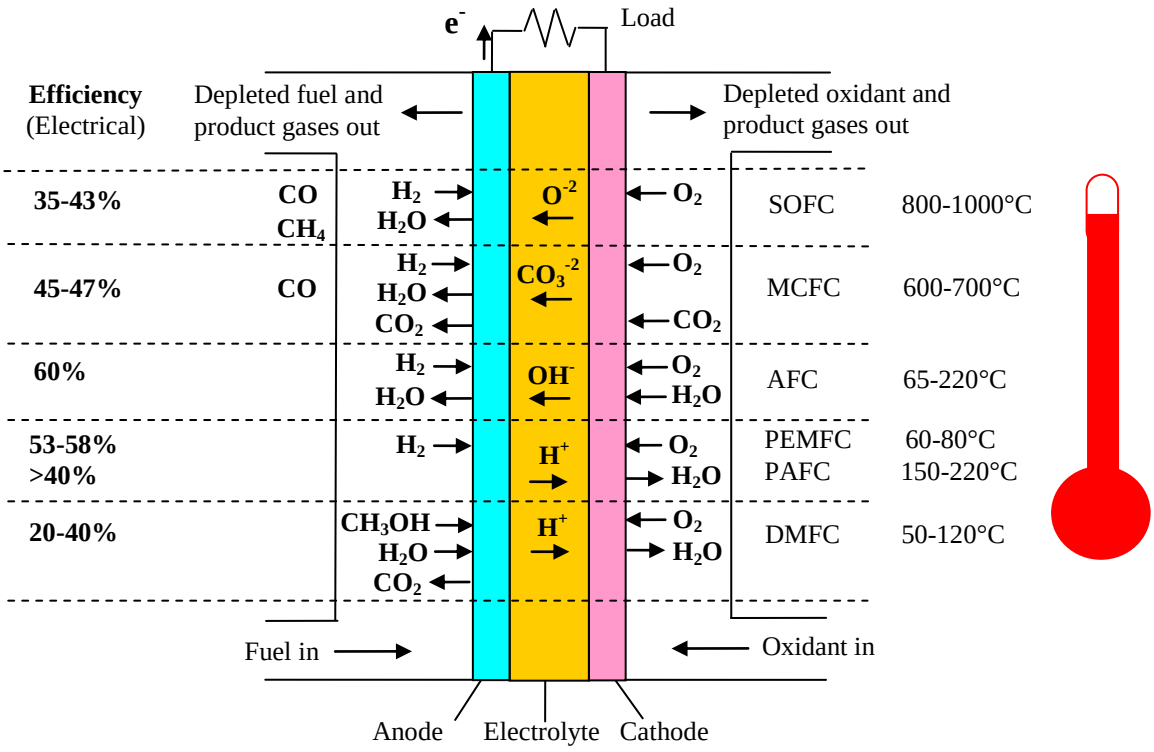

Figure 1.6: Types of fuel cells, their reactions and operating temperatures

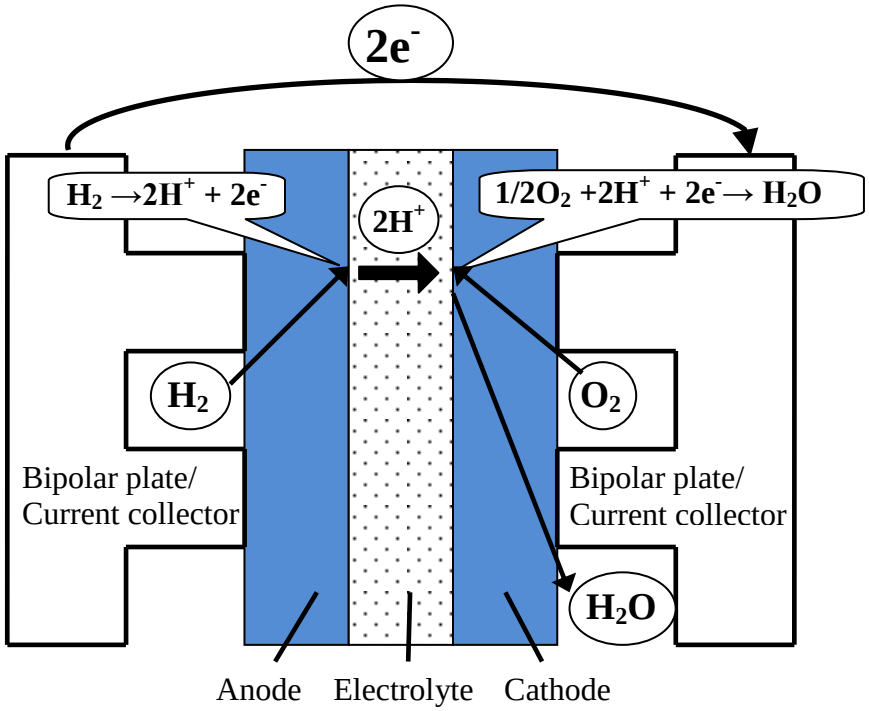

Figure 1.7: Description of PEM fuel cell operation

1.4 Technical challenge in PEM fuel *c*ell

Though there are many advantages of PEM fuel cell technology and many demonstration units in both automotive and stationary power applications have been built successfully, the main hurdles facing the PEM fuel cell industry from commercialization and competing with other power generation systems are high cost, durability, optimization of the fuel cell component materials and operating conditions and the fuel availability.

1.4.1 Durability

The durability of fuel cell systems has not been established. However, fuel cell power systems used in the automotive industry will be required to be as durable and reliable as current internal combustion engines which can last for at least 5,000 hour lifespan (150,000 miles equivalent) and able to function over the full range of vehicle operating conditions (-40° to +40° C) [12]. Impurity of fuel and corrosive bipolar plate material can contribute to the power degradation over a period of time depending on the rate of pollutant supplied to the MEA. In addition, MEA is the most fragile component in PEM fuel cells which can cause instant termination of power output. The mechanical failure of MEA will allow H_2 and air cross over within the fuel cell resulting in termination of electrochemical reaction within the cell and immediate power interruption.

1.4.2 Cost

For any technology, high material and manufacturing cost is always one of the biggest obstacles for commercialization. As mentioned in the earlier sections, bipolar plates and membrane electrode assembly (MEA) are the two main repeated items in PEM fuel cell technology. Currently, the membrane (Nafion) used in MEAs costs \$500 - \$800/m^2 and platinum used as catalyst in the electrode costs about \$15.4/g. The common platinum loading is 0.2-0.4 mg/cm^2 and it costs \$32-\$64/m^2 for both anode and cathode. The bipolar plate material costs \$50-100/m^2. A typical fuel cell has 0.6V - 0.7V and 0.5A-1.5A/cm^2 current density, depending on the Pt loading and MEA structure, which gives the average of 6.5kW/m^2 [4,13-16].

At present, the material and fabrication cost of a typical PEM fuel cell is around \$2000/kW which makes this technology out of reach for commercialization in

automobile industry. In order to replace internal combustion engine, the cost of a fuel cell has to be lower than $50/kW [12,17,18]. Automated assembly lines for fuel cell stacks and high volume production can reduce the cost of a fuel cell; however, at this point, the material cost still far exceeds the target price.

1.4.3 Fuel and its availability

The PEM fuel cell uses pure H_2 as a fuel. Water electrolysis for H_2 production is too expensive. Reforming technologies have been considered to extract H_2 from H_2-rich sources such as methanol and natural gas. However, producing pure H_2 from reforming hydrocarbon can also be very costly. The impurities such as carbon monoxide (CO) in H_2 gas could cause degradation in performance because CO adsorbs on the catalyst surface and blocks the sites needed for H_2 oxidation. It has been reported in literature that in the PEMFC, CO concentration greater than 10 ppm in reactant gases will decrease the cell performance [19,20].

Another difficulty in PEM fuel cell technology is the lack of H_2 infrastructure. A cost-effective and energy-efficient H_2 delivery infrastructure is needed. However, fuel cell vehicles are still in the R & D stage and the installation of H_2 refueling stations, across the country, is still considered impractical at the present time. In addition, the price of H_2 is much higher than that of gasoline, which presents one of the major challenges to the fuel cell technology and the "Hydrogen Economy".

1.4.4 Optimization of the fuel cell component materials and operating conditions

1.4.4.1 Membrane electrode assembly (MEA)

The MEA is the heart of a fuel cell and consists of a polymer membrane electrolyte and two electrodes (anode and cathode) that sandwich the polymer membrane. Three components of the MEA are compressed and fused together by high pressure and temperature. The industry standard of polymer membrane is "Nafion" (a trademark of Dupont). It is an excellent conductor of hydrogen ions. The Nafion material consists of a fluorocarbon polymer backbone, which is similar to the structure of Teflon, with the side chain of sulfonic acid (HSO_3) groups (Figure 1.8). The Teflon-like backbone is highly hydrophobic and it prevents flooding which causes the chemical reaction to stop. The

HSO_3 groups are covalently bonded to the polymer and highly hydrophilic. The protons on these acid groups are free to migrate through the electrolyte especially when they are well hydrated [8,21].

The electrodes are made of highly porous materials, usually carbon paper or carbon cloth and contain ≤ 1 mg/cm^2 of Pt. The Pt catalyst in the form of very small particles is deposited on high surface area carbon particles for a better reaction. The main function of the Pt is to catalyze the conversion of H_2 molecule into electrons and protons. Also on the oxygen side, Pt helps the O_2 molecule to split into two atoms and then combine with the electrons and protons from H_2 to produce water.

Fuel cell performance can be improved by operating at higher temperature and hydrated Nafion membrane because as the temperature and hydration levels increase, more ions are allowed to transfer across the membrane efficiently [8,21,22]. This ion transfer is due to the dissociation of sulfonic acid groups into SO_3^- (fixed charge) and H^+ (mobile charge). The sufficient membrane hydration allows hydrogen ion to travel more easily in such condition that enhances the kinetic reactions; hence higher power output. However, over heating can dehydrate the membrane to cause reduction of ionic conductivity and cell performance. On the other hand, over hydration in a membrane can result in flooding in the cells obscuring the catalyst and terminating of electrochemical reaction. Membrane hydration is strongly related to the humidity of the reactant gases and the cell temperature. Therefore thermal and water management are the key factors in fuel cell optimization and it is essential for the performance enhancement in PEMFC stacks. A typical commercially available Nafion membrane thickness is between 50-254 μm (0.002" to 0.01") [21]. The thickness of the membrane is another factor that affects the fuel cell performance: a thick membrane decreases the ionic conductivity whereas a thin membrane could result in mechanical failure.

In the early development of fuel cells, the Pt catalyst loading was as high as 28 mg/cm^2. In recent years, the Pt loading is reduced to less than 1 mg/cm^2 without sacrificing the fuel cell performance or power output. In addition, optimizing the membrane thickness and the Pt loading will greatly affect the fuel cell performance. Furthermore, the electrochemical reaction happens at the "three phase boundary" where

porosity, ionomer and catalyst particles come together. Therefore, the structure of the MEA plays an important role in fuel cell performance as well [8].

1.4.4.2 Bipolar plates

Bipolar plates serve several functions in a fuel cell stack. They constitute the backbone of a fuel cell stack, isolate the individual cells, conduct current between cells, facilitate water and thermal management through the cell, provide conduits for reactant gases and remove reaction products (Figure 1.9) [23]. Because MEAs are made to be very thin, typically between 50 and 600 microns, bipolar plates comprise more than 60% of the weight and account for 30% of the total cost of a fuel cell stack [7,8,14,15]. The weight, volume and cost of the bipolar plates can be reduced significantly by improving the layout configuration of flow-field and the use of lightweight materials.

Poco graphite has been considered as the PEM fuel cell industry's reference standard for bipolar plates because of its excellent corrosion resistance, surface energy and low interfacial contact resistance (ICR). However, due to the graphite's brittleness and lack of mechanical strength combined with its relatively poor manufacturability and cost effectiveness for large production volume, Poco graphite bipolar plate material is deemed unsuitable for automotive application and commercialization. A number of materials are currently being developed and tested in laboratories around the world to produce cost effective and durable bipolar plates for PEM fuel cell. Varieties of non-coated and coated metals, metal foams and non-metal graphite composites are being reviewed for possible replacement of Poco graphite.

The ideal characteristics of a bipolar plate's material are to possess high corrosion resistance and low interfacial contact resistance, high mechanical strength, no permeability to reactant gases and no brittleness. Currently, graphite composite is considered suitable material for bipolar plate due to its relatively high corrosion-resistance. In addition, lower interfacial contact resistance and higher electrical conductivity can be obtained by having higher carbon to polymer ratio in the graphite composite [24]. However, this higher carbon ratio will increase the composite's brittleness and will elevate the volumetric power density when compared to thin metallic plates which is not favorable in automobile industry. Metal, on the other hand, provides

robustness and more flexibility in fabrication. The main challenge of metallic bipolar plate, however, is that corrosion-resistant metal develops a passive oxide-layer on the surface. Although this passive layer protects the bulk metal from progression of corrosion, it also causes an undesirable effect of high interfacial contact resistance. This causes the dissipation of some electric energy into heat and a reduction in the overall efficiency of the fuel cell power stack. The advantages and disadvantages of using graphite, graphite composite and metal as bipolar plate material are briefly summarized in Table 1.1. The key characteristics of bipolar plate's material that are suitable for transportation applications are [25-27]:

- Electrochemically stable in the fuel cell environment
  - High corrosion resistance with corrosion current at -0.1 V (SCE)and H_2 purge: < 1 Micro A/cm^2
  - High corrosion resistance with corrosion current at 0.6 V(SCE) and Air purge: < 1 Micro A/cm^2
- Possess steady low ohmic resistance throughout the operation
  - Interfacial Contact Resistance (ICR) at 140 N/cm^2: 10 milliohm.cm^2
- High surface tension with water contact angle close to 90^{o}C – i.e. high dehydration
- Light weight
- High mechanical strength: < 200 N/m2
- High volume cost effective manufacturability: $10/kW

The flow-field design also plays an important role in the optimization of a fuel cell stack [7,28]. It guides the reactant gases to flow within the active area (Figure 1.9) and affects the temperature, pressure and current density distribution and power output. Appropriate distribution of gas flow-fields can significantly increase the output power density [7,29,30].

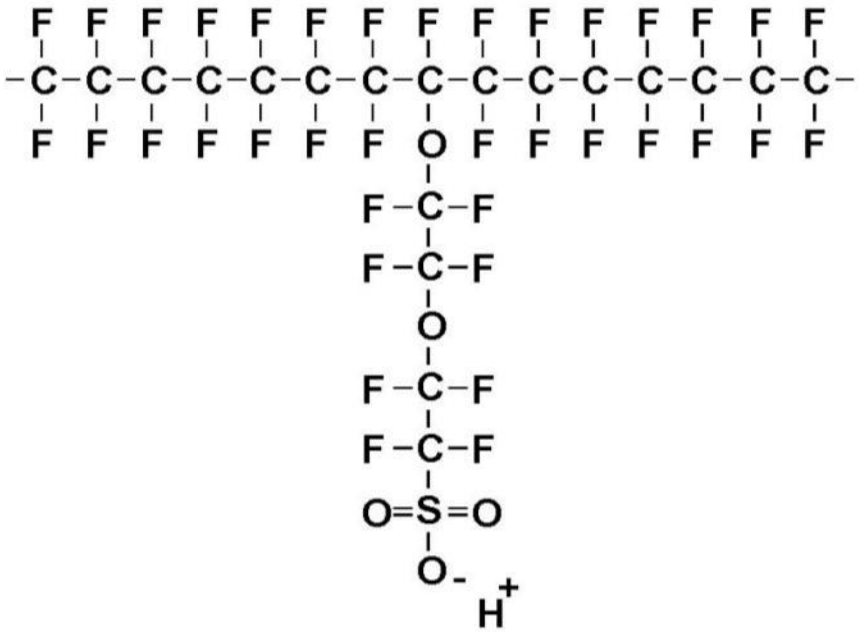

Figure 1.8: Structure of perfluorocarbon ion exchange polymers

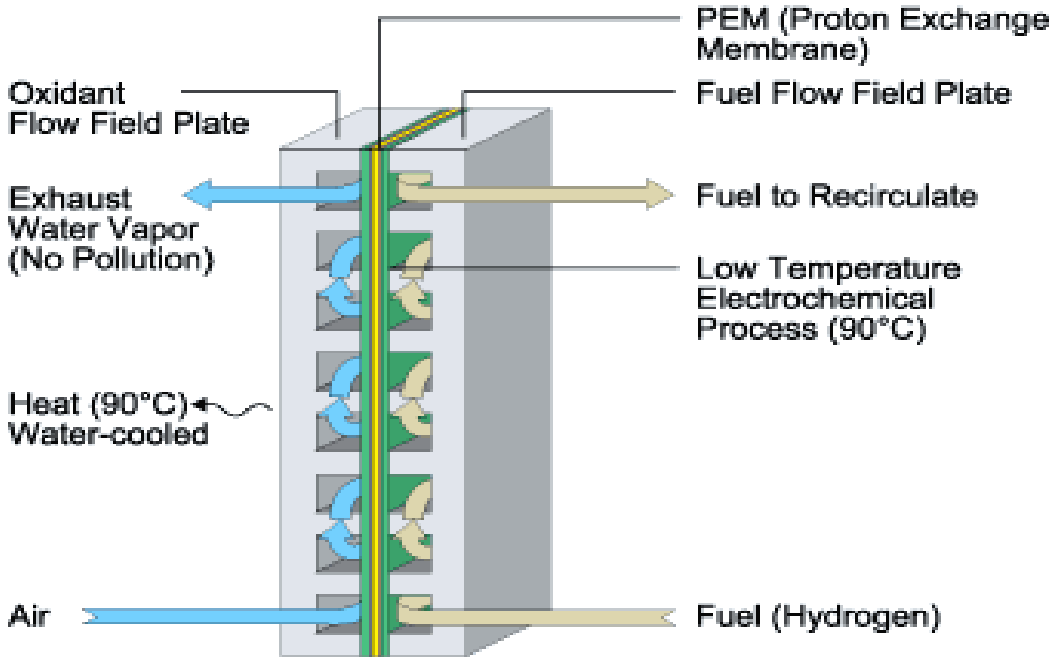

Figure 1.9: Flow paths in PEMFC bipolar plates (Ballard Power Systems **[23]**)

Table 1.1: Advantages and disadvantages of Poco graphite, graphite composite and metallic bipolar plates

Bipolar plate Material	Advantages	Disadvantages
Poco graphite	• Corrosion resistance • Low ICR • High power density	• Porous • Poor machinability • Brittle • Relatively expensive
Industrial graphite composite (Carbon powder + polymer resin)	• Corrosion resistance • Low ICR • Good machinability and can be mass produced	• moderate electrical conductivity (Higher electrical conductivity can be achieved by having higher carbon to polymer ratio. However, this will increase material's brittleness [24]) • Low thermal conductivity
Metal	• None porous • High electrical conductivity and thermal conductivity • Good machinability and can be mass produced • Durable • Relatively inexpensive	• Corrode in acidic environments • High ICR

In summary, material, flow-field design and fabrication technique of bipolar plates and MEAs as well as proper water and heat management can greatly affect the cost, efficiency, and performance of the PEM fuel cell power stacks. The following key areas in which improvements can be made to achieve higher power densities are recognized for further development:

- Material selection and optimization in electrolyte membrane, catalyst and bipolar plate.
- Structure of MEA and catalyst loading.
- Corrosion and interfacial contact resistance (ICR).
- Water and heat management.
- Flow-field configuration.
- Operating conditions: temperature, pressure, flow rates, humidification of reactant gases.

1.5 Research goals and approach

Metals hold an excellent potential for fuel cell power stack applications, particularly these related to the automotive industry, because metallic bipolar plates have higher mechanical strength, better durability to shocks and vibration, very low permeability to gases and much superior manufacturability and cost effectiveness in relation to carbon-based materials, namely, carbon–carbon and carbon–polymer composites. However, the main disadvantage of metals is their susceptibility to corrosion in acidic and humid environment inside the PEM fuel cell. Metals easily form a passive oxide layer that causes considerable output power degradation. Therefore, the main goal of this research work was to evaluate metallic bipolar plates and optimize key engineering design and manufacturing aspects necessary for PEM fuel cell power stack application. Thus, the research work focused on the implementation of the following two phases:

Phase I: Develop highly-conductive and corrosion-resistant coating material for metallic bipolar plates and conduct single fuel cell testing.

Phase I consisted of the following procedures:

1. Perform interfacial contact resistance and accelerated corrosion testing on a selected number of candidate metals and alloys such as stainless steel, nickel and chromium based super alloy, and carbide based material that could perform efficiently as bipolar plate material and/or coating. Graphite composite and Poco graphite were used as the baseline materials in this study because of their known corrosion resistance and relatively low interfacial contact resistance.
2. Design and fabricate single cells using graphite composite and selected metal(s) with the least interfacial contact resistance and the highest electrochemical stability. Examine the metallic bipolar plate fuel cells and compare their performance, efficiency, and hydrogen consumption in relation to graphite composite bipolar plate fuel cells over 1000 hours of operation.
3. Improve the bipolar plate flow-field design to enhance humidity conservation with the least pressure drop to minimize parasitic power. Fabricate single cells using the newly developed flow-field design and compared the power output to the standard triple serpentine flow-field design.
4. Conduct characterization studies on PEM metallic bipolar plates and membrane electrode assembly (MEA) after one thousand hours of operation using various spectroscopic techniques such as scanning electron microscopy (SEM), energy dispersive x-ray (EDX) analysis and x-ray diffraction (XRD).

Phase II: Design and develop high efficient PEM fuel cell stack and optimize the fuel cell stack performance

Phase II consisted of the following procedures:

1. Evaluate the thermal and water management effect on a fuel cell stack performance. The fuel cell stack was fabricated of graphite composite bipolar plates to eliminate the possible effect of metal corrosion and the associated increase of interfacial contact resistant over time on the stack power output.
2. Develop a finite element analysis (FEA) model of a bipolar plate to predict the temperature distribution within the bipolar plate for different materials. Investigate

the cooling capacity and fin design such that the fuel cell stack can maintain the temperature of 80°C or less during its operation.

3. Design and fabricate a three cell power stack based on the positive results obtained from the previous experimental work. Perform 750 hours of lifetime test on a three cell power stack and evaluate the fuel cell stack performance such as, voltage, current, power, air/hydrogen consumption and temperature.
4. Conduct characterization studies on PEM metallic bipolar plates, MEA and water collected after 750 hours of operation utilizing SEM, EDX and inductively coupled plasma - optical emission spectroscopy (ICP-OES).

CHAPTER 2

Literature survey of metallic bipolar plates in PEM fuel cells

Considerable attention was recently given to metallic bipolar plates for their particular suitability to PEMFC automotive applications. As mentioned earlier, metals provide many advantages over graphite based material and the only disadvantages of using metals are lower corrosion resistance and higher interfacial contact resistance (ICR) which both can cause considerable power degradation. This section describes each of the material candidates and their state of advancement for potential application in fuel cell bipolar plate technology.

2.1 Precious non-coated metals

Nobel metals such as gold and platinum have low ICR and high corrosion resistance, therefore their fuel cell performance when used as a bipolar plate perform very similar to Poco graphite bipolar plates [31,32]. In some cases, they showed better performance than Poco graphite. However, the high cost of these metals has prohibited their utilization for commercial use.

2.2 Non-coated metals

Major concerns have focused on metal corrosion and a decrease in ICR values once surface passivation film forms. Candidates such as stainless steel have been tested and used as bipolar plates. For example, Hermann et al. [27] reported that aluminum, stainless steel, titanium and nickel bipolar plates exposed to an operating environment similar to that of a fuel cell (pH: 2-3; T ~ 80^{o}C) were prone to corrosion or dissolution. A corrosion layer on the surface of a bipolar plate increases electrical resistance and decreases cell output. While this surface oxide layer protects the metal and stops the corrosion from progressing to the lower layers, it forms an electrically insulating interfacial layer. As the thickness of the oxide layer increases, ICR also increases that accordingly causes a decrease in electric power output.

Davies et al. [17] observed that under compaction pressure of 220 N/cm^2 imposed in fuel cell experiments, the relative ICR of various grades of stainless steel decreased in the

order 321 > 304 > 347 > 316 > Ti > 310 > 904 > Incoloy 800 > Inconel 601 > Poco graphite. For high alloy materials, the same authors observed that the oxygen was not as prominent as it was in other grades of stainless steel, which suggested that the passive film was thinner in these samples. The results showed that the passive film decreased in thickness according to the order 321 > 304 > 316 > 347 > 310 > 904 > Incoloy 800 > Inconel 601. Poco graphite, with the lowest surface resistive losses, produced the highest potentials, with increased polarization observed for metal plates in the order of Poco graphite < 310 < Ti < 316. The data indicated that the performance of the bipolar plates is related to thickness of the passive layer and ICR: as the thickness and ICR increase, more heat energy is generated and less output electric energy is produced.

Wang et al. [33,34] found that both austenitic (349TM) and ferritic (AISI446) stainless steel with high Cr content showed good corrosion resistance and could be suitable for bipolar plate application, though AISI446 requires some improvement in ICR due to formation of a surface passive layer of Cr_2O_3. The same authors also verified that Cr in the alloy formed passive film on the surface of stainless steel. As the Cr content in stainless steel increased, the corrosion-resistance improved as it is commonly known in the corrosion field and the results agreed with the findings of Davies et al. [17]. However, a thick non-conductive surface passive layer of Cr_2O_3 will produce an undesirable high ICR. Wang and Turner [34] studied stainless steel samples of AISI434, AISI436, AISI441, AISI444, and AISI446. They noted that in both PEM fuel cell anode and cathode environments, AISI446 steel underwent passivation and the formed passive films were very stable. An increase in ICR between steel and carbon backing material due to passive film formation was also reported. The same authors indicated that the thickness of passive film on AISI446 was estimated to be 2.6 nm for the film formed at 0.1V in the simulated PEM fuel cell anodic environment and 3.0 nm for the film formed at 0.6V in the simulated PEM fuel cell cathodic environment. The authors recommended that further improvement in the ICR would require some modification of the passive film, which was dominated by chromium oxide. They also stated that ICR for AISI446 increased after passivation. The XPS depth profiles indicated that air-formed surface film composed of iron oxides and chromium oxide but neither dominated. The passive films on AISI446 were mainly chromium oxide, and the iron oxides played only a minor role. In

simulations of the PEMFC, the passive film formed on the cathode was thicker than that formed on the anode, with the former resulting in higher ICR.

Metals such as Al, Ti, Ni, etc. similarly form a surface passive layer, in fuel cell acidic environment, which has good corrosion resistance but poor ICR. Moreover, for uncoated metals, ions and oxides could directly foul the solid electrolyte and tarnish the catalyst in the MEA that result in considerable adverse effects on the cell performance. Specifically, as unprotected metal bipolar plates are exposed to a corrosive environment inside a fuel cell in which, relative humidity (> 90%), acidity (pH = 2-3) and temperature (60-80^{o}C), metal dissolution will occur. The dissolved metal ions diffuse into the membrane and then get trapped in the ion exchange sites inside the ionomer, resulting in lowered ionic conductivity as described by Mehta and Cooper [25]. A highly conductive corrosion resistance coating with high bonding strength at the interfacial layer between base metal substrate and coating layer is required to minimize this problem.

2.3 Coated metals

Metallic bipolar plates are often coated with protective coating layers to avoid corrosion. Coatings should be conductive and adhere to the base metal without exposing the substrate to corrosive media [26]. Two types of coatings: carbon-based and metal-based, have been investigated [25,26,35]. Carbon-based coatings include graphite, conductive polymer, diamond-like carbon and organic self-assembled monopolymers [27]. Noble metals, metal nitrides and metal carbides are some of the metal-based coatings that have been explored [32,35-39]. To be effective, the coefficient of thermal expansion of base metal and coating should be as close as possible to eliminate formation of micropores and microcracks in coatings due to unequal thermal expansion [35]. In addition, some coating processes are prone to pinhole defects and viable techniques for coating bipolar plates are still under development [27]. Mehta and Cooper [25] presented an overview of carbon-based and metallic bipolar plate coating materials. Table 2.1 lists bipolar plate coatings and coating techniques summarized by several groups [25,27].

Woodman et al. [35] concluded that the coefficient of thermal expansion (CTE), corrosion resistance of coating, and micro-pores and micro-cracks play a vital role in protecting bipolar plates from the hostile PEM fuel cell environment. The authors also

argued that even though PEM fuel cells typically operate at temperatures less than 100^{o}C, vehicle service would impose frequent start up and shut down conditions, and temperature differentials of 75-125^{o}C would be expected during typical driving conditions. A large difference in the CTE of the substrate and coating materials may lead to coating layer failure. One technique to minimize the CTE differential is to add intermediate coating layers with less CTE mismatch between that of adjacent layers. Materials such as Al, Cu, Sn, Ni and Ni phosphorous are very susceptible to electrochemical corrosion in acidic solutions that are typical of PEMFC operating conditions. However, gold shows very high resistance to electrochemical corrosion, comparable to graphite, the traditional bipolar plate material.

Table 2.1: Coating materials and coating processes for metallic bipolar plates

Coating method	Coating materials	Coating processes	Base plate materials				Ref.
			Al	SS	Ti	Ni	
Conductive polymers coating	Polyaniline (PANI) and Polypyrrole (PPY).	Cyclic voltammetry	X	X			[40]
Diamond-like carbon coating	YZU001 like-diamond film	Physical vapor deposition (PVD) coating	X	X			[41]
Gold topcoat layering	Gold over nickel over copper	Pulse current electrodeposition	X				[35,36]
Graphite foil layering	(1) Sublayer—sonicated graphite particles in an emulsion, suspension or paint (e.g. graphite particles in an epoxy resin thinned by an organic solvent, such as toluene); (2) topcoat—exfoliated graphite in the form of sheets of flexible, graphite foil	Painting OR pressing	X		X	X	[42]
Graphite topcoat layering	(1) Sublayer— titanium over titanium–aluminum-nitride; (2a) overcoat— transient metal sublayer of Cr (Ti, Ni, Fe, Co) followed by sulfuric/chromic acid OR; (2b) topcoat—graphite	PVD (closed-field, unbalanced, magnetron sputter ion plating) and chemical anodization/oxidation overcoating	X	X	X	X	[42]
Indium doped tin oxide layering	Indium doped tin oxide (Sn(In)O2)	Electron beam evaporation		X			[43]
Lead oxide layering	(1) Sublayer—lead; (2) topcoat—lead oxide (PbO/PbO2)	Vapor deposition and sputtering		X			[43]
Organic monopolymer coating	Organic self-assembled monopolymers	Not specified		Not specified			[26]
Silicon carbide layering	(1) n-Type silicon carbide (SiC); (2) Gold	Glow discharge decomposition and vapor deposition		X			[43]
Stainless steel layering	(1) Sublayer—chromium/nickel/molybdenum-rich stainless steel OR nickel-phosphorus alloy; (2) topcoat—titanium nitride	Physical vapor deposition (PVD) (e.g. magnetron sputtering), or chemical vapor deposition (CVD), and electroless deposition for Ni-Ph alloy	X	X	X		[44]
Titanium–aluminum nitride layering	Titanium–aluminum-nitride layer	RF-planar magnetron (sputtering)	X				[43]
Titanium nitride layering	Titanium nitride (TiN) layer	RF-diode sputtering/ Hollow cathode discharge (HCD)	X		X		[43,45, 46]
Chromium nitride layering	Chromium nitride layer	Thermal nitridation spraying		X		Ni/Cr	[37,38, 39]

2.3.1 Metal-based coatings

2.3.1.1 Gold plated aluminum

Hentall et al. [31] machined current collectors from Al to the exact dimensions of graphite bipolar plates, then coated it with Au by a solution process. The plates were then used in a fuel cell and during initial warm-up, the data indicated performance very similar to graphite (1.2 A/cm^2 at 0.5V) because an Au coated Al plate had a similar ICR with gas diffusion media (GDM) to graphite. However, the performance degraded quickly to 60 mA/cm^2 at 0.5V. The analysis revealed that some of the Au coating lifted from the plate and physically embedded in the membrane. Wind et al. [32] also indicated that Au-coated bipolar plate (SS 316L) clearly demonstrated no difference between the metal-based and graphite plates due to the same reason mentioned above.

Woodman et al. [35] measured the coefficient of thermal expansion (CTE) for aluminum to be approximately 24 µ in./in./°C (over 0 - 400°C) while the CTE for Au, for example, was approximately 14 µ in./in./°C over the same temperature range. The authors concluded that the differential of thermal expansion was 0.11% at 120°C and the mechanism for coating failure was an initiation of plastic deformation of the coating material. The failure of Au coating would be expected at a differential expansion of only 0.08% once the plastic deformed.

Due to high price of Au-coated bipolar plates, this technology stands to face extreme competition from other less expensive corrosion resistant coatings for bipolar plates (Table 2.2). Also, coating techniques and surface preparation must be optimized to improve the bonding strength between Au coating and the substrate base plate to eliminate the possibility of separation. The graphite bipolar plate has a material cost of $89/kW whereas the Au-coated Al has a cost of $346/kW. Using a non-coated Al bipolar plate gives a material cost of $2.71/kW. For example, using an electroless nickel coating on Al gives a bipolar plate cost of $3.20/kW [36]. However, as indicated earlier, Ni phosphorous coatings are very unstable in the PEM fuel cell environment even though their cost as compared to gold might make them very attractive coating from a cost prospective.

Table 2.2: Bipolar Plate Materials and High-Volume Material Costs

Material	Material Cost ($/g)	Density (g/cm3)
Graphite	0.105	1.79
Aluminum	0.0088	2.7
Gold	9.97	19.32
Electroless nickel	0.034	8.19

2.3.1.2 TiN coated bipolar plates

Li et al. [46] investigated the corrosion behavior of TiN coated 316 stainless steel in a simulated PEMFC environment. Pure O_2 and H_2 gases were bubbled through 0.01M HCl/0.01M Na_2SO_4 solutions by using electrochemical measurement techniques. The authors observed that TiN coatings had better corrosion resistance and passivity under both simulated conditions than stainless steel with no significant degradation of TiN coatings in four hours under typical load conditions of a fuel cell. The authors reported a loss of small part of coatings that had occurred during the immersion tests of TiN coatings in the O_2 environment for 1000 hours and in the H_2 environment for 240 hours, respectively, but the exposed substrate areas were passivated in both environments. The results revealed that TiN coating could offer higher corrosion resistance and electric conductivity than SS316. Further effort to improve the coating quality and evaluation of the long-term stability of SS316/TiN coating system under simulated conditions are required.

Similar work was conducted by Cho et al. [45]. They observed significant improvement in the lifetime of AISI 316 stainless steel bipolar plates coated with corrosion-protective TiN layer. The coating process began with chemical etching of 1.5mm thick AISI 316 stainless steel bipolar plates to form flow channels. This was followed by coating the surface of the plates with TiN layer using hollow cathode discharge (HCD) ion plating method. The HCD system consisted of a vacuum chamber with a pressure of 3×10^{-6} Torr which was then purged with Ar gas in which the etched

plates were placed and a Ti target was evaporated at a discharge voltage of 260V. N_2 gas with an operating pressure of 6.3×10^{-3} Torr was fed at a flow rate of 160 standard cubic centimeter (sccm) to form a 1 μm thick TiN layer on the surface of the plates.

Surface energy and ICR of bipolar plates are other important factors affecting cell performance, particularly at high current densities since water produced by the cathode reaction should be immediately removed to avoid flooding and power degradation due to catalyst submergence. High ICR of the bipolar plates will also reduce electric energy output due to partial conversion to heat energy. Bipolar plates with low surface energy, low water contact angle smaller than 90^o and high surface wetability could directly contribute to flooding of cathode side of the fuel cell. To evaluate surface energy of different materials, the water contact angle could be measured and evaluated. A larger contact angle is an indication of high surface energy or surface tension of a material and low surface wetability. For instance the water contact angle of graphite and TiN-coated 316 was almost same and equal to 90^o while that of 316 stainless steel was 60^o. The results obtained by Cho et al. [45] imply that the 316 stainless steel has low surface energy and more readily floods the cathode side than graphite and TiN-coated SS316. The authors also stated that the dissolution of metallic elements such as Fe, Ni, Cr, and Ti from TiN-coated 316 bipolar plates into the MEA could increase ohmic resistance and charge transfer resistance of the single cell by contaminating the membrane and active catalytic sites.

2.3.1.3 CrN/Cr_2N coating on a model Ni-Cr alloy

Brady et al. [47] recently developed a preferential thermal nitridation process to form defect-free coatings or a pinhole free CrN/Cr_2N coating on a Ni–Cr alloy base plate, which show promise with excellent corrosion resistance and negligible ICR. They pointed out that dense, electrically conductive, corrosion-resistant Cr-nitride surfaces can be formed on Ni-Cr and Ni(Fe)-Cr base alloys at Cr levels < 35 weight percent by thermal nitridation. They nitrided 446 stainless steel (and likely other Fe-Cr base alloys), under certain conditions that modify the native passive oxide layer but do not form a dense Cr-nitride surface, can lower ICR by over an order of magnitude without

compromising corrosion resistance. Both of these surface modifications show promise for protecting metallic bipolar plates in PEMFC environments.

2.3.1.4 Carbide based amorphous metallic coating alloy

Natesan and Johnson [48] studied the oxidation and sulfidation of SS310 and chromium-carbide and Cr-coated alloy in high O_2 and S environment in a temperature range of 650-875°C. The use of appropriate corrosion resistant coatings on metallic components offers an avenue to minimize material degradation and extend their lifetime. The coatings for the test were developed by an electro-spark deposition process in which short duration and high-current electrical pulses were used to deposit the electrode material on the metallic substrate. They observed that in a high sulfur environment, the uncoated alloy exhibited severe sulfidation corrosion by means of (Fe, Ni) sulfide formation; the Cr-coated alloy exhibited moderate corrosion whereas the chromium-carbide-coated alloy exhibited the least corrosion. Vickers hardness measurements made by Natesan and Johnson [48] on the surface and as a function of depth showed that the initial high hardness values of chromium-carbide coated specimens were retained even after oxidation and sulfidation treatment.

2.3.2 Conducting polymer based coatings

Shine et al. [40] electrochemically coated 304 stainless steel with conducting polymers polyaniline (PANI) and polypyrrole (PPY). Cyclic voltametry was used for polymerization and deposition of these polymers. The polymer-coated stainless steel plates were tested for corrosion and ICR under PEM fuel cell conditions. An improved corrosion resistance with acceptable ICR was observed but cost, durability, and volume production were not mentioned in the study.

2.3.3 Fe-based amorphous alloys

Jayaraj et al. [49] investigated the corrosion behavior of two Fe-based amorphous alloys: $Fe_{48}Cr_{15}Mo_{14}Y_2C_{15}B_6$ and $Fe_{50}Cr_{18}Mo_8Al_2Y_2C_{14}B_6$, under conditions that simulate the fuel cell environment in comparison with those of a stainless steel. H_2 gas and pressurized air were bubbled into a 1M H_2SO_4 + 2ppm F^- solution at 75^oC throughout the experiment to simulate the respective anodic and catholic PEMFC environment. The

$Fe_{50}Cr_{18}Mo_8Al_2Y_2C_{14}B_6$ amorphous alloy displayed significantly higher corrosion resistance in relation to the SS316L of identical Cr content. Also, the data indicated that higher Cr content played an important role in improving corrosion resistance.

2.3.4 Diamond like coating

Lee et al. [41] applied PVD coating of YZU001 like-diamond film on the 5052 Al alloy and SS 316L and compared their performance to that of graphite. The corrosion rates were determined by Tafel-extrapolation method from the polarization curves. The coated Al, 316L stainless steel and graphite were fabricated into a single cell to measure ICR and to test cell performance. The metallic bipolar plates, PVD coated 5052 aluminum and SS 316L, performed better than the graphite material at low voltage but experienced shorter cell life. It was also observed that the SS316L plate with its naturally formed passive film had better corrosion rate than the YZU001 coated Al plate. The ICR of stainless steel was higher thus reducing its single cell performance. The coated Al plates had better ICR and single cell performance; however, the cell life was shorter.

2.3.5 Porous materials and metal foams

Kumara and Reddy [50] investigated three different porous materials namely, Ni–Cr metal (Fe: up to 8%, C: up to 2%, Cr: 30–54%, Ni: balance) foam with 50 PPI (pores per inch), SS316 metal foam with 20 PPI, and carbon cloth. The MEA metal ion contamination can be minimized to a great extent by optimizing the fluid-flow in metal foams. In this system, any metal ion products that are formed will not stagnate in the cell stack but are exhausted along with the by-product water [51]. The data were consistent with the metal foams performing better than the conventional channel design flow-field. Furthermore, it was seen that with a decrease in permeability of the metal foam, the cell performance increased. The performance could be further increased by carefully tailoring the size, shape and distribution of pores in the metal foam. An additional advantage will accrue as these metal foams could possibly be used for catalyst support in the electrochemical reactions within the fuel cell, thereby eliminating the need to use carbon electrodes. However the metal foam will most likely corrode when in direct contact with the acidic membrane and would lead to severe MEA contamination.

2.3.6 Untreated 316 SS screens and foils

Wilson et al. [52] focused on development of non-machined and low-cost bipolar plates based on the use of untreated 316SS screens and foils. After building and testing a single cell, they examined the MEA by EDS and found the membrane to be relatively clean. However, EDS cannot quantitatively distinguish metal ions that are present in stainless steel because the scope itself was made of the same material. In order to accurately assess the presence of various metals that might be present in the MEA, XRF spectra were obtained before and after testing the MEA for 2000 hours. The final XRF data were consistent with the presence of metals such as Fe and Ni in appreciable quantities.

Many types of alloys have been developed for applications where common stainless steels such as SS304 or SS316 do not provide adequate interfacial contact resistance. In general, the compositions of these alloys are similar to their stainless steel or nickel-base counterparts except that certain stabilizing elements, such as Ni, Cr and Mo are added or are present in much higher concentrations in order to obtain desirable corrosion properties. However, in neutral to oxidizing media, a high Cr content (which is often accompanied by the addition of Mo) is necessary. These cells were operated at 0.3 MPa and at 80ºC. The humidifiers on the anode and cathode sides were heated to 100 and 80^{o}C, respectively. Purified H_2 was introduced at 0.3 standard liters per minute (SLPM). Compressed room air was provided to the cell at 1.8 SLPM.

The Ni levels of 0.85, 0.56, 2.4 ppm were measured in the anode-face exposed solutions and 0.034, 0.019, 0.027 ppm Ni in the cathode-face exposed solutions for 0-1500, 1500-3400, and 3400-4100 hour segments of exposure, respectively. Cr was not detected and visual analysis of the test coupon showed no evidence of corrosive attack. The Ni–50Cr alloy (no nitridation treatment) had a lower ICR than 316L stainless steel.

XRF was used to examine the anode- and cathode-side membranes and ELAT backings from the two, 500 h tests. Only trace levels of Ni and Cr were found, in the range of 0.01-0.3 μg/cm^2, which is on the order of the detection limit in the measurements. This low level of contamination indicates inert and protective behavior by the CrN/Cr_2N surface with few, if any, through thickness pin-hole defects. To put this result in context, Wind et al. [32], for example, reported that 316L stainless steel tested

for 100 hours at 75 ºC as a bipolar plate material resulted in Ni contamination levels of 76 μg/cm^2 (see Ref. [32] for specifics of these fuel cell test conditions). It should be noted that some stagnant Cr-rich liquid was found in one of the alignment pin ports on disassembly of the cell. However, no membrane contamination was found in this area. A small Cr–O–C rich surface region (~0.5 - 1mm) found at this location was likely the source of the Cr-rich liquid. A major casting flaw or inclusion may have led to local poor nitridation, making this area vulnerable to attack, although the stagnant liquid may also have led to more corrosive local conditions against which the Cr-nitride was not sufficiently resistant.

2.4 Composite plates

Composite plates can be categorized as metal or carbon based. A metal-based composite bipolar plate has been developed by a group at the Los Alamos National Laboratory [27]. This design combines porous graphite, polycarbonate plastic and stainless steel in an effort to leverage the benefits of different materials. Since porous graphite plate production is not as time consuming or expensive as producing nonporous graphite plates, it can be used while impermeability is provided by the stainless steel and polycarbonate parts. Stainless steel also provides rigidity to the structure while the graphite resists corrosion. The polycarbonate provides chemical resistance and can be molded to any shape to provide for gaskets and manifolds. The layered plate appears to be a very good alternative from stability and cost standpoints.

2.5 Summary

Durability of bipolar plates is defined by the length of its lifetime in combating corrosion while maintaining low ICR without experiencing any drastic loss of power and this is one of the key requirements in fuel cell technology. Metallic plates were proven to surpass the mechanical strength of graphite composite plates. As indicated earlier, metallic plates are prone to corrosion in the fuel cell environment. Considerable research work has been conducted to combat the metallic bipolar plate durability issue to enhance the material's corrosion resistance and interfacial contact resistance. The accelerated corrosion test and interfacial contact resistance test are widely used to evaluate the

bipolar plate durability. In addition, actual fuel cells were built using different bipolar plate materials to investigate their lifetime performance. Table 2.3 shows a detailed list of metallic bipolar plate durability test results from different researchers. In addition, the overall comprehensive testing and evaluation of various materials for metallic and non-metallic bipolar plates are compiled in Table 2.4 to provide a quick reference of the most up to date research findings in this area of the PEM fuel cell technology. The current bipolar plate specifications and the DOE technical and cost targets are also listed in Table 2.4.

In summary, the literature survey indicated that replacing graphite composite plates with metallic bipolar plates holds a promising potential. This survey presented in this thesis gives a clear distinction between metal and graphite suitability for PEM fuel cell application.

Table 2.3: Summary of metallic polar plate materials and their durability study

Material	Accelerated durability/corrosion test method	ICR (Before corrosion/life-time testing)	ICR (After corrosion/life-time testing)	Single cell/ Stack lifetime testing	Ref
AISI446	Polarized at 0.6V for 7.5 hours vs SCE	190 mΩ cm2 at 140 N/cm2	~260 mΩ cm2 at 140 N/cm2	-	[53]
AISI446 (Nirtided)	Polarized at 0.6V for 7.5 hours vs SCE	6 mΩ cm2 at 140 N/cm2	~16 mΩ cm2 at 140 N/cm2	-	
Modified446	Polarized at 0.6V for 7.5 hours vs SCE , Air Purge	4.8 mΩ cm2 at 140 N/cm2	~8 mΩ cm2 at 140 N/cm2	-	
Modified446	Polarized at -0.1V for 7.5 hours vs SCE , H2 Purge	4.8 mΩ cm2 at 140 N/cm2	~9.6 mΩ cm2 at 140 N/cm2	-	
Ni-50Cr (Nitrided)	4100 hours in Simulated PEM FCcorrosion test cell	10 mΩ cm2 at 140 N/cm2	~10 mΩ cm2 at 140 N/cm2	1000 hours	[47]
Proprietary coating on SS316L	-	-	-	1000 hours	[32]
Proprietary coating (FC5) on Ti	-	<10 mΩ cm2 at 200 N/cm2	<10 mΩ cm2 at 200 N/cm2	10000 hours	[54]
Proprietary coating (FC6) on SS316	-	<15 mΩ cm2 at 200 N/cm2	-	3000 hours	
Proprietary coating (FC7) on SS316	-	<10 mΩ cm2 at 200 N/cm2	-	2000 hours	
Proprietary coating on Superferritic SS (E-Brite)	-	-	-	200 hours	[52]
TiN on SS316	-	-	Ohmic & Charge transfer resistance increased 20%	700 hours	[53]
SS316	-	-	Ohmic & Charge transfer resistance increased 200%	200 hours	
TiN on SS316 (1kW stack)	-	-	degradation rate 11%mV/ 1000hour	1000 hours	

Material	Accelerated durability/corrosion test method	ICR (Before corrosion/life-time testing)	ICR (After corrosion/life-time testing)	Single cell/ Stack lifetime testing	Ref
SS316	-	~50 mΩ cm2 at 140 N/cm2	~70 mΩ cm2 at 140 N/cm2	3000 hours	[55]
SS310	-	~40 mΩ cm2 at 140 N/cm2	~60 mΩ cm2 at 140 N/cm2	3100 hours	
SS904	-	~40 mΩ cm2 at 140 N/cm2	-	1100 hours	
SS349TM	Polarized at 0.6V for 7.5 hours vs SCE	~120 mΩ cm2 at 140 N/cm2	~200 mΩ cm2 at 140 N/cm2		[33]
SS316L	-	-	Deteriorted continuously	300 hours	[56]
SS316L (Electrochemical processed)	-	-	Steady performance	300 hours	
Gold on Stainless steel	-	-	Steady performance	300 hours	[57]
SS304	Polarized at 0.6V for 8 hours vs SCE	~140 mΩ cm2 at 240 N/cm2	~112 mΩ cm2 at 240 N/cm2	-	[58]
Ti2N/TiN on SS304	Polarized at 0.6V for 8 hours vs SCE	~19 mΩ cm2 at 240 N/cm2	~37 mΩ cm2 at 240 N/cm2	-	
TiN on SS304	Polarized at 0.6V for 8 hours vs SCE	~19 mΩ cm2 at 240 N/cm2	~25 mΩ cm2 at 240 N/cm2	-	
Hastellloy G35	-	30-75 mΩ cm2 at 100-200 N/cm2	-	-	[59]
Hastellloy G35 (Nitrided)	Polarized at 0.84V for 7.5 hours vs SHE	~10 mΩ cm2 at 140 N/cm2	~20 mΩ cm2 at 140 N/cm2	2500 hours	
Ferritic stainless steel (AL 29-4C)	-	>100 mΩ cm2 at 100-200 N/cm2	-	-	
Ferritic stainless steel (AL 29-4C) (Nitrided)	Polarized at 0.84V for 7.5 hours vs SHE	~10 mΩ cm2 at 140N/cm2	~20 mΩ cm2 at 140N/cm2	-	

Table 2.4: Summary of metallic polar plate materials, coatings and their corrosion current density and interfacial contact resistance

Plate Material	Coating material (thickness)	Corrosion current density (DOE Target 1μA/cm2) / Corrosion rate	Contact resistance (DOE Target 10mΩcm2),	Cost (DOE2010 Target $10/kw)	Ref.
316SS	Cr-nitride	316SS(~300μA/cm2). Cr-Nitrided SS316 (1μA/cm2), 0.5 M H_2SO_4 + 5 ppm F at 70C	Before operation, 316SS(55mΩ cm2). Cr-Nitrided SS316 (10mΩ cm2)		[60]
Ni-Cr base alloys (Hastelloy G-30, G-35), Ferritic stainless steel (AL 29-4C)	Thermal nitridation	Anode current at 70C, 1M H_2SO_4+2ppmF- with hydrogen purge, Nitrided G-35 (0.5μA/cm2), Nitrided AL29-4C (0.3μA/cm2)	Before operation, G-30 & G-35 (30-75mΩ cm2). AL29-4C (>100mΩ cm2), Nitrided G-30 & G-35 (10mΩ cm2), Nitrided AL29-4C (>10mΩ cm2)		[59]
AISI446, 316LSS, 349TM, 2205	Nitrided AISI446	Anode potential CD at -0.1V at 70C, 1M H_2SO_4+2ppmF- with hydrogen purge, AISI446(-2.0~-1.0μA/cm2), 2205(-0.5~0.5μA/cm2), 349TM(-4.5~-2.0μA/cm2), Nitrided AISI1446(-1.7~-0.2μA/cm2), Modified AISI446(-9.0~-0.2μA/cm2) Cathode potential CD at 0.6V at 70C, 1M H_2SO_4+2ppmF- with air purge, AISI446(0.3~1.0μA/cm2), 2205(0.3~1.2μA/cm2), 349TM(0.5~0.8μA/cm2), Nitrided AISI1446(0.7~1.5μA/cm2), Modified AISI446(1.5~4.5μA/cm2)	Before operation, AISI446(190mΩ cm2), 2205(130mΩ cm2), 349TM(110mΩ cm2), Nitrided AISI446 (6mΩ cm2), Modified AISI446 (4.8mΩ cm2), at 140 N/cm2	AISI446(4.76$/kW), 349TM(4.22$/kW), 2205(3.14$/kW), Nitrided AISI446 (N/A), Modified AISI446 (N/A)	[53]
Ni-50Cr alloy, 349TM SS	Thermal nitridation on Ni-50Cr (3-5μm) and 349TM	Anode environment CD at -0.1V, at 70C, 1M H_2SO_4+2ppmF-, with hydrogen purge, Nitrided Ni-50Cr(3-4μA/cm2), Nitrided 349TM(15-20mA/cm2), Cathode environment CD at 0.6V, with air purge, 349TM(~0.25mA/cm2)	Before operation, Ni-50CrL(~60mΩ cm2), nitrided Ni-50Cr(~10mΩ cm2), 349(~100mΩ cm2), Nitrided 349 (~10mΩ cm2) at 150 N/cm2	-	[37]
AISI446	Thermal nitridation on AISI446 (~1μm)	Anode environment CD at -0.1V, at 70C, 1M H_2SO_4+2ppmF-, with hydrogen purge, Nitrided AISI1446(~-1μA/cm2). Cathode environment CD at 0.6V, with air purge, Nitrided AISI1446(~0.6μA/cm2)	Before operation, Polarized 7.5h at 0.6V, Nitrided AISI446 (<40mΩ cm2), at 150 N/cm2	-	[38]
Ni-Cr alloy	Thermal nitridation (3-5μm)	-	Before operation, 316L(~160mΩ cm2), Ni-50CrL(~60mΩ cm2) Nitrided Ni-50CrL(~10mΩ cm2) at 140 N/cm2	-	[39]

Plate Material	Coating material (thickness)	Corrosion current density (DOE Target 1μA/cm2) / Corrosion rate	Contact resistance (DOE Target 10mΩcm2),	Cost (DOE2010 Target $10/kw)	Ref.
Ni-Cr alloy, AISI446	Thermal nitridation	-	Nitrided AISI446 (20mΩ cm2), at ~150 N/cm2	-	[47]
AISI434, 436, 441, 444, 446	-	Anode environment CD at -0.1V, at 70C, 1M H_2SO_4+2ppmF-, with hydrogen purge, AISI446(10-15μA/cm2), 444(50μA/cm2), 436(60μA/cm2), 434(200μA/cm2), 441(300μA/cm2) at 70C, 1M H_2SO_4+2ppmF-	Before operation AISI446>434>441>436>444 (between100-200mΩ cm2) at 140 N/cm2 (small different)	-	[34]
		Cathode environment CD at 0.6V, with air purge, AISI446(10-15μA/cm2), 444(20μA/cm2), 436(20μA/cm2), 441(60μA/cm2), 434(100μA/cm2) at 70C, 1M H_2SO_4+2ppmF-	After passivation AISI446(280mΩ cm2 anode environment), (350mΩ cm2 cathode environment) at 140 N/cm2		
316LSS, Ni-Cr alloy	Thermal nitridation	-	Before operation, 316L(~160mΩ cm2), Ni-50CrL(~60mΩ cm2), Nitrided Ni-50CrL(~10mΩ cm2) at 140 N/cm2, After passivation, Nitrided Ni-50CrL(no increase)	-	[61]
349TM SS, 316L, 317L,904L	-	Anode environment CD at -0.1V, at 70C, 1M H_2SO_4+2ppmF-, with hydrogen purge, 349TM >904L>317L>316L	Before operation (mΩ cm2) 316L>317L>904L>349(160-100mΩ cm2) at 140 N/cm2	-	[33]
		Cathode environment at 0.6V, with air purge, 349TM >904L>317L>316L	After passivation (mΩ cm2) 349(200mΩ cm2) at 140 N/cm2		
316LSS	Electrochemical process	Electrochemical processed 316L (~0.030mmpy), 0.5M H_2SO_4	Before operation 316L(48mΩ), Electrochemical processed 316L(~7-27mΩ) at 15kgf	-	[56]
316LSS	Electrochemical process	0.6V Potential, 0.5M H_2SO_4, 316L(60μA/cm2), Electrochemical processed 316L(15μA/cm2), 316LSS(0.1mmpy), Electrochemical processed 316L(~0.030mmpy)	-	-	[62]
316LSS, Aluminum 5052, Graphite	YZU001 On Aluminum 5052	Al(1.16mmpy), Al-coated(0.247mmpy), 316LSS(0.1mmpy), Graphitel(0.019mmpy), 0.5M H_2SO_4	-	-	[41]

Plate Material	Coating material (thickness)	Corrosion current density (DOE Target 1μA/cm2) / Corrosion rate	Contact resistance (DOE Target 10mΩcm2),	Cost (DOE2010 Target $10/kw)	Ref.
low-carbon steel AISI 1020	reforming pack chromization process	AISI 1020 (634μA/cm2), 1020-Cr (1.24μA/cm2), 1020-EMD-Cr (<1μA/cm2) 0.5 M H_2SO_4	AISI 1020 (403.8 mΩ cm2), 1020-Cr (39mΩ cm2), 1020-EDM-Cr (<17mΩ cm2),	-	[63]
316SS	TiN (2-4μm)	TiN coating(0.25μA/cm2 with O2 bubbled solution) & (0.32μA/cm2 with H2 bubbled solution), 316SS (4.4μA/cm2 with O2 bubbled solution) & (27.1μA/cm2 with H2 bubbled solution), at 80C, 0.01M HCI+0.01M Na2SO4	-	-	[46]
316SS		Anode potential CD at -0.11V, at 80C, 0.01M HCI+0.01M Na2SO4 bubbled with hydrogen, 316SS(~1.6μA/cm2),	-	-	[64]
316SS, Titanium	Ti-FC5, SS316FC6, SS316FC7		Before operation 316SS(~40mΩ cm2), FC5,6,7(~10-15mΩ cm2) at 200 N/cm2	-	[54]
321SS, 304SS, 347SS, 316SS, Ti, 310SS, 904LSS, Incoloy800, Inconel601, Poco Graphite	-	-	Before operation 321SS(100mΩ cm2), 304SS(51mΩ cm2), 347SS(53mΩ cm2), 316SS(37mΩ cm2), Ti(32mΩ cm2), 310SS(26mΩ cm2), 904SS(24mΩ cm2), Incoloy800(23mΩ cm2), Inconel 601(15mΩ cm2), Poco Graphite(10mΩ cm2) at 220 N/cm2 After 1200h operation Ti(250mΩ cm2), SS316(44mΩ cm2), SS310(28mΩ cm2), Poco Graphite(10mΩ cm2) at 220 N/cm2	-	[17]
310SS, 316SS, 904LSS	-	-	Before operation 904LSS< 310SS<316SS. After operation SS310<SS316	-	[55]
Titanium, 316SS, Poco Graphite	FC5(1μm) on Ti (proprietary)	-	Before operation 316SS(37mΩ cm2), FC5(~13mΩ cm2), Graphite(10mΩ cm2) at ~220 N/cm2	-	[65]
Aluminum	Gold plated aluminum (2μm)	Aluminum(~250μmpy), Copper(>500μmpy), Gold plated aluminum(~750 μm/year), 316LSS(<100μmpy), Graphite(<15μmpy), Silver(<15μmpy), Gold(<15μmpy), Nickel(>1000μmpy), Phosphorous copper(~500μmpy), Phosphorous Nickel(<30μmpy), Tin(>10000μmpy), Titanium(<100μmpy), Tungsten(<100μmpy), Zinc(>2000μmpy), 0.5 M H_2SO_4	-	Graphite ($75/kg), conductive plastics ($5-$30/kg), Gold plated aluminum ($7/kg)	[35]

Plate Material	Coating material (thickness)	Corrosion current density (DOE Target 1μA/cm2) / Corrosion rate	Contact resistance (DOE Target 10mΩcm2),	Cost (DOE2010 Target $10/kw)	Ref.
Aluminum	Multi layer coating, (Ni, Au) conductive polymers (polyaniline)	-	-	Graphite ($89/kW), Gold plated ($346/kW), Nickel plated, ($3.2/kW), Aluminum ($2.71/kW)	[36]
Fe- and Ni-base amorphous alloys, Fe-Al2, Fe-Al1N1, Ni-Ta5	-	Anode potential at -0.1V at 80C, 1M H_2SO_4+2ppmF- with hydrogen bubbling, Fe-Al2(140μA/cm2), Fe-Al1N1(48μA/cm2), Ni-Ta5(52μA/cm2)	Before operation , (8-20mΩ cm2)	-	[66]
316LSS, Fe based alloys - Fe50Cr18Mo8Al2YC14B6	-	Anode potential at -0.1V at 75C, 1M H_2SO_4+2ppmF- with hydrogen bubbling, Fe based alloy(2.48μA/cm2) Cathode environment at 0.6V, at 75C, 1M H_2SO_4+2ppmF- with air bubbling, Fe based alloy(0.12mA/cm2)	-	-	[49]
304SS	TiC on 304SS	Corrosion current density, Icorr, 304SS(8.3μA/cm2), 304SS/TiC(0.034μA/cm2), 1 M H_2SO_4	-	-	[67]
316SS, Graphite	TiN on 316SS (1μm)	-	Before operation 316SS(34.2mΩ cm2), 316SS/TiN(32.7mΩ cm2), Graphite(30.2mΩ cm2) at 180 N/cm2	-	[45]
304SS	TiN on 304SS	Corrosion current density, Icorr, 304SS(2.6μA/cm2), 304SS/TiN(0.145μA/cm2), 0.5 M H_2SO_4 +2 ppm HF	Before operation 304SS(~140mΩ cm2), 316SS/TiN(19mΩ cm2) at 240 N/cm2	-	[58]
Titanium, 304SS	Plasma-polymerized HFP	-	-	-	[68]
304SS	NiAl (1μm)	Corrosion current density, Icorr (49μA/cm2), 0.5M H_2SO_4 at 25C	-	-	[69]

Plate Material	Coating material (thickness)	Corrosion current density (DOE Target 1μA/cm2) / Corrosion rate	Contact resistance (DOE Target 10mΩcm2),	Cost (DOE2010 Target $10/kw)	Ref.
Ni-Cr metal foam, 316SS metal foam, 316SS channel, Carbon cloth	-	-	-	-	[50]
304LSS, 304LN, 316L, 316LN, 317L, 904L, E-brite, SAF2205, SAF2507, AL29-4-2, AL-6XN	-	-	-	-	[70]
316LSS	Gold, Proprietary coatings	-	Oxide resistance -19.6 to 668.36mΩ/cm	-	[32]
Aluminum	graphite overmolded	-	-	-	[71]
SS felt, Nickel foam, carbon paper, graphite	-	-	-	-	[72]
SS316, E-Brite, AL600 (Nickel based alloy)	-	E-brite (<1μm/year) better than SS316 and AL600	-	-	[52]
Aluminum, 316LSS, Titanium	Gold plated aluminum and 316LSS,	-	Before operation 316SS(~110mΩ cm2), Titanium(~70mΩ cm2), Graphite(10mΩ cm2) at ~140 N/cm2	-	[31]
Fe-based alloys	-	-	Before operation Fe Based(~100mΩ cm2), Ni Based(~10mΩ cm2), Au-plated(~2mΩ cm2) at ~140 N/cm2	-	[73]
316SS	Sand Blasted and Etched	-	-	-	[74]
304SS	Conductive polymers polyaniline (PANI) and polypyrrole (PPY)	Corrosion current density, Icorr, 304SS(10μA/cm2), PPY(1μA/cm2), PANI(0.1μA/cm2), 0.1M H_2SO_4	Before operation 304SS(~100mΩ cm2), PPY(~800mΩ cm2), PANI(~800mΩ cm2), Graphite(80mΩ cm2) at ~140 N/cm2	-	[40]
316LSS, Zr75Ti25	-	-	-	-	[75]

CHAPTER 3

Experimental

3.1 Material preparation

Bulk materials; Poco graphite, graphite composite, SS316, SS310, incoloy 800, titanium carbide and zirconium carbide were selected as candidate materials to be tested for PEMFC bipolar plate application. Poco graphite, graphite composite, SS310 and SS316 were selected as reference of comparison for interfacial contact resistance (ICR) and corrosion current density value. A graphite composite (BMC940) sheet was obtained from Bulk Molding Compounds, Inc. Other materials were also selected based on their potential stability in the fuel cell corrosive environment [17,27,35].

Samples of these selected materials were prepared into 25.4mm x 25.4mm coupons for ICR and corrosion resistance measurement which are the main properties necessary for bipolar plate material selection. In addition to the bulk materials, chromium carbide coating material was selected as a potential candidate for bipolar plate coating material based on the previous work [76].

Thermal spray technique, namely High Velocity Oxygen Fuel (HVOF), was employed to apply the chromium carbide coating on SS316 and aluminum substrate coupons. Pure chromium carbide (Cr_3C_2) feedstock powder was acquired from Praxair Tafa as the coating material. However, binding alloys were added to the chromium carbide coating material to enhance its bonding strength with the substrate and eliminate the coating layer porosity and the possibility of delamination. Several binding materials were investigated to enhance the bonding strength of the chromium carbide coating. The composition of the chromium carbide powder with different binding materials is the following: Cr_3C_2-7%NiCr, Cr_3C_2-25%NiCr, Cr-C-Ni, Cr_3C_2-25%Mo, Cr_3C_2-25%CoMoCrSi, and Cr_3C_2-25%CoCrAlY. The former three chromium carbide feedstock powders (Cr_3C_2-7%NiCr, Cr_3C_2-25%NiCr and Cr-C-Ni) were commercially available from Praxair Tafa and their item numbers were CRC-184-1, 1375VM and CRC-410-1, respectively. The remaining three different chromium carbide powders were 75% of pure chromium carbide (Cr_3C_2) feedstock powder (item # CRC-105-2) blended into Praxair

Tafa feedstock powder 25% Mo (item # MO-102), 25% CoMoCrSi (item # CO-109) and 25% CoCrAlY (item # CO-110) respectively.

Figure 3.1 shows the SEM images of the chromium carbide powder; a). Pure Cr_3C_2, b). Cr_3C_2-7% NiCr, c). Cr_3C_2-25% NiCr and d). Cr-C-Ni. The NiCr in Cr_3C_2-7% NiCr feedstock powder is blended into the Cr_3C_2 feedstock powder whereas it is agglomerated in the Cr_3C_2-25% NiCr feedstock powder and the Cr-C-Ni feedstock powder is an alloy of the three elements. The chemistry of these four different powders and their spray parameter are shown in Table 3.1.

The thickness of these coatings varies from few microns to three hundred microns depending on the type of binding material and the powder structure. In addition to the normal spraying operation conditions in an open atmospheric environment, inert gases such as nitrogen and helium were applied to shroud the flame and isolate the powder and coating from the environment during the HVOF spray process to minimize coating oxidation and to maintain high electrical conductivity. The inert gas shielding orifice compartment was mounted around the thermal spray gun barrel (Figure 3.2) to produce uniform inert gas distribution shield around the flame and coating during spraying to isolate the flame from the oxygen of the air in the surrounding environment.

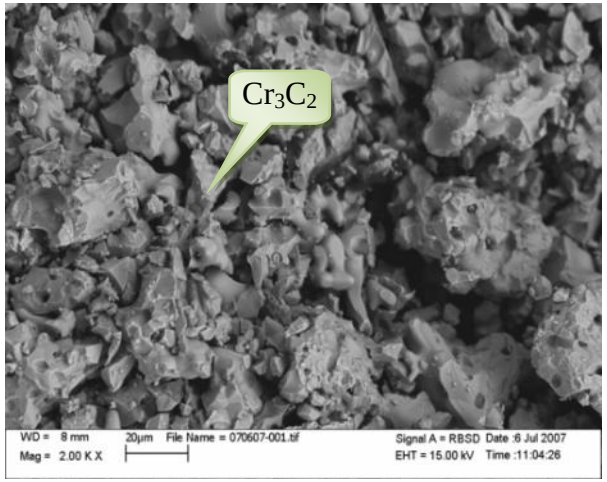

(a)

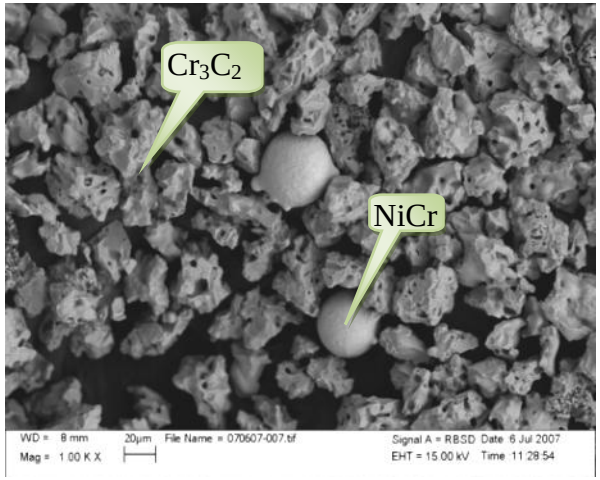

(b)

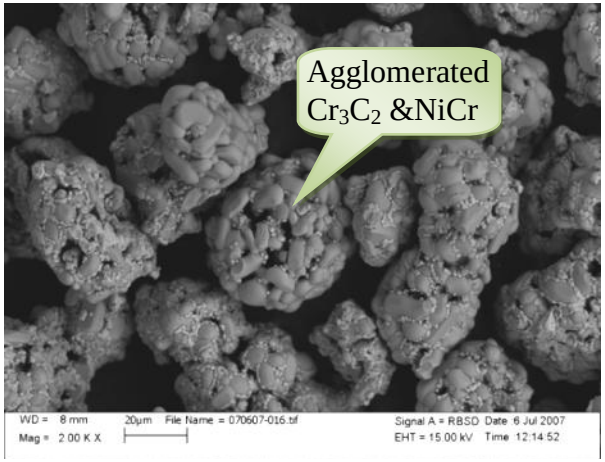

(c)

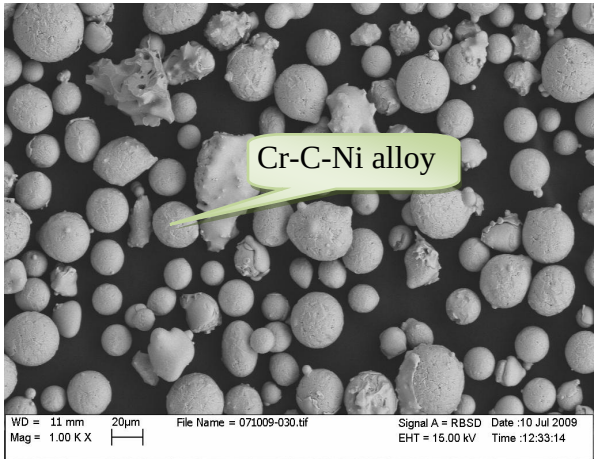

(d)

Figure 3.1: (a) Pure chromium carbide powder, (b) chromium carbide - 7% NiCr powder (blended), (c) chromium carbide - 25% NiCr powder (agglomerated) and d) Cr-C-Ni alloy powder (activated)

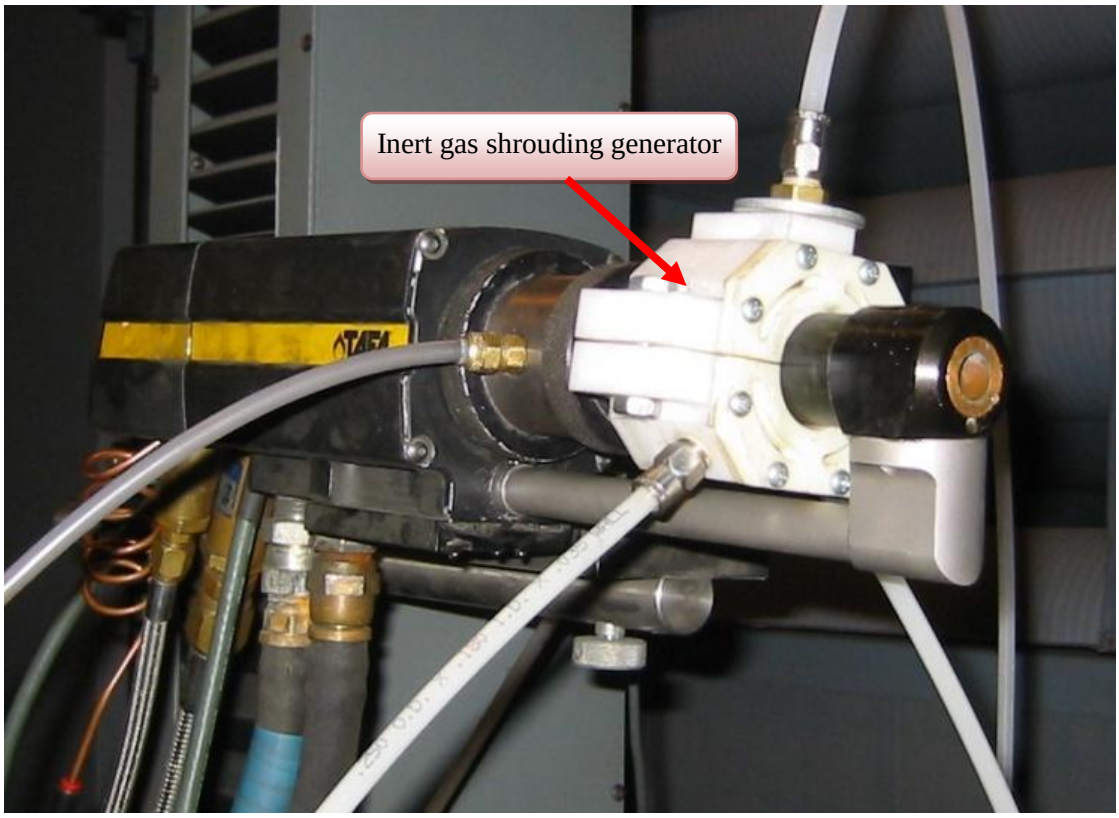

Figure 3.2: HVOF spray gun with inert gas shielding generator

Table 3.1: Chemistry and spray parameters for chromium carbide powder

Powder compositions	Pure Cr_3C_2	Cr_3C_2-7%NiCr	Cr_3C_2-25%NiCr	Cr-C-Ni
TAFA #	CRC-105-2	CRC-184-1	1375VM	CRC-410-1
Figure 3.2	a	b	c	d
Manufacturing process	Sintered	Blended	Agglomerated	Activated
Nominal Chemistry				
Ni	None	5.5%	20.0%	8.0%
C	13.0%	12.5%	10.0%	4.0%
Cr	Balance	Balance	Balance	Balance
Spray parameters				
Fuel flow rate	6.0 Gal/hr	6.0 Gal/hr	6.0 Gal/hr	6.0 Gal/hr
Oxygen flow rate	1850 SCFH	1850 SCFH	1850 SCFH	1850 SCFH
Oxygen pressure	210 PSI	210 PSI	210 PSI	210 PSI
Nitrogen flow rate	21±2 SCFH	21±2 SCFH	21±2 SCFH	21±2 SCFH
Nitrogen pressure	50 PSI	50 PSI	50 PSI	50 PSI
Combustion Pressure	98±5 PSI	98±5 PSI	98±5 PSI	98±5 PSI
Power feed rate	58g/min	58g/min	58g/min	58g/min
Stand-off distance	14”	14”	14”	14”
Gun barrel	6”	6”	6”	6”

3.2 Interfacial contact resistance (ICR) measurement setup

The interfacial contact resistance of a bipolar plate's candidate material can be determined by sandwiching the bipolar plate material between two gas diffusion layers (GDL) to simulate the actual cell condition and measuring the voltage drop (or the resistance, R=V/I) between the materials. The flexible and nonwoven GDL (LyFlex™) used in this experiment was manufactured by Lydall Inc. The interfacial contact resistance (ICR) test setup and its schematics are shown in Figure 3.3. The setup consisted of a faraday cage that encompassed a motorized press and a load sensor. Both were acquired from Mark-10 Corp. This setup also included a high accuracy Agilent Technologies nano volt / micro ohm meter to measure the voltage drop between the GDL materials and a DC power supply to provide current during the measurement (Figure 3.3a).

Two gold plated copper terminals with a $1cm^2$ contact area were mounted on the two jaws of the motorized press as shown in the schematics Figure 3.3b and c. The voltage drop between the materials has a strong function with the clamping force and the pressure on the test sample. Pressure ranging from 25 to $300N/cm^2$ was applied on both sides of the testing section as the sample was positioned between these jaws to obtain the relationship between the pressure and the ICR for each material candidate. These gold plated copper terminals were introduced due to their known corrosion resistance to avoid the formation of oxide layer on the testing surfaces that can greatly affect the ICR measurement. One centimeter contact area of the gold plated copper terminals was also selected to minimize the need of conversion from the measurement since the unit of ICR in the field of PEM fuel cell is known as $m\Omega\ cm^2$. This experimental setup has been widely used by many researchers [17,21,33,40,63].

The faraday cage was installed to protect the system from any external electrical charge that may cause disturbance to the system and jeopardize its accuracy. A current of one amp was applied across the two gold plated copper plates by the external power supply to simulate the PEM fuel cell current density. The voltage V1 across the one ohm shunt resistance (R) with +/- 0.5% ohm accuracy, shown in Figure 3.3b, was precisely identical to the current applied through this one ohm resistance (R) according to the Ohm's Law. The total resistance R1 is equivalent to twice the interfacial contact

resistance between copper terminal and GDL. The bulk resistance of the materials was ignored because it was much smaller than the ICR. The total resistance R2, as shown in Figure 3.3c, is equivalent to twice the summation of the ICR value between the gold plated copper terminal and the GDL added to the value of ICR between the sample material and the GDL. Therefore, using ohm's law both R1 and R2 can be measured by dividing V2 by V1. The ICR between the bipolar plate sample material and the GDL can then be calculated from the following equation:

ICR = (R2 – R1) /2

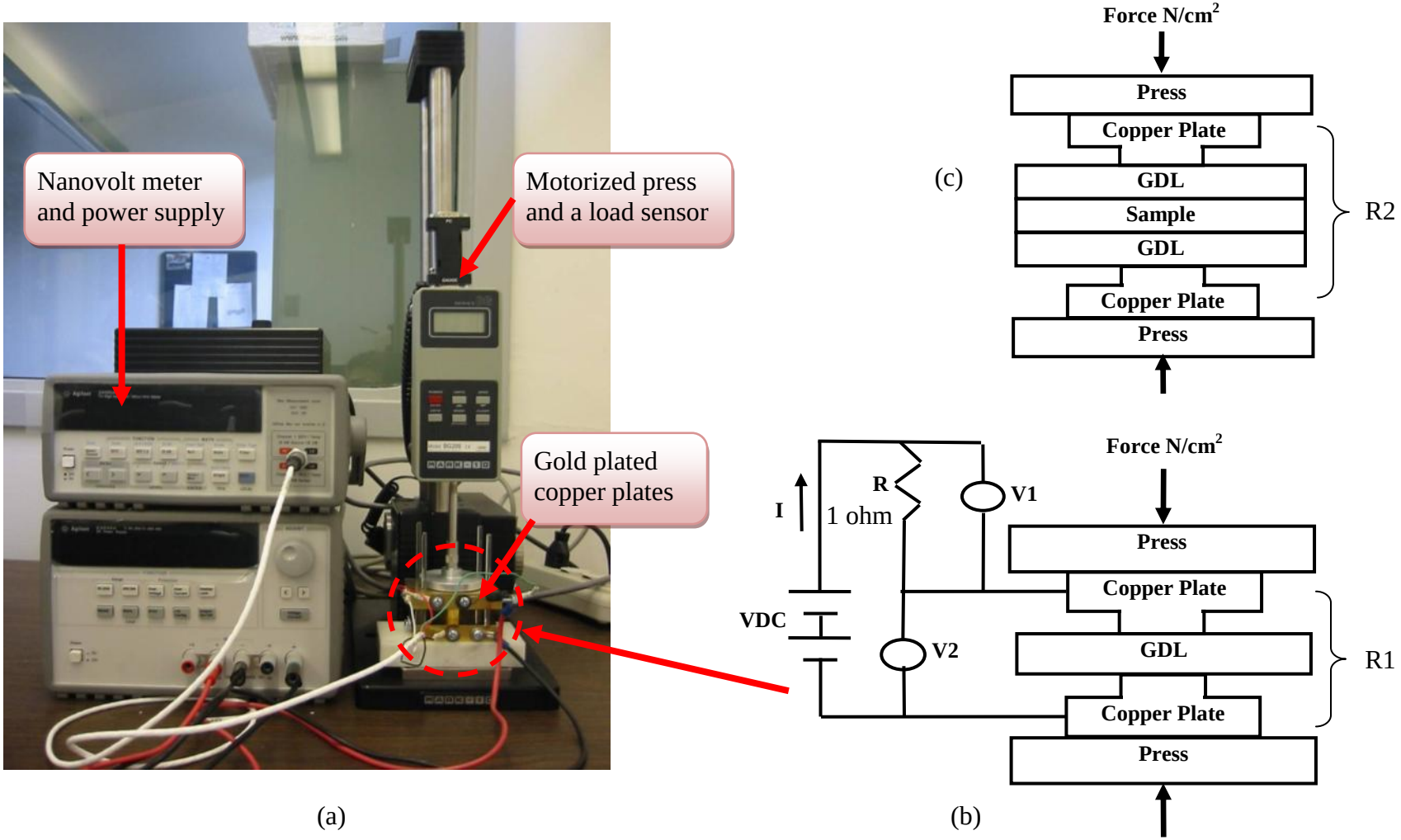

Figure 3.3: (a) Interfacial contact resistance (ICR) measurement setup, (b) test fixture schematic with one GDL and (c) test fixture schematic with combined sample and GDLs

3.3 Accelerated corrosion resistance test cell setup

A conventional three-electrode system was used to conduct the electrochemical experiments. Figure 3.4 shows a schematic diagram of a corrosion cell coupled with a platinum sheet as counter electrode (CE), saturated calomel electrode (SCE) as reference electrode (Ref) and a test sample as working electrode (WE). The cell is connected to a potentiostat to measure the corrosion current and corrosion rate of the bipolar plate's candidate material. Figure 3.5 shows the actual $1cm^2$ testing area corrosion test cell that was used in this experiment and was acquired from Princeton Applied Research. The cell was interfaced with Gamry potentiostat to obtain the corrosion current and voltage generated by the test coupons. The fuel cell electrochemical simulation solution was obtained by using H_2SO_4. Antunes et al. [77] recently published a list of different concentration of H_2SO_4 solutions that have been used by different researchers. The most frequently used H_2SO_4 solution is pH3 acidic level with minimum amount of HF.

The electrochemical experiment was conducted in de-aerated 0.5 M H_2SO_4 + 200 ppm HF solution at 25°C (This aggressive testing solution was recommended by United Technology Corp.) and aerated and de-aerated pH3+0.1 ppm HF (fuel cell simulated solution) at 80°C to select the bipolar plate material with the low dissolution rates, i.e. low corrosion current. Samples of 25.4mm x 25.4mm (1" x 1") test coupons mentioned from the previous section were tested using this experimental setup.

Both potentiodynamic and potentiostatic accelerated testing techniques were employed to compare the corrosion resistance of different materials. In these tests, samples were stabilized at the open circuit potential (OCP). For the potentiodynamic testing, the potential was swept between the potentials 0.5V below OCP and 1V above OCP with a scanning rate of 1 mV/s. For the potentiostatic testing, the potential was set at a constant voltage 0.6V (SCE) for long period of time (2.5 hours, 9.5 hours and 72 hours) to provide understanding of the material behavior under simulated fuel cell environment without having to build an actual fuel cell and testing it for long period of time which both are expensive and time consuming processes.

Considerable attention was exercised when preparing the test solutions from concentrated sulfuric acid (H_2SO_4) & hydrofluoric acid (HF) because they are extremely

dangerous and harmful to human body if contacted directly. The basic safety requirements for solution preparation were as follows:

- Ventilation - acidic solution preparation must be performed under chemical fume hood to avoid breathing of acidic vapor.
- Eye Protection - Wear chemical splash goggles together with a face shield.
- Body Protection - Wear a laboratory coat with a chemical splash apron that is made of natural rubber, neoprene, or viton material.
- Gloves - Wear gloves that are made of medium or heavyweight viton, nitrile, or natural rubber material to avoid direct contact of acidic solution. A second pair of nitrile exam gloves should be worn under the gloves for protection against leaks.

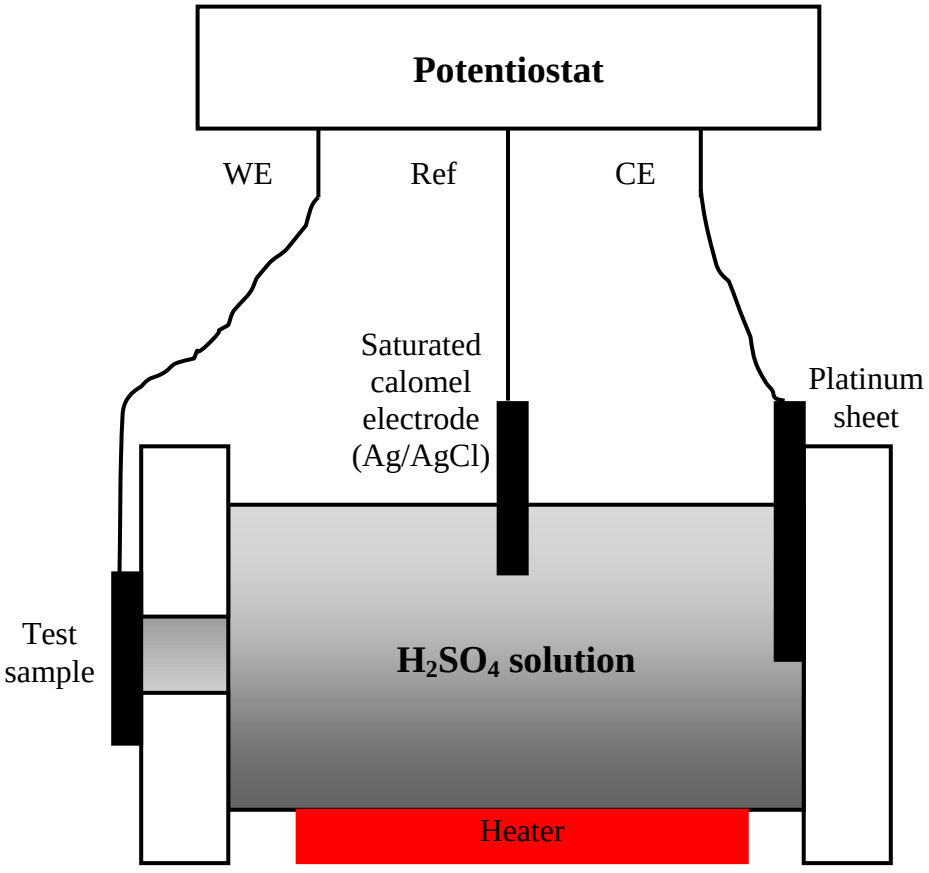

Figure 3.4: Schematic diagram of corrosion test cell and potentiostat

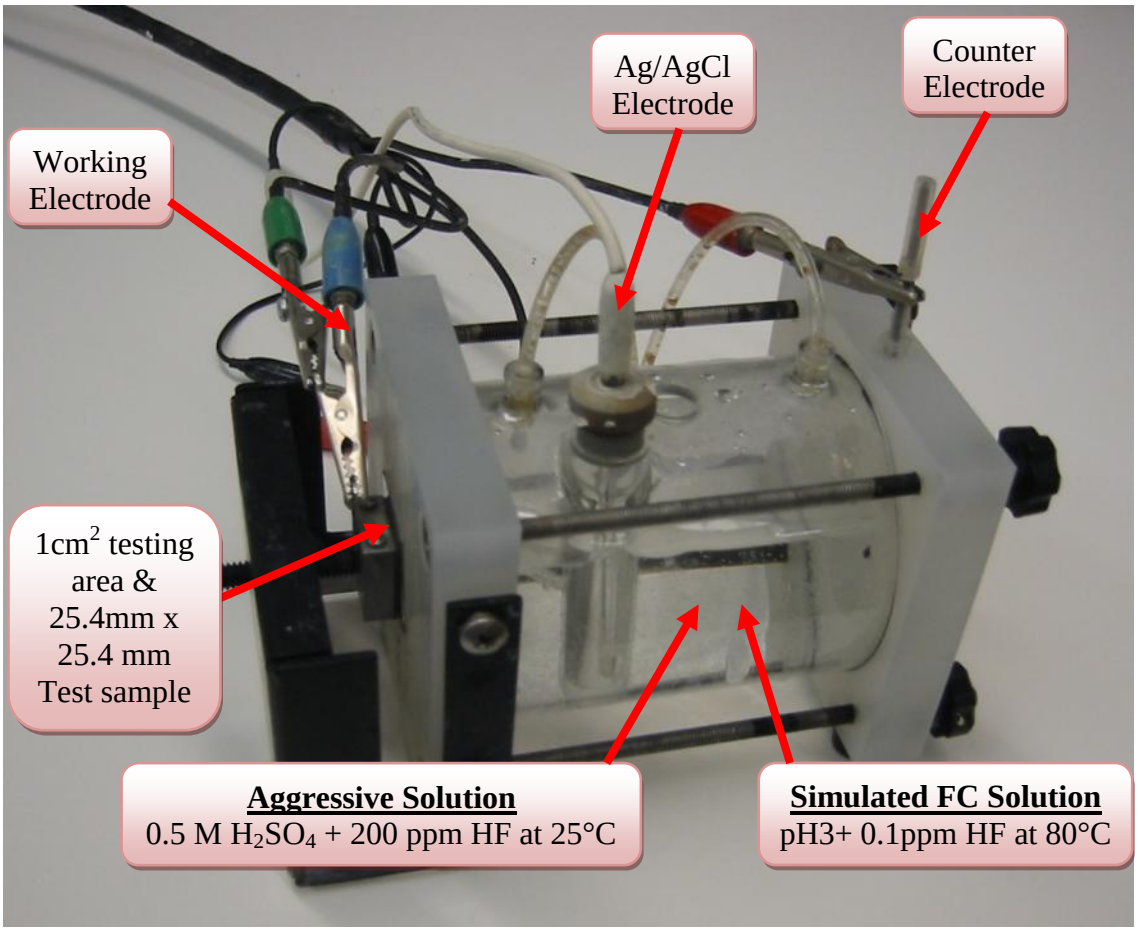

Figure 3.5: Corrosion test cell and testing solutions

3.4 Fuel cell testing station and single fuel cell test setup

Additional experimental work was carried out to investigate the effect of different bipolar plate materials, terminal designs, and the flow-field configurations on fuel cell performance and power output at the single-cell level. Single cell testing was conducted inside a hydrogen safety enclosure with a negative pressure test station and connected to data acquisition system (Figure 3.6). All single fuel cells operating parameters, such as current, voltage, and power as well as temperature, back pressure and reactant gases volume flow rate were measured and recorded by the data acquisition system (LabView 8.0). The testing station provided the reactant gases (hydrogen and air) to the fuel cells while the data acquisition system recorded the fuel cell system's data information measured by the sensors and flow meters. Polarization, power output, efficiency, and hydrogen consumption curves were measured and plotted individually using the data acquisition system, programmable electronic load (MCL488 DYNALoad) and reactant gas volume flow meters.

Two single fuel cells were designed with two different reactant flow-fields, namely triple serpentines and humidity conservative designs to explore the effect of reactant flow-field on performance and power output of the fuel cells. These fuel cells were machined from Poco graphite plate material. Their active areas were 50cm^2 and the dimension of the channels was 1mm x 1mm with 1mm spacing between the channels. Figure 3.7a shows the triple parallel serpentines flow-field design which was fabricated according to US fuel cell council single cell test protocol [78]. Figure 3.7b shows the newly developed humidity conservative flow-field design that was designed to reduce the pressure drop within the cell and preserve the humidity from the electrochemical reaction. The electrode membrane assemblies (Series ES12E-W-5L) with 50 cm^2 active electrode area used in this experiment were acquired from BASF Inc. They were fitted into the two different flow-field design single fuel cells with PFA gaskets. The hydrogen and air flows of both triple serpentines and humidity conservative single cells were oriented parallel to each other to allow for efficient protons and electrons transport.

Four single fuel cells were fabricated with 6.45cm^2 active area bipolar plates. Two of which were fabricated of coated aluminum bipolar plates, and the other two cells were fabricated of graphite composite bipolar plates. All plates were machined identically and

the graphite composite bipolar plates were used as the control reference because they are currently classified as the industry standard. Figure 3.8 shows the exploded view of a 6.45cm^2 active area single cell used in this experiment. Each single cell consisted of two back plates and two bipolar plates that contained a humidity conservative flow-field to allow the passage of hydrogen and air to the anode and cathode of the cell respectively. Metal pins were press-fitted into the aluminum and graphic composite bipolar plates as electrical terminals (Figure 3.9). The 6.45cm^2 active area flow-field pattern was machined onto 12mm thick aluminum (6061 T6) and graphite composite blank plates. The graphite composite blank plates were acquired from Bulk Molding Compound Inc. The channel width was approximately 1mm wide and the cross section of each channel was machined into a "V" shape to simplify the thermal spray process on the aluminum bipolar plates (Figure 3.10). For meaningful comparison, the coated aluminum and graphite composite single cells share the same flow-field and channel design. The channeled side of the aluminum bipolar plates was sand blasted to provide a rough surface before applying the thermal spray coating. Chromium carbide (Cr_3C_2-25% NiCr) corrosion resistant coating was applied on two pairs of aluminum bipolar plates for testing and comparison with graphite composite plates as control reference. The electrode membrane assemblies (series 14-W) used in the 6.45cm^2 active area single cells were acquired from BASF Inc. The MEAs consisted of carbon cloth GDL, thickness of Nafion <50 microns, and <1mg/cm^2 total platinum loading for both anode and cathode sides. The MEAs were sandwiched between the bipolar plates into four replicas of single fuel cells with silicon gaskets and operated under identical conditions. To compensate for the thickness of the gasket, an extra carbon paper (GDL) was added on each side of the electrodes. These four single cells were operated for one thousand hours at 70°C to investigate their lifetime performance.

Finally, two additional single fuel cells were fabricated of 50cm^2 active area. One of the single cells was made of coated aluminum bipolar plates and the other was made of graphite composite plates as control reference (Figure 3.11). Double-layer coating material (Cr_3C_2 and Cr-C-Ni) was sprayed on the 50cm^2 active area aluminum bipolar plates for investigation. The dimension of the channel cross section of these single cells was approximately 1mm wide and machined into "V" shape which was the same as the

6.45cm^2 active area fuel cells. The humidity conservative flow-field design was scaled up to fit into a 50 cm^2 active area. In addition, two different terminal designs were installed on these two fuel cells for comparison of power output and design optimization. Thus, metal screws and tapped holes were used in the first design as directly tapped terminals into the bipolar plates to reduce the need for two extra front and back terminal plates (Figure 3.12a). Gold plated stainless steel plates were utilized as second terminal design to reduce the possibility of surface corrosion and to sandwich the bipolar plates together (Figure 3.12b). Membrane electrode assemblies used in the 50cm^2 active area fuel cell polarization curve evaluation were obtained from two different manufacturers to examine for the repeatability of tests. MEAs obtained from BASF Inc. were series ES12E-W-5L with proprietary Pt loading and the Pt loading in MEAs obtained from BCS Fuel Cell Inc. were 0.2 mg/cm^2 in the anode side and 0.5 mg/cm^2 in the cathode side.

In the fuel cell performance testing, all cells were operated under identical conditions of controlled temperature (20°C), air flow rate of 1.8 SLM, air and hydrogen pressure 0.034 MPa (5 psig). The hydrogen was dead-ended at the exhaust manifold for all cells. The fuel cell operated with ambient air obtained from an industrial compressor and dry industrial grade hydrogen supplied from a metal hydride storage tank. Polarization curves and power output plots from these cells were plotted for comparison. For lifetime performance investigation at 70°C, incoming air was supplied through air bubbler for external humidification.

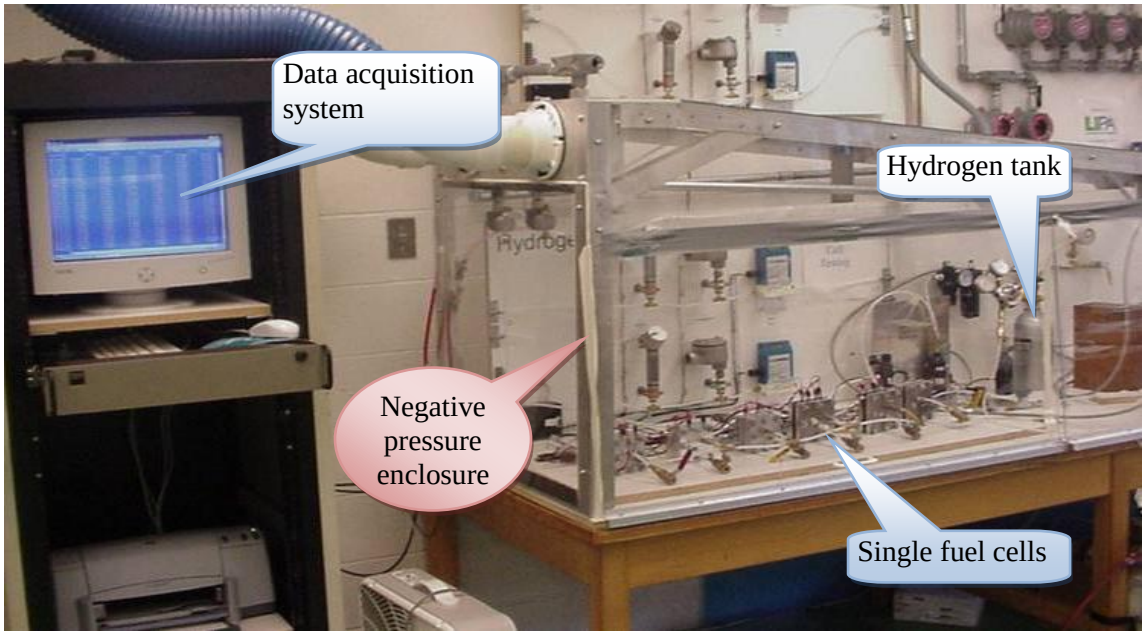

Figure 3.6: Fuel cell testing station with negative pressure enclosure

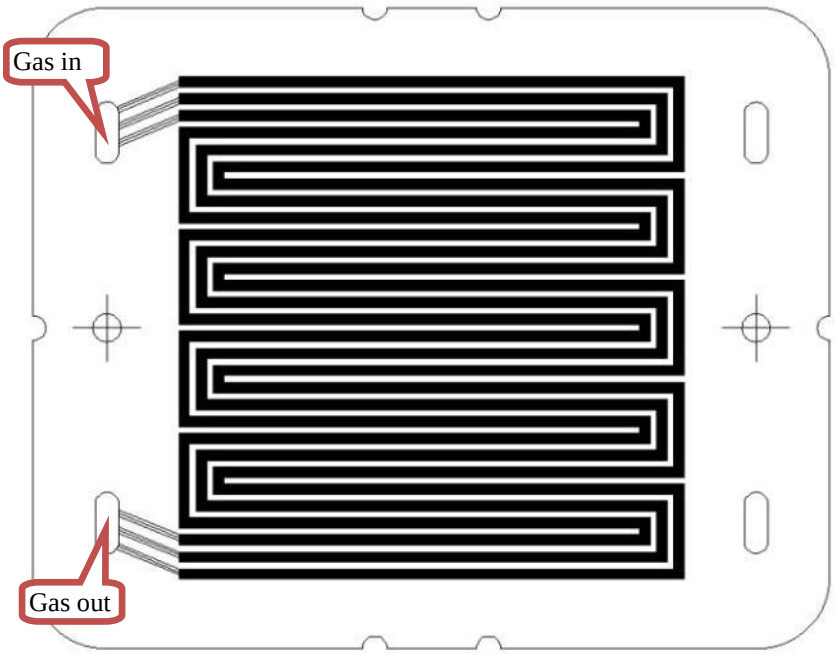

(a)

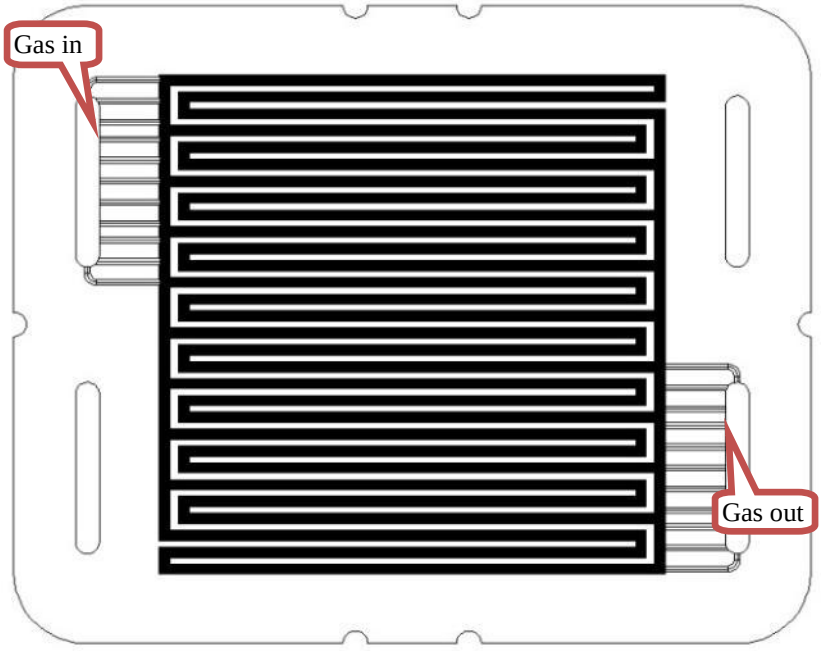

(b)

Figure 3.7: (a) 50 cm^2 active area triple serpentines flow-field design, (b) 50 cm^2 active area humidity conservative flow-field design

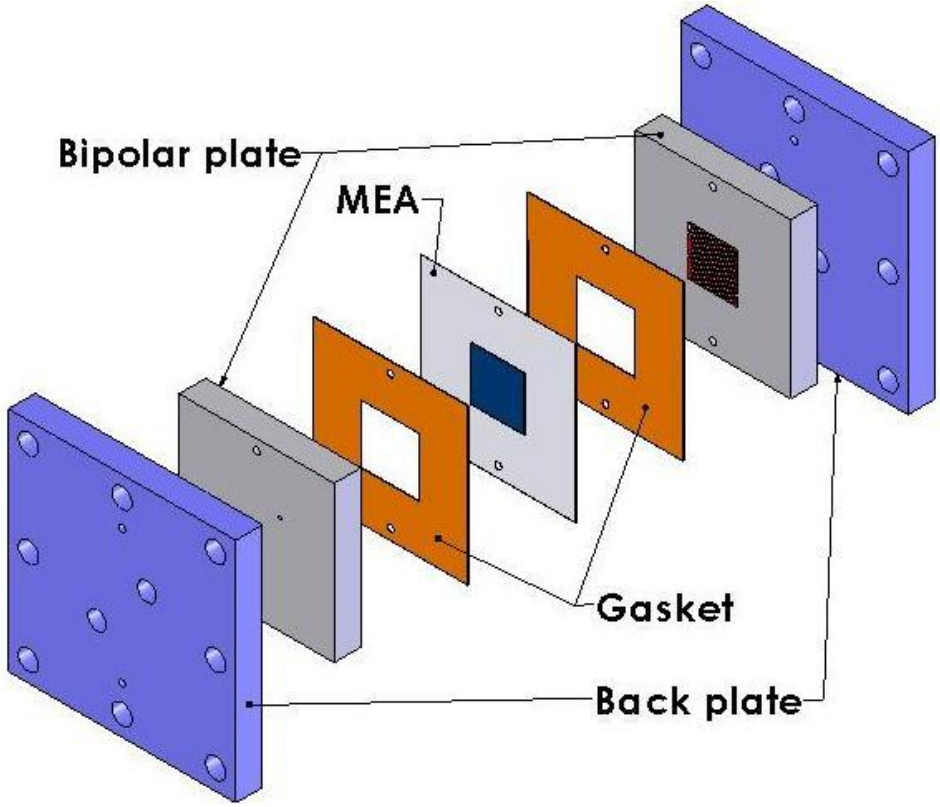

Figure 3.8: Single cell exploded view

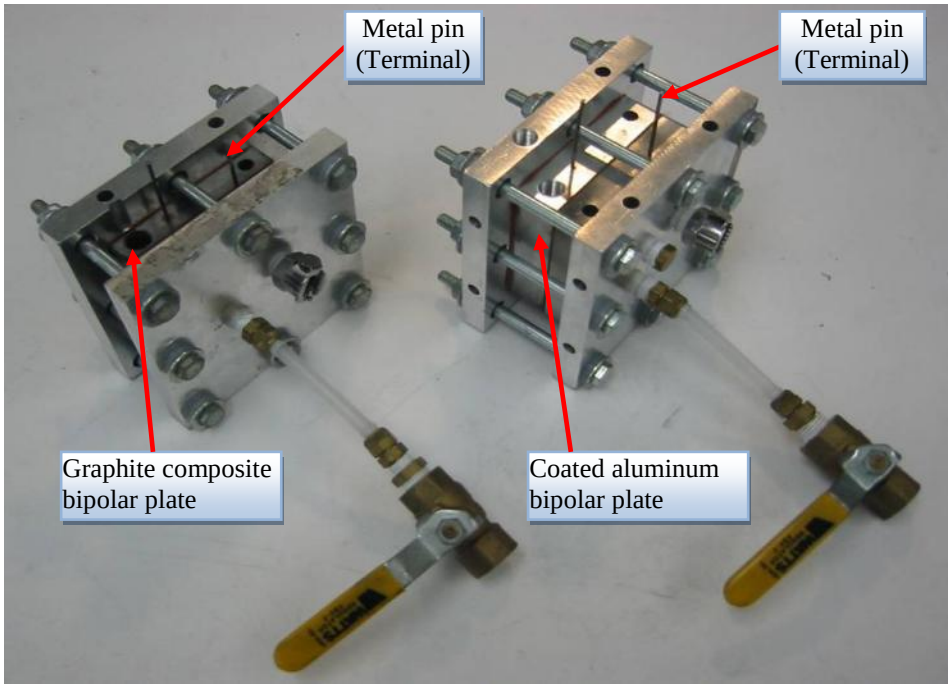

Figure 3.9: Graphite composite and coated aluminum single cells ($6.45\ cm^2$ active area)

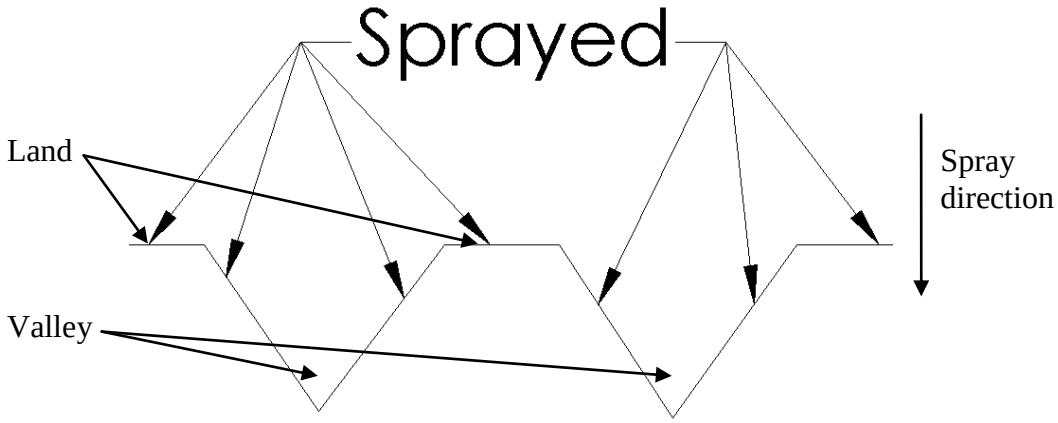

Figure 3.10: Cross section of "V" shape channels

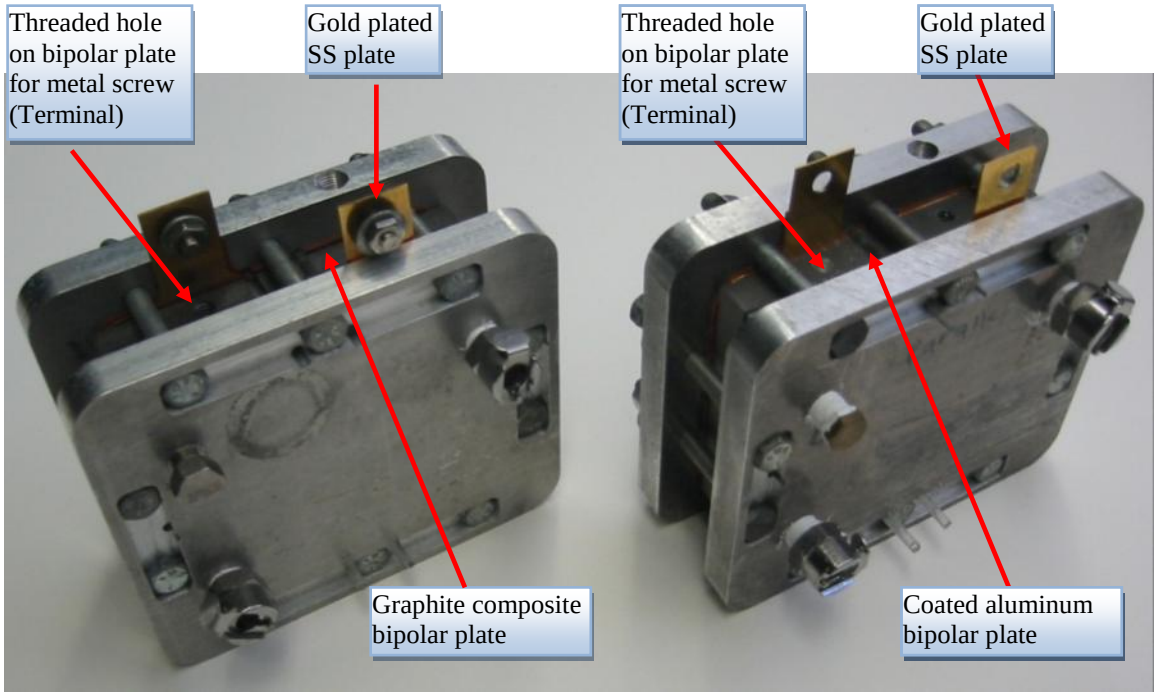

Figure 3.11: Graphite composite and coated aluminum single cells (50 cm^2 active area)

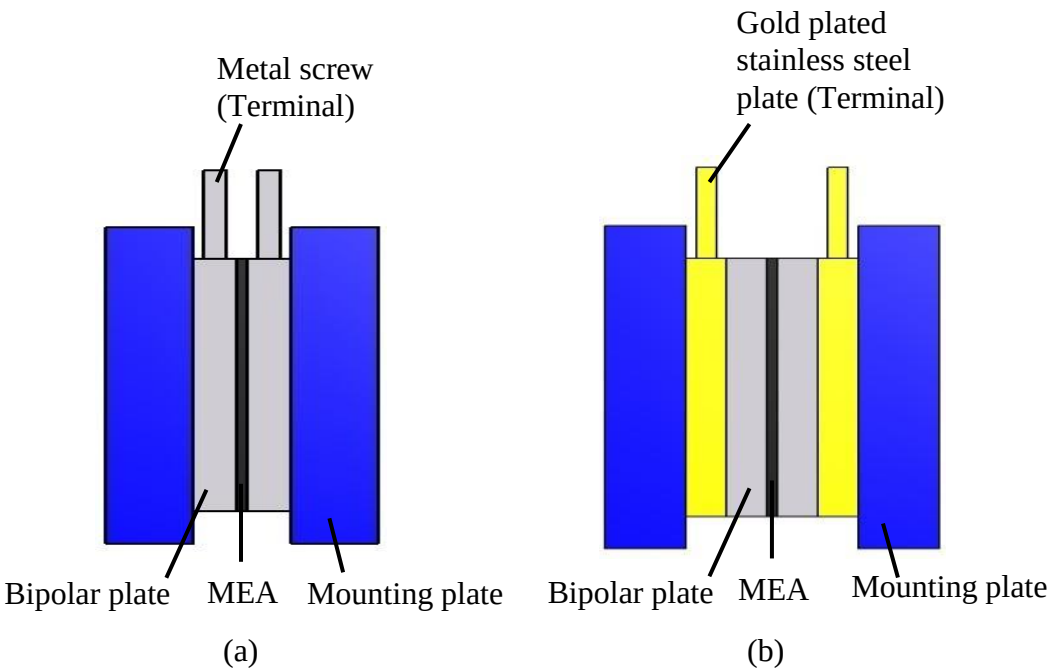

Figure 3.12: Structures of single fuel cell with different terminal designs (a) Metal screws (Terminals) (b) Gold plate stainless steel plates (Terminals)

3.5 Experimental setup for thermal and water management

A ten cell stack was fabricated of eleven graphite composite bipolar plates to evaluate the thermal and water management within a fuel cell stack. The active area of each cell was 40cm^2 and a triple serpentine flow-field design was machined onto the bipolar plates. The cross section of each channel was 1mm x 1mm and the spacing between the channels was 1mm. Fifteen thermocouples were fitted into the ten cells stack, five in each end plate and five in the middle plate of the stack. Mass flow, humidity and temperature sensors were also attached to the stack at the inlet and outlet sides of both hydrogen and air (Figure 3.13). The schematic diagram of the thermal and water management experimental setup is also shown in Figure 3.14.

Ten of 40 cm^2 active electrode area MEAs, series ES12EP-W-5L, premium performance, thin configuration, woven web GDL were acquired from BASF Inc. and used in this study. They were assembled into the fuel cell stack with PFA gaskets and the ten-cell stack was operated at room temperature of 22^{o}C, air and hydrogen pressures were set at 0.034MPa (5 psig). The air flow rate was 17 SLM and the hydrogen was dead-ended at the exhaust manifold. Air supplied to the stack was humidified through a humidifier. The humidity level of the reactant gases could be adjusted between 10% and 100% by the precision needle valves. If the humidity level could not be reached with the needle values fully opened, heat would be added to the container to vaporize the water and hence increase humidity level. This experimental work was conducted to identify the optimal operating conditions of the humidity of the reactant gases in addition to monitoring the average cells' temperature of the power stack.

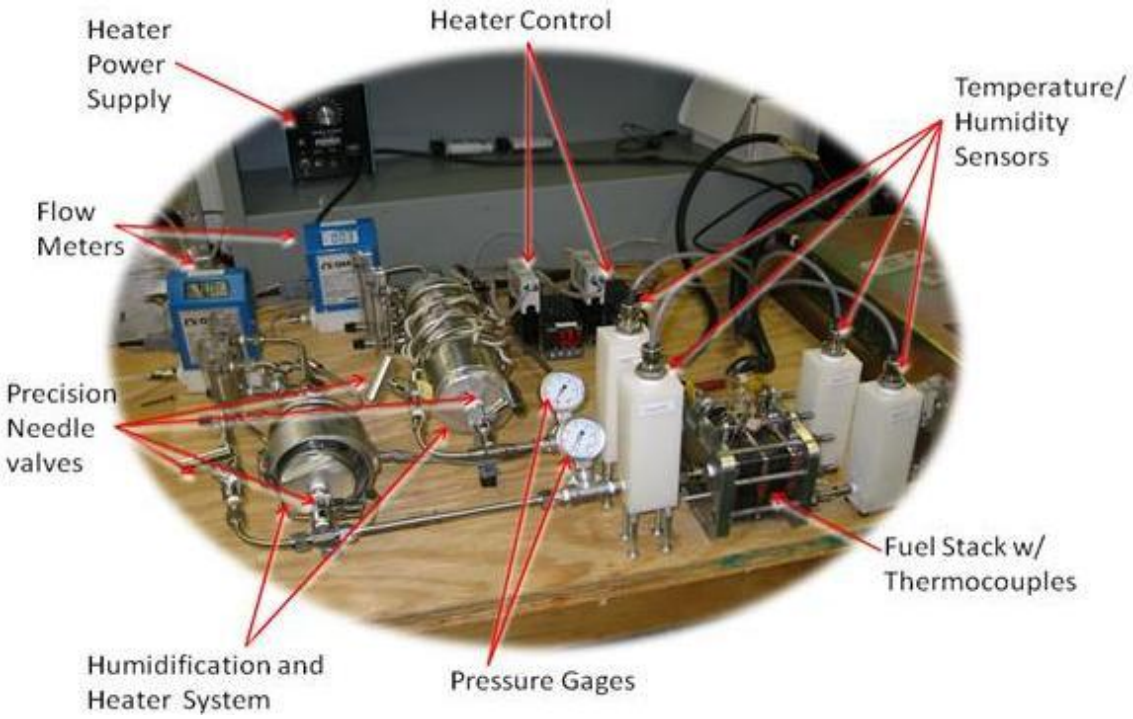

Figure 3.13: Ten cell stack, hydrogen and air humidifiers as well as various sensors

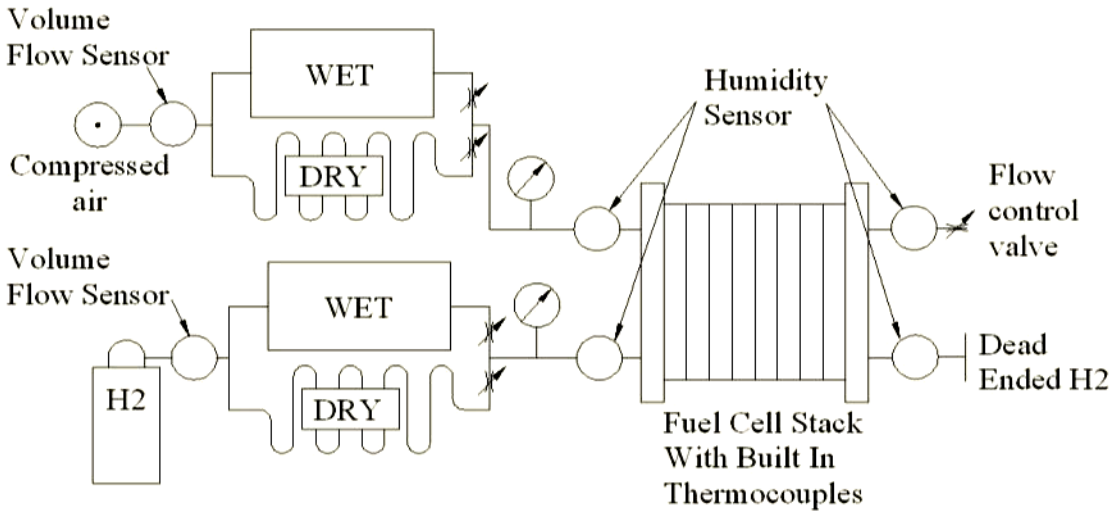

Figure 3.14: Schematic of the 10 cells stack, hydrogen and air humidifiers and various sensors

3.6 Numerical prediction of local temperature for both forced air and forced convection PEM fuel cell stack design

This task was focused on designing a cooling system that would allow the fuel cell stack to operate at maximum power output without reaching the temperature limit of 80^{o}C and damaging the Nafion membrane. In order to maximize the lifetime of the relatively expensive polymer membrane and avoid the time consuming machining and laboratory testing of fuel cell stack, a finite element analysis (FEA) model of a bipolar plate was developed by computer simulation. The FEA model was created and analyzed using commercially available software packages Autodesk Inventor 2009 and Algor V23. The FEA model's parameters were computed based on a steady state heat transfer condition of a PEM fuel cell stack.

Two air supply systems for PEM fuel cell technology namely "forced air" and "forced convection" air supply systems were investigated in this study. The amount of heat generated by the electrochemical reaction inside the fuel cell during its steady state operation is comparable to the electrical power output from the pwer stack [8]. Nominal power densities of MEA acquired from BCS Fuel Cells Inc. were $0.3W/cm^2$ and $0.15W/cm^2$ for forced air and forced convection fuel cell design, respectively. In a forced air fuel cell stack design, compressed air was supplied externally to the fuel cell stack and directed to the cathode side of each MEA through internal manifold that was integrated into the bipolar plates (Figure 3.15) and exited the fuel cell through another internal manifold. In a forced convection fuel cell stack design, the air was driven along the cathode side of the bipolar plates and through the channels of the active area using cooling fans (Figure 3.16) and the cooling fans served dual purposes; 1). Supply air to the each cell as reactant, 2). Dissipate excess heat generated from the electrochemical reaction in the fuel cell stack. Figures 3.15 and 3.16 show that the cooling fin design was integrated onto each bipolar plate to remove the excess heat generated during the electrochemical reaction in the fuel cell stack. Cooling fins are known of their cost effectiveness and efficient performance as a heat removal system. It has been widely used in computer and automobile industries such as CPU heat sink and automobile radiator. Thus, cooling fins were modeled and simulated as heat sink to remove the excess heat generated during the fuel cell electrochemical reaction using FEA computer package

(Algor). The goal of this study was to define the proper fin length, evaluate the cooling effect of the aluminum and graphite composite as possible fin materials and select the proper cooling fan capacity for this application. Cost analysis optimization for both forced air and forced convection fuel cell stack designs was also conducted in this work.

Steady state heat transfer analysis considering the different thermal conductivity of each bipolar plate and fin material namely, aluminum 6061-T6 and graphite composite were also part of this work. The parasitic power consumption in compressed air was calculated basing on 10 psi pressure different between the inlet and outlet of the forced air fuel cell design. Ninety millimeter cooling fans were selected basing on their air capacity, power consumption and commercial availability. Cooling air driven by the cooling fans was assumed passing along the fin area vertically (Figure 3.17). Since both MEAs and bipolar plates were repeated items in a fuel cell stack and their boundary conditions were the same on each plate, the FEA model can be simplified as a single bipolar plate with 0.3W/cm^2 and 0.15W/cm^2 heat flux on the active area. The FEA model was computed based on a steady state heat transfer aspects of a PEM fuel cell.

The dimensions of the bipolar plate and location of fin are shown in Figure 3.18. Fin lengths between 0mm to 50mm were analyzed in the FEA model for both materials. In addition, different air flow cooling fans were investigated to obtain an optimum average heat transfer coefficient of air for convective heat transfer, moreover, 90mm commercial cooling fans with 50 CFM (4.3W) and 100 CFM (9W) were found suitable and were selected for this steady state heat transfer analysis. Physical properties of aluminum 6061-T6, graphite composite and air used in the analysis are shown in Table 3.2 and average heat transfer coefficient of air was calculated from the following equations [79-81]:

$$Q = V \times A$$

$$Re = \frac{VL}{\upsilon}$$

$$Gz = RePr\left(\frac{d_h}{L}\right)$$

$$h_{air} = Nu \times \frac{k}{L}$$

Flat plate in laminar and parallel flow:

$$Nu = 0.664Re^{1/2}Pr^{1/3}$$

Parallel plates in laminar flow:

$$Nu = 7.54 + \frac{0.0289 \times Gz^{1.37}}{1 + 0.0438 \times Gz^{0.87}}$$

Parallel plates in turbulent flow: (2500<Re<7000)

$$Nu = 0.407Re^{0.55}\left(\frac{d_h}{L}\right)^{0.3}$$

Parallel plates in turbulent flow: (7000<Re<20000)

$$Nu = 0.0358Re^{0.8}\left(\frac{d_h}{L}\right)^{0.2}$$

Duct in laminar flow:

$$Nu = 3.66 + \frac{0.104 \times RePr/(\frac{L}{d_h})}{1 + 0.016 \times \left[RePr/(\frac{L}{d_h})\right]^{0.8}}$$

Duct in turbulent flow:

$$Nu = 0.023Re^{0.8}Pr^{0.5}\left(1 + \frac{1.4}{(L/d_h)}\right)$$

Where

Q = Fan air flow rate

A = Fan area

V = Velocity of air

h_{air} = Average heat transfer coefficient of air

Nu = Nussult number

Re = Reynolds number

Pr = Prandtl number

Gz = Graetz number

k = Thermal conductivity of air

d_h = hydraulic diameter

L = Length of plate or duct (parallel to the air flow)

υ = Kinematic viscosity of air

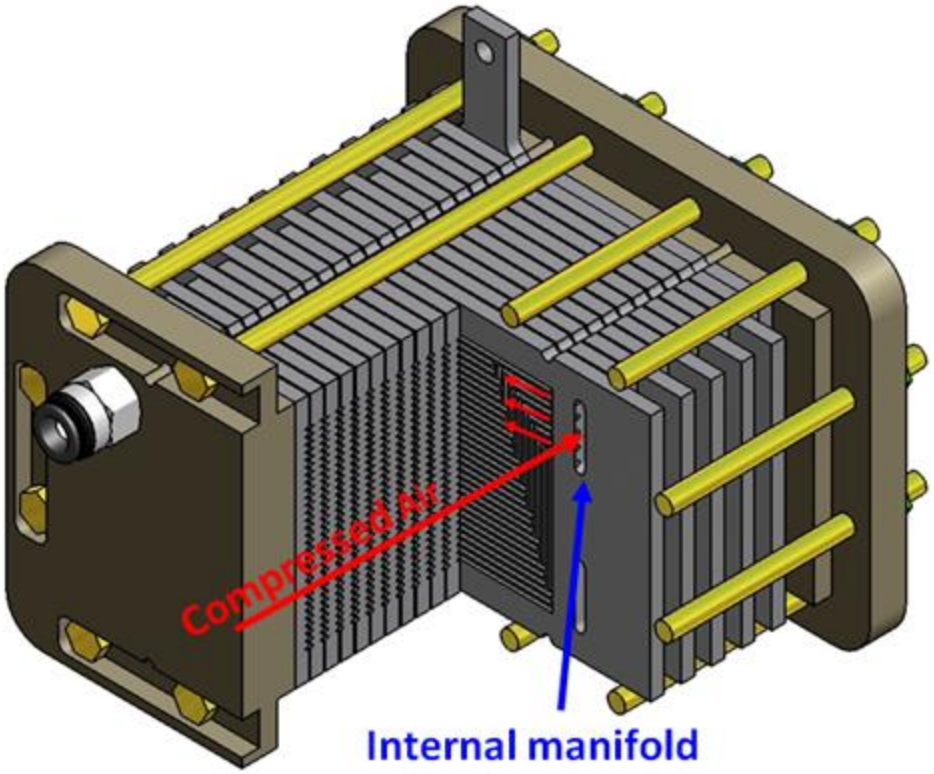

Figure 3.15: Forced air fuel cell stack design

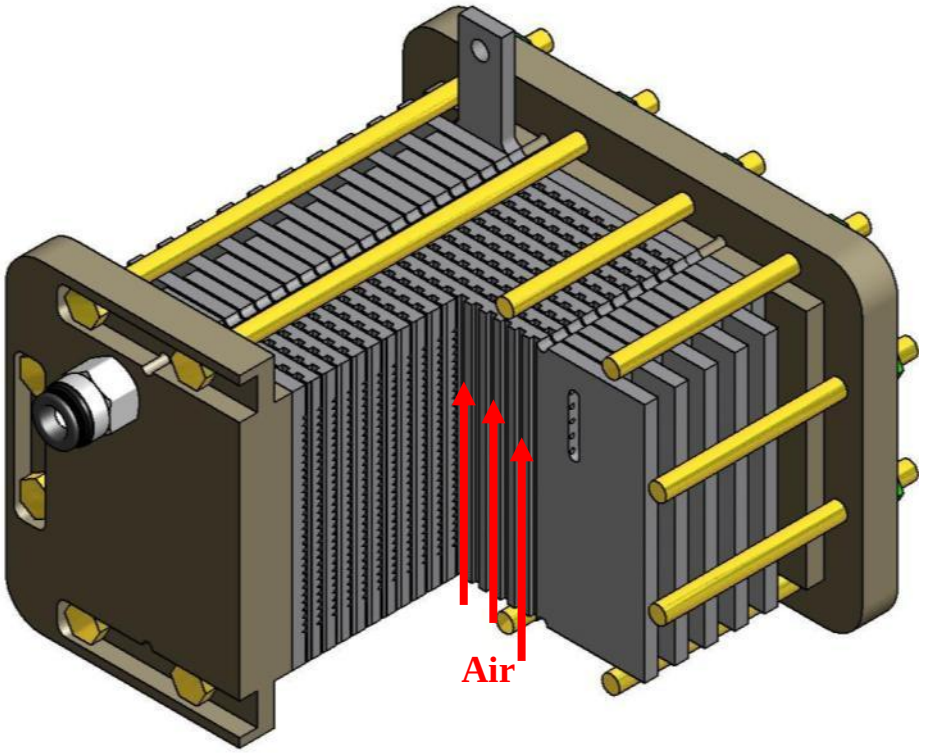

Figure 3.16: Forced convection fuel cell stack design

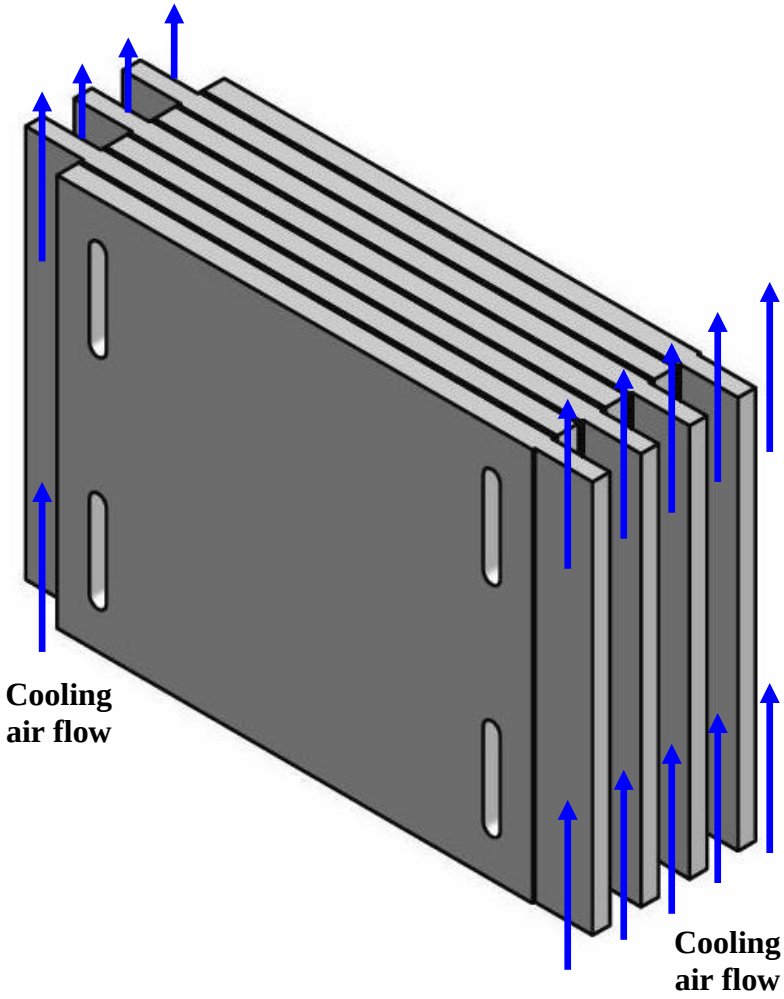

Figure 3.17: Air flow direction in the fuel cell stack with cooling fin design.

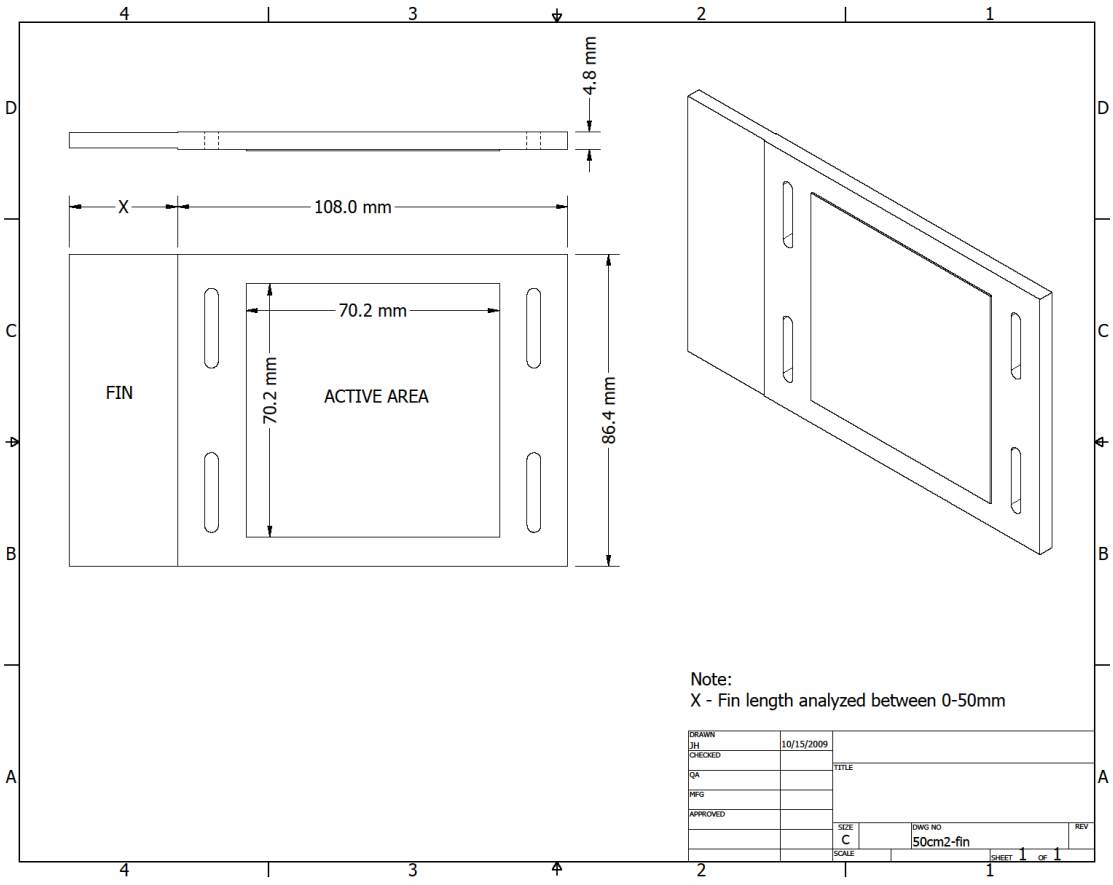

Figure 3.18: Dimensions of bipolar plate with 50cm^2 active area and fin feature

Table 3.2: Physical properties of aluminum 6061-T6, graphite composite and air

	Materials		
	Aluminum 6061 T6 [82]	**Graphite composite BMC 940 [82]**	**Air at 20°C [83]**
Physical properties			
Density (kg/m^3)	2700	1820	1.205
Thermal conductivity (W/m·k)	167	46.2	0.0257
Specific heat (J/kg·k)	896	1004	1005

3.7 Design and fabrication of 50cm^2 active area coated aluminum bipolar plate fuel cell stack

The lifetime performance of a three cell stack was investigated in this study. A forced air fuel cell stack (Figure 3.19) was designed and fabricated. The stack consisted of three MEAs, four coated aluminum bipolar plates and two terminals that were directly machined and anchored on the first anode and last cathode plates in the stack to eliminate the need for additional current collectors. The stack also included two end plates that were used to sandwich and hold the entire main components of the stack including the MEAs and bipolar plates together. Figure 3.19 shows that the end plates were designed with bolt locking feature which allows tightening the fuel cell stack using a single wrench and this could save considerable amount of time during the assembly and repair of the fuel cell stack. The active area of each cell was 50cm^2. A cooling fin, humidity conservative flow field, and internal manifolds were collectively machined onto the aluminum bipolar plates to include all the new and innovative stack design features gained from the current research work. Double layer chromium carbide corrosion resistant coating (Cr-C-Ni and Pure Cr_3C_2) was thermally sprayed onto the aluminum bipolar plates to protect the aluminum from corrosion during the electrochemical reaction while maintaining low ICR. Briefly, the manufacturing processes of bipolar plates included CNC machining and HVOF thermal spraying processes. Figure 3.20a shows the humidity conservative flow field pattern that was machined onto an aluminum plate. In order to maximize the gasket contact area located between the internal manifold and flow field pattern to prevent any possibility of internal gas leak, the internal manifold was machined at steep angle to increase the gasket contact ares as Figure 3.20b shows. After the CNC machining was completed, the bipolar plates were sand blasted by 80 mesh size aluminum oxide to obtain rough surface that would enhance the adherence of the coating layer with the substrate. This was a necessary preparation for the thermal spray process to apply the chromium carbide coating using HVOF thermal spray system (Figure 3.21).

Figure 3.22 shows both coated aluminum (left) and uncoated aluminum plates (right). Internal manifolds which were not covered by the thermal spray coating were coated with acrylic conformal coating (Figure 3.23) to isolate the contact between the aluminum substrate and the water generated from the electrochemical reaction. This acrylic

conformal coating is commercially available and widely used in electronic application to prevent corrosion on printed circuit boards and soldered connections. The slight color change around the gas inlets and outlets in Figure 3.23 represents the excess acrylic conformal coating which was absorbed onto the chromium carbide coating making the coating material's color darker.

Three five-layer MEAs with 50 cm^2 active area were acquired from BCS Fuel Cells Inc. and assembled into the fuel cell stack with silicon gaskets. To study the three cell stack's behavior at different operating conditions, the stack was operated and observed at two different operating temperatures and different current densities. The stack was initially operated at 37°C and current density of 0.4A/cm^2 for 250 hours and then operated at 80°C and current density of 0.5A/cm^2 for additional 500 hours to examine the bipolar plate's resistance to corrosion and the lifetime performance of the stack. The stack was self-heated during its electrochemical reaction. A cooling fan was placed under the fuel cell stack to remove the excess heat generated from the electrochemical reaction and to maintain its temperature at 37°C and 80°C. The operation of the stack was shut off daily to allow the stack to cool off to room temperature and to apply thermal cycling (20°C – 80°C) to the stack.

Figure 3.24 shows complete lifetime test setup for the three cell stack. The experimental setup includes cooling fans, an air bubbler to humidify the incoming air, two flow meters to monitor the flow rate of the air and hydrogen fed to the stack. Electronic load and LabView as a data acquisition system were an integral part of this experimental setup. Air and hydrogen pressures were set at 0.034MPa (5 psig). The air flow rate was set at 4 SLM and was supplied to the stack through a bubbler. The hydrogen was dead-ended at the exhaust manifold and purged periodically. Current, voltage, power output and temperature of the stack as well as back pressure and volume flow rate of the reactant gases fed to the three cell stack were measured and recorded by the data acquisition system.

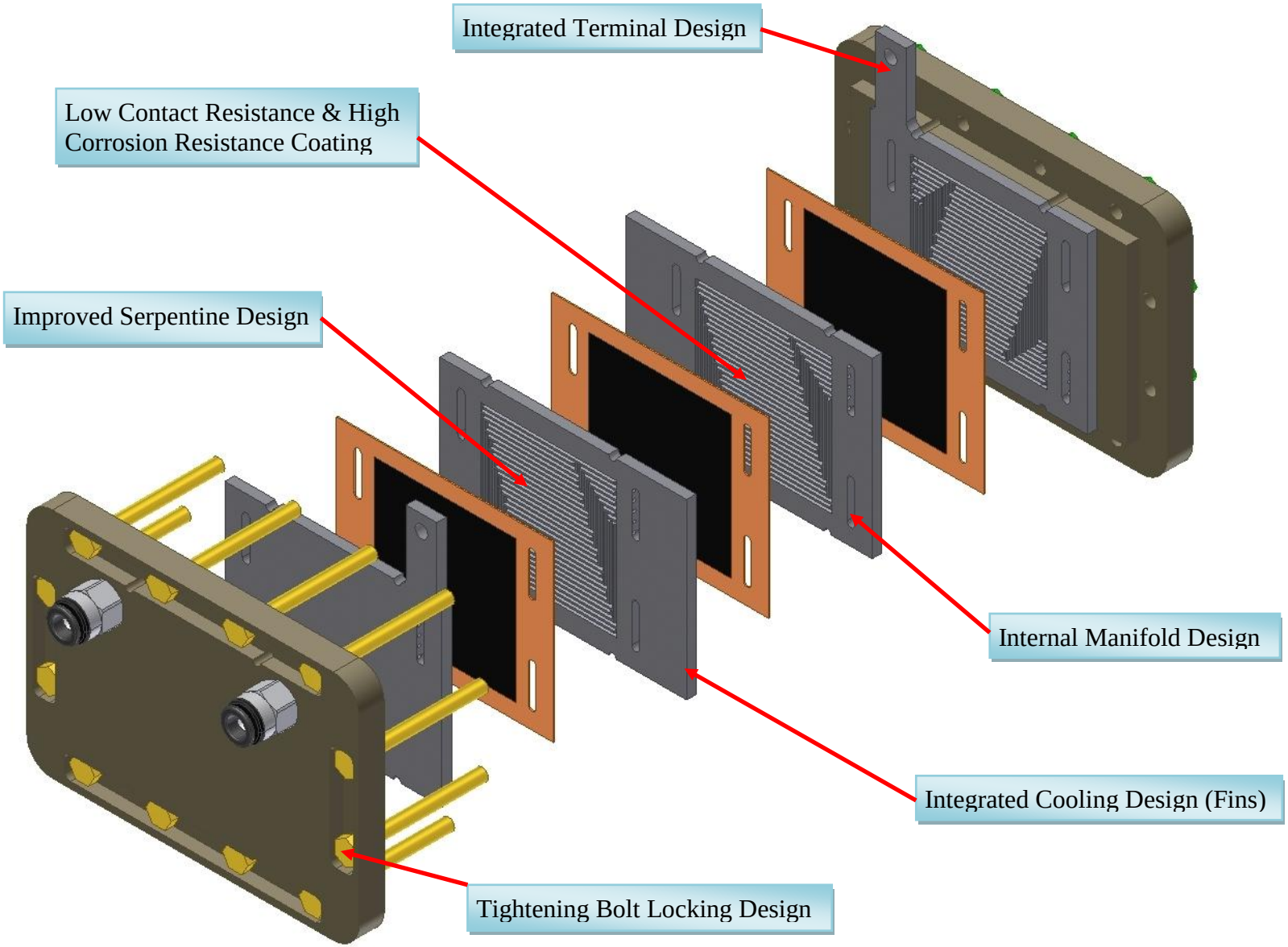

Figure 3.19: 50cm^2 active area forced air fuel cell stack featured with coated aluminum bipolar plates, integrated fin design, integrated terminal design, improved serpentine design, tightening bolt locking design and internal manifold design.

(a)

(b)

Figure 3.20: CNC machining process on aluminum bipolar plates (a) flow pattern (b) internal manifold

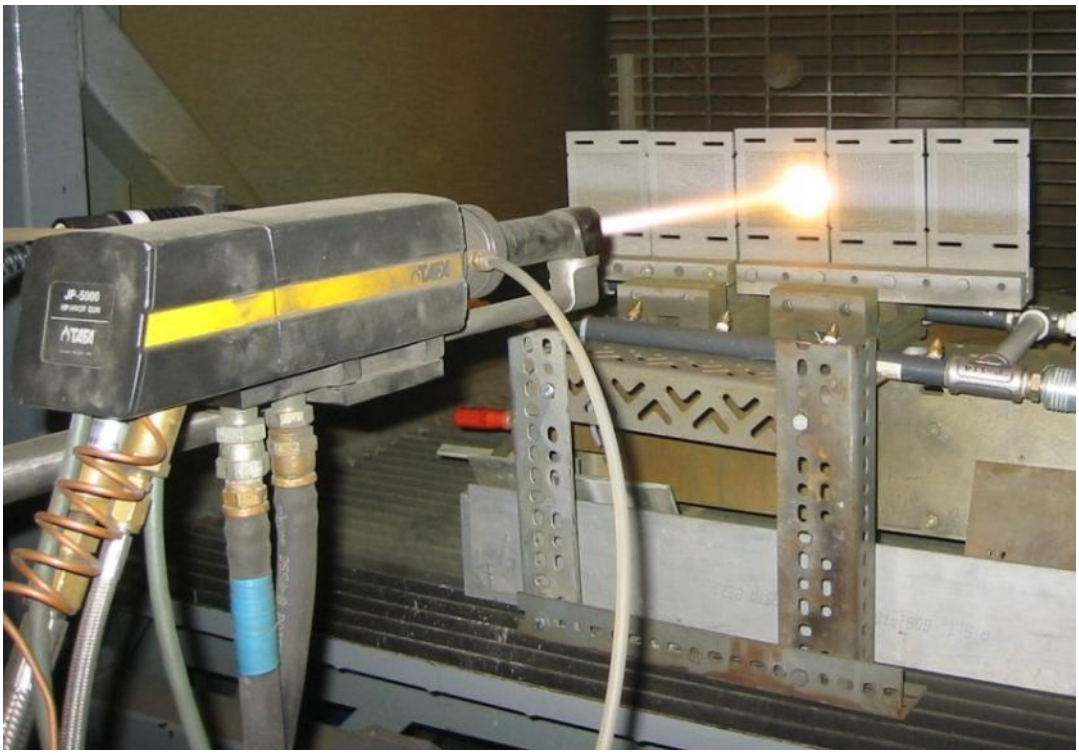

Figure 3.21: Thermal spray process for aluminum bipolar plates

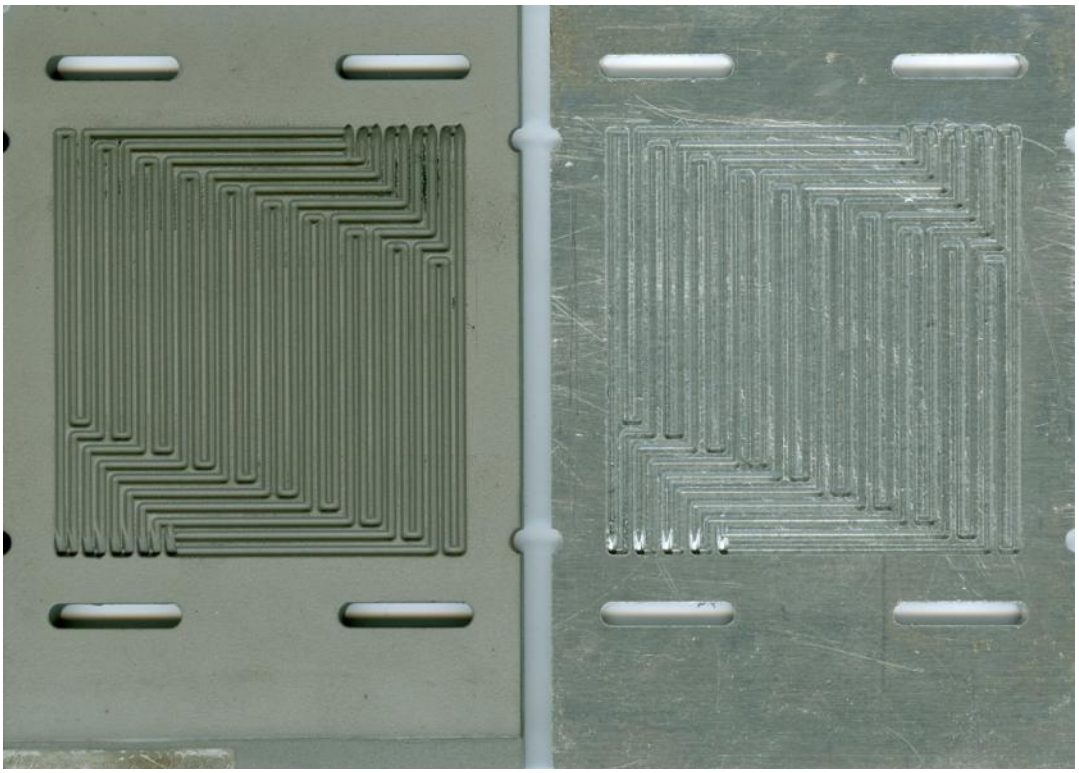

Figure 3.22: Coated aluminum bipolar plate (left) and uncoated aluminum bipolar plate (right)

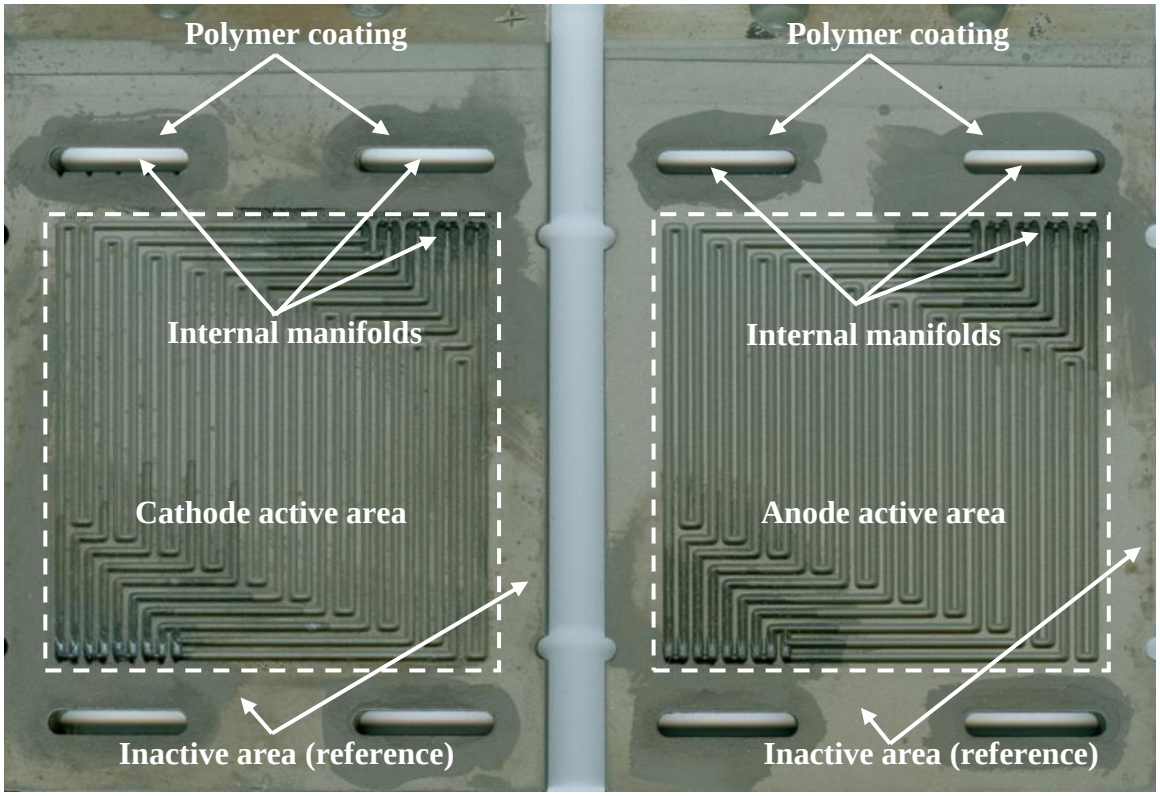

Figure 3.23: Coated aluminum bipolar plates with acrylic conformal coating (polymer coating) applied onto the internal manifolds: cathode (left) and anode (right) before lifetime testing

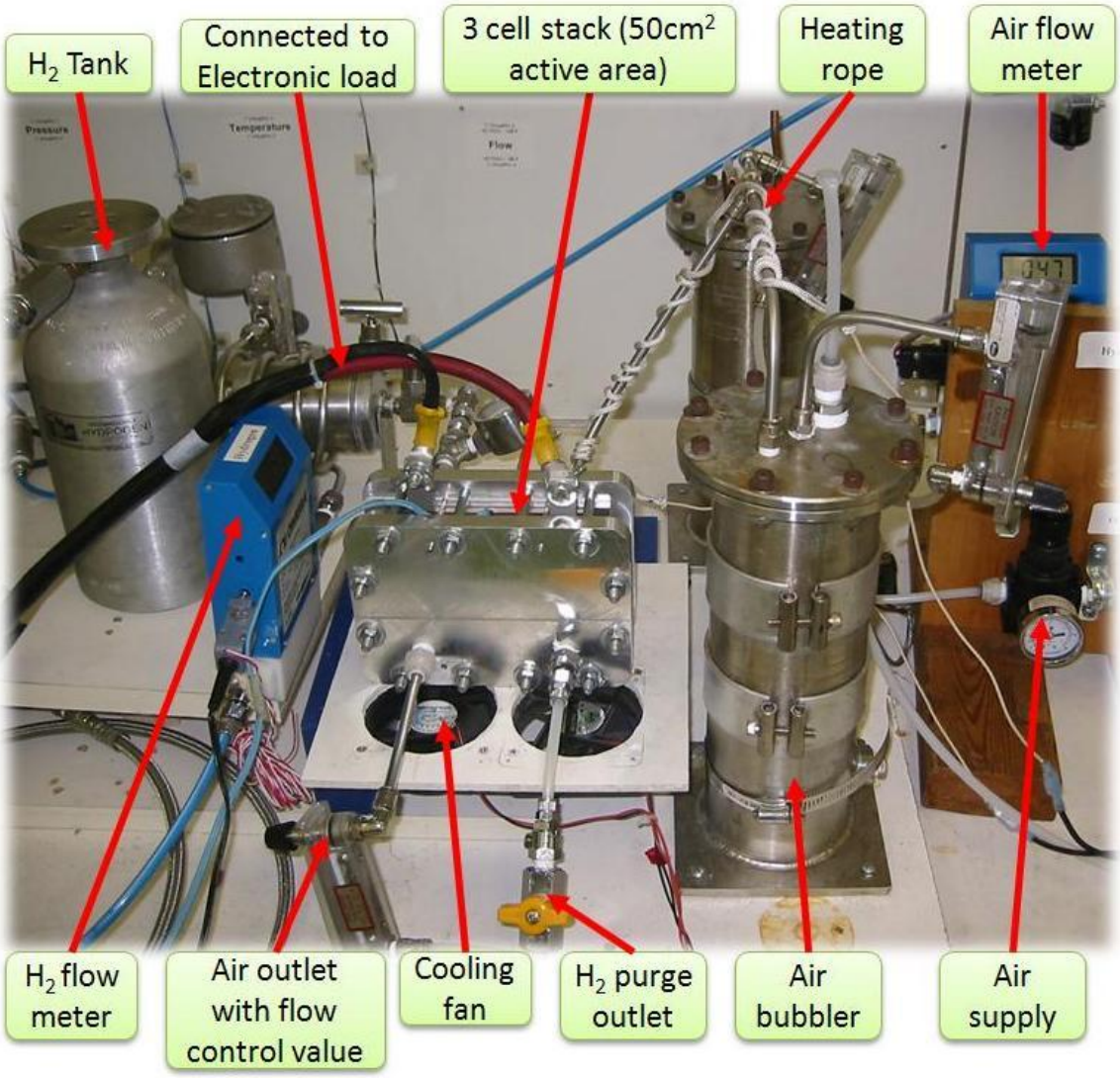

Figure 3.24: Experimental setup for fuel cell lifetime testing.

3.8 Metallic bipolar plates and membrane electrode assembly characterization studies setup

Single fuel cell and fuel cell stack, made of coated aluminum bipolar plates, were fabricated and operated for 1000 hours and 750 hours respectively to investigate their long term performance as described in the previous sections. After 1000 hours and 750 hours of operation, both single fuel cell and fuel cell stack were dismantled. The bipolar plates were cleaned with alcohol to remove excess carbon fibers from the gas diffusion layer and unwanted debris during the handling in preparation for surface characterization. The surface characterization was conducted by SEM (LEO 1550) equipped with backscattered, secondary, in-lens and energy dispersive x-ray (EDX) detectors. Each x-ray spectrum was taken at 200 seconds real time and three x-ray spectra were recorded and averaged in each area for consistent spectrum comparison.

Figure 3.25 shows the 6.45 cm^2 active area aluminum bipolar plate which was coated with Cr_3C_2-25%NiCr coating and operated for 1000 hours in the single fuel cell. Figure 3.26 shows the 50 cm^2 active area aluminum bipolar plates which was coated with double layer chromium carbide (Cr-C-Ni and Pure Cr_3C_2) coating and operated for 750 hours in a fuel cell stack. The figures indicate the valleys (channels) and lands (ribs) in the active area where they were characterized to identify the chemical change on the bipolar plate surface. The inactive (unutilized) areas of the bipolar plates were used as the control reference for comparison between before and after 1000 hours and 750 hours of operation respectively. In addition, the 50 cm^2 active area coated aluminum bipolar plate used in the fuel cell stack was also cut along the active area and polished to examine the cross section of the bipolar plate substrate and the coating material (Figure 3.27). The polishing of cross section of the bipolar plate was performed using Buehler Beta grinder-polisher with different grinding discs and 3μm polycrystalline diamond suspensions to achieve smooth and flat cross section for both substrate and coating material to obtain higher quality SEM images.

Single fuel cell MEA was characterized using XRD. Small portions of both new and 1000 hour operated MEA's surfaces were scraped and grounded into powder form for the characterization study. Three samples of anode and cathode of the MEA were collected for XRD analysis and patterns were obtained at beam line X7B of the National

Synchrotron Light Source (NSLS) at Brookhaven National Laboratory [84-86]. The beam line was equipped with MAR345 image plate detector and is capable of fast data collection. The wavelength of the beam was adjusted to 0.922 angstroms. Each sample was filled inside a capillary and was rotated while the XRD patterns were taken to minimize the effect of preferred orientation.

Finally, the MEA used in the three cell stack and the produced water during the fuel cell electrochemical reaction was collected and analyzed by ICP-OES at Intertek USA Inc. [87] to detect any dissolved metals or any other impurities. The characterization results are reported in this work.

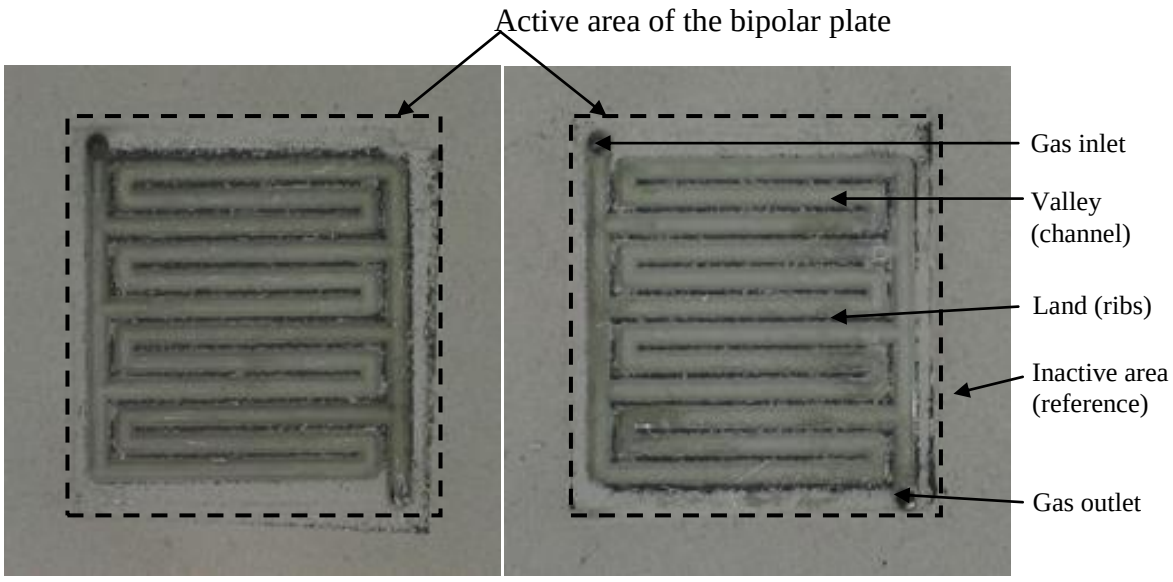

Figure 3.25: Photos of 6.45cm^2 active area coated aluminum bipolar plates used in the 1000 hour lifetime testing: cathode (left) and anode (right)

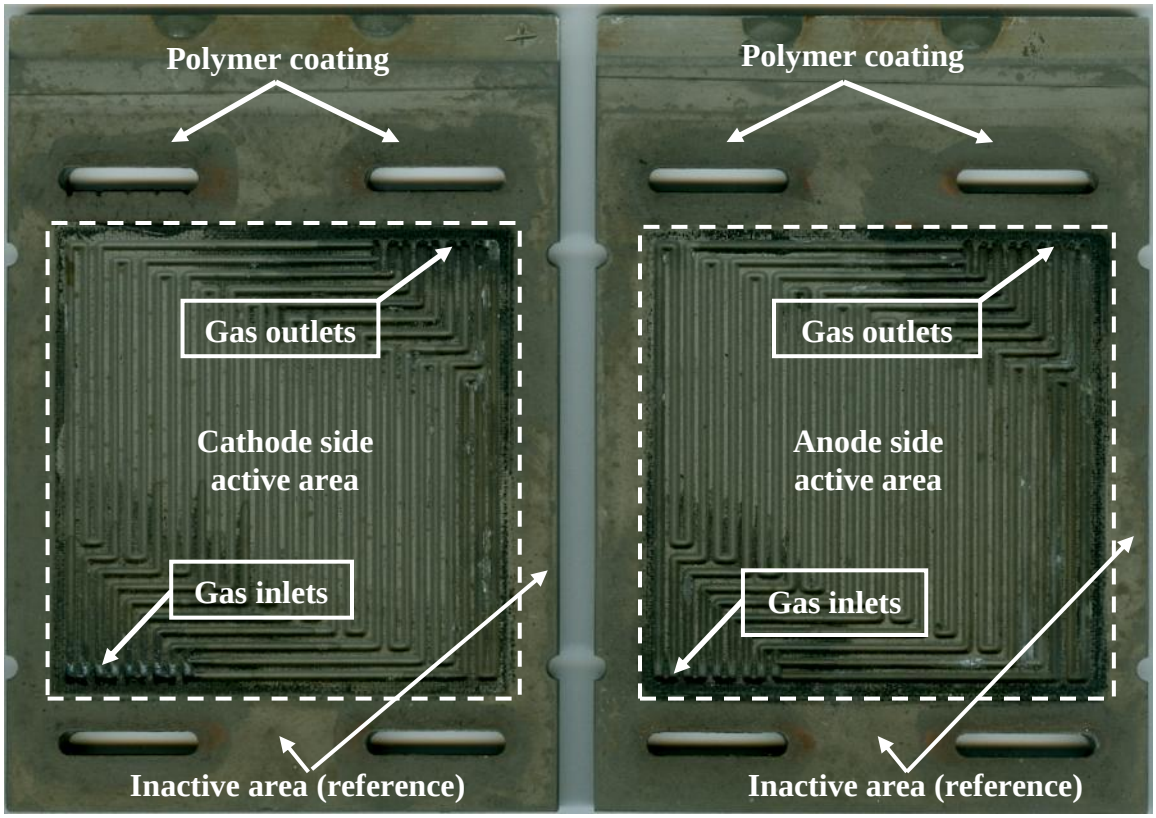

Figure 3.26: Photos of 50cm2 active area coated aluminum bipolar plates used in the 750 hour lifetime testing: cathode (left) and anode (right)

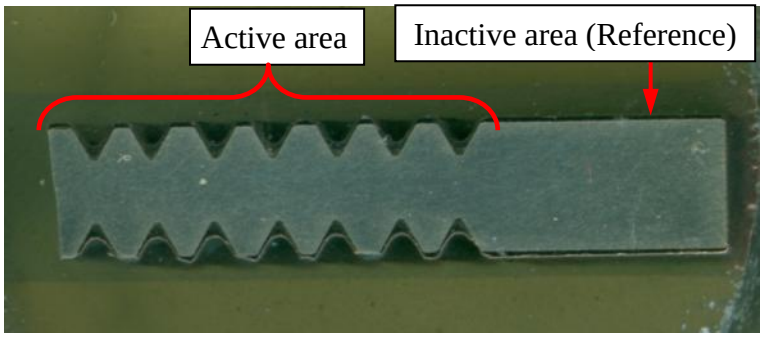

Figure 3.27: Cross section of the 50cm^2 active area bipolar plate and location of active area and reference area

CHAPTER 4

Results and Discussion

4.1 Interfacial contact resistance (ICR) and corrosion measurements for pre-selected bipolar plate materials and coating materials

ICR and accelerated corrosion tests were conducted on selected bipolar plate materials: commercial stainless steels SS316 and SS310, incoloy 800, Poco graphite, composite graphite, titanium carbide and zirconium carbide, to assess their potential to meet the United States Department of Energy (US DOE) ICR target. In addition to the bulk materials mentioned above, chromium carbide coated stainless steel and aluminum substrates were also evaluated for their ICR and corrosion resistance. The study provided an understanding of the effect of higher acidic solution (0.5M H_2SO_4+200 ppm HF) used in accelerated corrosion testing in comparison to the simulated fuel cell environment solution (pH3+0.1 ppm HF). Additional investigations were also conducted to evaluate the effect of different feedstock powder structures, thermal spraying processes, binding materials in the coating and roughness of material surface in relation to the material's ICR and corrosion resistance.

4.1.1 Interfacial contact resistance (ICR) measurements

Figure 4.1 shows the measurements of ICR between GDL and different materials with potential to serve as bipolar plates for PEM fuel cell stacks. The ICR measurements were conducted at various compression pressures (ranging from 25 to 300 N/cm^2) between the GDL and the material tested. As the pressure increased, the conductivity at the interface improved and the ICR was reduced. All materials showed similar behavior (Figure 4.1). This was attributed to increase in interfacial contact points between the materials and the GDL carbon papers when pressed together with increasing pressure enhancing both electrical and thermal conductivity.

Figure 4.2 shows the ICR values of different materials at the typical fuel cell stack compression force of 140 N/cm^2. The ICR of Poco graphite material showed the lowest ICR measured value in comparison to other sample materials. The data in Figure 4.2 also

indicated that stainless steel had a higher ICR value than the commonly used graphite composite material. The result of the stainless steel samples agrees with the trend observed by Davies et al. [17] and Wang et al. [33]. Stainless steel tends to form a layer of chromium, iron and nickel oxides passive film that inhibits electrical conductivity at the interfacial layer. However, the ICR can be relatively improved by increasing the Cr content of the alloy which can reduce the surface passive film thickness by hampering the oxidation of other elements existing in the stainless steel such as iron, nickel etc. [33]. The relatively lower ICR of chromium carbide coating in comparison to SS316 was attributed to stable and conductive Cr_3C_2 particles. A higher surface roughness of the chromium carbide coating compared to the uncoated SS316 sample directly contributed to the enhancement of the ICR by increasing both the pressure and actual contact area between the coating and the GDL. More explanation of the effect of roughness on ICR and corrosion resistance will be discussed in a later section (4.1.6 Effect of roughness). Thus, the ICR measurement gives the following ascending order: poco graphite < chromium carbide coating with a SS316 substrate < graphite composite < titanium carbide < incoloy 800 < SS310 < SS316 < zirconium carbide. The experimental measurement has proven that chromium carbide coating can be an excellent candidate coating for PEMFC metallic bipolar plates since its ICR value was the second lowest after Poco graphite. Despite the superiority of Poco graphite to metals in both corrosion and ICR, it is not a good candidate as a bipolar plate material due to its brittleness, porosity and lack of durability.

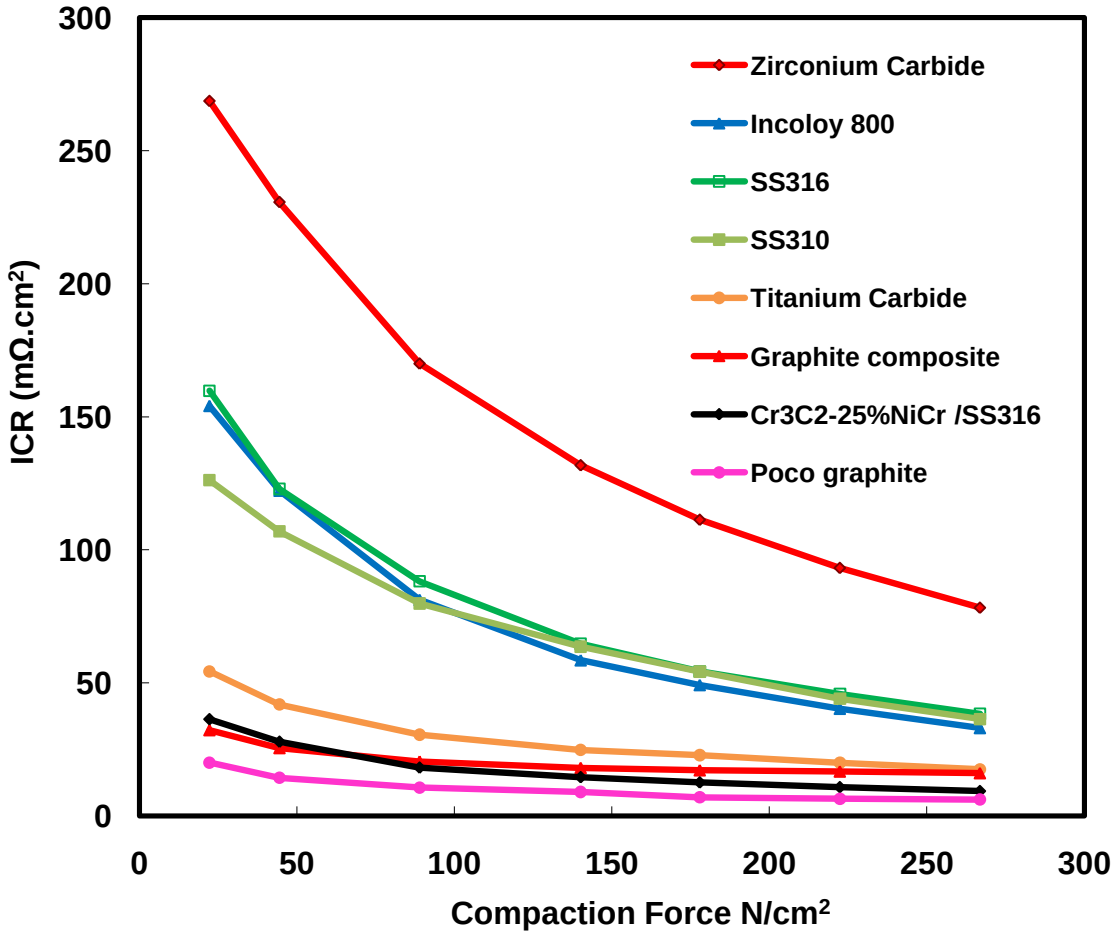

Figure 4.1: Interfacial contact resistance of preselected bipolar plate materials.

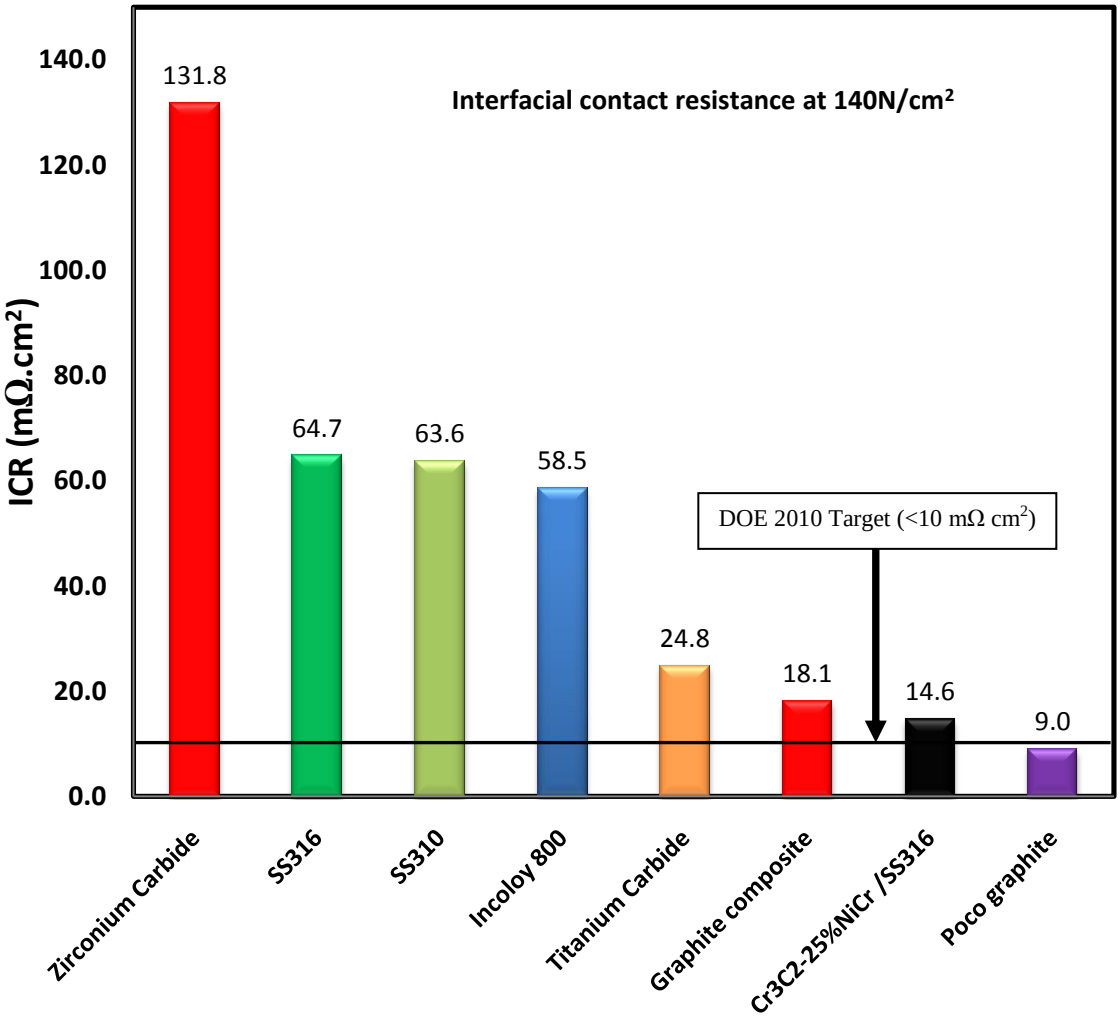

Figure 4.2: Interfacial contact resistance of preselected bipolar plate materials at 140 N/cm^2 (203psi).

4.1.2 Testing under solution media 0.5M H_2SO_4 +200 ppm HF at 25°C

Corrosion testing was conducted in this section to sort out materials based on their corrosion resistance under the harsh corrosive environment (0.5M H_2SO_4 + 200ppm HF) at 25°C. Potentiodynamic measurements on the candidate materials were performed and the corrosion current density of Poco graphite, composite graphite, chromium carbide coating on SS316 substrate, titanium carbide, zirconium carbide, SS310, SS316, and Incoloy 800 were 3.9, 0.4, 54.7, 10.7, 3.0, 0.6, 2.2 and 2.1 $\mu A/cm^2$, respectively (Figure 4.3). The corrosion current density (Icorr) was measured using tafel analysis (Figure 4.4) and the results showed the candidate materials' performance in the ascending order as follows: Graphite composite < SS310 < Incoloy 800 < SS316 < zirconium carbide < Poco graphite < titanium carbide < chromium carbide coating with a SS316 substrate.

Corrosion resistant of chromium carbide coating in such acidic environment (0.5 M H_2SO_4 + 200 ppm HF) could be improved by reducing the NiCr binder content in the coating because of possible separation of Ni from Cr during the thermal spray process and exposure to the acidic environment. As expected, chromium carbide coating on a SS316 substrate with relatively lower NiCr content exhibited a decrease in the corrosion current as Figure 4.5 depicts. Pure Cr_3C_2 coating on SS316 substrate showed the lowest corrosion current among three different chromium carbide coatings due to the absence of NiCr binder. However, an opposite behavior was observed when these coatings were applied on aluminum substrate (Figure 4.5). The corrosion current measurement of pure Cr_3C_2 and Cr_3C_2-7%NiCr exhibited much higher values than that of SS316 substrates. This was attributed to the porosity of the pure Cr_3C_2 and Cr_3C_2-7%NiCr coating due to the lack of NiCr as a binding agent. On the other hand, Cr_3C_2-25%NiCr coating showed comparable corrosion current in both SS316 and aluminum substrates which indicated that this coating was much denser and had lower porosity than the other two coatings.

Potentiostatic test is a reliable accelerated testing technique to evaluate the bipolar plate behavior under long period of time while subjected to acidic environment without the actual operation of the fuel cell saving both time and money. The coating with the lowest corrosion current (i.e. pure Cr_3C_2 coating on a SS316 substrate) was evaluated using this technique and uncoated SS316 coupon was also tested as a control reference. In such high concentration of acidic environment (0.5M H_2SO_4 +200ppmHF at 25°C),

the ICR values of both Cr_3C_2 coating and SS316 decreased after 72 hours of potentiostatic test at 0.6V(SCE) as shown in Figure 4.6. This was attributed to relatively high concentration of the solution that etched away the oxide layer formed on the uncoated SS316 and the Cr_3C_2 coating. In addition, the drastic ICR reduction in uncoated SS316 sample was due to the relatively stable form of the uncoated SS316 that had thicker and denser oxide film than pure Cr_3C_2 coated SS316. The low ICR of pure Cr_3C_2 coating was due to the surface roughness which will be explained in the later section 4.1.6 (effect of roughness). Therefore the removal of this passive layer as a corrosion product could result in misleading improvement in ICR measurement.

The etching process in both materials can be explained in the potentiodynamic curves (Figure 4.7). The potentiodynamic scans under high concentration acidic solution (0.5M H_2SO_4 +200 ppm HF) did not show passivation in both materials during the full scan. Current increased as voltage increased from open circuit potential which showed that no further oxide film was built up to protect their surfaces from further corrosion. As a result, when potentiostatic test was performed on both materials at 0.6V(SCE) for 72 hours, the initial oxide film on the both material surfaces were broken down by the acidic solution. Therefore, this high concentration acidic solution (0.5M H_2SO_4 +200ppm HF) was not categorized as the actual fuel cell condition but it was used to sort out the corrosion resistance of different materials and coating as depicted in Figure 4.3.

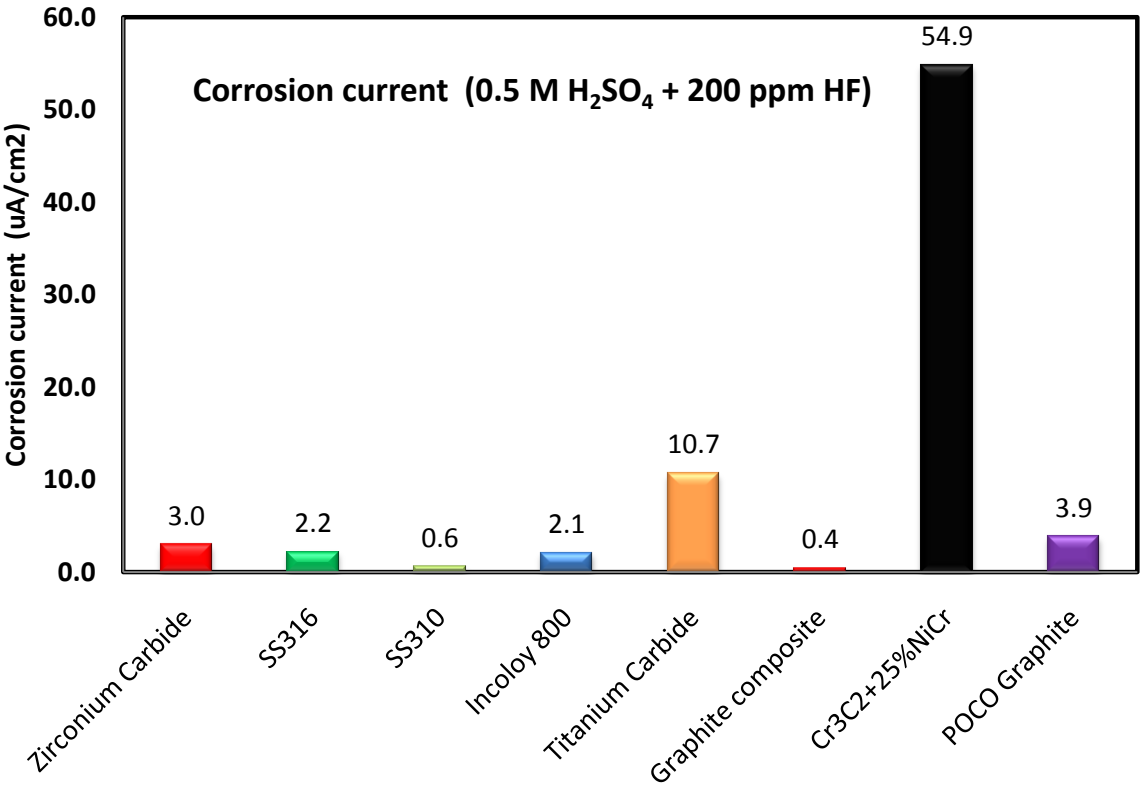

Figure 4.3: Corrosion currents (potentiodynamic) of preselected bipolar plate candidate materials.

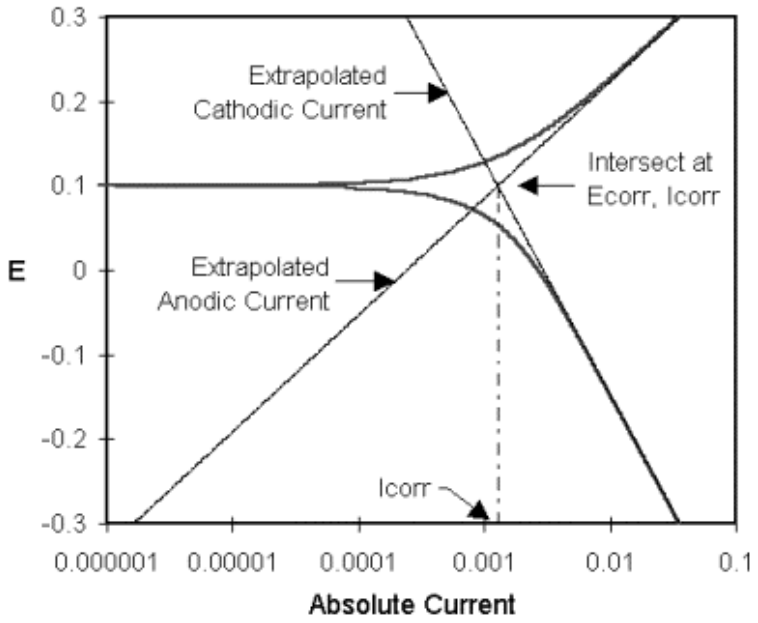

Figure 4.4: Classic tafel analysis, potentiodynamic scan and corrosion current (Icorr) [88]

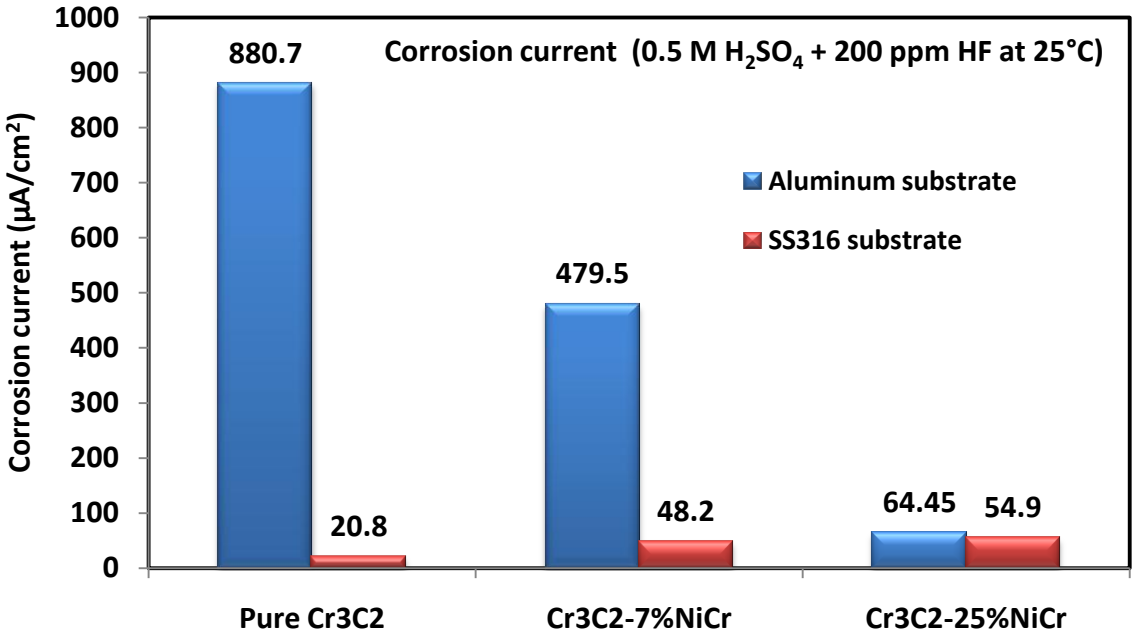

Figure 4.5: Corrosion current (potentiodynamic) of chromium carbide with different NiCr contents and different metal substrates

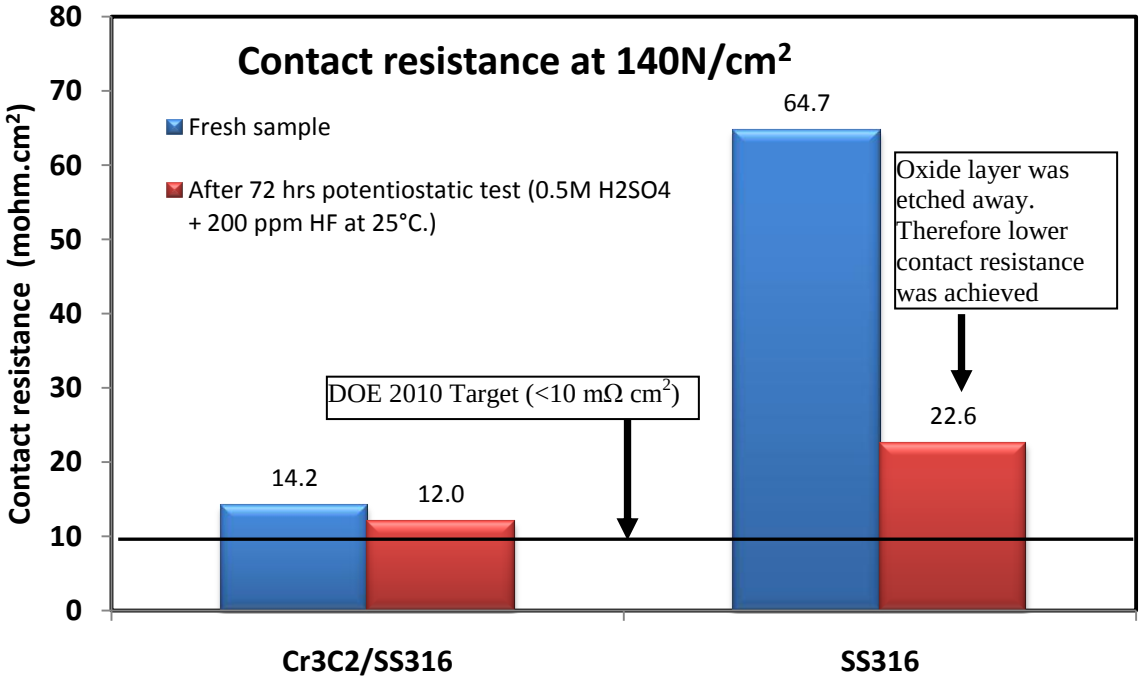

Figure 4.6: Interfacial contact resistance of pure Cr_3C_2 coated SS316 substrate and uncoated SS316 (before and after the 72 hours of Potentiostatic test) at 140 N/cm^2

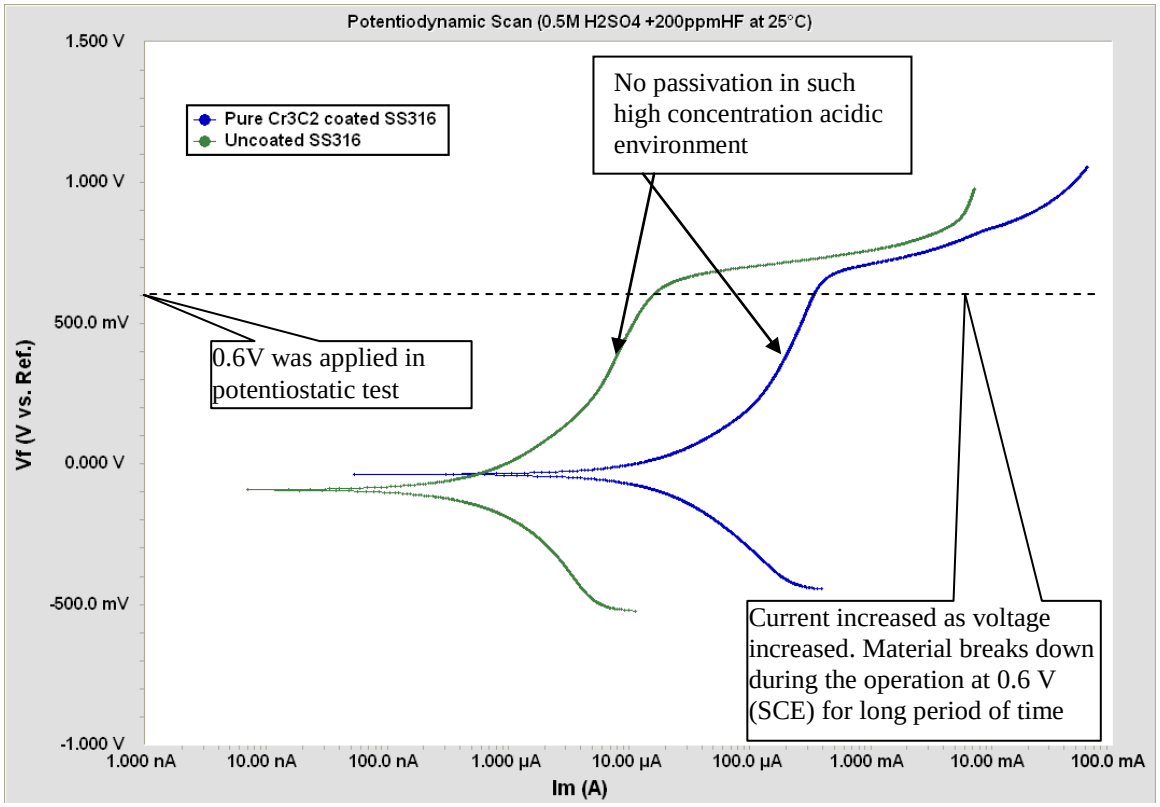

Figure 4.7: Potentiodynamic polarization curve of pure Cr_3C_2 coated SS316 and uncoated SS316.

4.1.3 Testing under solution media pH3 +0.1 ppm HF at 80°C

Similar corrosion testing was also performed with a lower concentration solution (pH3 + 0.1ppm HF) and at a higher temperature of 80°C to determine the corrosion current of chromium carbide coating with different percentage of NiCr binder (Pure Cr_3C_2, Cr_3C_2-7%NiCr and Cr_3C_2-25%NiCr), as well as uncoated SS316 and graphite composite. This simulated corrosive environment is close to that encountered in an actual PEM fuel cell. As expected, similar corrosion behavior obtained from a higher concentration solution (0.5M H_2SO_4+200 ppm HF at 25°C) was observed as shown in Figure 4.8. The corrosion currents obtained from the relatively lower concentration solution (pH3 + 0.1 ppm HF) at 80°C were much lower than those obtained from higher concentration solution (0.5M H_2SO_4+200 ppm HF) at 25°C. Figure 4.8 also shows similar trends when SS316 and aluminum substrates were used and explanations were given in the previous section as aggressive solution was used. Unlike the previously used higher acidic solution at 25°C, the interfacial contact resistance of uncoated SS316 and chromium carbide coated SS316 showed higher values after 2.5 hours of potentiostatic test at 0.6 V in pH3 + 0.1ppmHF solution at 80°C, especially uncoated SS316 coupons (Figure 4.9). This was due to the oxide layer built up on the surface of uncoated SS316 samples and possible oxidation of the dissociated chromium and nickel from the chromium carbide coating and the nickel chromium binder, respectively.

This phenomenon of relatively thick and continuous oxide layer blanketing the uncoated SS316 coupon can be explained by the potentiodynamic polarization curve of the material. Figure 4.10 shows that uncoated SS316 passivated approximately below 0.65V (SCE) at 8μA. The current remained relatively constant when voltage increased from 0V to 0.65V (SCE). This was attributed to a relatively low acidic solution and the low voltage allowed the formation and maintenance of an oxide film on the material surface. This oxide film continued its built up within these operating voltages to prevent further corrosion on the surface. Also, due to the relatively low acidic solution used in this experiment, transpassivation was not reached at 0.6V as depicted in Figure 4.10. Therefore, the passive layer remained intact on the material during the potentiostatic test causing an increase in the interfacial contact resistance as shown in Figure 4.9. However,

a breakdown and removal of the oxide film can occur due to transpassivation at 0.65V. This oxide film removal could result in lower ICR but cause MEA contamination and considerable power degradation if this material is used as fuel cell bipolar plate. Similar result was also observed in other chromium carbide coatings on SS316 substrates except the passivation currents of the coatings were between 100 to 200 µA which were higher than that of uncoated SS316. On the other hand, graphite did not show any signs for passive and transpassive stages as anticipated by the absence of a passive oxide film. Therefore graphite composite is widely used in the fuel cell industry due to its excellent corrosion resistance as mentioned in Chapter 1.

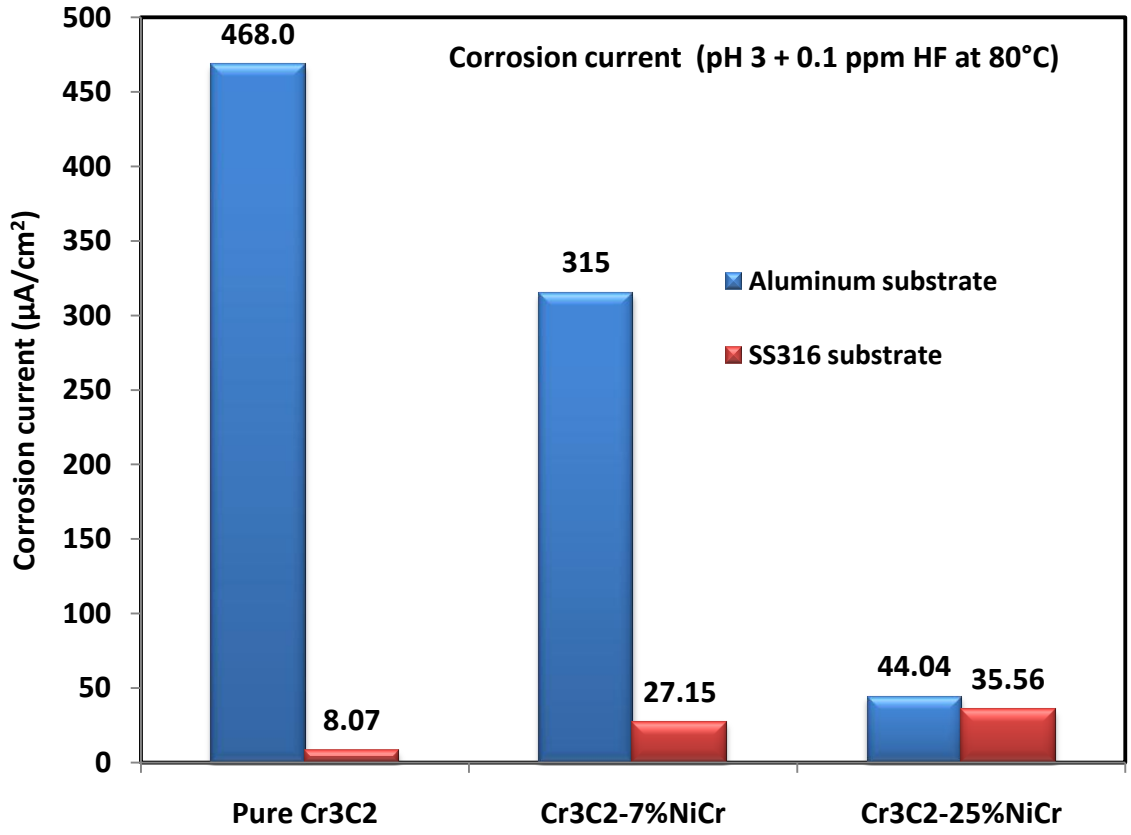

Figure 4.8: Corrosion current (potentiodynamic) of chromium carbide with different NiCr contents and different metal substrates

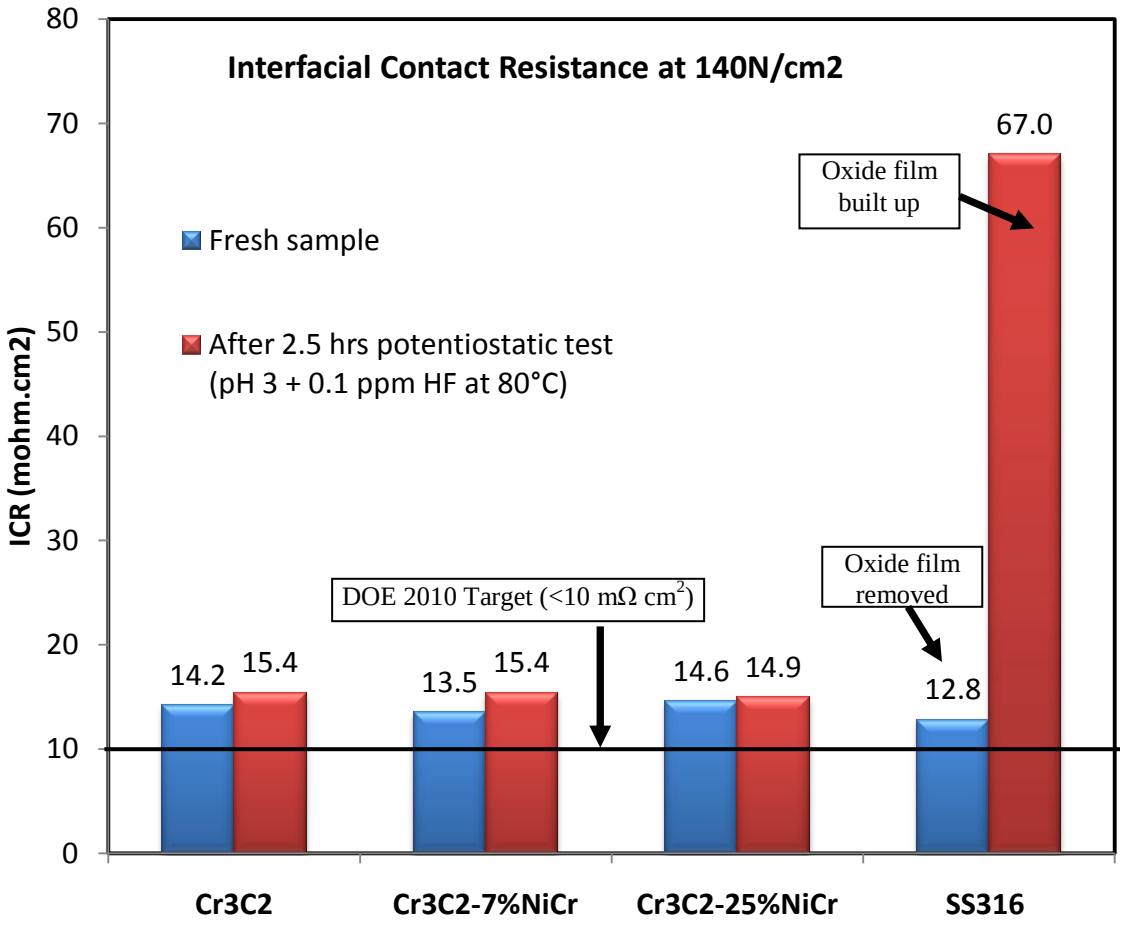

Figure 4.9: Interfacial **c**ontact resistance of Cr_3C_2 coated SS316 substrate and uncoated SS316 sample (before and after the 2.5 hours of Potentiostatic test) at 140 N/cm^2

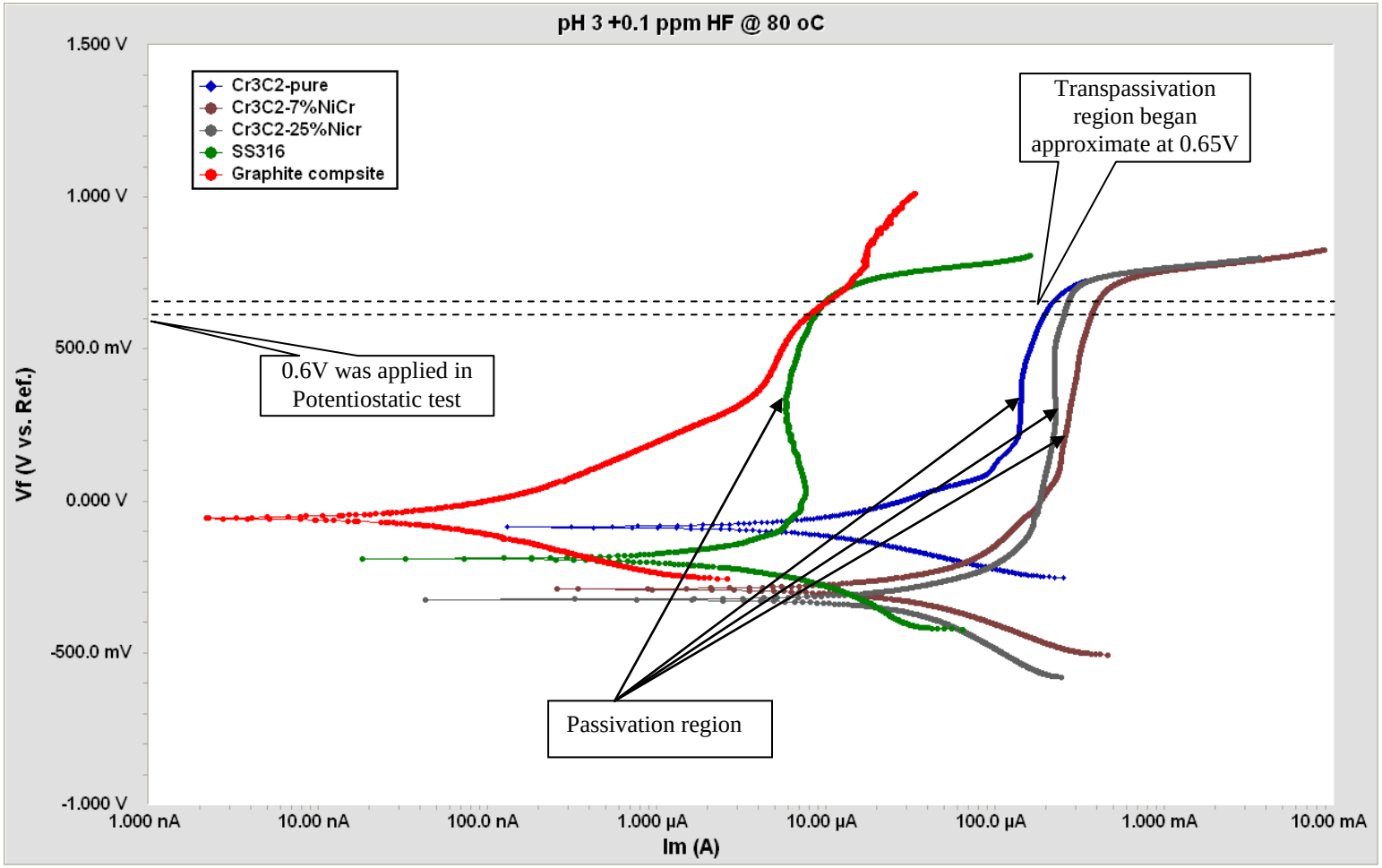

Figure 4.10: Potentiodynamic polarization curve of uncoated SS316, graphite composite and chromium carbide coating with different NiCr binders coated SS316 substrates.

4.1.4 Effect of different feedstock powders, coating structures and substrate material

Potentiodynamic tests in previous sections have shown that reducing NiCr content in chromium carbide coating on SS316 substrate can reduce the corrosion current as depicted in Figures 4.5 and 4.8. However, in aluminum substrate samples, the opposite behavior was observed due to increase in porosity as the NiCr alloy content was decreased. Moreover, it was noted that the coating material and the structure of feedstock powder played an important role in the coating's ICR and corrosion resistance. The coating properties depend strongly on the manufacturing process of the feedstock powder. Figure 3.1 shows four different types of chromium carbide feedstock powders. Figures 3.1a and 3.1b show that pure Cr_3C_2 and Cr_3C_2-7%NiCr powders had a very similar structure except that there were 7% NiCr particles blended into the Cr_3C_2-7%NiCr powder. These NiCr particles were randomly placed in between the Cr_3C_2 particles as shown in Figure 3.1b. When pure Cr_3C_2 powder was used, porosity occurred in the coating due to lack of binding agent in the powder during thermal spraying. Therefore, pure Cr_3C_2 coating with no NiCr as a binding agent on aluminum substrate gave very high corrosion current as shown Figures 4.5 and 4.8. Corrosion resistance was improved slightly when Cr_3C_2-7%NiCr powder was employed because the 7%NiCr binding agent provided better binding strength between the powder and the aluminum substrate hence reducing the porosity in the coating.

Furthermore, unlike the blended Cr_3C_2-7%NiCr feedstock powder, the agglomerated Cr_3C_2-25%NiCr feedstock powder showed uniform distribution of the NiCr particles as exhibits in Figure 3.1c. The NiCr content increased in the powder in comparison to the Cr_3C_2-7%NiCr powder, and the NiCr particles were smaller and agglomerated with Cr_3C_2 particles as shown in Figure 3.1c. Thus, this agglomerated powder produced a much denser coating, better bonding strength with the substrate and lower porosity in the coating than the blended powder. Therefore, pure Cr_3C_2 and Cr_3C_2-7%NiCr coatings on aluminum substrates had higher corrosion current than these same coatings on SS316 substrates. This was attributed to the porosity of pure Cr_3C_2 and Cr_3C_2-7%NiCr coatings that allowed more corrosion to take place on the aluminum substrates than that on SS316

substrates. The Cr_3C_2-25%NiCr coating showed comparable corrosion current on both SS316 and aluminum substrates due to a relatively low porosity of the coating (Figures 4.5 and 4.8).

Though the Cr_3C_2-25%NiCr coating provided adequate corrosion resistance to the aluminum substrate, it was found by many authors [32-34] that increasing Cr and reducing Ni content in bipolar plates can improve the corrosion resistance in fuel cell environment. Accordingly, Cr-C-Ni powder was chosen due to its higher Cr and lower Ni ratio. This powder did not have any of the Cr_3C_2 phase. It was manufactured as an activated feedstock powder which meant each particle was an alloy of chromium, carbon and nickel as shown in Figure 3.1d. Therefore, this feedstock powder could produce dense coating due to the homogeneous Ni and Cr elements with carbon in each particle. The corrosion current of Cr_3C_2-25%NiCr and Cr-C-Ni coatings on aluminum and SS316 substrates were measured in pH3+0.1ppm HF solution at 80°C by potentiodynamic technique. Figure 4.11a shows that the combination of higher Cr and lower Ni ratio in the material and denser coating improved the corrosion resistance of Cr-C-Ni coating in comparison to Cr_3C_2-25%NiCr coating. The corrosion current of both coatings on SS316 substrates was very close to that on aluminum substrates due to the low porosity and highly dense coating with strong bonding strength between the coating and the substrate provided by the agglomerated and active feedstock powder structures. Figure 4.11b shows that the Cr-C-Ni coating without chromium carbide (Cr_3C_2) layer had higher ICR due to absence of oxide free Cr_3C_2 particles and an increase in oxide formation such as Ni_2O_3 and Cr_2O_3 on the Cr-C-Ni coating, as indicated in the EDX spectrum (Figure 4.12). Figure 4.11b also shows that both chromium carbide coatings on either aluminum or SS316 substrates had almost no effect on the ICR value.

The corrosion resistance and interfacial contact resistance of Cr-C-Ni coating can be improved by applying pure Cr_3C_2 coating on top of the Cr-C-Ni coating. This double-layer coating provided more blanketing effect to protect the substrate from the fuel cell corrosive environment while maintaining relatively low ICR. The bottom layer of the coating was made of Cr-C-Ni that was a fairly dense coating as demonstrated in Figure 4.11a. The top layer of the coating was made of pure Cr_3C_2 that was a relatively porous coating and provided some protection of the bottom layer by reducing the exposure of Ni

and Cr to the corrosive acidic solution which resulted in a lower corrosion current and less oxide film. In addition, this pure Cr_3C_2 layer had reduced the ICR value of the coating due to the conductive Cr_3C_2 particles (Figure 4.11b).

The potentiodynamic scan in Figure 4.13 shows that corrosion current density of the double-layer coating on aluminum and SS316 substrates remained relatively constant as voltage increased from 0.1V(SCE) to 0.7V(SCE) and from 0.1V(SCE) to 0.65V (SCE) respectively due to formation of an oxide film on the coating surface. This oxide film was formed within these operating voltages to prevent further corrosion of the coating material. However, the double-layer coating had higher passivation current than the uncoated SS316, as shown in the comparison of Figures 4.10 and 4.13. This comparison also indicated that the oxide film formed on the coating surface was not as thick and dense as the oxide film on an uncoated SS316. Thus, a thinner oxide film on coating surface results in desirable low ICR (Figure 4.11b).

Potentiostatic tests were also performed on the double-layer coating (pure Cr_3C_2 and Cr-C-Ni) on aluminum substrate in pH3+0.1ppm HF solution at 80°C to examine the durability of the coating. Since the potentiodynamic scans in Figure 4.13 indicated that coatings were in the passivation stage at 0.6V (SCE), the potentiostatic scans at 0.6V (SCE) in Figure 4.14 show that corrosion current remained relatively constant for 9.5 hours without any sign of increasing dissolution or further oxidation of the coating material. In addition, the ICR measurement of the double-layer coating remained unchanged after 9.5 hours of potentiostatic tests (Figure 4.15). Therefore, aluminum can also be used as bipolar plate material when coated with this dense, low ICR and high corrosion resistance double-layer coating.

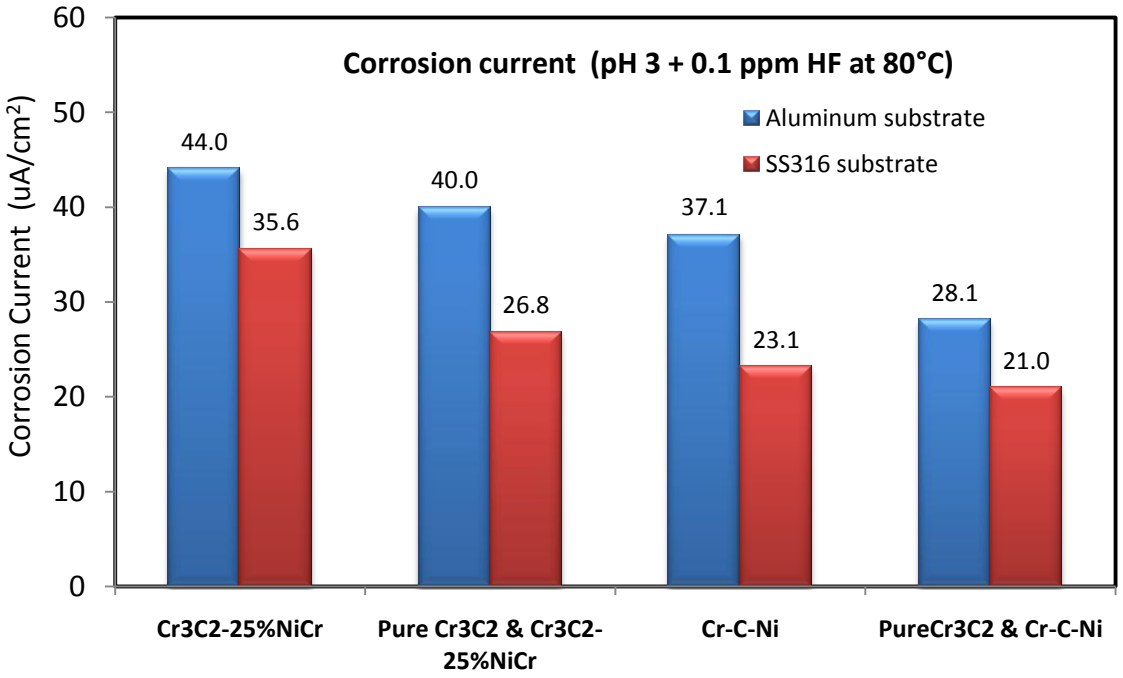

(a)

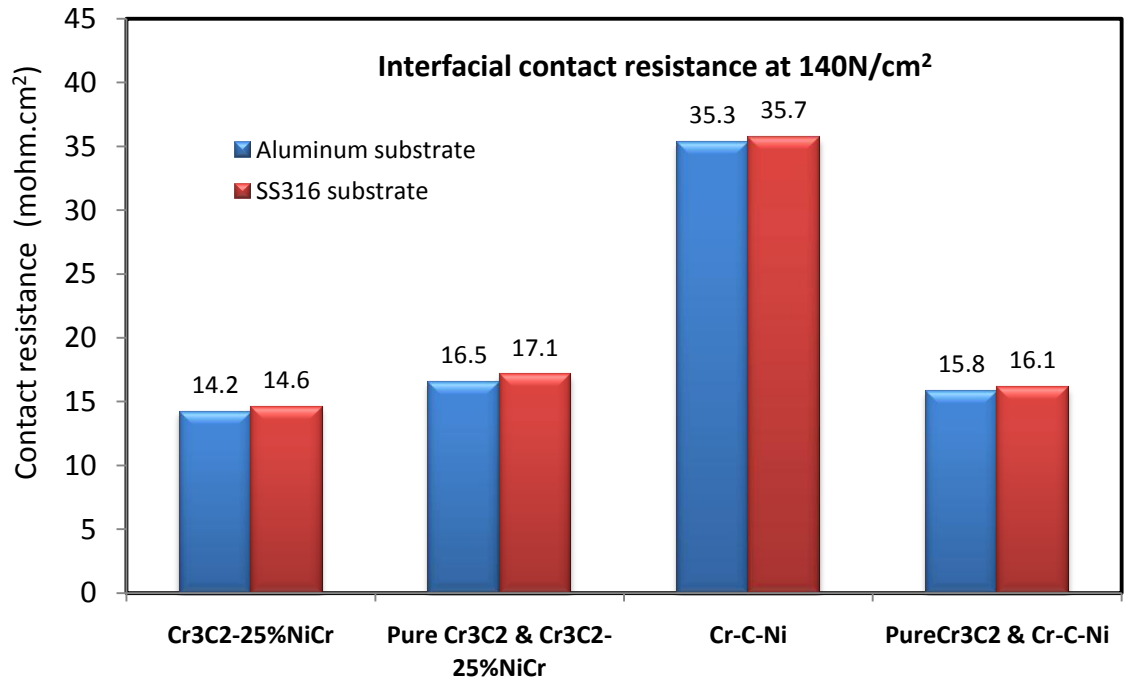

(b)

Figure 4.11: (a) Corrosion current (potentiodynamic) and (b) Interfacial contact resistance at 140 N/cm^2 of Cr_3C_2-25%NiCr coating and Cr-C-Ni coating on aluminum and SS316 substrates

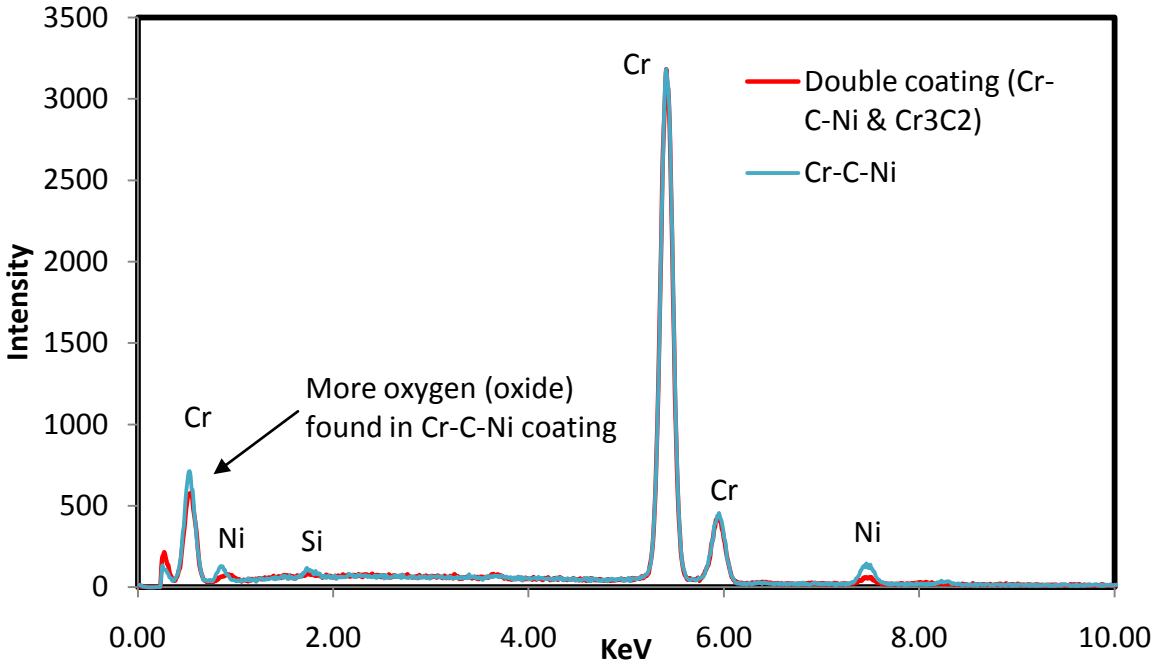

Figure 4.12: Superimposed EDS spectrum for the Cr-C-Ni and double layer coating (pure Cr_3C_2 and Cr-C-Ni)

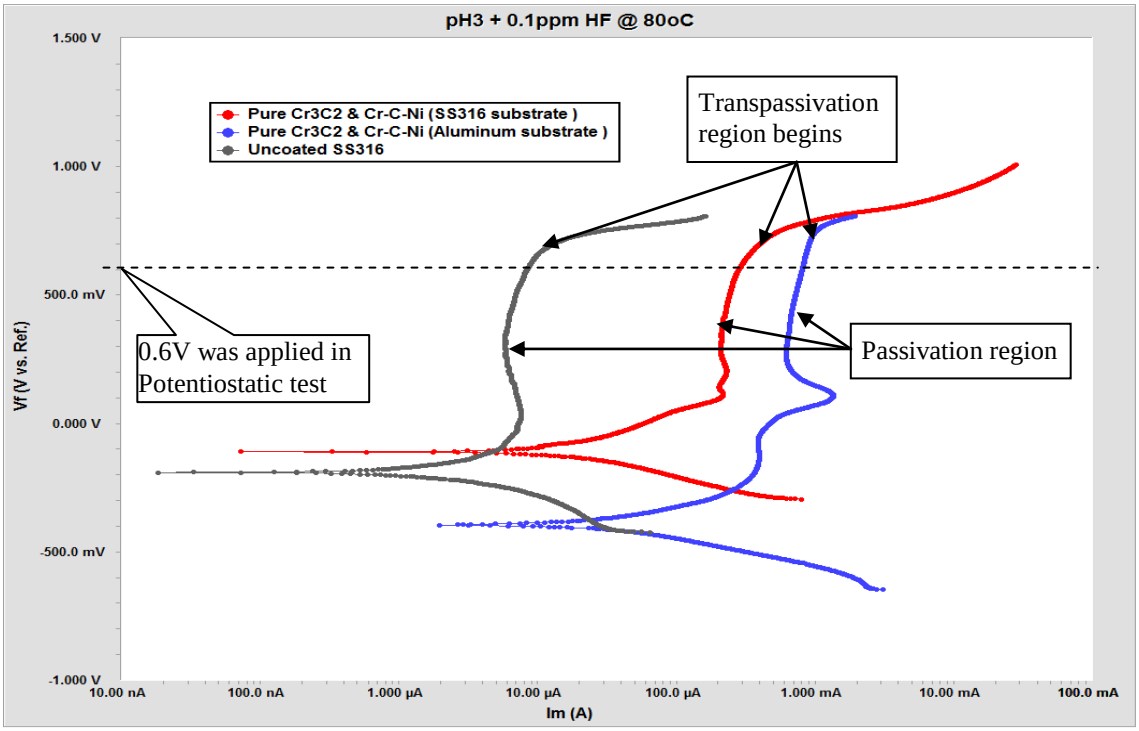

Figure 4.13: Potentiodynamic polarization curves of double-layer coating (pure Cr_3C_2 and Cr-C-Ni) coated aluminum and SS316 substrate.

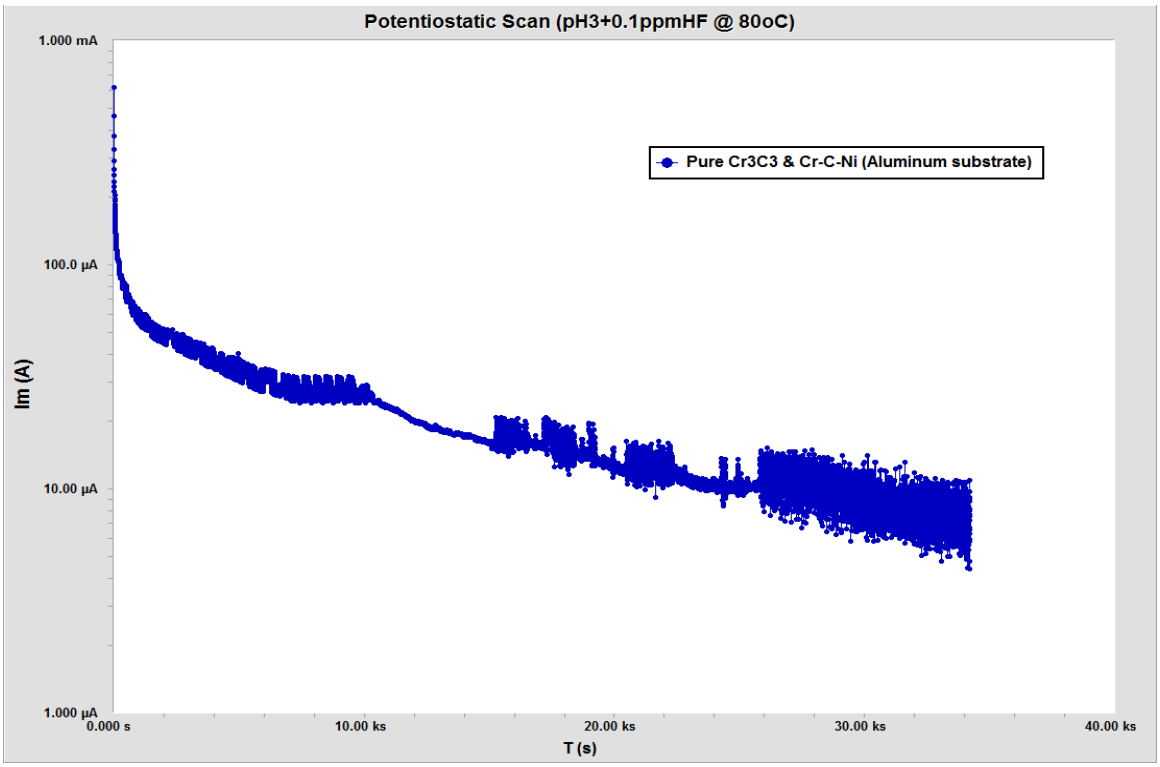

Figure 4.14: Potentiostatic scan of double-layer coating (pure Cr_3C_2 and Cr-C-Ni) coated aluminum substrate.

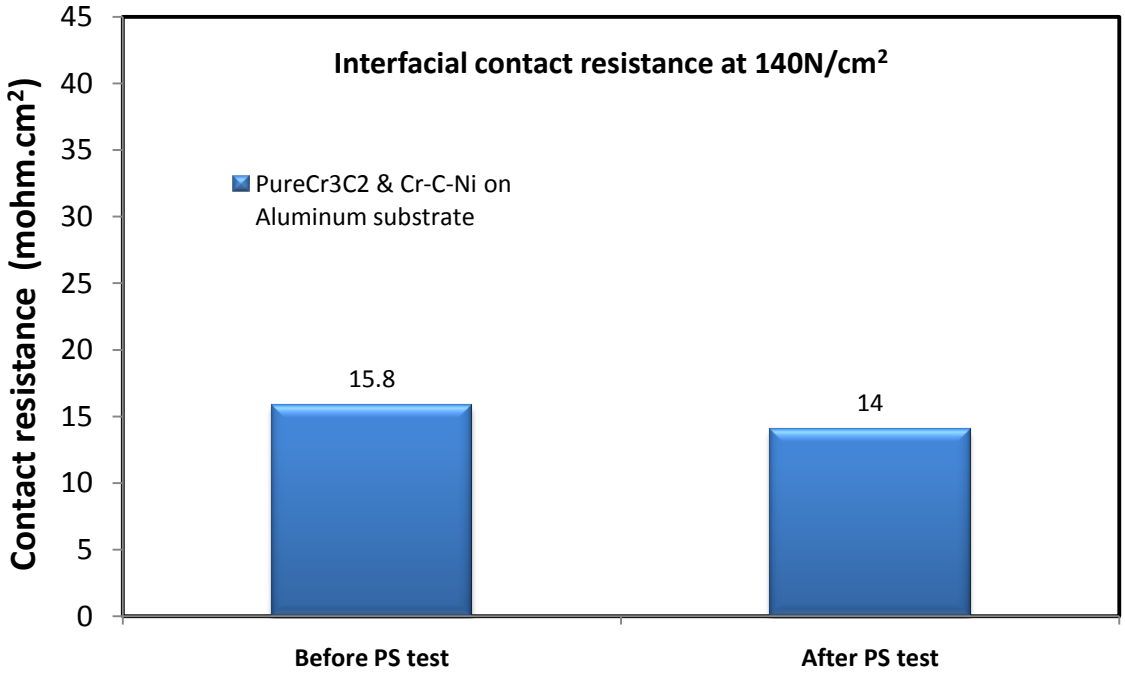

Figure 4.15: Interfacial **c**ontact resistance of double-layer coating (pure Cr_3C_2 and Cr-C-Ni) coated aluminum substrate (before and after the 9.5 hours of Potentiostatic test) at 140 N/cm^2

4.1.5 Effect of inert gas blanket during thermo spraying process and different binding materials

Further improvement in the ICR of chromium carbide coating with a SS316 substrate was achieved by blanketing with nitrogen or helium during thermal spraying. An average 7% reduction in the ICR was obtained (Figure 4.16a). This was attributed to a reduction in the oxide formation during thermal spraying process as the inert gas shielded the plume from the oxygen in the ambient air. The inert gas blanket prevented the Cr_3C_2 and NiCr powder from oxidation during spraying but it increased the corrosion current of the coating because of the existence of free Cr and Ni resulting from alloy dissociation of Cr_3C_2 and NiCr during the spraying process. These free elements oxidized during the corrosion testing process under the acidic environment and increase coating's dissolution and corrosion current (Figure 4.16b). The data indicated that the use of inert gas shrouding during the thermal spraying process of fuel cell bipolar plates was not recommended.

Figure 4.16b demonstrates that the NiCr binder alloy was not adequately stable in the fuel cell environment. Additional binding materials were investigated in an effort to improve corrosion resistance of the coating. Molybdenum and cobalt based alloys were selected and tested as binding agent for the chromium carbide coating. Molybdenum has been frequently utilized to improve the corrosion resistance of stainless steel alloys and cobalt has been used as a binding material for other thermal spray coatings. Three binding agents namely, Mo, CoMoCrSi and CoCrAlY were selected and blended into the pure Cr_3C_2 powder for thermal spraying to form three different chromium carbide coatings that were made of Cr_3C_2-25%Mo, Cr_3C_2-25%CoMoCrSi and Cr_3C_2-25%CoCrAl, respectively.

Figure 4.17a shows that thermal spray coating made of chromium carbide with molybdenum binder (Cr_3C_2-25%Mo) on both aluminum and SS316 substrates yielded the lowest ICR value. This was due to less oxide formation on the Cr_3C_2-25%Mo coating and the coating with a SS316 substrate also had the similar corrosion current to the Cr_3C_2-25%NiCr coating with a SS316 substrate examined in previous sections. Chromium carbide with cobalt based binders, on the other hand, did not show any promising results on both SS316 and aluminum substrates. Figure 4.17b also shows that the corrosion

current on these coatings with aluminum substrates were very high due to non-uniform blended feedstock powder and high coating porosity. Therefore, these materials were not investigated further in this study.

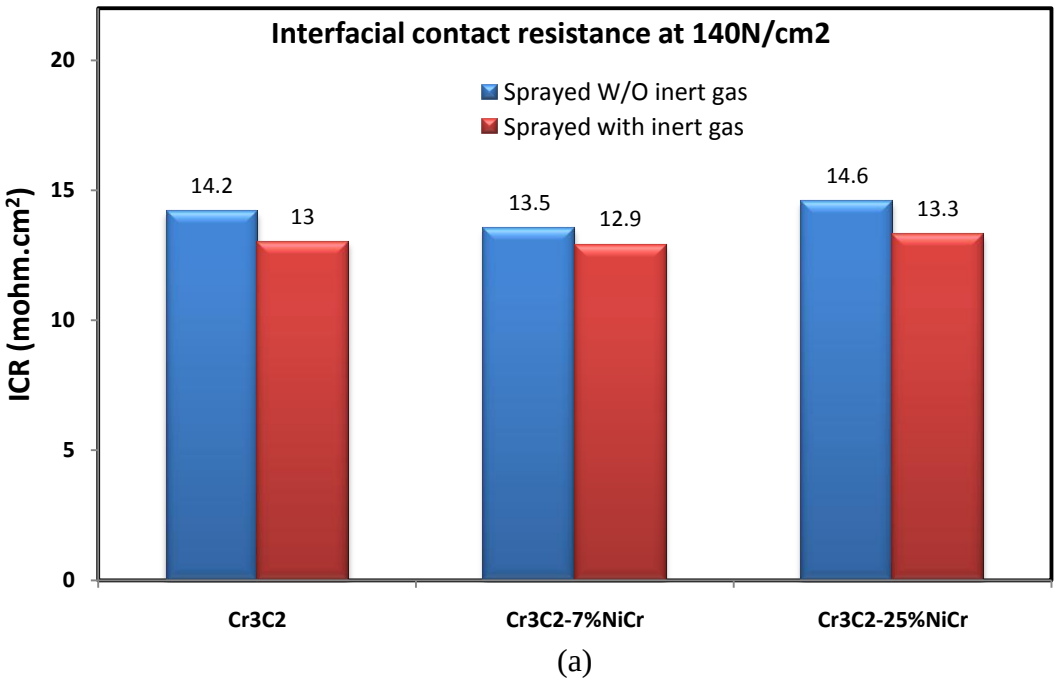

(a)

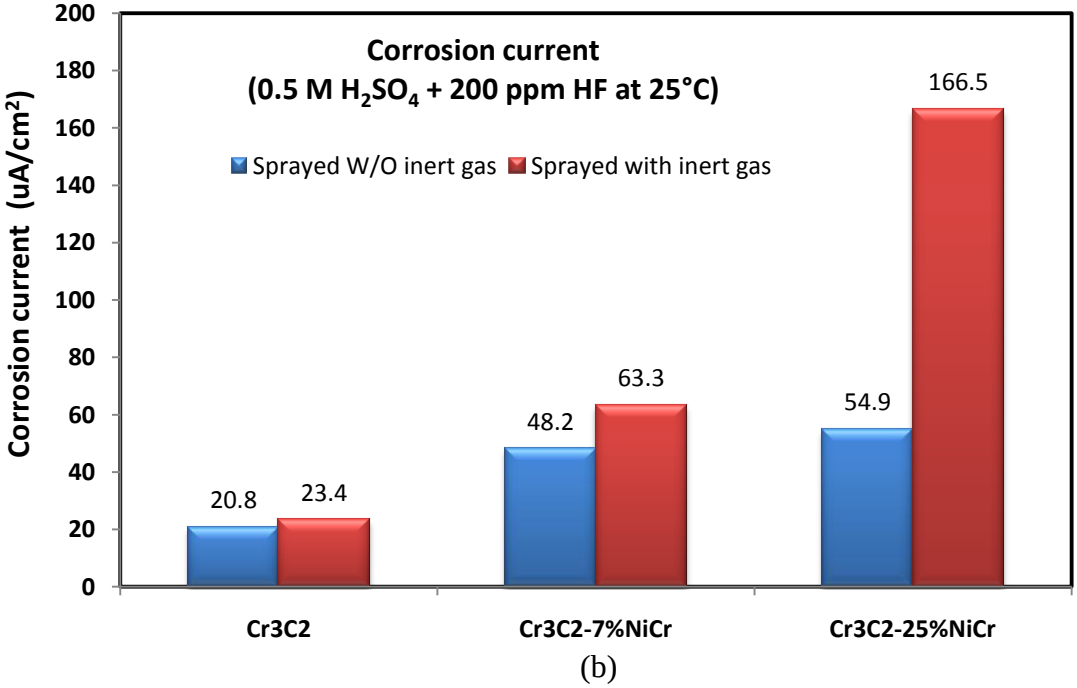

(b)

Figure 4.16: (a) Interfacial contact resistance at 140 N/cm^2 and (b) Corrosion current (potentiodynamic) of chromium carbide coating with different NiCr content on SS316 substrate

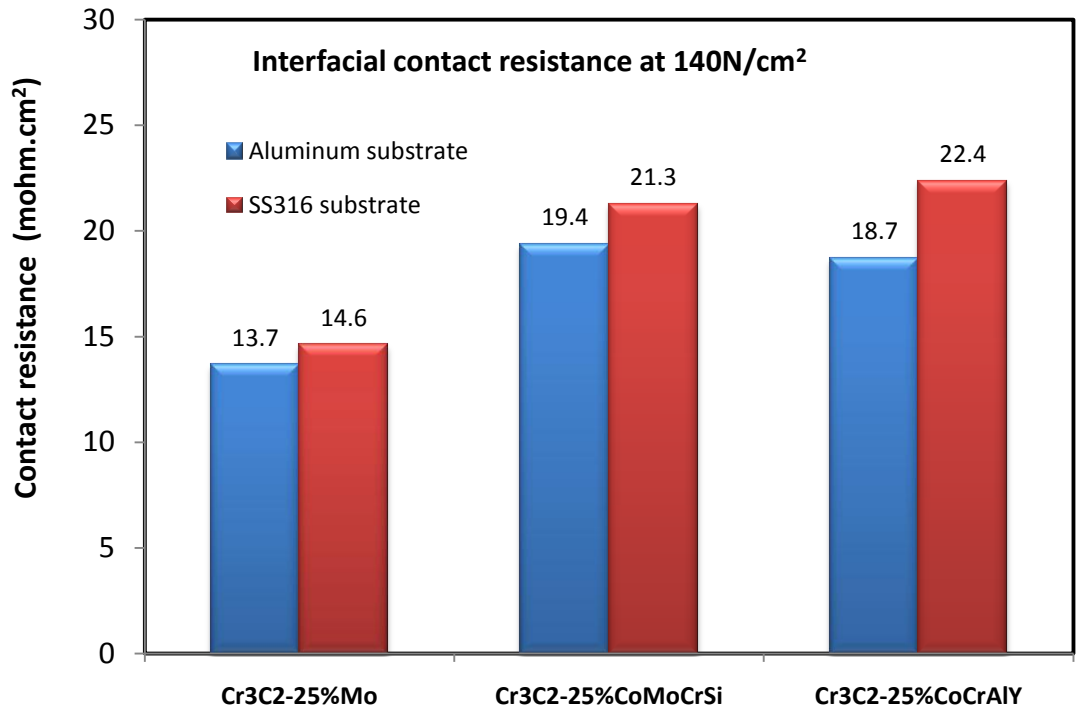

(a)

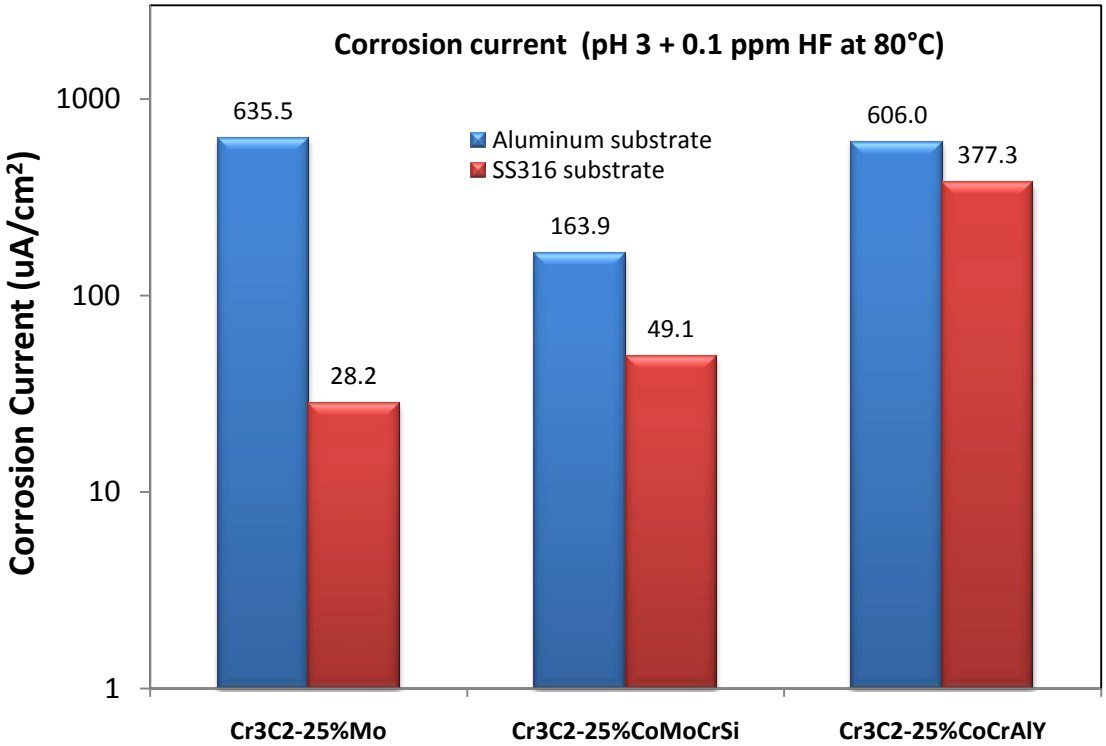

(b)

Figure 4.17: (a) Interfacial contact resistance at 140 N/cm^2 and (b) Corrosion current (potentiodynamic) of chromium carbide coating with different binding materials on aluminum and SS316 substrate

4.1.6 Effect of surface roughness

The effect of surface roughness on corrosion and interfacial contact resistance (ICR) was also examined. Due to relatively thin coating thickness of 200 µm combined with distortion of the samples caused by local thermal expansion during the spray process, it was not possible to highly polish this coating and achieve low roughness levels. Accordingly, the coating roughness was limited to 3 to 4 µm. In such small range, the effect of roughness against interfacial contact resistance and corrosion current did not show clear correlations (Figures 4.18 and 4.19).

In order to demonstrate the effect of roughness on corrosion resistance and ICR, commercially available SS316 flat sheet of thickness 0.79mm (0.031") was utilized as a test sample. The SS316 sheet was cut into 1" x 1" samples and they were polished with 1000 grit sand paper and sand blasted with 80 mesh size aluminum oxide to obtain two different surface roughness. The polishing and sand blasting of the samples removed the oxide layer on the sample surfaces that could negatively affect the ICR measurement. The roughness measurements (Ra) were about 0.2µm for the polished samples and 3 µm for the sand blasted samples.

The ICR measurements at different surface roughness were recorded immediately after the surface treatment such that the effect of the oxide layer or the passive film on ICR was minimal. The existence of passive film could complicate the ICR measurement on a smooth and a rough surface because passive films acted as electrical insulators and considerably affect the ICR measurements. Without the passive film on the sample surfaces, Figure 4.20 shows that the rougher surface (Ra~3µm) had slightly less ICR value when compared to the smoother surface (Ra ~0.2µm) on the carbon gas diffusion layer (GDL). This result agrees with the observation by Avasarala et al. and Kraytsberg et al. [89,90]. Figure 4.21 shows the SEM image of GDL carbon fibers used in this experimental work. The width of each carbon fiber was approximately 10µm. Figure 4.22 illustrates the two different scenarios of carbon fibers contacting on smoother and rougher surfaces. The reduction of ICR measurements due to relatively high roughness was explained by the fewer number of contact points and smaller area of contact between the GDL and the sample surface area. This resulted in higher pressure and better

conductivity between the two surfaces at the contact points. On the other hand, smoother surface would generate more contact points and larger surface area between the GDL and the sample surface area. This had lowered the pressure between the contact surfaces and resulted in higher ICR since the compression force remained the same in both cases.

However, corrosion testing in solution pH3+0.1ppm HF at 80°C shows that the rougher surface had higher corrosion current than the smoother surface as shown in the potentiodynamic polarization curves (Figure 4.23). It was attributed to a higher apparent surface area of the rougher surface per unit area exposed to the acidic solution allowing passive film to grow very sporadically and slowly on the rougher surface causing less protection to the surface, higher dissolution rate and material degradation.

In addition, the original ICR value of SS316 sample (Ra = 0.2μm) showed higher ICR value than the rougher SS316 sample (Ra = 3μm) after 2.5 hours of potentiostatic testing at 0.6 V (SCE) in pH3 +0.1ppmHF solution at 80°C (Figure 4.20). This was due to a layer of dense and continuous passive film formed on the smoother surface that protected the stainless steel sample from further corrosion and resulted in relatively low corrosion current (Figure 4.23). However, due to poor conductivity of the passive film, electrical conductivity between the stainless steel and GDL surfaces decreased and the ICR of stainless steel increased (Figure 4.20). Similar result was also observed in the SS316 sample with roughness Ra = 3 μm. Although a passive film formed on the rougher surface after 2.5 hours of potentiostatic testing causing an increase in ICR, the increase in ICR was much less than that with the SS316 sample of roughness Ra = 0.2 μm. This was attributed to slowly grown, discontinuous passive film formed on the rough surface allowing some points of contacts between SS316 and GDL surfaces.

In summary, the ICR and corrosion measurements for pre-selected bipolar plate and coating materials indicated the following:

- The relatively high acidity test solution (0.5M H2SO4 + 200 ppm HF) is not recommended for potentiostatic test and ICR measurement due to dissolution of passive film resulting in impractical ICR value for fuel cell application.
- Cr_3C_2 based coating material has low ICR value, which is desired in PEM fuel cell application, in comparison to other candidate materials.

- Reducing Ni in the coating material can improve both ICR and corrosion resistance of the coating.
- Agglomerated feedstock powder (Cr_3C_2-25%NiCr) and activated feedstock powder (Cr-C-Ni) produced much denser coating, better bonding strength with the substrate and lower porosity in the coating than the blended powder (Cr_3C_2-7%NiCr).
- Pure Cr_3C_2 coating gives the lowest corrosion current among other coating materials when SS316 substrate was used, however Cr_3C_2 coating experienced some acceptable level of porosity.
- When aluminum substrate is used, Cr-C-Ni coating should be utilized as intermediate coating between the Cr_3C_2 coating and the aluminum substrate because Cr-C-Ni alloy produces relatively dense coating which can effectively protect the aluminum substrate from the fuel cell acidic environment.
- Inert gas blanket during thermo spraying process can slightly improved the ICR of the coating but it negatively affected the corrosion resistance of the coating material.
- The relatively high surface roughness of the material can improve the ICR value but it also harms the material corrosion resistance.

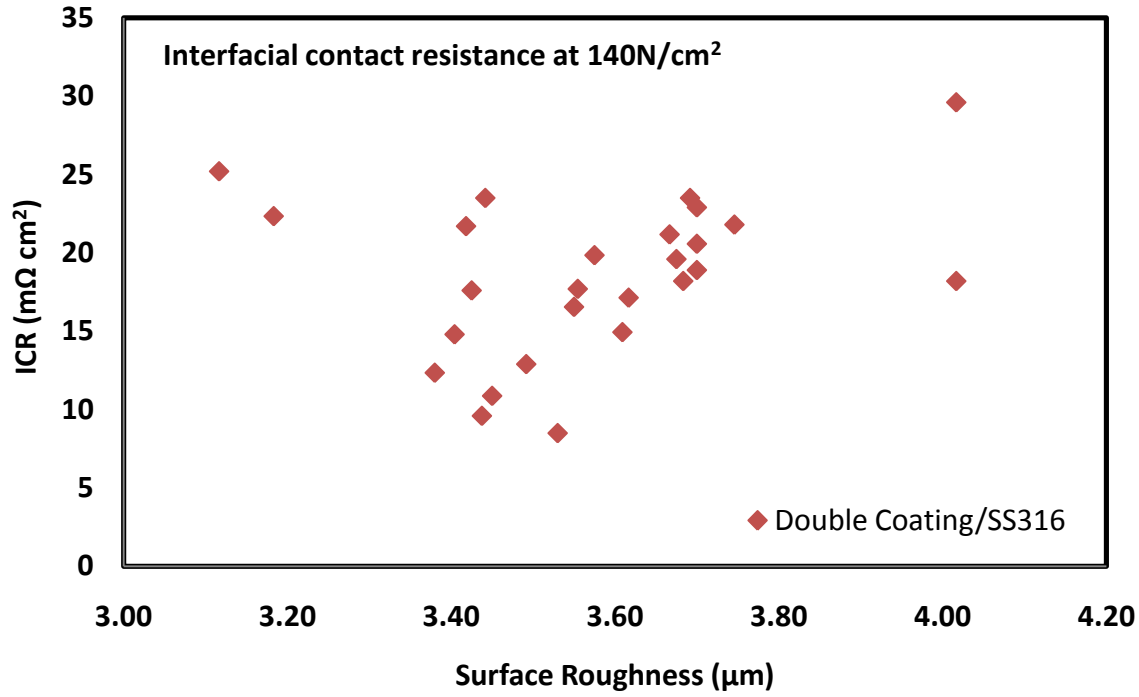

Figure 4.18: Effect of roughness against interfacial contact resistance.

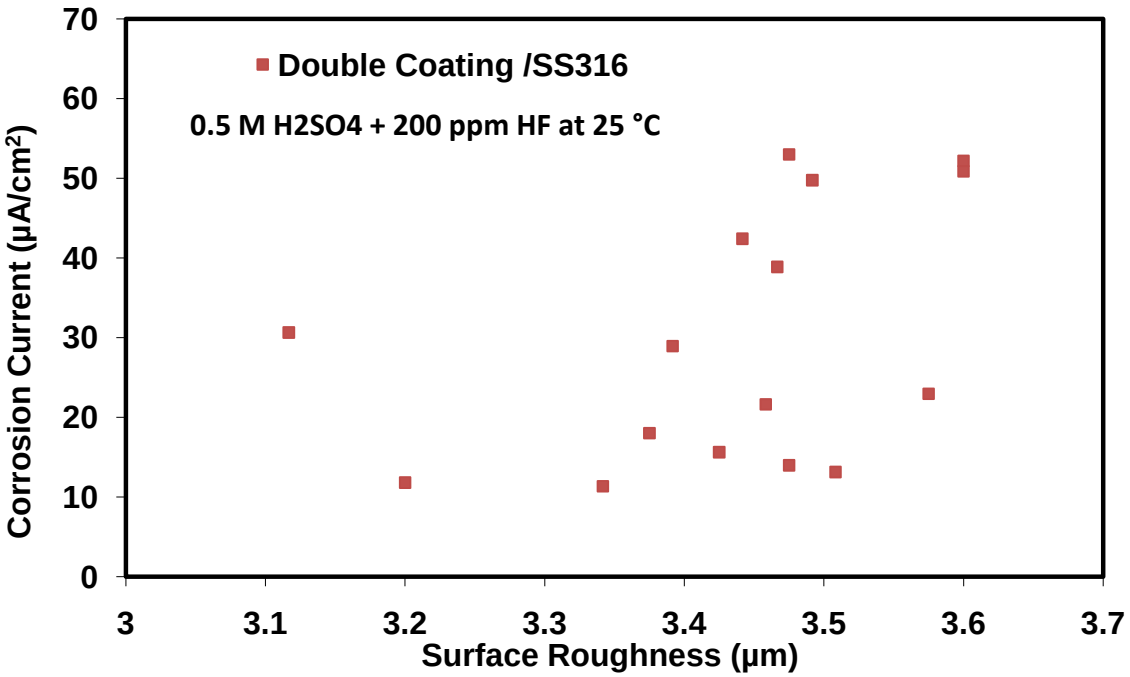

Figure 4.19: Effect of roughness against corrosion current

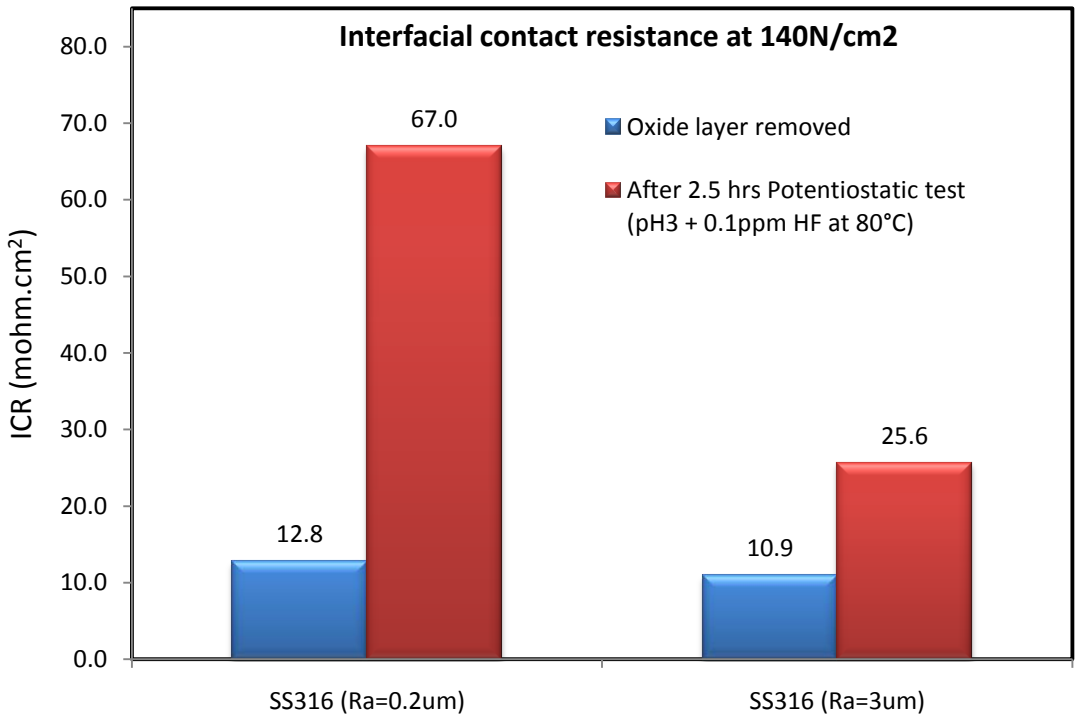

Figure 4.20: Interfacial contact resistance at 140 N/cm^2 on SS316 with roughness Ra = 0.2µm and 3µm

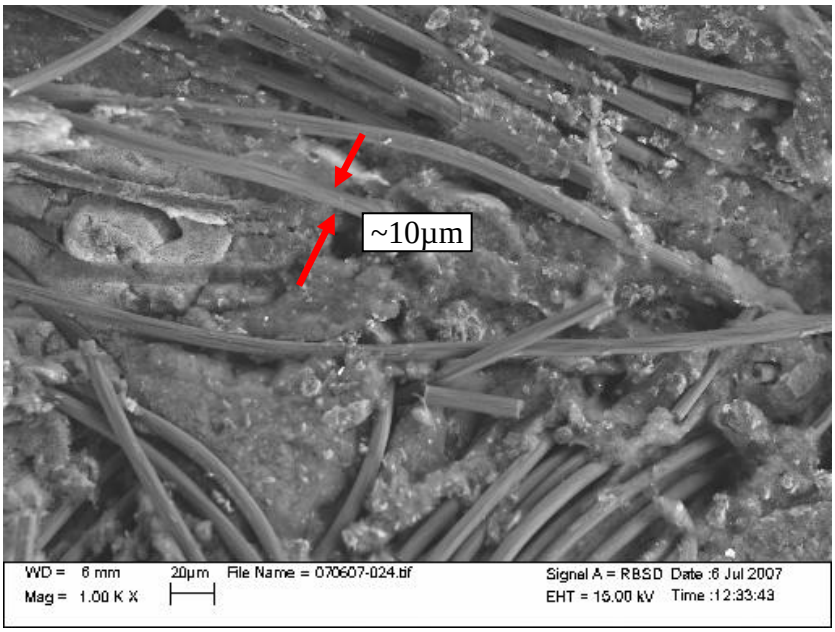

Figure 4.21: SEM image of gas diffusion layer (GDL) at 1 kx magnification

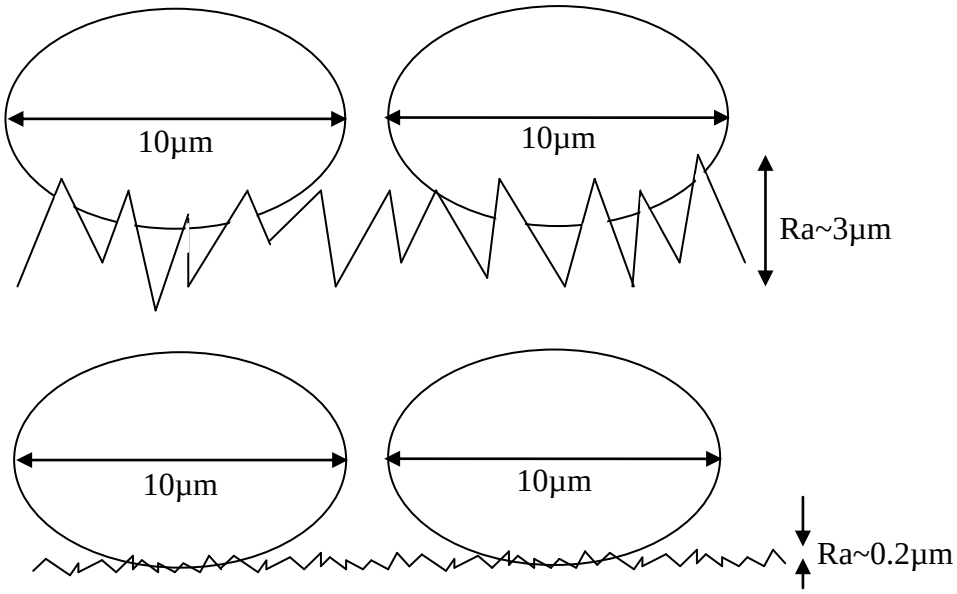

Figure 4.22: Illustration of carbon fibers in contact with rough (Ra~3µm) and smooth (Ra~0.2µm) surfaces

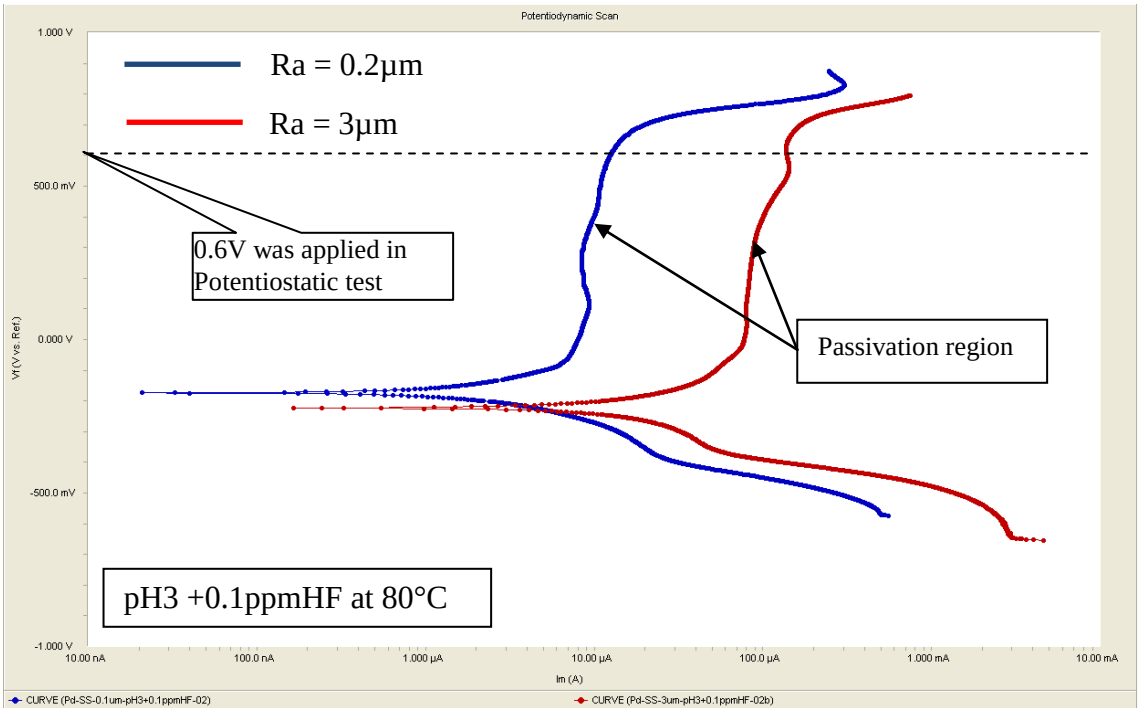

Figure 4.23: Potentiodynamic polarization curve of SS316 samples with roughness Ra = 0.2µm and 3µm

4.2 Performance comparison of graphite vs metallic bipolar plate materials in single cell operation and surface characterization of the bipolar plates and MEAs

4.2.1 Polarization curves, power density and hydrogen consumption measurements

Fuel cell performance can be greatly affected by their cell internal resistance. Different variation of bipolar plate materials and fuel cell structures can affect the cell internal resistance. Figure 4.24 shows the cell internal resistance measurement of 50 cm^2 active area single cells with different bipolar plate materials namely coated aluminum and graphite composite. In addition, different terminal designs as shown in Figures 3.12a and 3.12b were tested in the current research work. For quantitative investigation of the cell internal resistance, excluding the electrical resistance of the Nafion membrane, the MEAs were simply replaced by a layer of GDL in these single cells. Figure 4.24 also shows that the cell internal resistance measurements of coated aluminum and graphite composite cells with gold plated terminal plate design were 6.62 mohm and 6.82 mohm respectively. The internal resistances of both fuel cells with such terminal design were almost identical. However, the resistance measurement of direct threaded terminal design for coated aluminum bipolar plate was 3.56 mohm and for graphite composite bipolar plate was 18.52 mohm. This was attributed to the brittleness of graphite plates that had resulted in a lack of tight contact between the plate and the metal screw terminal.

The advantage of using the bipolar plate as a terminal was to eliminate the existence of additional internal electrical resistance in the cell due to the extra terminal plates. In addition, direct threaded terminal design in coated aluminum single cell showed a 46% reduction of cell internal resistance in comparison the gold plated terminal plate design (Figure 4.24). This was due to low ICR between the metal screw terminal and the aluminum plate as the screw was tightly screwed into the coated aluminum plate. However, the relatively loosely threaded terminal design in the graphite composite single cell showed an increase of 172% in cell internal resistance in comparison to the gold plated terminal plate design. This increase was due to the poor ICR between the metal screw terminal and the graphite composite bipolar plate. In addition, one of the most considerable disadvantages of graphite or graphite composite compared to metal is their

high brittleness. Therefore, it is not recommended to have terminals directly mounted on the graphite composite plates due to their weak mechanical strength and higher clamping force could damage the graphite bipolar plates.

To further investigate the cell performance in different bipolar plate materials, two sets of single cells with active areas 6.45 cm^2 and 50 cm^2 were examined using metallic and graphite composite plates. Figure 4.25 shows the polarization curves and power curves of both 50 cm^2 active area coated aluminum and graphite composite single cells with the gold plated terminal plate design and BASF's MEA at operating temperature of 20°C. As expected, since the cell internal resistance of these two cells was similar, their performance and peak power densities were almost the same at approximately 0.11W/cm^2. However, coated aluminum bipolar plate combined with the directly threaded terminal design had enhanced the maximum power density to 0.135 W/cm^2 as shown in Figure 4.26. This was due to the lower cell internal resistance between the two metal components as demonstrated in Figure 4.24. The results obtained from both aluminum and graphite plates have also exhibited that at the same operating current density, higher voltage and power output can be achieved by using the directly threaded terminal design on coated aluminum single cell. For example, when both single fuel cells operated at the current density of 0.30 A/cm^2, the graphite composite and aluminum coated cells produced the power density of 0.110 W/cm^2 and 0.130 W/cm2, respectively as shown in Figure 4.26. Moreover, these two respective cells had also produced voltage at the level of 0.367V and 0.45V at the current density of 0.30 A/cm^2. The advantage of producing higher voltage or power output from each cell at the same current density was that the coated aluminum cell with a higher power output had proven to be more efficient than the graphite composite cell because hydrogen consumption was the same for both cells and was almost linearly proportional to current density.

Figure 4.27 shows that hydrogen consumption per watt for coated aluminum single cell using a threaded terminal design was less than that for the graphite composite single cell using a gold plated end plate design. For example, at the current density of 0.30 A/cm^2, the hydrogen consumption per watt was 16.2 SCCM/W and 19.1 SCCM/W for coated aluminum and composite graphite single cells, respectively. This represents 15% savings in hydrogen consumption at 0.30 A/cm^2 when coated aluminum bipolar plates

with directly threaded terminals were used. It also shows an average of 18% savings in the overall hydrogen consumption (Figure 4.28). Repeatable results for energy and hydrogen savings were obtained when using MEAs acquired BCS Fuel Cell Inc. (Figure 4.29).

Figure 4.30 shows similar results for the 6.45 cm^2 active area single cells. The maximum output power density was 0.14 W/cm^2 and 0.12 W/cm^2 for coated aluminum and composite graphite single cells, respectively. This was also attributed to the lower interfacial contact resistance at the interface between the metal pin (terminal) and the coated aluminum bipolar plate compared to graphite composite plate. The results from both 6.45 cm^2 and 50 cm^2 active area single cells has proven that the use of coated aluminum bipolar plate with threaded terminal design can enhance the power density of a fuel cell in relation to the gold plated end plate terminal design. In addition, due to excellent mechanical strength of the metallic bipolar plate and lack of brittleness, terminal can be mounted directly into the bipolar plate to reduce the need for extra terminal plates. However, due to the brittleness of the graphite composite plates, directly mounted terminals were unfeasible.

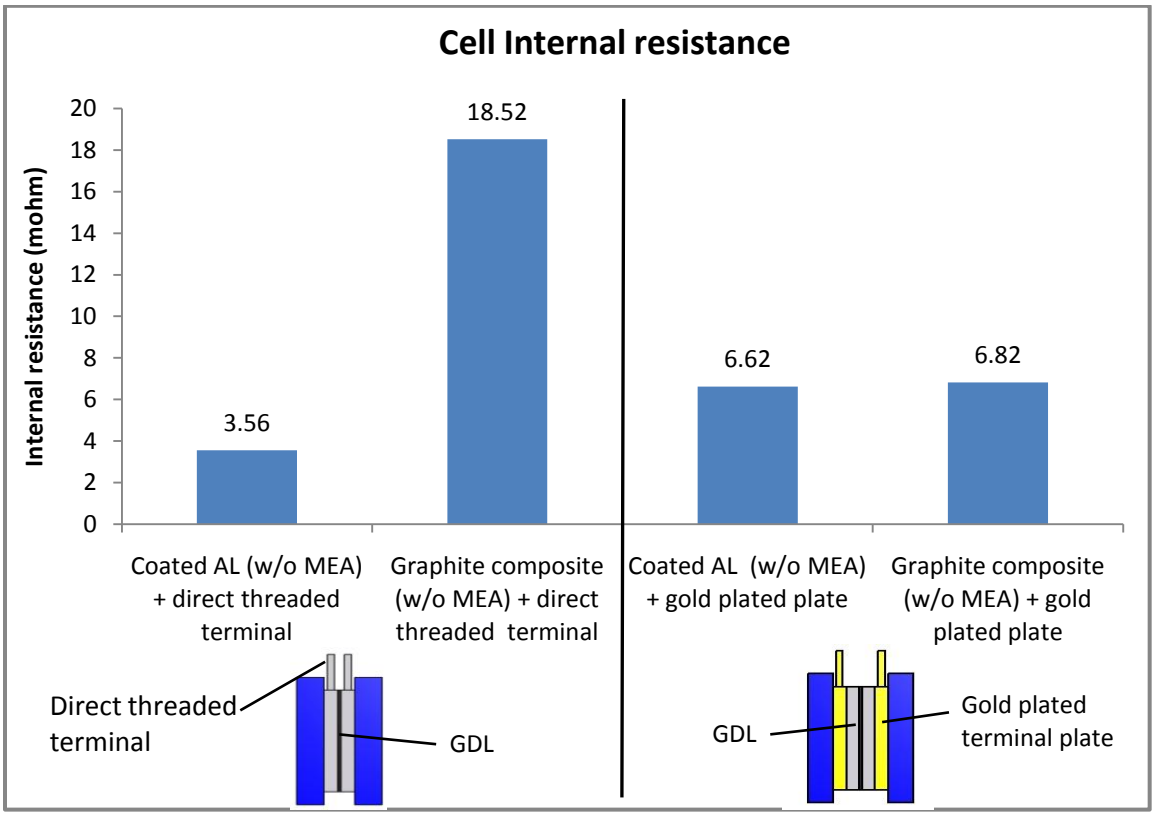

Figure 4.24: Internal resistance of 50 cm^2 single cells at clamping pressure (200 N/cm^2) (MEA replaced by GDL)

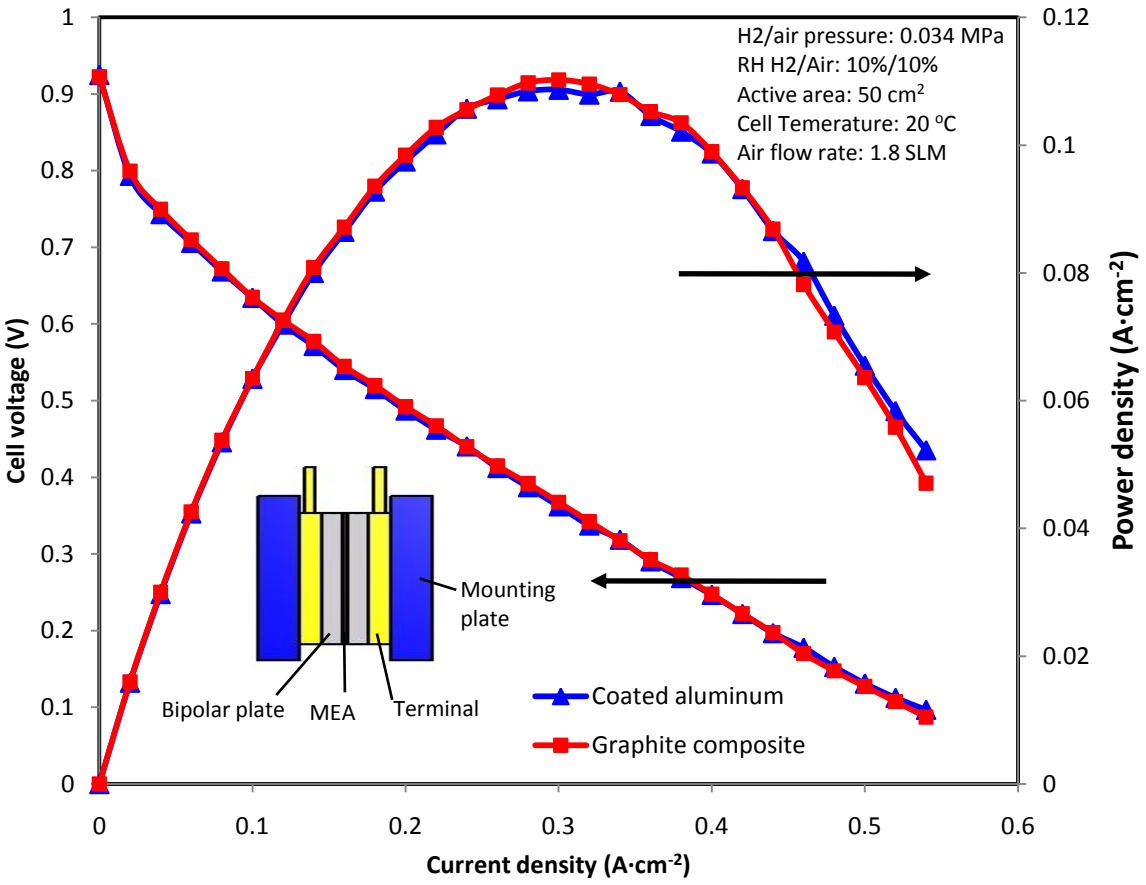

Figure 4.25: Polarization curve and power density curve comparison of 50 cm^2 active area single cells with end plate terminal design and BASF's MEA at clamping pressure (200 N/cm^2)

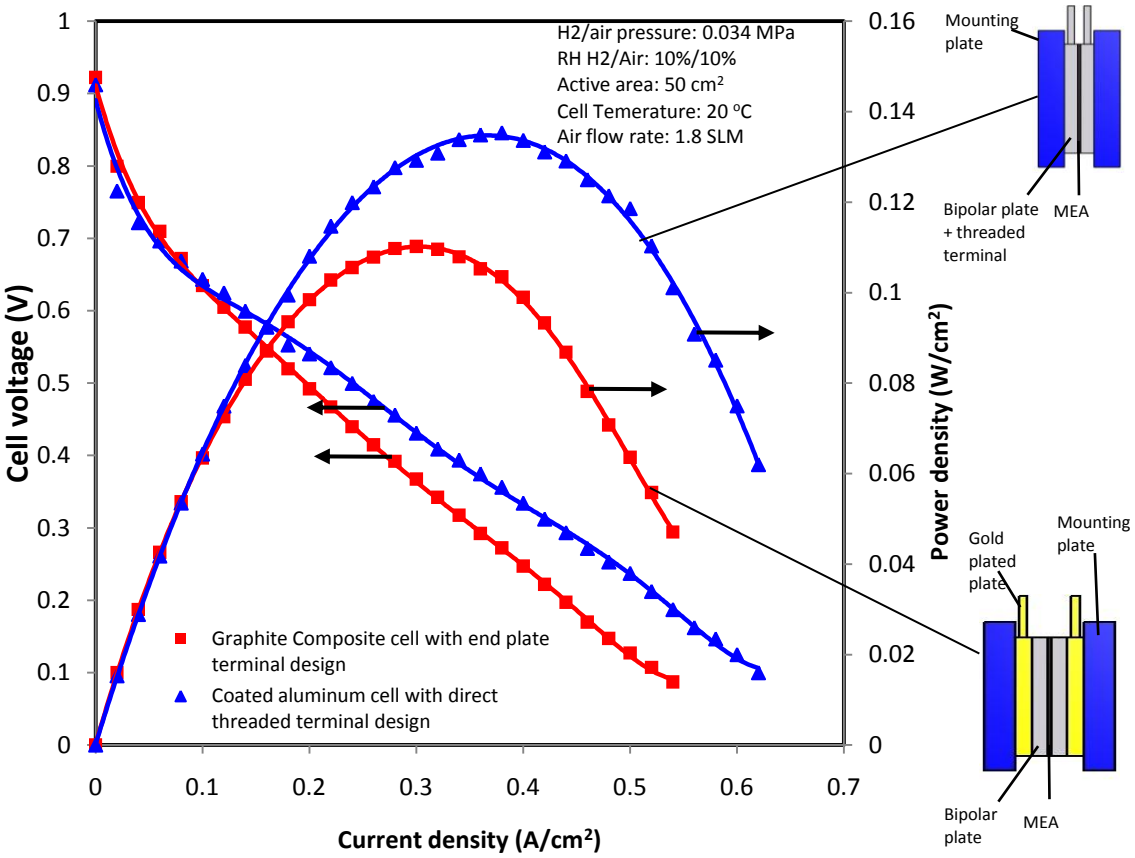

Figure 4.26: Polarization curve and power density curve comparison between graphite composite single cell with end plate terminal design and coated aluminum single cell with directly threaded terminal design at clamping pressure (200 N/cm^2) (BASF's MEAs)

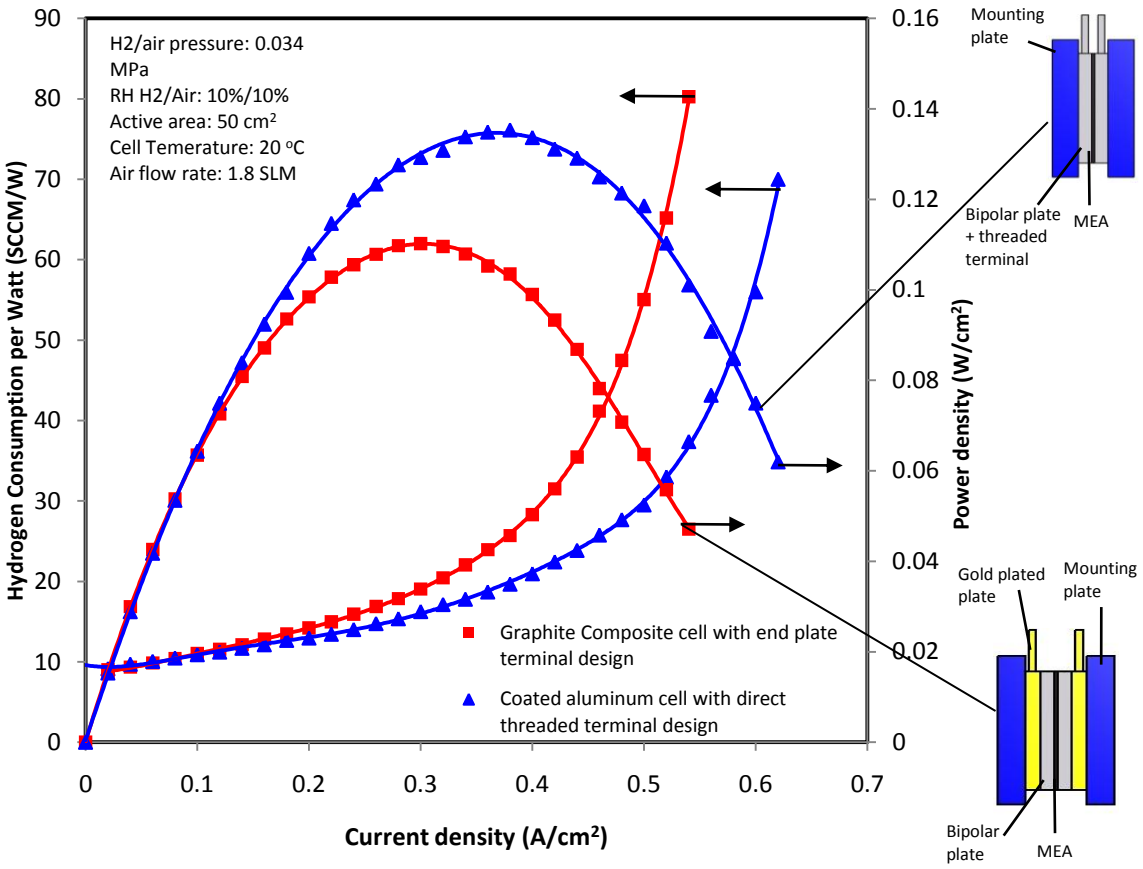

Figure 4.27: Power density curve and hydrogen consumption per watt comparison between graphite composite single cell with end plate terminal design and coated aluminum single cell with directly threaded terminal design at clamping pressure (200 N/cm^2) (BASF's MEAs)

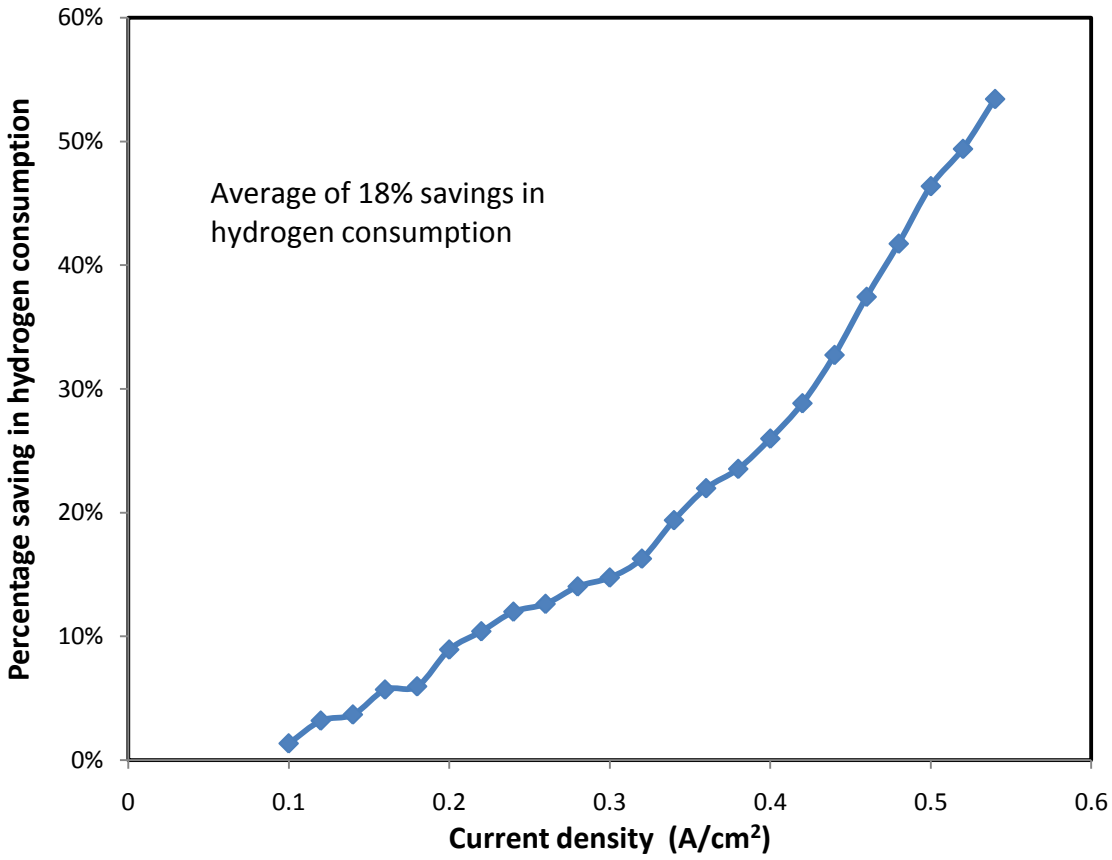

Figure 4.28: Percentage savings in hydrogen consumption using coated aluminum single cell with directly threaded terminal design in comparison to graphite composite single cell with end plate terminal design

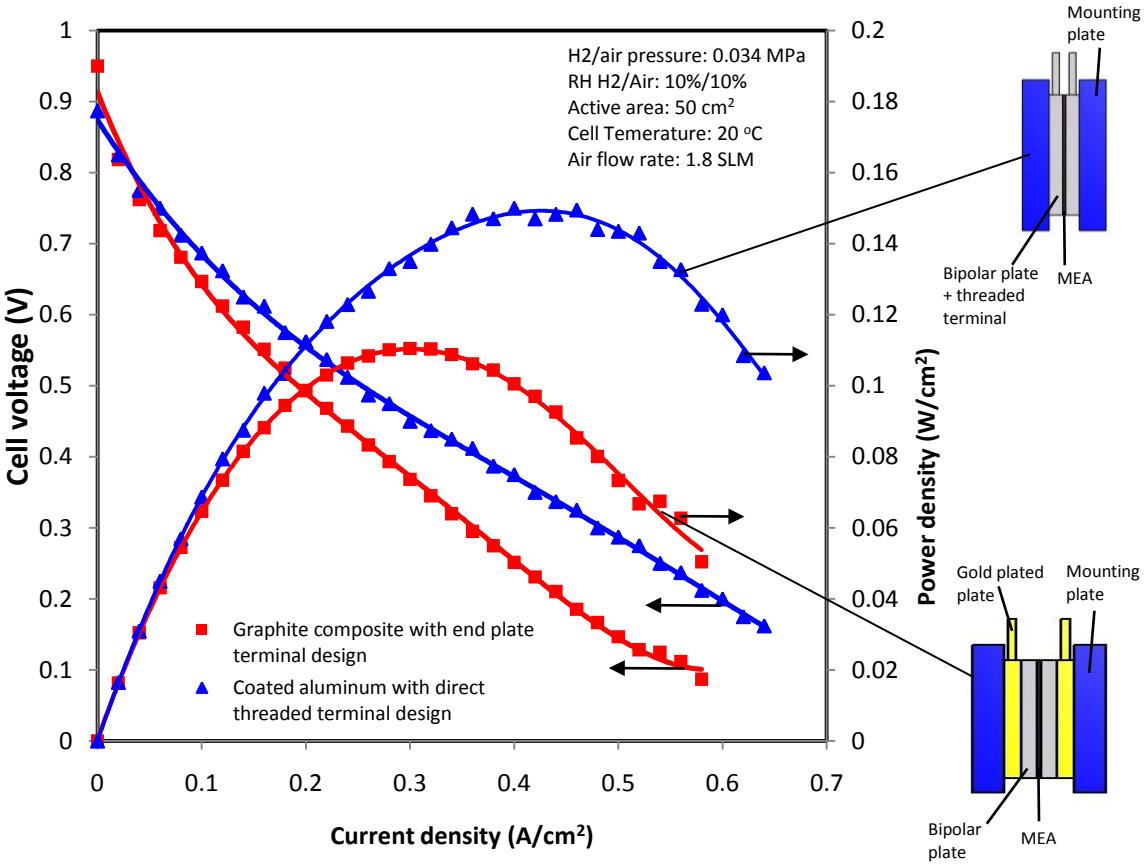

Figure 4.29: Polarization curve and power density curve comparison between graphite composite single cell with end plate terminal design and coated aluminum single cell with directly threaded terminal design at clamping pressure (200 N/cm^2) (BCS's MEAs)

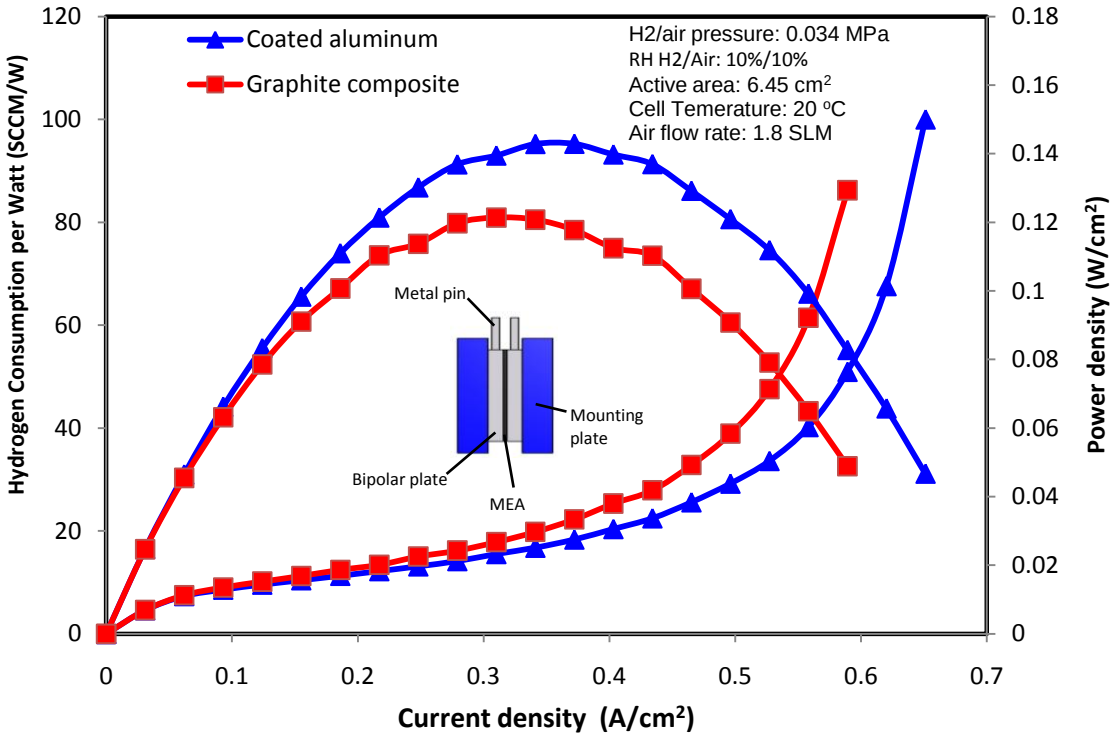

Figure 4.30: Power density curve and hydrogen consumption per watt comparison of 6.45 cm^2 active area single cells

4.2.2 Effect of clamping pressure

The effect of clamping pressure on the electrochemical performance of single fuel cells was examined. The 50 cm^2 active area graphite composite single cell with BCS Fuel Cell Inc. MEA that was used in the previous analysis was employed. The electrochemical performance of single fuel cells was conducted at clamping pressure of 140, 200 and 250N/cm^2 respectively.

Figure 4.31 shows that higher power output and better performance of the single fuel cell was achieved by applying higher clamping pressure to the cell. An average savings of 11.6% and 7.8% in hydrogen consumption was obtained by applying 250N/cm^2 and 200N/cm^2 clamping pressure, respectively, in relation to the recommended 140N/cm^2 clamping pressure for graphite composite plate (Figure 4.32). This was due to the lower ICR between bipolar plate and GDL. As it was mentioned earlier, higher ICR can result in electrical loss of fuel cells. Figure 4.1 demonstrated that as pressure increased, lower ICR between GDL and material was achieved. The result agrees with the trend observed

by Chang et al. [91]. Therefore, it is recommended to apply proper clamping pressure to the fuel cell to minimize electrical loss. However, due to weakness and poor shear strength of graphite composite material, higher clamping pressure combined with vibration and impact force can result in fracture of bipolar plate particularly when it is used in automobile application.

It should be noted that clamping pressure of the cell combined with porosity and hydrophobicity of GDL, plate material and flow field design will have direct contribution to the maximum power output and limiting current. Further study of this aspect and cell durability is recommended as part of the future work.

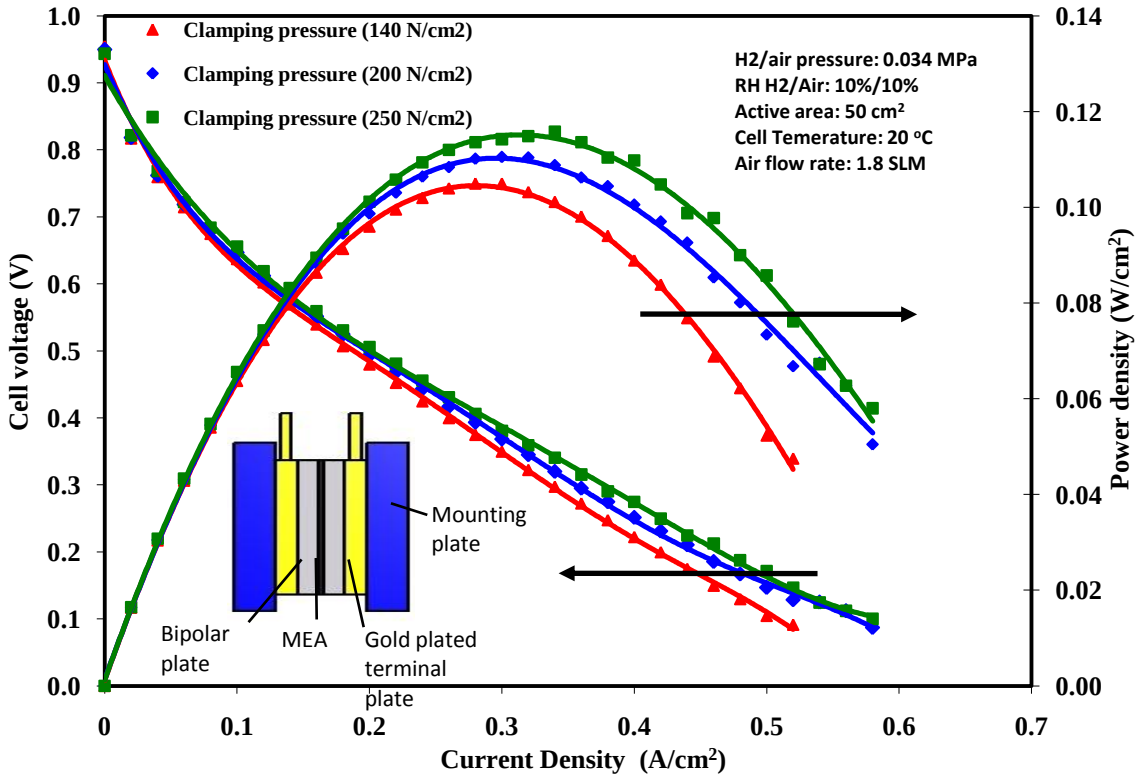

Figure 4.31: Polarization curve and power density curve comparison of 50 cm^2 graphite composite single cells with end plate terminal design and BCS's MEA at different clamping pressure

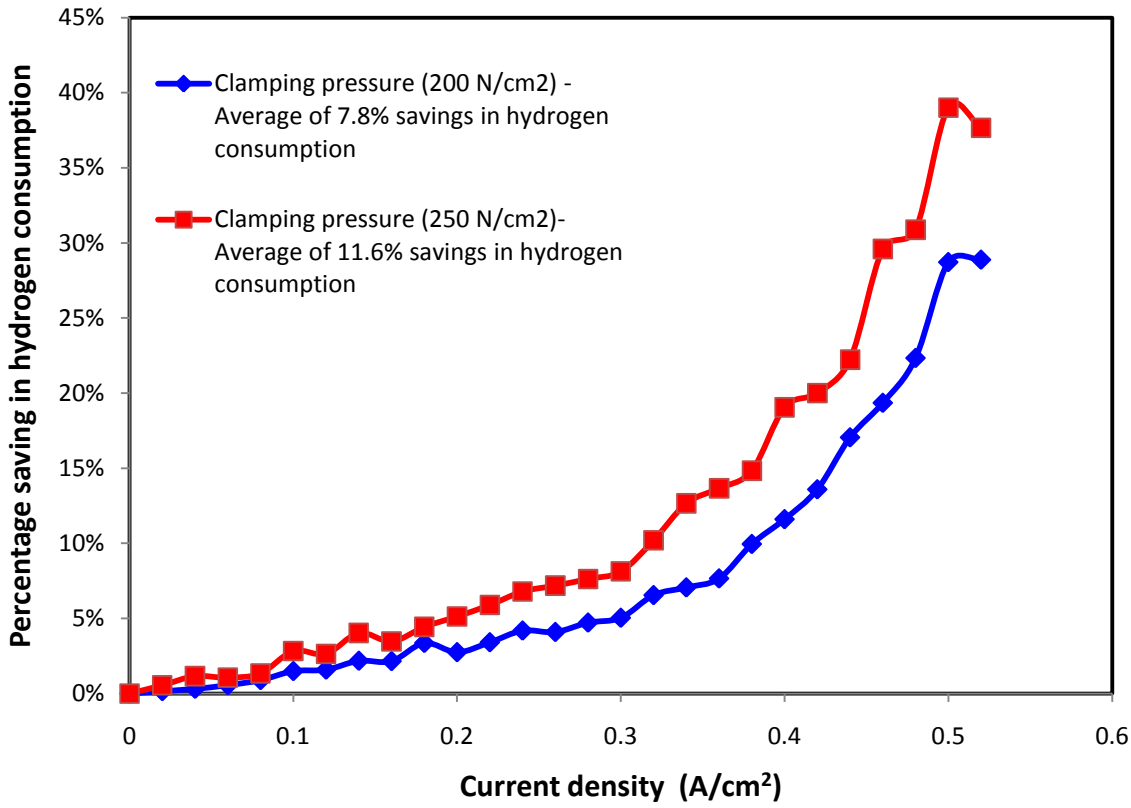

Figure 4.32: Percentage savings in hydrogen consumption using 50 cm^2 graphite composite single cells with end plate terminal design at clamping pressure of 200 and 250N/cm^2 in comparison to clamping pressure of 140N/cm^2

4.2.3 Effect of flow field designs

Figure 4.33 shows the base line performance of two single cells with two different reactant flow-field designs. They are namely triple serpentine flow-field design and humidity conservative flow field design. These flow-field designs were described earlier in section 3.4 and were shown in Figures 3.7a and 3.7b. Figure 4.33 also shows that the performance of two different designs was almost identical from open circuit voltage until about 0.5V. However, as the current density increased, the single cell with humidity conservative flow field design produced higher power density than the triple serpentine flow field design. Figure 4.34 exhibits that an average of 8% savings in hydrogen consumption was obtained by using the humidity conservative flow-field design in comparison to the standard triple serpentine design.

The reason for improvement of the power output in the humidity conservative flow field in relation to the standard flow-field design can be explained by the combined effect of the following two aspects. 1) the flow-field design provides relatively uniform reactant gas pressure distribution over the MEA by using short individual zigzag channels which reduces pressure drop and 2) better humidification of Nafion membrane when gases travel and exchange humidity between the inlet and outlet sections. Figure 4.35 illustrates that the reactant gases enter the serpentine with relatively dry condition. As the air flows in the conduit on the cathode side and approaches the outlet, it gains humidity because water is produced as by-product during the power generation operation. When the dry and wet gas channels are placed in the vicinity of each other by design, water can be diffused from wet to dry areas through the Nafion membrane. This water diffusion mechanism is also demonstrated in Figure 4.35.

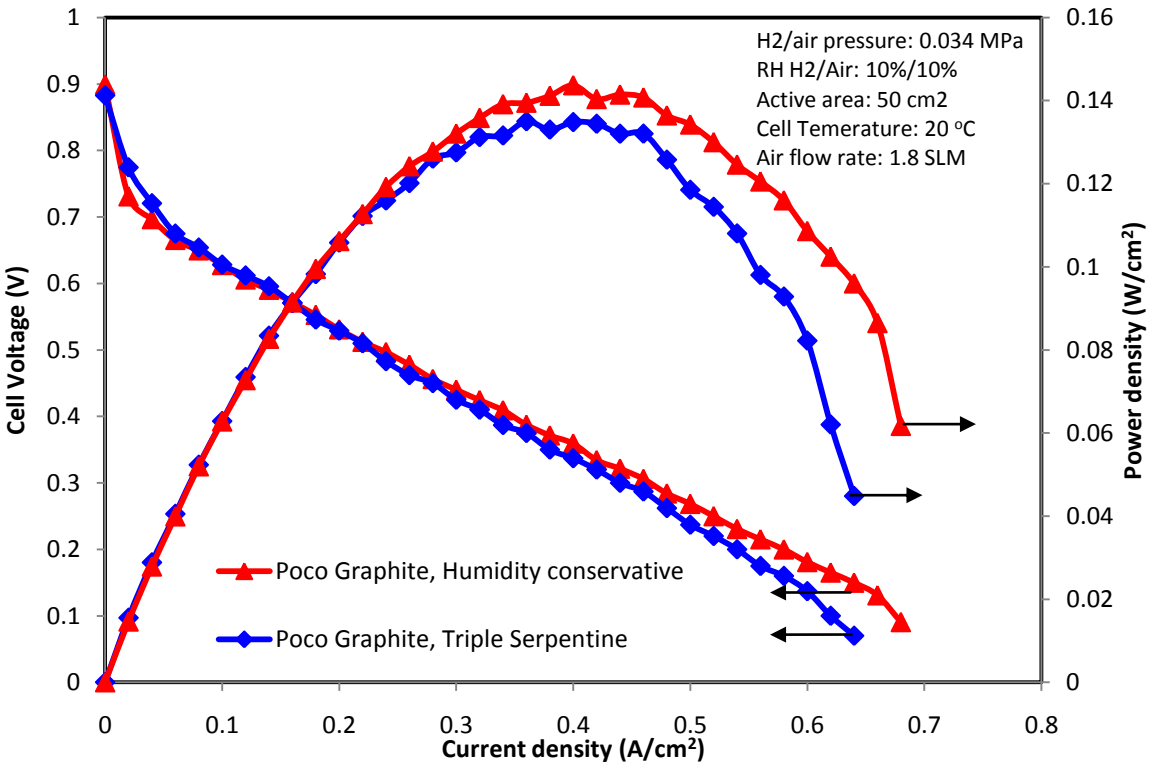

Figure 4.33: Power output curves for triple serpentine and humidity conservative flow field design

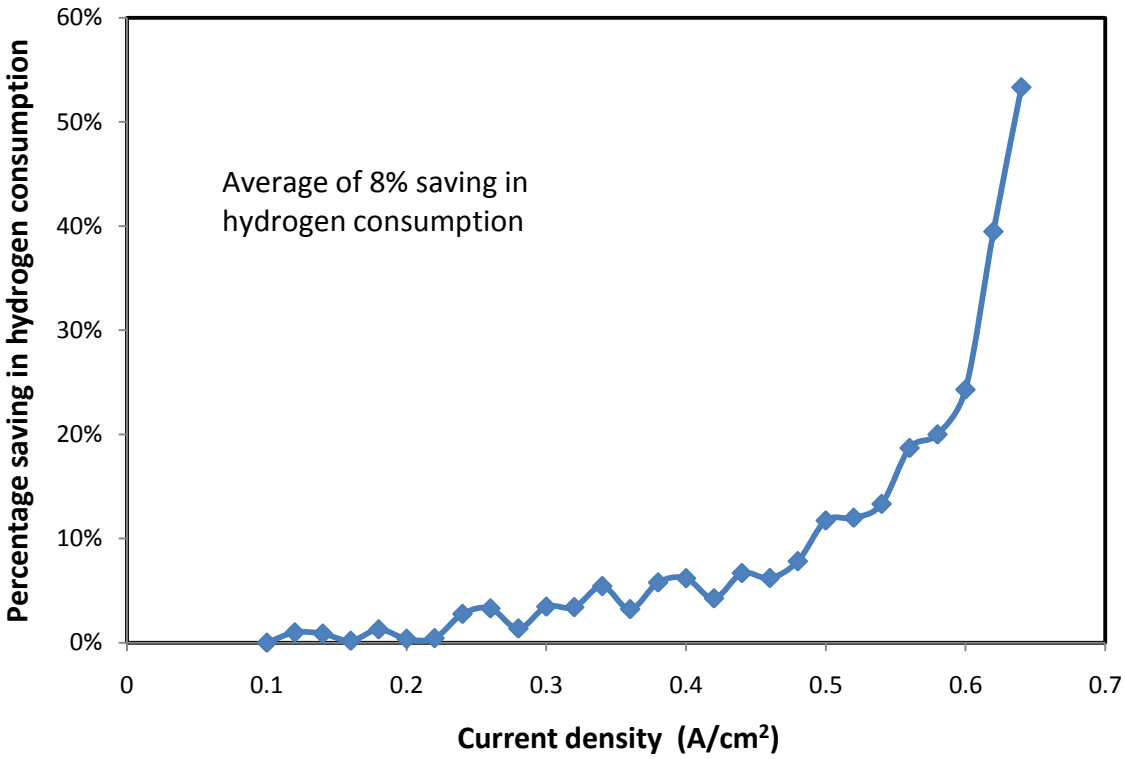

Figure 4.34: Percentage savings in hydrogen consumption using humidity conservative flow field design in comparison to the triple serpentine flow field design

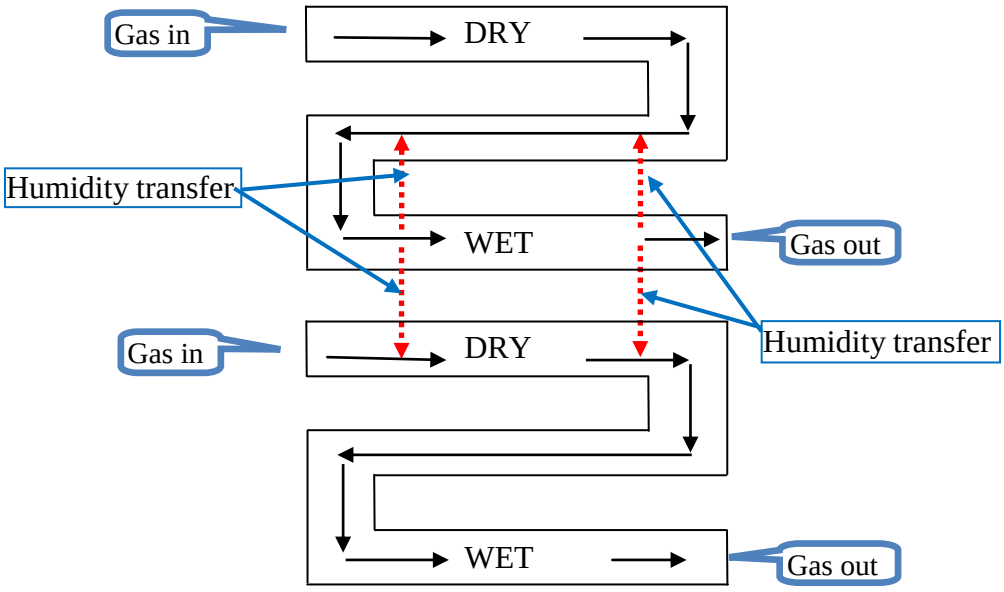

Figure 4.35: Water paths in humidity conservative flow field design

4.2.4 Durability test

Besides the short term tests mentioned above, the fuel cell durability is also one of the important tests in the fuel cell industry. Figure 4.36 shows the power output results of four 6.45cm^2 active area single cells tested under similar operating conditions when subjected to same electric resistance. These single cells performed under cyclic loading at 70^{o}C for approximately 1000 hours. The output power of the pair of Cr_3C_2-25%NiCr coated aluminum and graphite composite single cells were averaged and plotted on the same graph for comparison. The parallel and very similar performance trends of graphite composite and coated aluminum plates suggest that minimal power degradation (<5%) was possibly caused by impurities leaching to the reactants and metal corrosion of uncoated components such as fittings, back plates, and manifolds. As demonstrated earlier in Figure 4.24, the lower performance of the graphite composite single cells was due to the higher ICR between the graphite composite plate and the metal pins (terminals). Graphite composite is considered the industry standard because it is known to be electrochemically stable within the potential domain of the PEM fuel cell environment (≤1 volt) and therefore it was used as a control reference in this study.

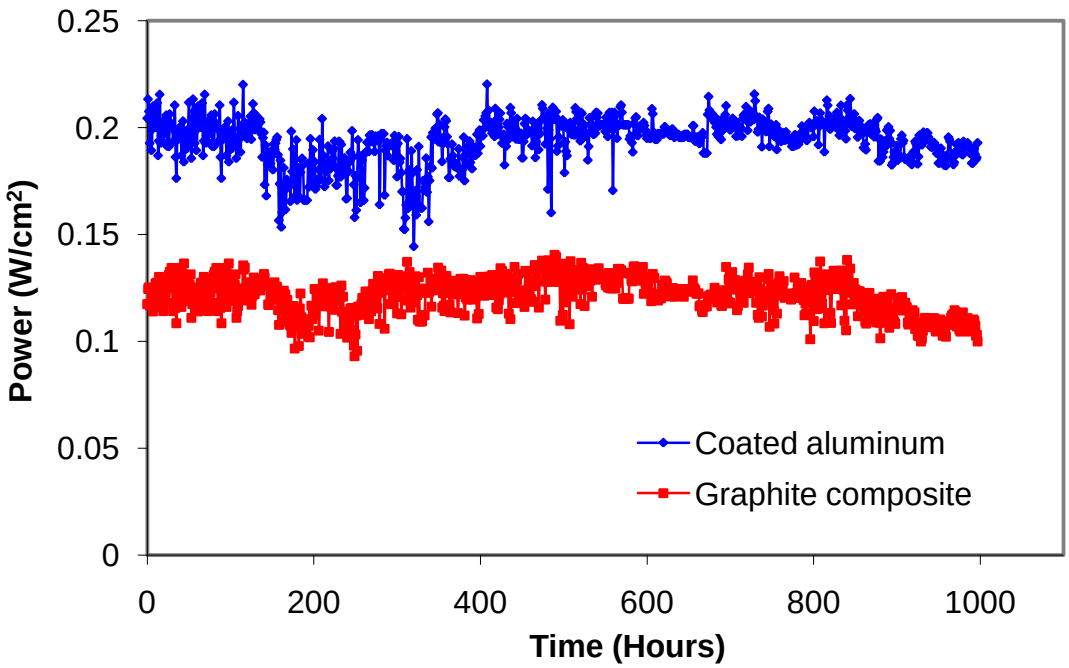

Figure 4.36: Durability test of coated aluminum and graphite composite single cells operated under cyclic loading at 70^{o}C.

4.2.5 Cost comparison between coated aluminum and graphite composite bipolar plate

Preliminary experimental results showed an average of 18% savings in hydrogen consumption when running a coated aluminum single fuel cell against a graphite composite single cell. This was because combining terminals into metallic bipolar plate can reduce the total electrical resistance of the cell. Hypothetically, at hydrogen price of $4.3/kg, the running cost of graphite composite and metallic single fuel cells are $0.26/kW hr and $0.216/kW hr, respectively. In the long term running (hydrogen) cost, approximately $2000 savings in 5 year period can be obtained by operating a one kilowatt metallic bipolar plate single fuel cell rather than a graphite composite single cell.

In terms of the manufacturing cost of bipolar plates, since flow field pattern can be stamped on the relatively thin metal plate utilizing the relatively inexpensive stamping process, the processing cost of metallic plate can be very low. On the other hand, flow field pattern must be CNC machined onto graphite composite plate rather than injection molded or stamped due to its brittleness. The machining operation is very time consuming and therefore, it is a costly process. Injection molding is a manufacturing operation that could also be used to mass produce graphite composite bipolar plates but it will require relatively higher polymer content to facilitate the molding operation. However, high polymer content in the graphite composite would result in high bulk and interfacial contact resistances. Table 4.1 shows the cost comparison of metallic and molded graphite bipolar plates based on 250cm^2 active area and power density at 0.65W/cm^2 [14-16,36]. The Poco graphite bipolar plate was not included in the comparison due to their high cost and other disadvantages such as porosity and brittleness.

Under the same plate thickness, the average cost of stamped and coated aluminum bipolar plate ($50.28/kW) is less than that of machined graphite composite bipolar plate ($121.2/kW). The CNC machining cost is based on a commercial rate at $55/hour. Moreover, extra capital cost for two additional gold plated terminal plates is required in the case of graphite composite fuel cell, which is not considered in the above calculation.

Table 4.1: Cost comparison based on 250cm^2 active area bipolar plates

Cost type	Metallic – coated aluminum	Graphite composite
Substrate material cost [$/plate]	$1.13	$1.90
Processing cost (stamping vs CNC machining) [$/plate]	$1.07	$18.30
Coating cost [$/plate]	$6.18	none
Total cost [$/plate]	$8.38	$20.20
Total stack cost of bipolar plates [$/kW]	$50.28	$121.2

4.2.6 Surface characterization of coated aluminum bipolar plates and GDLs after 1000 hours of operation

A visual inspection of the Cr_3C_2-25%NiCr coated bipolar plates showed that the carbon fibers from the gas diffusion layer (GDL) were found to be strongly adhered to the coating of both the cathode and the anode plates even after performing some sample cleaning. Small white particles were also observed in the active area of both plates. The characterization study showed that these white particles were aluminum oxide as confirmed by the EDX spectrum (Figures 4.37).

The coating on the land, valley and reference areas of both cathode and anode plates after 1000 hours of operation that was described in section 3.8 (Figure 3.25) was characterized and the EDX spectra of these areas are shown in Figures 4.38 and 4.39. Chromium had the highest ratio in the coating as demonstrated by its peaks in each spectrum. These chromium peaks were scaled to the same level in the EDX spectrum of the land, valley and reference areas for meaningful comparison between the conditions of before and after one thousands hours of operation as they were superimposed in Figures 4.38 and 4.39. Oxygen was detected on both anode and cathode sides and was most likely linked to the aluminum oxide observed on the coating. Small amount of silicon was detected and assumed to originate from the silicon gaskets. Similarly, very small amount of potassium, sodium and phosphorus were also found on the coating which could be

deposited to the plates due to the existence of impurities in the fuel cell system as well as during sample handling.

The EDX spectra of the cathode plate coating material shown in Figure 4.38 also indicate the possibility of partial dissociation of the NiCr alloy responsible for binding the coating material together and its adherence to the substrate. This was depicted by a change in the Ni peaks of the land and valley areas of the cathode plate in comparison to the reference area (Figure 4.38). Figure 4.39 shows that the change in Ni also occurred at the anode plate; however the change was less than that of the cathode plate. This was attributed to the lower humidity and anodic activity on the anode plate.

In addition to the bipolar plates, the GDL used in the cathode side of the graphite composite cell was also analyzed and the EDX analysis of the GDL showed a very small amount of aluminum trace (Figure 4.40). The results demonstrate that a small amount of aluminum was introduced and carried to the GDL used in the graphite composite cell by the cathodic air/oxygen flowing through the uncoated aluminum parts of the fuel cell such as back plates and manifolds. On the other hand, the EDX spectrum in Figure 4.41 shows that the GDL used in the cathode side of the coated aluminum cell had higher amount of aluminum than the graphite composite cells. This comparison proved that the aluminum found in Figures 4.38 and 4.39 was also from the oxidation of aluminum substrate through the coating. Therefore the detected aluminum on the coating of the metallic cell was believed coming from two different sources: 1). It was brought to the corrosion resistant coating from the aluminum substrate through the possible cracks or porosity. 2). It was carried to the surface of the active flow field area by the reactant gases passing through the back plate and the gas inlets, as they were not covered by sealant or any other type of corrosion resistant coating.

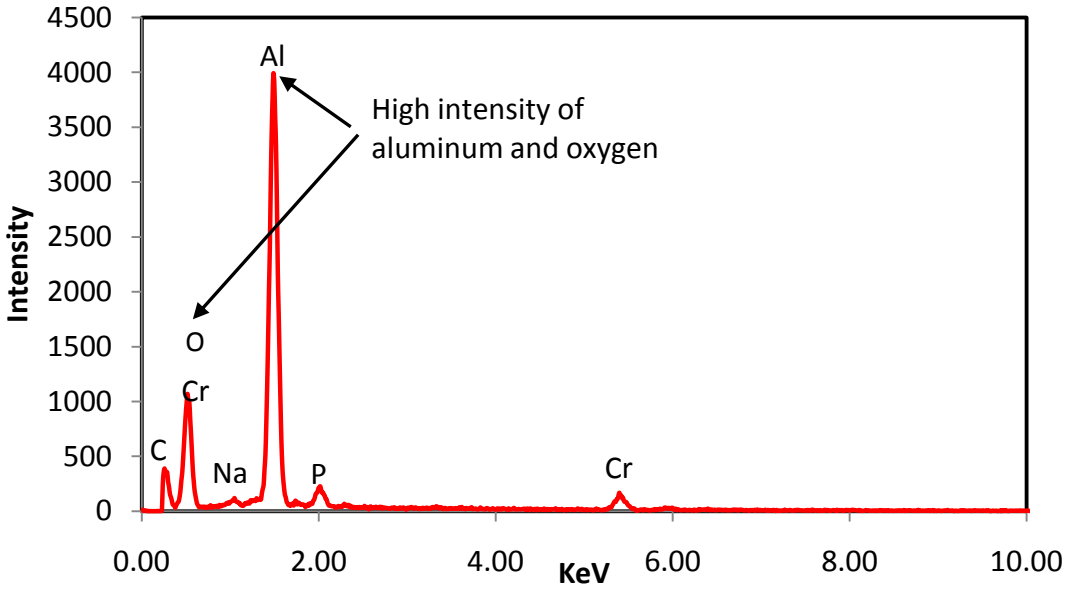

Figure 4.37: EDX spectrum of white particles (aluminum oxide)

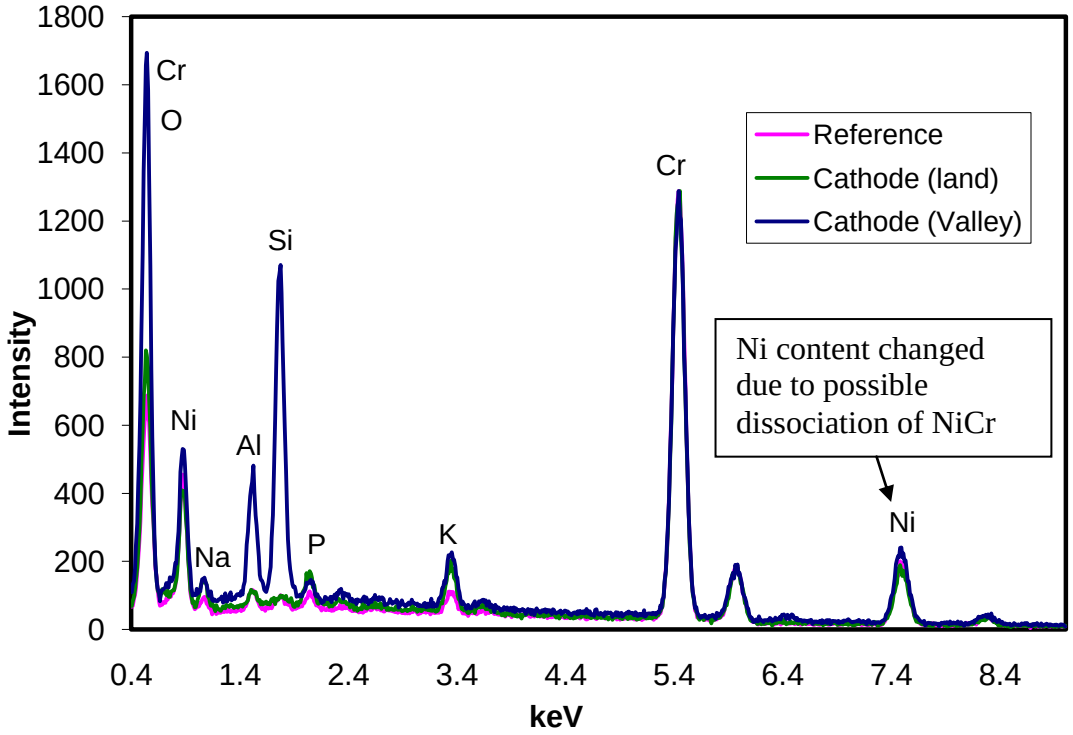

Figure 4.38: Superimposed EDX Analysis for the cathode plate (reference, valley and land)

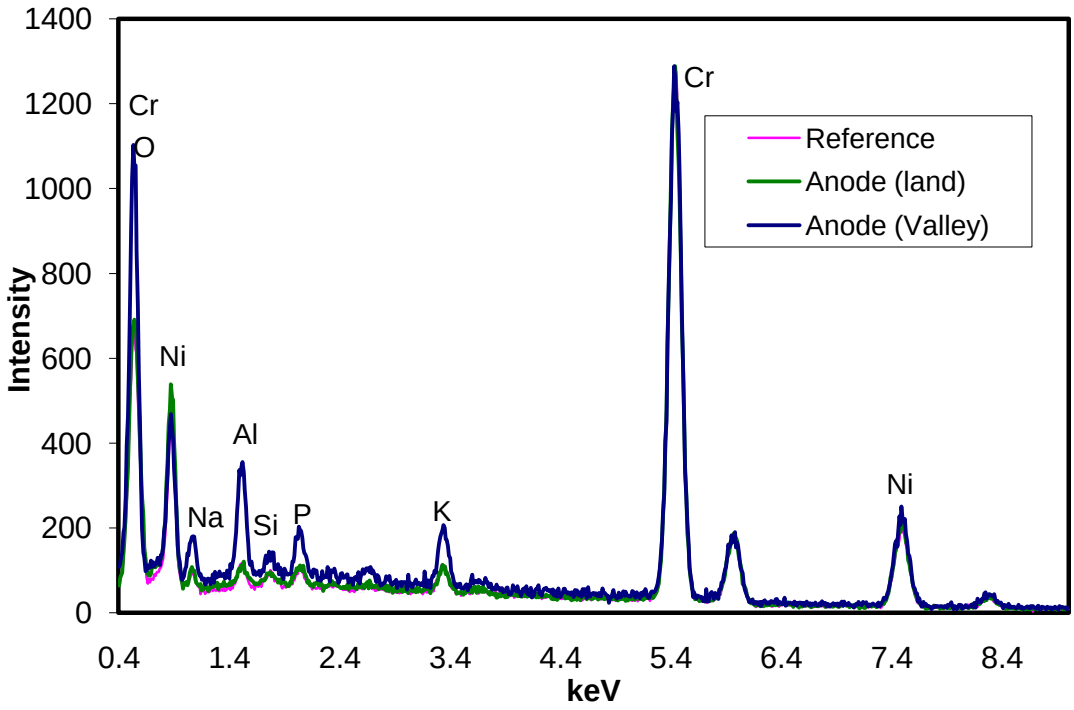

Figure 4.39: Superimposed EDX analysis for the anode plate (reference, valley and land)

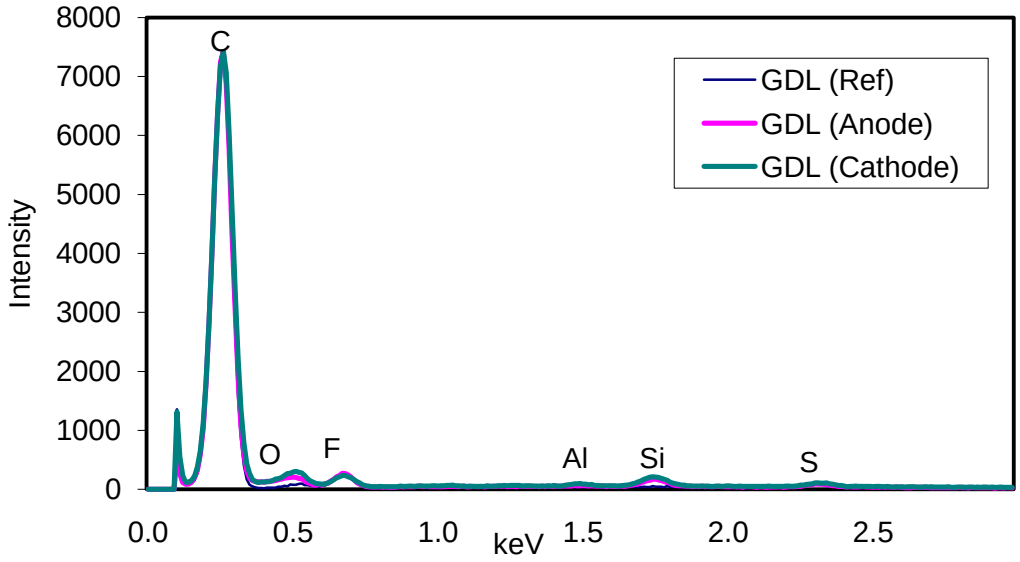

Figure 4.40: Superimposed EDX analysis for the GDL (reference, land and valley) used in the graphite composite plate

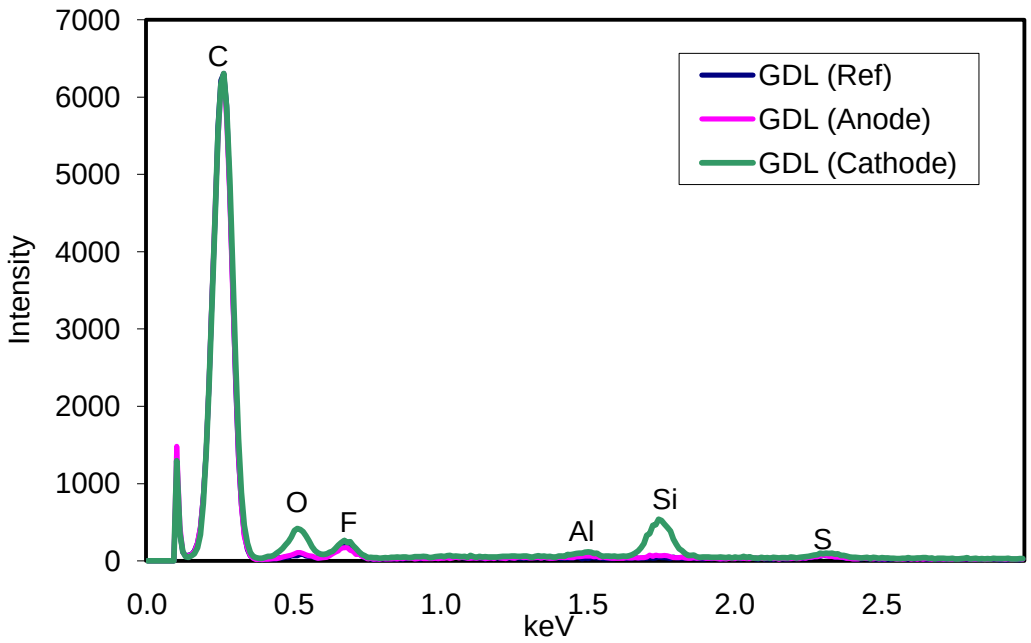

Figure 4.41: Superimposed EDX analysis for the GDL (reference, land and valley) used in the coated aluminum plate

4.2.7 X-ray diffraction (XRD) analysis of the membrane electrode assembly (MEA) after one thousand hours of operation

The XRD analysis was performed on six samples that were scraped from each of the cathode and anode sides of the MEA after operation in the coated aluminum single cell for 1000 hours. Another three samples were also scraped from a fresh unused MEA and were considered as a control. The XRD analysis on the samples indicated catalyst clustering or coarsening of Pt materials from both sides after 1000 hours of operation. This was demonstrated by an increase in the XRD intensity (Figures 4.42a and 4.42b). Similar observations were reported by other researchers [93,94] This is explained by the tendency of the catalyst to agglomerate to minimize its surface energy. In addition, small amount of chromium was detected in one of the three cathode samples of the MEA as shown in Figure 4.42b. Later in this work (section 4.5.2), chromium was proved to be physically embedded in the MEA due to the high compacting pressure within the single cell.

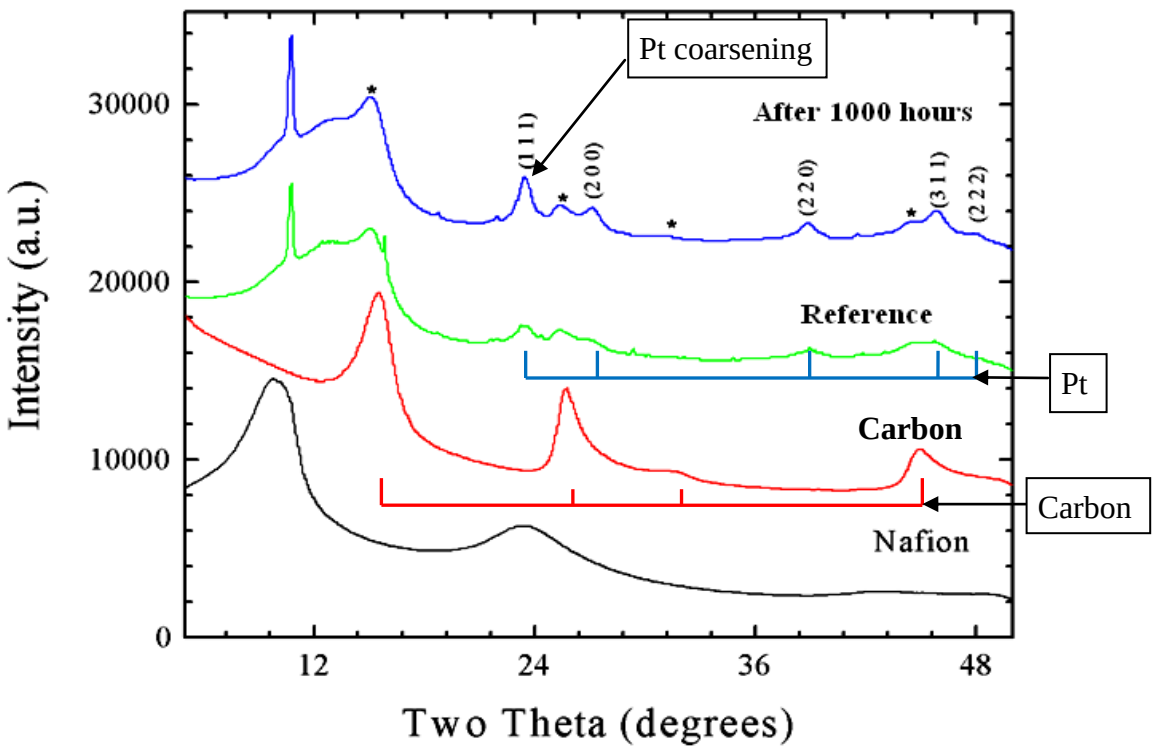

(a)

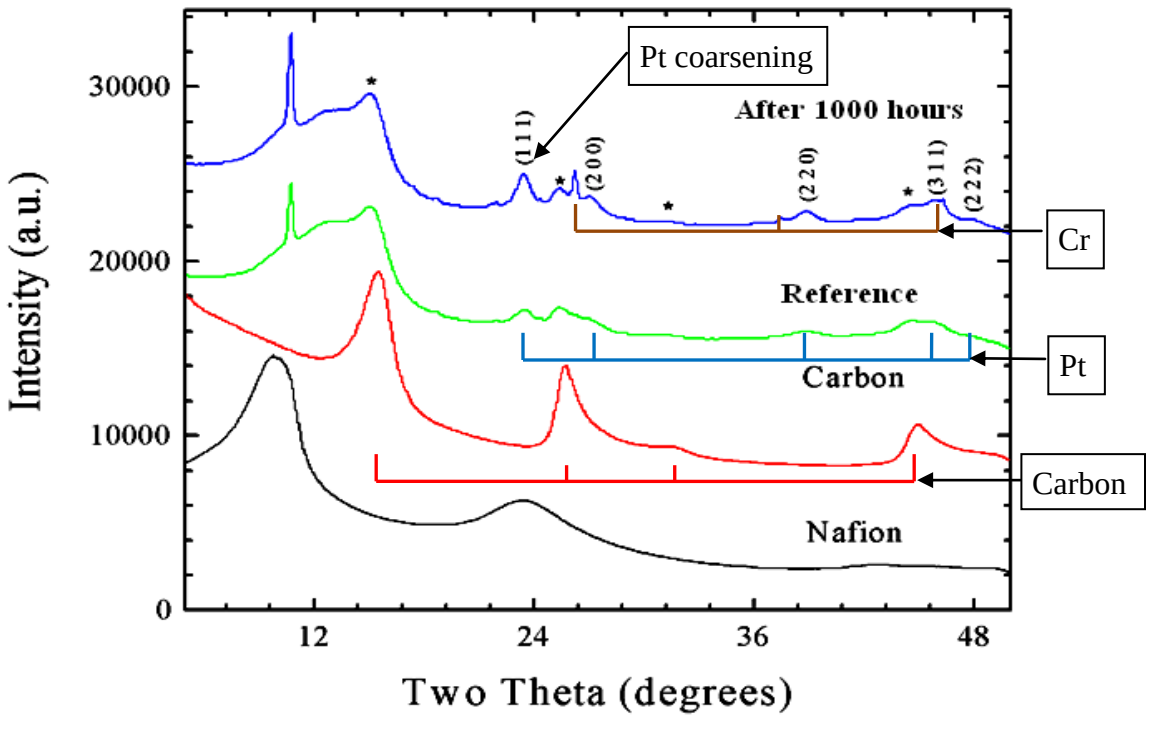

(b)

Figure 4.42: XRD patterns of the MEA (a) the anode side (b) the cathode side

4.2.8 Inductively coupled plasma - optical emission spectroscopy (ICP-OES) of the collected water samples

Water samples (by-product of the fuel cell electrochemical process) were collected during the 1000 hours of operation and analyzed using ICP-OES. The results showed the presence of Al, Cr, Pt, Fe and Ni at very low levels (< 1ppm each). Only carbon was found at 0.12%. The carbon was likely extracted from the gas diffusion layer that was assembled and strongly adhered to the MEA. The absence of Al and other coating materials in large quantities was noted as significant evidence that the coated aluminum plate had the potential to operate for longer time.

In summary, the results obtained from the graphite composite and metallic single cell testing as well as surface characterization of the bipolar plates and MEAs indicated the following:

- Graphite composite and metallic single cell performed almost identically due to their low ICR. However, metallic single cell can accommodate integrated terminal design which provided 18% average savings in hydrogen consumption and eliminated the need for extra current collector plates.
- Integrated terminal design is not recommended for graphite composite plates due to their weak mechanical strength and unsecured contact between the graphite bipolar plate and the terminal.
- Metallic bipolar plates can withstand higher cell clamping pressure which can improve the ICR value and as a result, an average savings of 11.6% and 7.8% in hydrogen consumption was obtained by applying 250N/cm^2 and 200N/cm^2 cell clamping pressure, respectively, in comparison to the 140N/cm^2 standard clamping pressure for graphite composite plates. However, the durability of MEA can be an issue.
- Metallic single cell performed as stable as graphite composite single cell for a 1000 hour testing period. The slight performance degradation in both cells was due to impurities leaching to the reactants and metal corrosion of uncoated components such as fittings, back plates, and manifolds.

- Humidity conservative flow-field design had demonstrated an average of 8% savings in hydrogen consumption in comparison to the traditional triple serpentine design.
- Surface characterization study showed that corrosion resistant coating or sealing is needed to be applied on manifolds, inlets and outlets where the aluminum is not covered by the thermal spray coating because humidified reactant gases can oxidize the aluminum and carry aluminum oxide particles to other areas of the cell.
- EDX analysis showed the possibility of partial dissociation of Ni from the Cr_3C_2-25%NiCr coating which indicated that less Ni is preferred in the corrosion resistant coating.

4.3 Effect of thermal and water management

A 40cm^2 active area 10 cell stack was assembled and operated under three levels of constant current (1, 3 and 5 amps). As mentioned earlier, the fuel cell performance was found to be sensitive to the humidity level of reactant gases. Figure 4.43a shows that as the relative humidity of both reactant gases increased, the 10 cell stack power output increased. This phenomenon becomes more pronounced as higher currents (3 and 5 Amps) were drawn from the stack. However, at low current (1 amp), the humidity level of reactant gases had almost no effect on the stack power output specially when a proper stoichiometric ratio was set to purge out the formation of water droplet that can potentially block the channels and cause significant voltage degradation. This was attributed to the fact that less hydrogen ions were required to be transferred from the anode to the cathode side through the Nafion membrane during the electrochemical reaction and therefore, less humidity was needed. However, when a higher current was drawn from the fuel cell stack, more hydrogen ions would be required to move more freely and conducted through the Nafion membrane from the anode to the cathode side. Therefore, higher reactant gas humidification was needed to hydrate the membrane and facilitate this electrochemical reaction.

In addition, Figure 4.43b shows that when the 10 cell stack was running at low relative humidity (RH) of 10% on either hydrogen or air side at 5 amp current, the power

output was lower than that when the stack was running with fully humidified hydrogen and air. Particularly, when air was at relative humidity (RH) of 10%, the power output of the stack dropped more than 25% in comparison to the power output produced by using air relative humidity (RH) of 95%. This was attributed to the dehydrated membrane causing deficiency of hydrogen ions transfer. Moreover, since the hydrogen side was dead ended, the water vapor carried by the hydrogen flow was not supplied as much as it was in the open ended air side and therefore humidifying the air gave higher the power output of the stack.

Figures 4.44a, b and c show the temperature profile of the stack while operating under a 5 amp current load. The temperature data collected from the 15 thermocouples (T1-T15) that were attached to the experimental fuel cell system indicated the averaged temperature of the front (T1-T5), middle (T6-T10) and the back (T11-T15) plates of the stack respectively. The three Figures 4.44a, b and c indicate that the temperature of the stack increased with time due to the heat generated from the electrochemical reaction of the stack, and when the fuel cells stack temperature reached approximately 37°C or above, the performance of the stack decreased and became unstable. This was explained by insufficient humidification and dehydration of the Nafion membrane due to the increase in the stack temperature and lowering of the membrane water content. On the other hand, if the cell temperature can be maintained below 37°C, the performance of the stack could be more stable but water management would be problematic. In addition, the middle cells of the stack heat up much faster than the front and the back cells of the stack. This was due to the insufficient cooling or heat removal in the middle stack zone to maintain uniform power density and temperature distribution that negatively reflected on the lifetime of the polymer membrane.

In summary, fuel cell performance is very sensitive to operating temperature and reactant gas humidity, particularly when a fuel cell operates at temperature higher than 37°C. Therefore, thermal and water management is needed within the stack to optimize the cell power output and prevent the MEA from drying up or flooding.

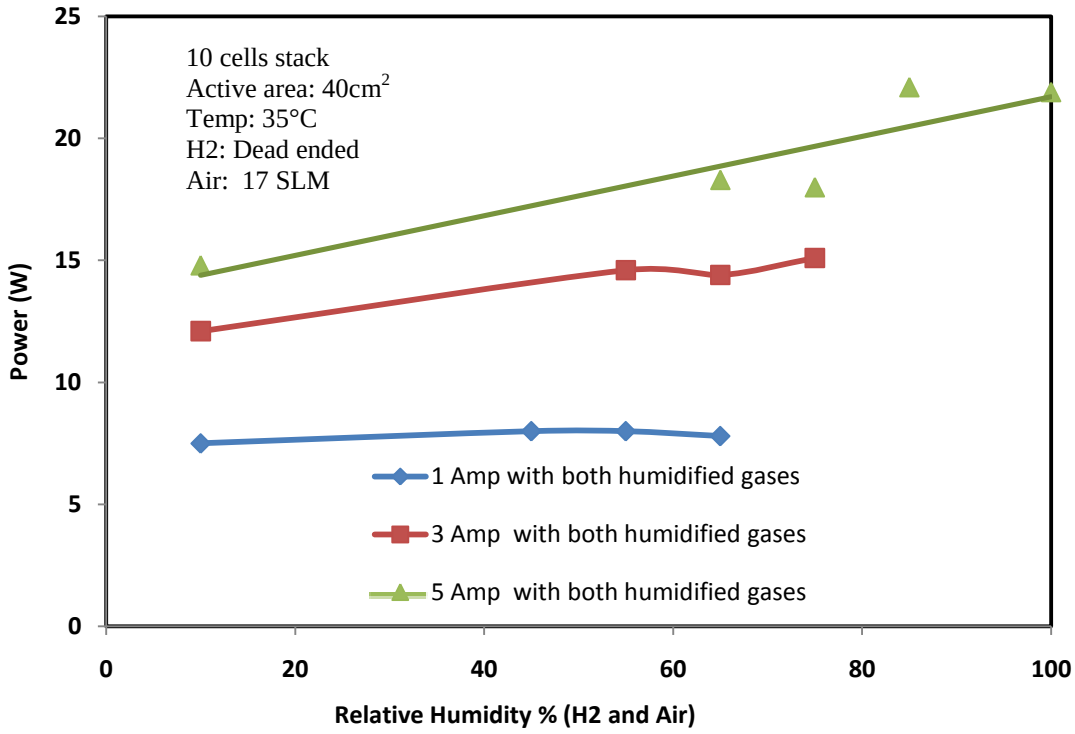

(a)

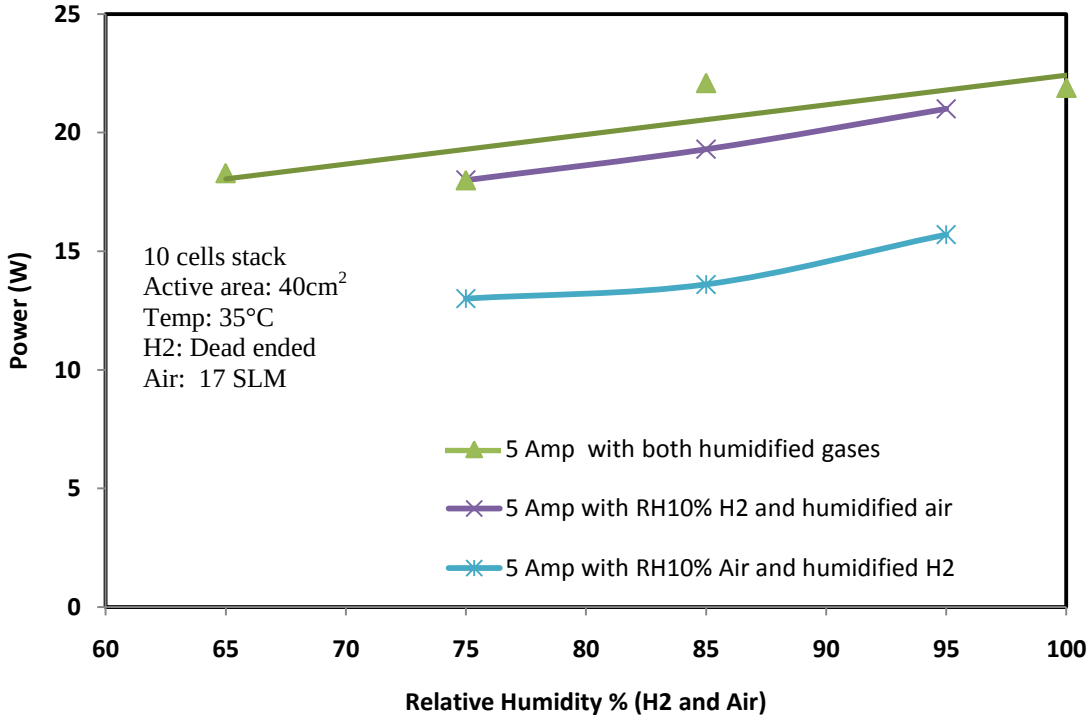

(b)

Figure 4.43: (a) Effect of both reactant gases' humidity level, (b) Effect of dry hydrogen (RH10%) and dry air (RH10%)

(a)

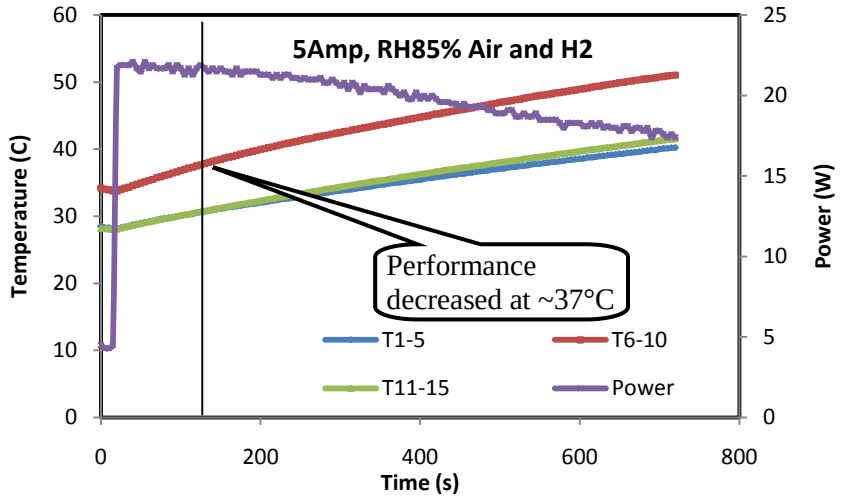

(b)

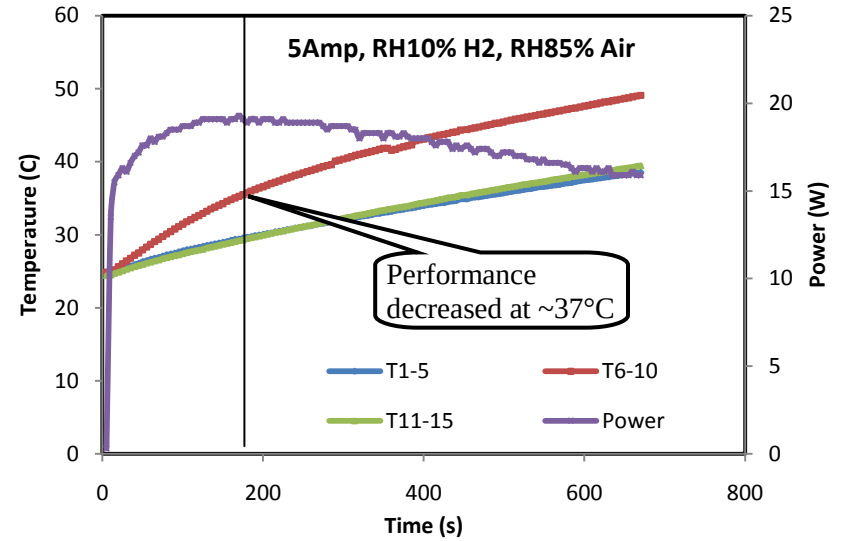

(c)

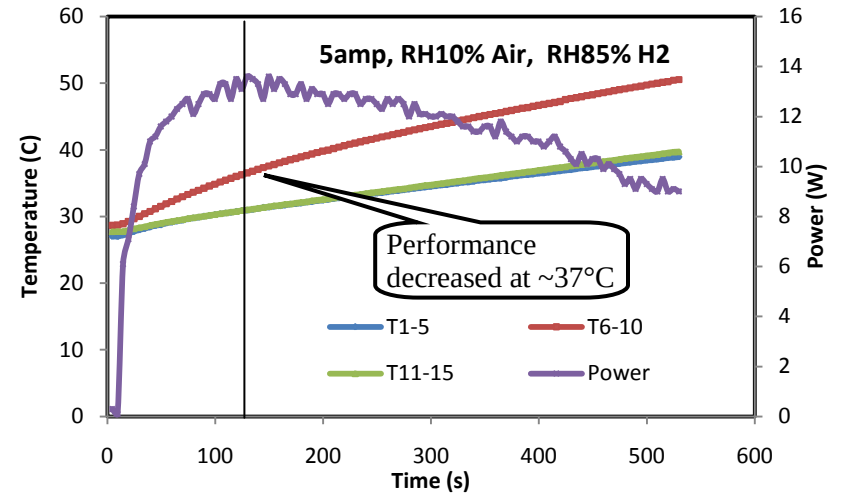

Figure 4.44: Effect of temperature (a) at 5 amp load, RH85% Air and H2, (b) at 5 amp load, RH10% H2 and RH85% Air, and (c) at 5 amp load, RH10% Air and RH85% H2

4.4 Cooling design and analysis

Thermal and humidity managements of PEM Fuel cells are necessary to produce optimal power output as demonstrated in the previous section. The cooling fins were designed and integrated into the bipolar plates to maintain the fuel cell operating temperature at 80°C or lower. Algor finite element simulation software was utilized to perform a steady-state heat transfer analysis considering fin cooling mechanism of a single bipolar plate. The bipolar plate shown in Figure 3.18 was designed such that it could be stacked alternatively to create fins on both sides of the fuel cell stack as shown in Figures 3.15 and 3.16. The air generated by cooling fans located underneath the stack was assumed to flow through the space between the fins located as extension on the side of each plate. Accordingly, convective heat transfer was the main mechanism to remove the excess heat generated by the electrochemical reaction of the fuel cell stack. Conductive heat transfer was also an important heat transfer mechanism to transfer the excess heat from the MEA to the fin. Therefore the bipolar plate material selection was important to the design and evaluation of the conductive heat transfer through the power stack.

Average heat transfer coefficients were required and calculated based on different air flow scenarios such as parallel air flow over a flat plate, air flow between parallel plates and internal flow through a duct. These scenarios were considered because they were similar to the actual air flow condition within the fuel cell system. In particular, when cooling fins were considered, average heat transfer coefficients were assumed and evaluated in parallel plates and rectangular duct flow condition. This was due to the similarity of their cross sections (Figures 4.45a, b and c). Average heat transfer coefficients in each design scenario with different air velocity were calculated and plotted in Figure 4.46. Flat plate assumption had lower average heat transfer coefficient than other two assumptions, namely parallel plates and rectangular duct, particularly when air velocity was higher than 5m/s. This was attributed to the air turbulent flow within the parallel plates and rectangular duct that results in higher rate of heat transfer. Two air velocities 3.7m/s and 7.4m/s were calculated from the cooling fan specifications and therefore the average heat transfer coefficients used in this study were 36W/m^{2}K (0.0036W/cm^{2}K) and 55W/m^{2}K (0.0055W/cm^{2}K).

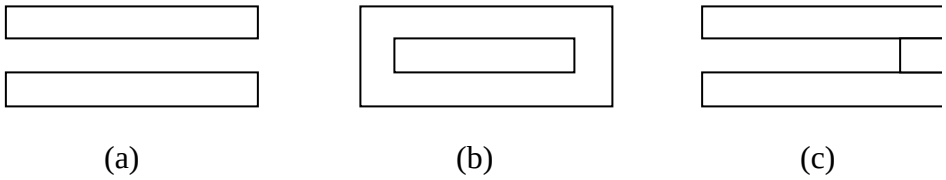

Figure 4.45: (a) Cross section of parallel plates, (b) Cross section of rectangular duct and (c) Cross section of bipolar plates with fins

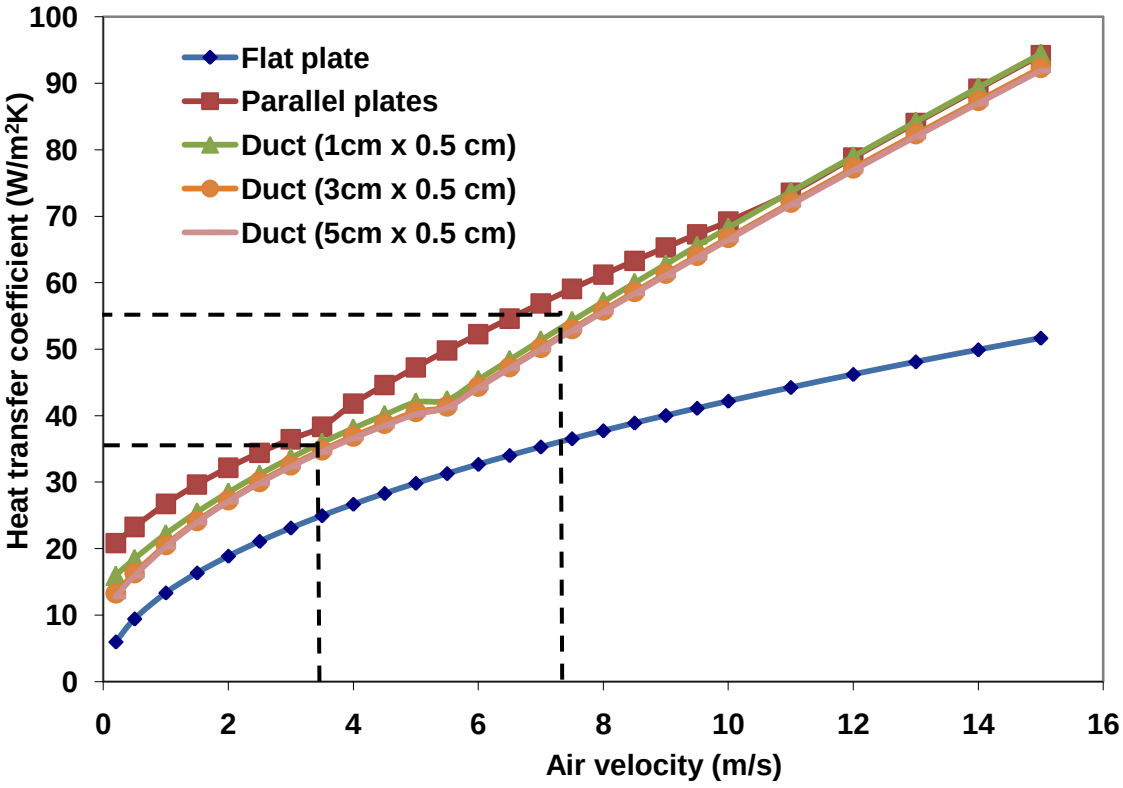

Figure 4.46: Average heat transfer coefficients VS air velocity for flat plate, parallel plates and rectangular duct condition.

In the case of forced air fuel cell, Figures 4.47a and b show temperature distribution of aluminum and graphite composite bipolar plates without fins. These temperature distribution simulations were computed in forced air and steady state heat transfer condition at power density of 0.3W/cm^2 and average heat transfer coefficient of 0.0036W/cm^2 K. The maximum temperature of the bipolar plates in both materials was higher than 300°C which was much higher than the fuel cell operating temperature (80°C). It was due to the lack of surfaces exposed to cooling air for convective heat transfer (Figure 4.47 a and b).

Figure 4.48 also shows the maximum and minimum temperature profile of a bipolar plate with different fin length and different materials at the same condition of power density of 0.3W/cm^2 and average heat transfer coefficient of 0.0036W/cm^2 K. As expected, fins enhanced the heat dissipation from the bipolar plate. The maximum temperature was in the active area where the heat source was located and the minimum temperature zone was in the fin area where the cooling air was flowing in a boundary layer tangential to the fin. The maximum temperature profile for an aluminum bipolar plate was initially very responsive to the fin length. This was demonstrated in the fin length ranging from 0mm to 20mm where the temperature of the bipolar plate was reduced significantly from 329°C to 118°C. However, when the fin length was increased further from 20mm to 50mm, the temperature reduction was only 39°C. This was attributed to the heat dissipated from the fin was much higher than the heat conducted from the heat source to the fin.

In addition, the temperature difference within the plate depended heavily on the thermal conductivity of the material. Since aluminum has higher thermal conductivity (167 W/m·K) than graphite composite (46.2 W/m·K), the temperature difference in the aluminum bipolar plate was less than that in the graphite composite plate as demonstrated in Figure 4.48. Though the graphite composite plate with 50mm long fin had a minimum temperature of 55°C at the fin area but the active area was at 112°C which was still above the fuel cell operating temperature of 80°C. However, the maximum temperature of aluminum bipolar plate with a 50mm long fin was able to be kept below 80°C. This was due to the higher thermal conductivity of the aluminum bipolar plate.

Figure 4.49 shows that lower temperature of the bipolar plate was obtained by increasing the average heat transfer coefficient to 0.0055W/cm^2 K. Maximum temperature of the aluminum bipolar plate could be kept below 80°C at 23mm long fin. It was attributed to the higher heat dissipation at the fin surfaces. However, maximum temperature of the graphite composite plate was unable to be maintained below 80°C due to its poor thermal conductivity.

In the case of forced convection fuel cell, the power density was assumed to be 0.15W/cm^2 which was 50% less than the forced air fuel cell stack. Therefore, the heat generated by the electrochemical reaction was also less than that for the forced air fuel cell stack. At a power density of 0.15W/cm^2 and an average heat transfer coefficient of 0.0036W/cm^2 K, the fin length for graphite composite and aluminum bipolar plates can be reduced to 23mm and 14mm, respectively to maintain the operating temperature of 80°C (Figure 4.50). For higher average heat transfer coefficient of 0.0055W/cm^2 K, the fin length for graphite composite and aluminum bipolar plates can be reduced further to 12mm and 9 mm, respectively (Figure 4.51).

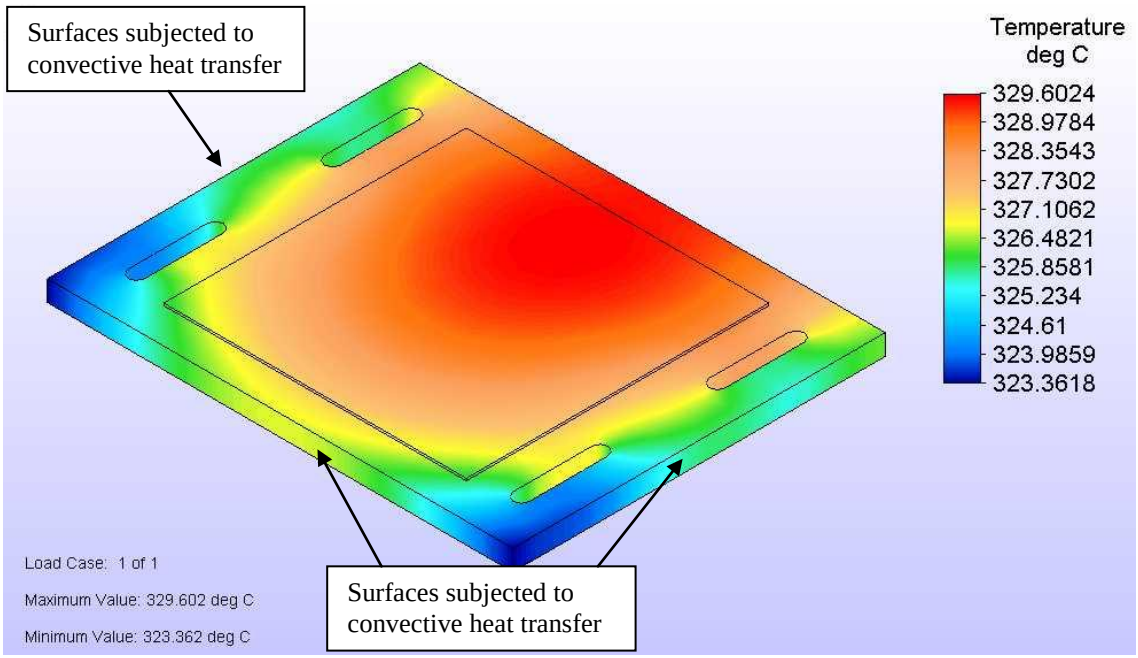

(a)

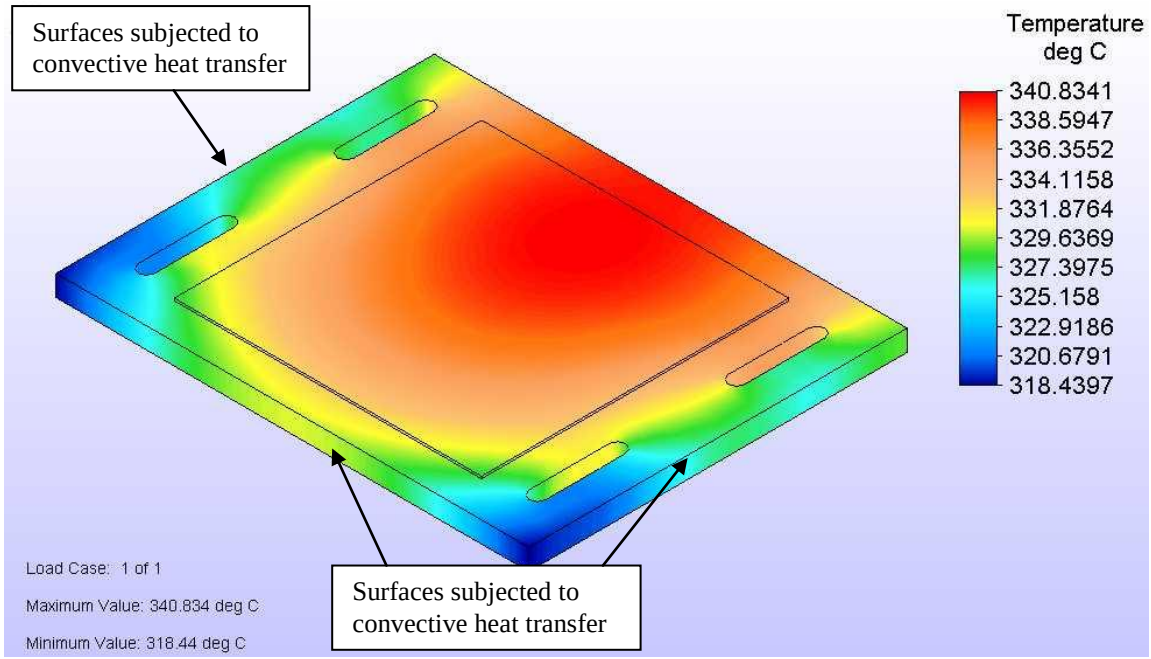

(b)

Figure 4.47: Temperature distribution of bipolar plates without fin (a) aluminum and (b) graphite composite

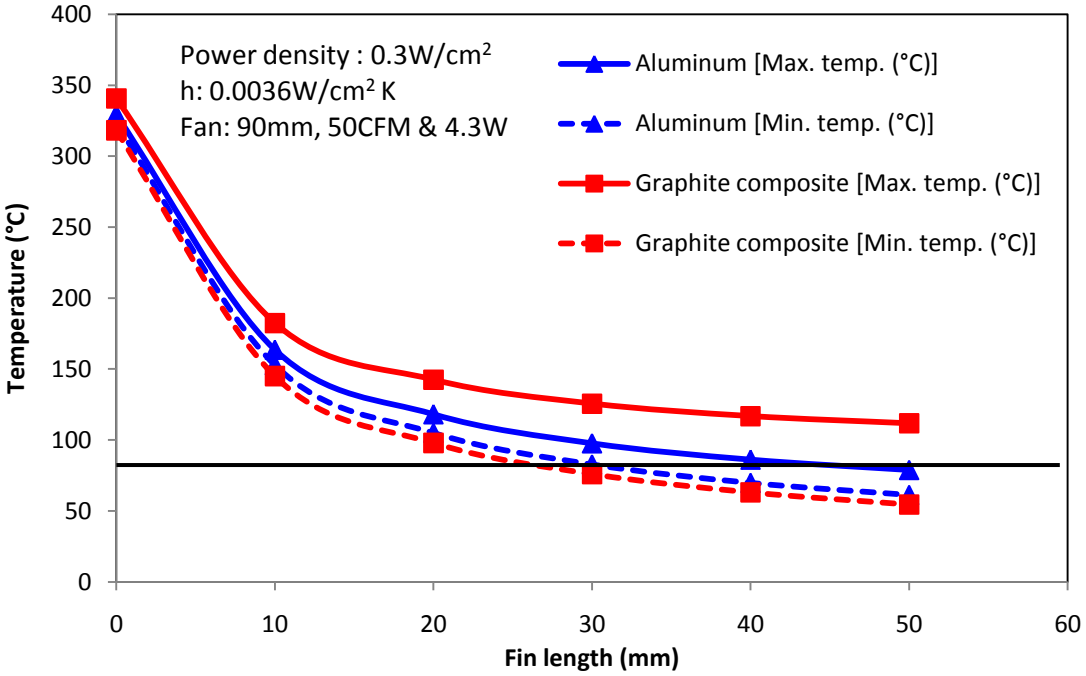

Figure 4.48: Maximum and minimum temperature profile for forced air bipolar plate in different fin length and different materials at power density of 0.3W/cm^2 with average heat transfer coefficient of 0.0036W/cm^2 K

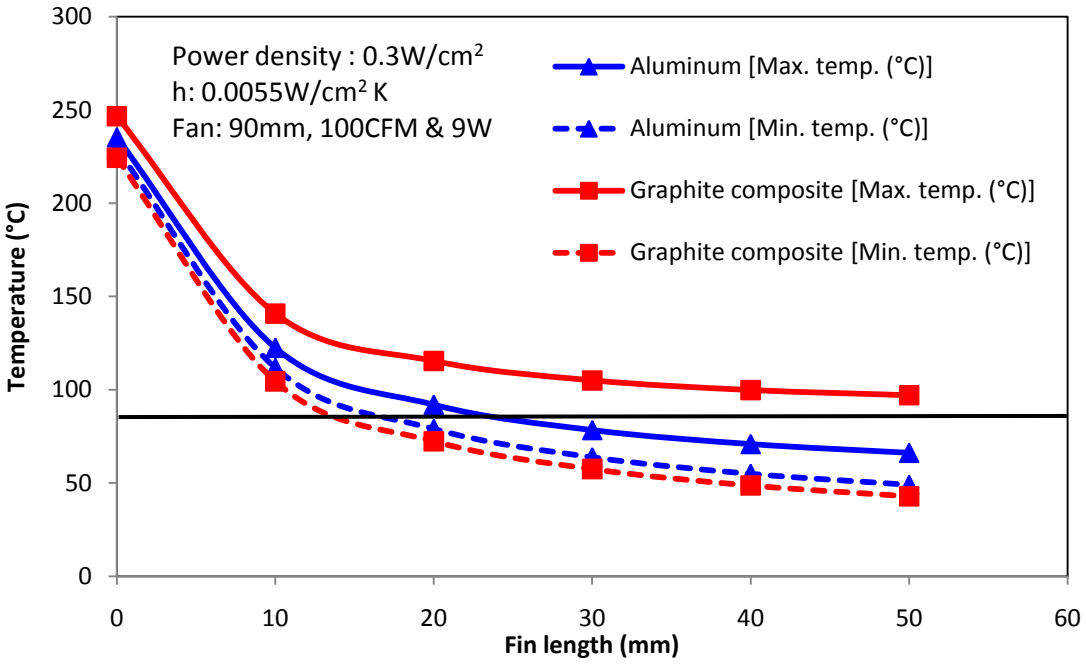

Figure 4.49: Maximum and minimum temperature profile for forced air bipolar plate in different fin length and different materials at power density of 0.3W/cm^2 with average heat transfer coefficient of 0.0055W/cm^2 K

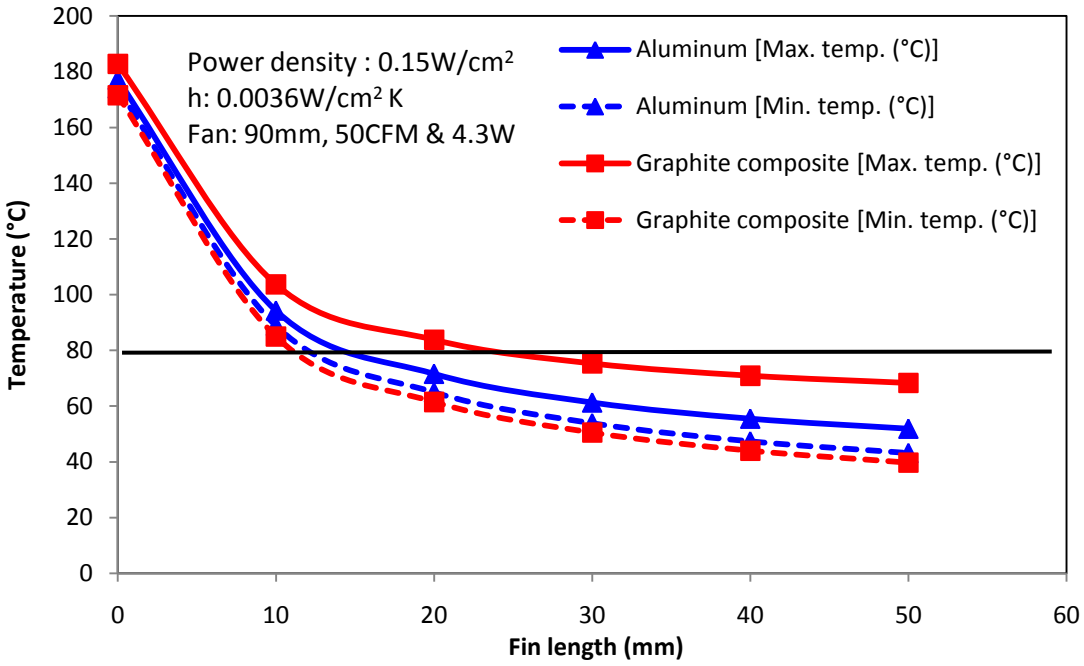

Figure 4.50: Maximum and minimum temperature profile for forced convection bipolar plate in different fin length and different materials at power density (0.15W/cm^2) with average heat transfer coefficient of 0.0036W/cm^2 K.

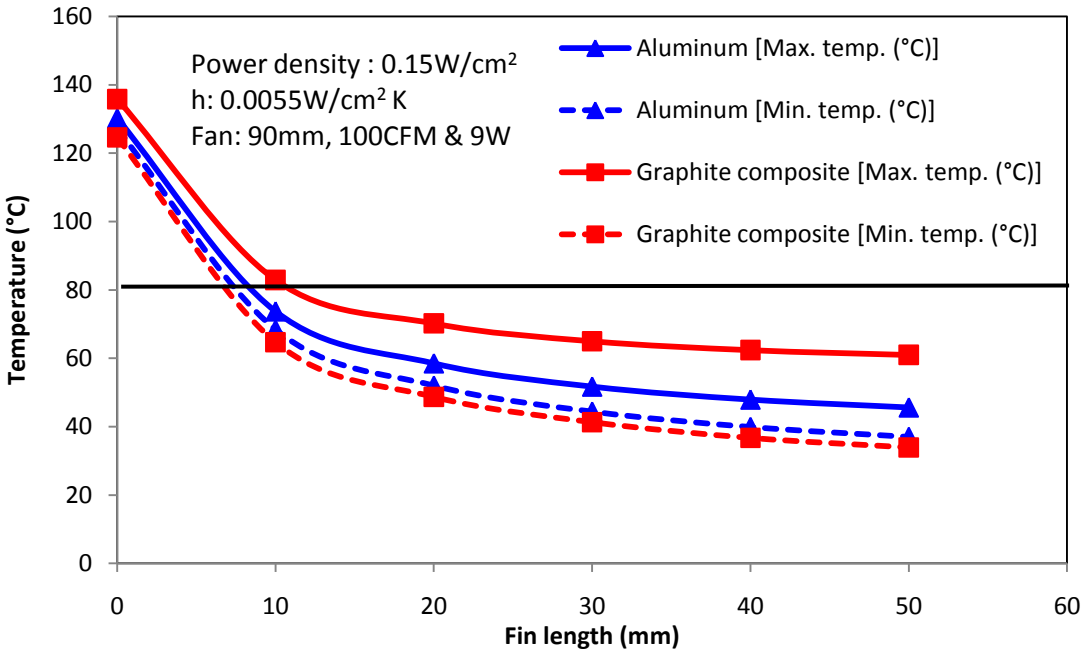

Figure 4.51: Maximum and minimum temperature profile for forced convection bipolar plate in different fin length and different materials at power density of 0.15W/cm^2 with averaged heat transfer coefficient of 0.0055W/cm^2 K

4.4.1 One kW forced air and forced convention fuel cell cost analysis

Both forced air and forced convection fuel cell stacks have their own advantages and disadvantages. Forced air fuel cell stack has an advantage of having higher power density than the forced convection stack. The number of cells used in the forced air fuel cell stack is less than that for the forced convection stacks which can reduce the overall stack cost. However, parasitic power used in the forced air stack design under consideration, will be increased due to the use of both compressed and cooling air in the power stack. On the other hand, the cooling fans used in forced convection stack serve dual purposes, cooling the stack and driving air/oxygen through the cells, which minimizes the parasitic power used in the stack; however higher number of cells as well as cost will be required in such design.

Table 4.2 shows the parasitic power calculation and comparison between both types of stacks. The table indicates that 17% and 4% of the power generated from the electrochemical reaction were used in parasitic power for forced air and forced convection fuel cell stacks respectively. At the hydrogen price of $4.3/kg, approximately $2000 savings in running cost can be obtained within 5 years using a 1kW forced convection design in comparison to the forced air design. However, this savings will be offset by the capital cost of the additional cells because of its low power density. The cost estimations for both stack design systems are shown in Table 4.3. Therefore, it is recommended to use the forced air stack design in automobile industry where power density and size are critical. On the other hand, the forced convection stack design can be used in power station application where size is not as important.

In summary, the power stack cooling system design and analysis considering different bipolar plate materials and stack configuration have indicated the following:

- Aluminum plate has better thermal conductivity than graphite composite plate which allows faster heat transfer and uniform temperature distribution within the plates. It can also adopt the fin design and air cooling system to remove excessive heat during the operation for better thermal management.
- The fin design does not remove excessive heat effectively in graphite composite plate due to its relatively poor thermal conductivity.

- Forced air stack design offers higher power density and relatively smaller size in comparison to forced convection stack design. However, the parasitic power used in forced air design is 13% higher than that of forced convection design.
- There is no noticeable savings in running cost and capital cost between the forced air and forced convection stack designs, considering a 1 kW system and a 5 year operation period.
- Forced air stack design is recommended in automobile industry where power density and size are critical. Forced convection stack design can be used in power station application where size is not as important.

Table 4.2: Parasitic power for 50cm^2 active area forced air and forced convention fuel cell stack design

	Hydrogen	**Forced air**	**Forced convection**
Power density (W/cm^2)		**0.3**	**0.15**
Active area (cm^2)		**50**	**50**
Power per plate (W)		**15**	**7.5**
Consumption per Amp per Cell (SLM/cell/A)	**0.00735**	**0.018375**	
Number of cells	**1**	**1**	
Amp per plate (Current density 0.5A/cm^2@ 0.6V)	**25**	**25**	
Stoichiometry	**1**	**3**	
Consumption (SLM)	**0.18375**	**1.378125**	
Pressure drop (N/m^2)		**68947.57**	
Compressor power per plate (W) (80% efficiency)		**1.98**	
Cooling fan power per plate (W) (15 plates per fan)		**0.60**	**0.29**
Total Parasitic Power (W)		**2.58**	**0.29**
Percentage lost		**17%**	**4%**

Table 4.3: Cost comparison for forced air and forced convention fuel cell

	Forced air system	Forced convection system
Cost of 1kW fuel cell	**$2,000.00**	**$4,000.00**
Hydrogen consumption per kW (SLM/kW) (Current density 0.5A/cm2 @ 0.6V)	**12.250**	**12.250**
Gas constant- R (kJ/kg.K)	**4.12**	**4.12**
Pressure- p (kN/m2)	**101.33**	**101.33**
Temperature- T (k)	**293.00**	**293.00**
mass flow rate per 1 kW (kg/min/kW)	**0.00103**	**0.00103**
Cost of hydrogen per kg	**$4.30**	**$4.30**
Hydrogen cost per kWh	**$0.265**	**$0.265**
Percentage lost in Parasitic Power	**17%**	**4%**
Net hydrogen cost per kWh	**$0.319**	**$0.276**
5 years (43800 kWh) running cost	**$14,019.35**	**$12,069.4**

4.5 Durability test and characterization study on a three-cell metallic fuel cell stack

Figure 4.52 shows the fuel cell stack operation performance over 750 hours. The fuel cell stack was initially operated at 37°C, current density of 0.4A/cm^2, air flow rate of 4 SLM, and approximately 0.57V per cell and 0.23W/cm^2 for 250 hours without external humidity applied to the reactant gases. The stack performance was rather stable at this operation temperature and conditions. The spikes in the stack performance depicted in Figure 4.52 were caused by the load cycling applied to the stack during the daily shut down and start up routine allowing the temperature of the stack to cool down to room temperature (20°C) and elevate to 37°C under load condition. After 250 hours of operation with cooling air to maintain stack temperature at 37°C, the cooling air flow rate was lowered to allow the stack temperature to elevate to 80°C as a result of the stack's own generated heat during the electrochemical reaction. Air flow to the cathode side of the stack was routed through an air bubbler to provide more than 90% relative humidity to the air. Hydrogen was fed directly from a gas cylinder to the stack with approximate relative humidity of 10%.

At 80°C, the stack was operated at 0.5A/cm^2, approximately 0.5V per cell and 0.25W/cm^2 for additional 500 hours. The lifetime performance of the stack was also stable at 80°C until two of the three MEAs failed after the total operating time of 550 hours and 670 hours. These two MEAs were replaced and the fuel cell stack continued to operate normally for a total of 750 hours which completed the lifetime testing. Both MEA failures were due to the tearing of the polymer membrane (Figure 4.53) causing crossover between hydrogen and oxygen and hampering the cell's electrochemical reaction. The tearing at the edge of the electrode could have been caused by both the thermal and humidity cycling applied to the membrane due to the variation in the load condition during the stack operation. The membrane usually absorbs relatively large amount of water during the operation due to its hydrophilic property. Thus, the membrane swelling causes significant dimensional changes. Moreover, operating the fuel cell stack at 80°C without maintaining sufficient humidity in the reactant gases allowed the open ended cathodic air to liberate the stack humidity to the outside environment. This combined with the overnight daily shut down of the stack had caused the membrane to dry up resulting in shrinkage of the membrane. Barbir [21] indicated that swelled membranes can have linear expansion in the order of magnitude of 10%. Therefore, due to pressure applied on MEAs by the bipolar plates and end plates which had constrained any movement of the polymer membrane, the frequent expansion and contraction of the polymer membrane during the operation could cause tensile and compression stress within the polymer membrane resulting in the tearing of the polymer membrane. Though two MEAs were replaced during the fuel cell operation, the remaining MEA had successfully operated throughout the 750 hours of testing as Figure 4.52 depicts.

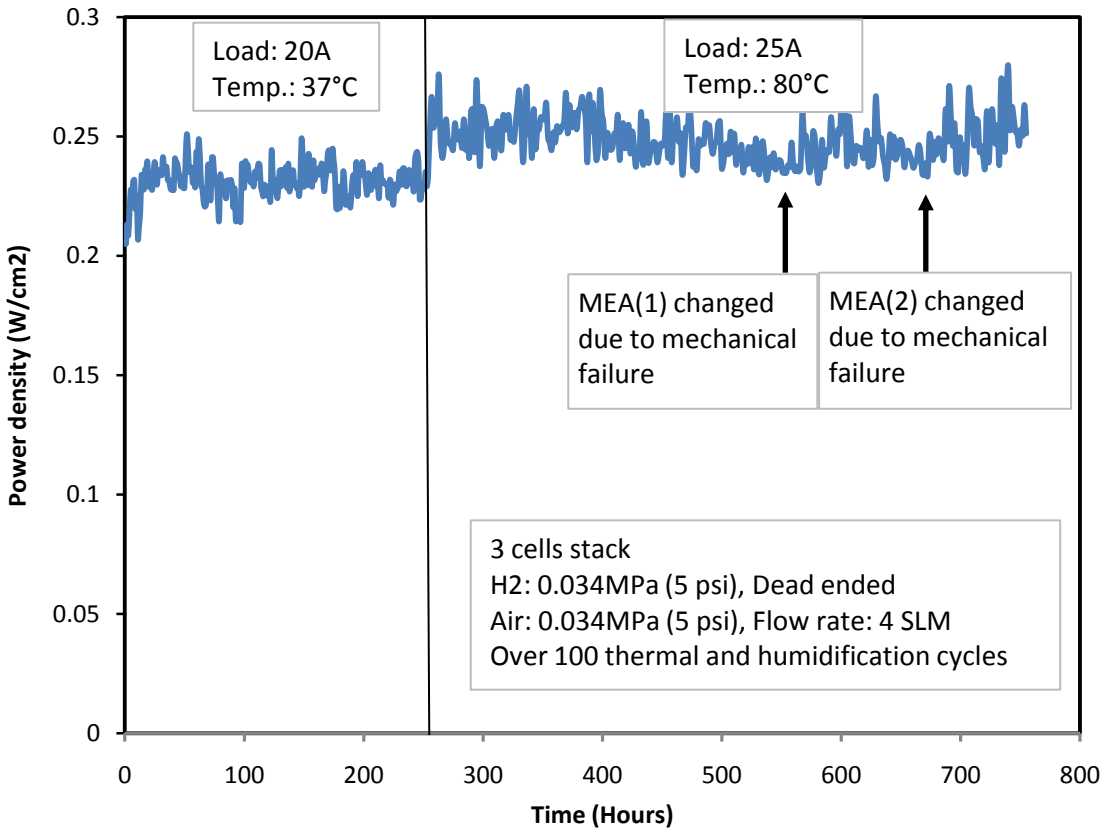

Figure 4.52: Durability test of the three cell stack using coated aluminum bipolar plate and operated under cyclic loading at 37C° and 80°C.

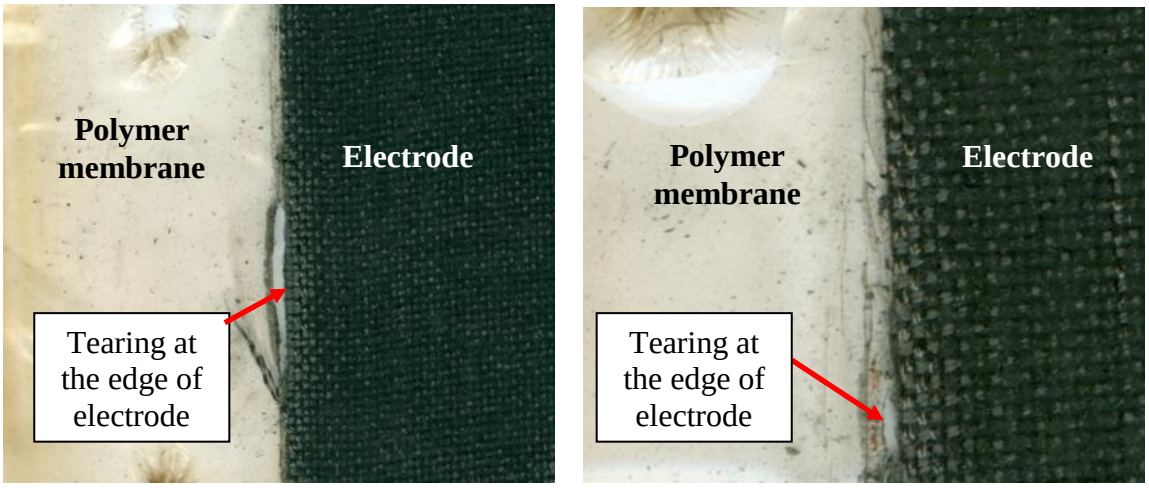

Figure 4.53: Images of the MEAs after 550 hours (left) and 670 hours (right)

4.5.1 Bipolar plate surface characterization

After 750 hours of fuel cell stack operation at various loading conditions, including different current density and temperature, this three cell stack was taken apart for surface characterization. One of the three bipolar plates was analyzed to check for any possible chemistry change on the coating surface. The cathode and anode sides and a cross section of the bipolar plate were examined and analyzed by SEM/EDX. Figure 3.26 shows a scanned image for both cathode and anode sides of the bipolar after 750 hours of operation. Gas inlets and outlets, lands (ribs) and valleys (channels) located in the active area of the cell were examined. Area outside the active area was treated as control reference. White small spots were visually observed on the active area of both cathode and anode sides of the bipolar plate surfaces, particularly within the valleys and at the gas outlet. Black particles were also visually observed on the top of the land surface, in which these findings were similar to the observation from the single cell surface characterization mentioned in section 4.2.6. The EDX spectrum shown in Figure 4.54 verifies that the white particles were aluminum oxide due to the high intensity peak of aluminum and oxygen and the black particles were found to be composed of carbon and fluorine (Figure 4.55). The surface morphology of the aluminum oxide particle and the carbon-fluorine rich fragment is shown in Figure 4.56.

Figure 4.57 shows a SEM image of the lands (ribs) and valleys (channels) that had many of aluminum oxide particles and carbon-fluorine rich fragments on the surfaces.

Aluminum oxide particles were found mainly locating within the valleys and occasionally they were found on the land surface. Though the surface of the land showed some aluminum oxide particles, the majority of the particles found there were carbon-fluorine rich fragments (Figure 4.57). These carbon-fluorine fragments were part of the MEA material which was stuck on the land surface due to relatively high clamping pressure between the bipolar plates and the MEA. It should be noted that aluminum oxide particles and the carbon-fluorine rich fragments were sporadically appeared on the land and valley surfaces in the active area.

Figures 4.58 and 4.59 show the EDX spectra of land, valley and inactive area (reference) on both cathode and anode sides of the coated aluminum bipolar plate where there were no aluminum oxides and carbon-fluorine rich fragments on the coating. The EDX spectra of the cathode and the anode surfaces showed only the Cr, Ni, and C peaks which were the known elements in the coating material. Aluminum was not detected in these two particular EDX spectra. In addition, the EDX spectra of land, valley and reference area were scaled according to their Cr peaks to observe the chemical change in other element in comparison to Cr. As a result, Figures 4.58 and 4.59 also shows that when the x-ray energy of the electron beam was above 1keV (where quantitative measurements were meaningful), the change in Ni on both the land and valley surfaces in comparison to the reference area was negligible so as all other elements of the coating as depicted in EDX spectra.

Figure 4.60 shows the surface morphology of the land, valley and reference areas of the cathode surface at 3kX and 10kX magnifications. The surface morphology of the land was very similar to the morphology of the reference area at 3kX magnification. The slightly darker SEM image of the valley surface at the same magnification was due to the 1mm deeper working distance as well as the side walls of the ribs causing difficulty for the electrons from the electron beam to escape to the signal detectors. However, the surface morphology of the land and valley in 10kX magnification clearly showed similar morphology to the reference area which indicated that there was no noticeable change on the coating surface in comparison to the reference surface. The observation confirmed and agreed with the results obtained from the EDX spectra (Figures 4.58 and 4.59).

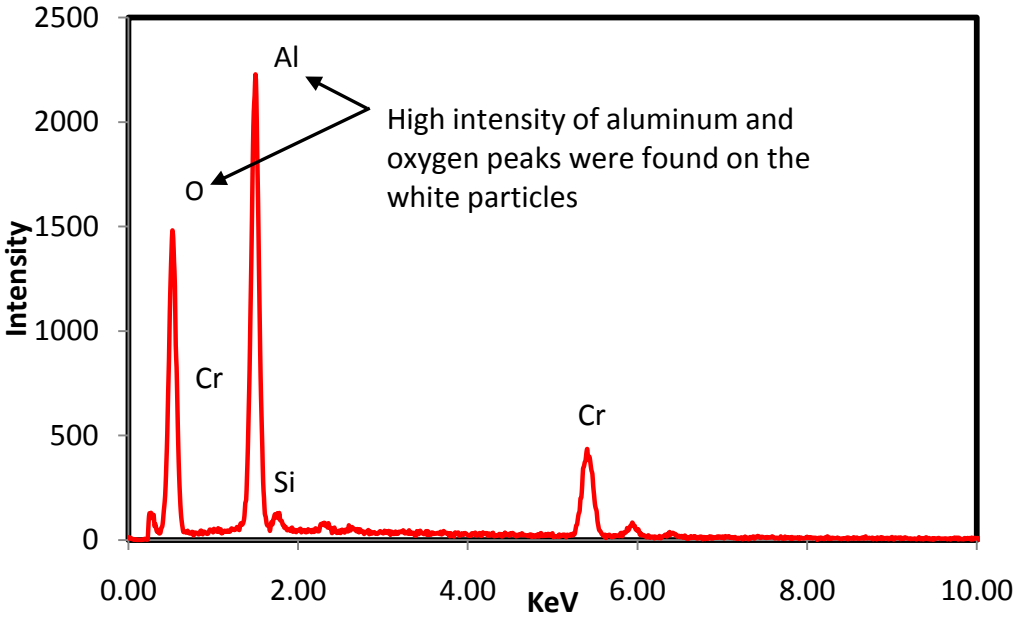

Figure 4.54: EDX spectrum of white particles (aluminum oxide) which were located on the valleys (channels) of the bipolar plate

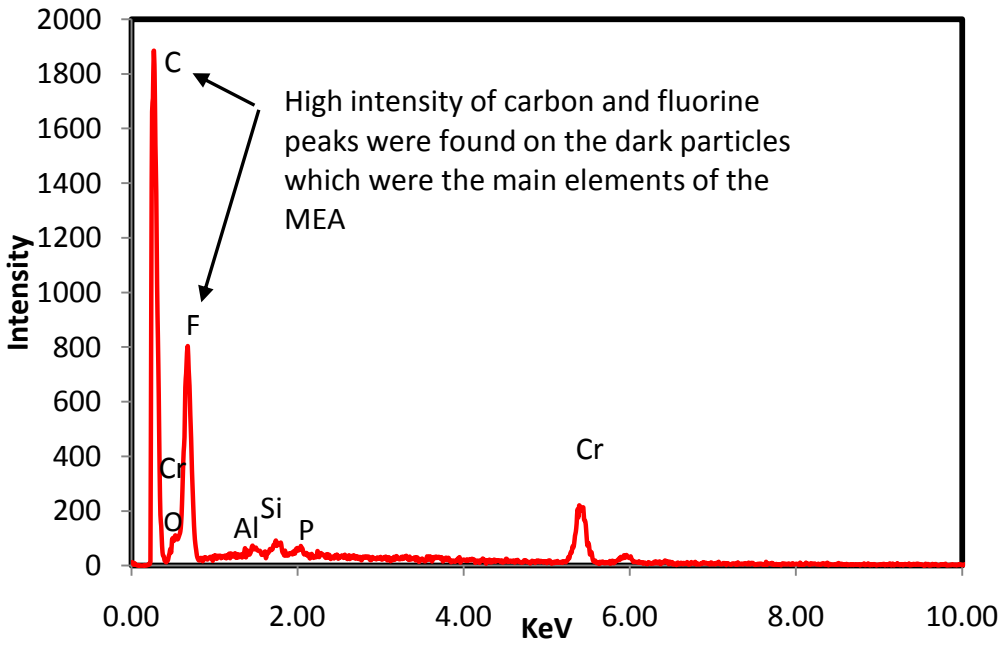

Figure 4.55: EDX spectrum of dark particles (carbon-fluorine fragments) which were located on the lands (ribs) of the bipolar plate

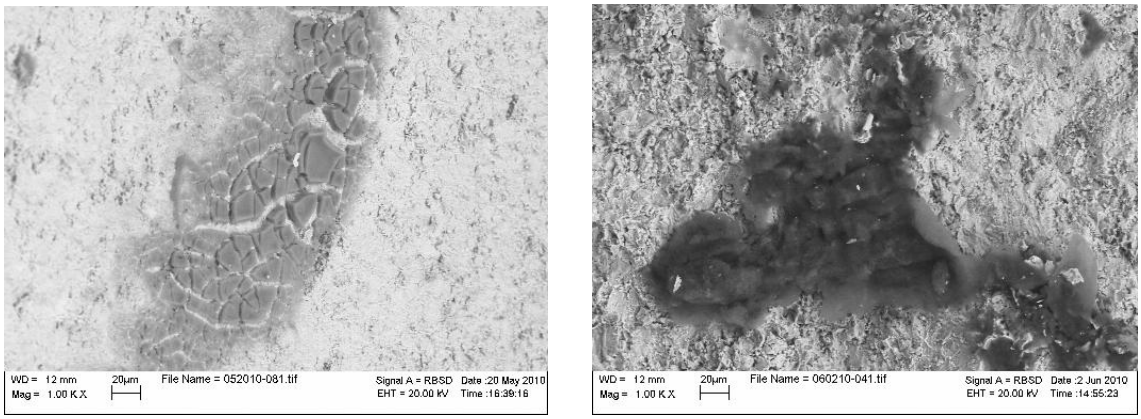

Figure 4.56: SEM images of aluminum oxide (left) and carbon & fluorine fragment (right)

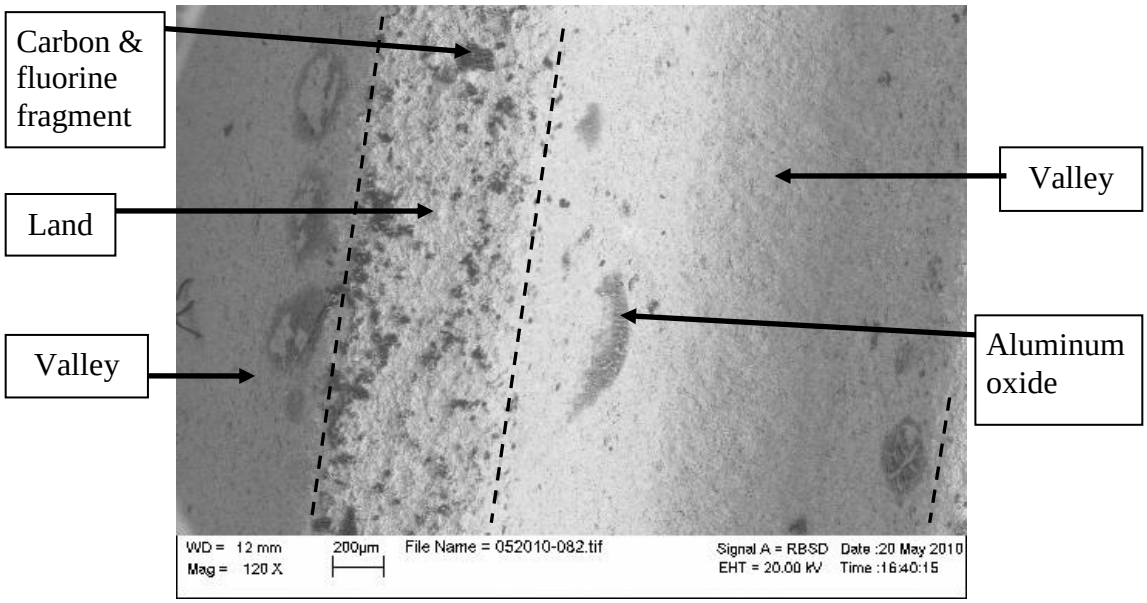

Figure 4.57: SEM images of land and valley of the bipolar plate

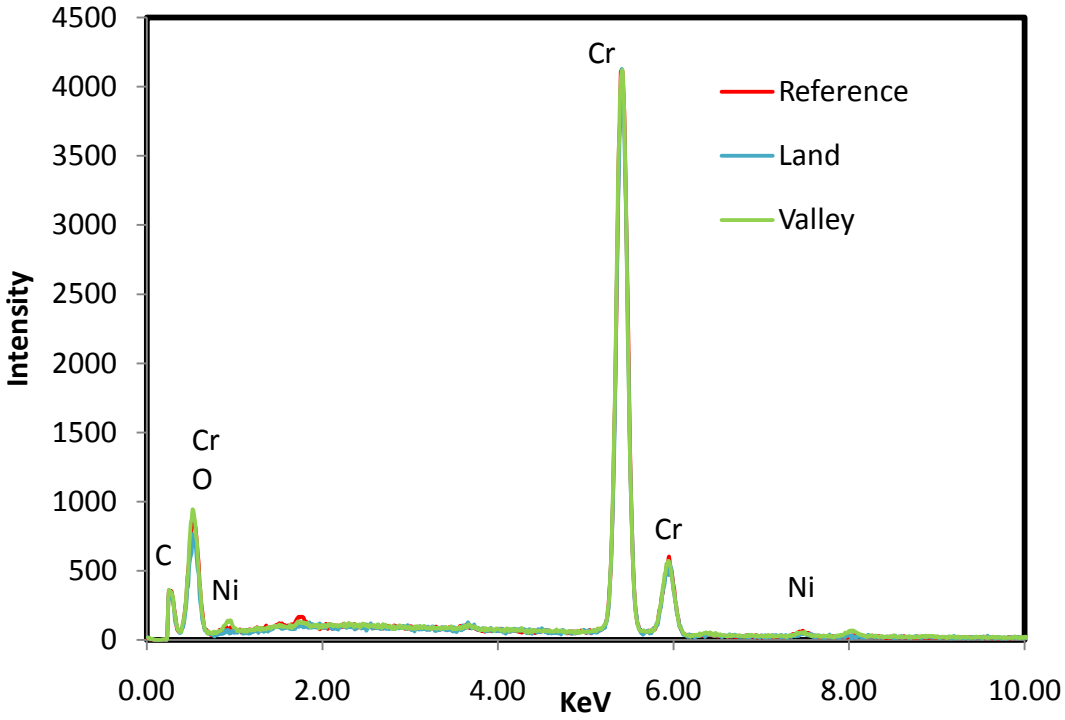

Figure 4.58: EDX spectrum of anode side of the bipolar plate

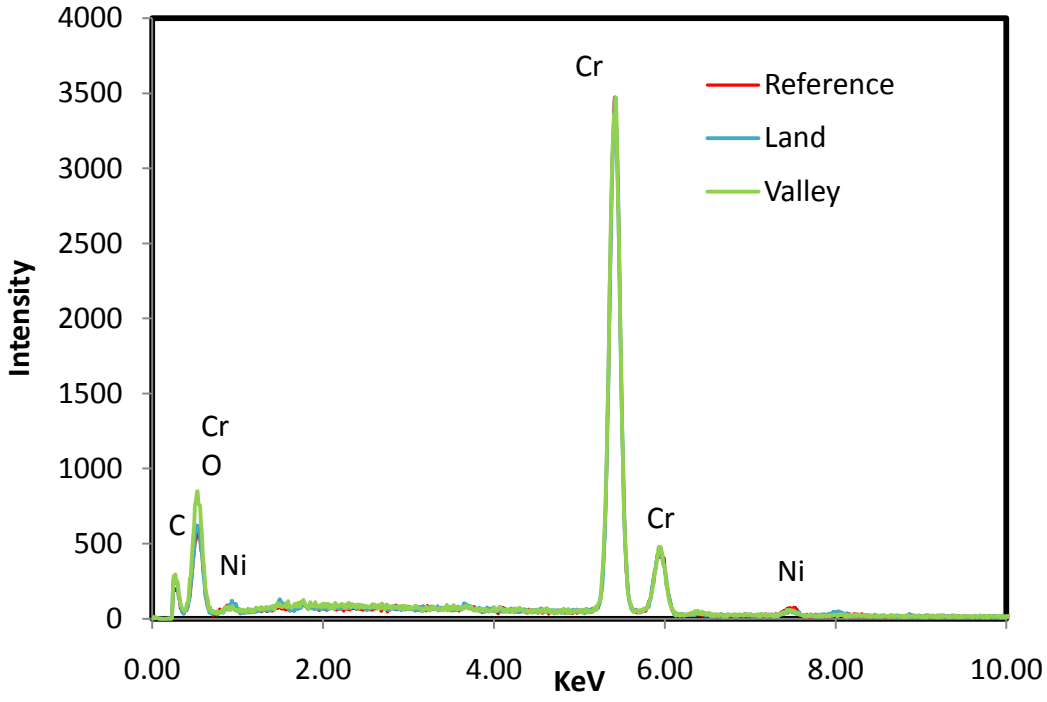

Figure 4.59: EDX spectrum of cathode side of the bipolar plate

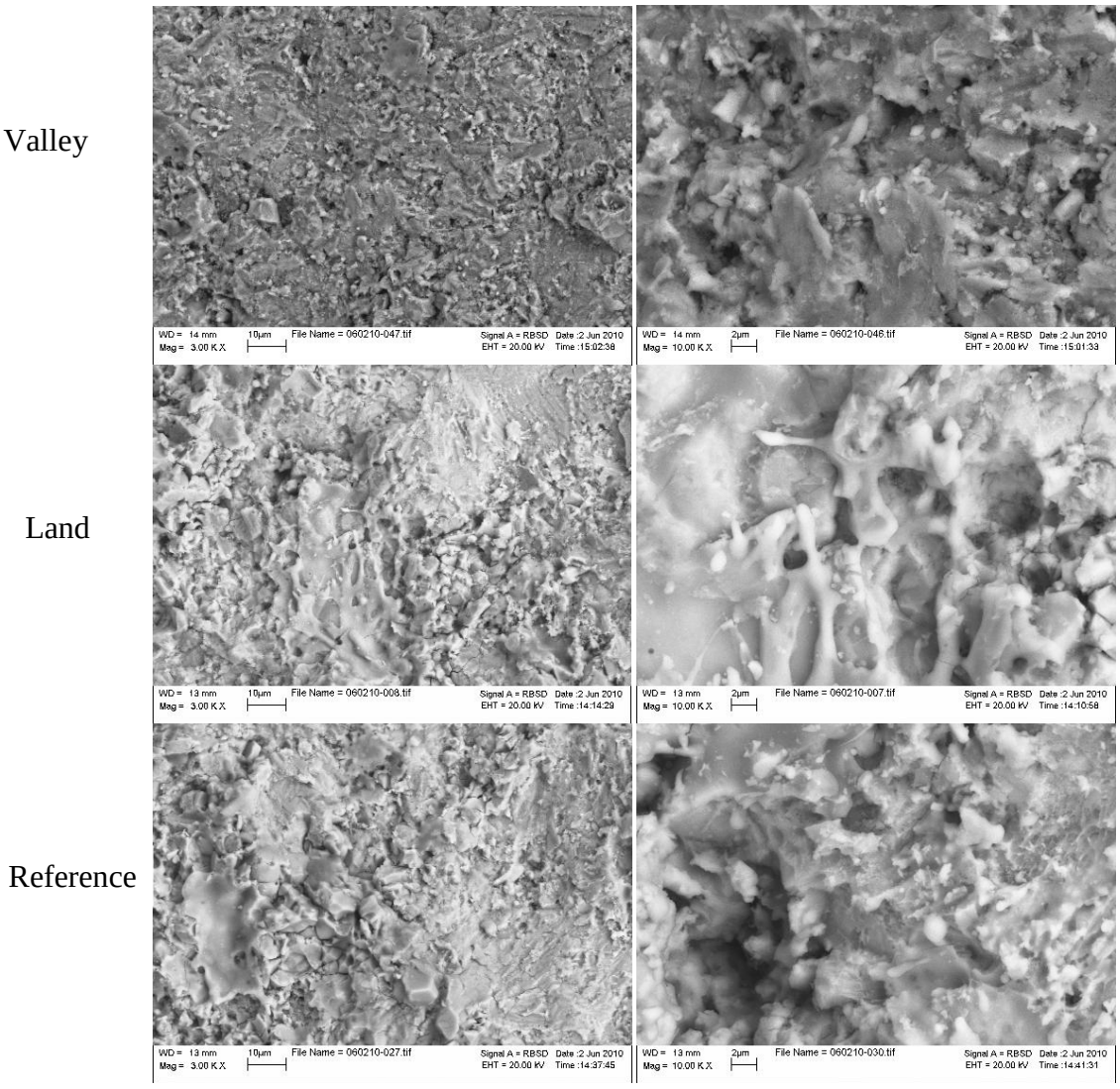

Figure 4.60: Surfaces morphology of the land, valley and reference of the cathode surface at 3kX and 10kX magnifications

Furthermore, a cross section of the reference and active areas of the same bipolar plate was analyzed. The active area of the plate was cut across and polished for SEM/EDX analysis as shown in Figure 4.61. The SEM measurements of the cross section indicated that the thickness of the chromium carbide coating on the top of the rib (land) in the cathode side was approximately 300μm which was the same as the coating thickness of the reference area. This measurement once again proved that the coating material was not changed or affected by the fuel cell electrochemical reaction because the coating did not show any significant amount of material dissolution during the 750 hours of operation as proven by the unchanged coating thickness or surface morphology. Though a few cracks in the coating were observed in some areas close to the substrate (Figure 4.62), these cracks were classified as imperfections of the coating and occurred randomly within the thickness of the coating and along the profile of the cross section of the bipolar plate. The coating imperfection could have been caused by any of the following reasons:

- Non-uniform coating thickness and weak bonding strength due to the complex and intricate geometry of the flow field design
- Temperature differential due to the multi-passes and layer by layer thermal spray process.
- Coefficient of thermal expansion of different materials.
- Coating surfaces such as the walls of valley were not perpendicularly to the spray direction
- The cross section cutting process taking place at high internally stressed zone

Over the whole 20mm long cross section span of the coating, only two 20 μm wide through cracks to the substrate surface were observed, which was equivalent to 0.2% imperfection in the total length. In addition, these through cracks were mainly located on the side walls of the valley where the coating thickness was approximately 150 μm which was 50% thinner than the land area. This was attributed to the intricate flow field geometry causing the non-perpendicular spray direction at the channels. Thus, the SEM images of the bipolar plate's cross section in Figures 4.61 and 4.62 had proved that small amount of aluminum oxides came from the oxidation of aluminum under the chromium carbide coating. Figures 4.63 and 4.64 show the EDX spectra of the cross section of the

reference and active areas on both anode and cathode sides of the bipolar plate. These two EDX spectra were taken ten microns below the outer surface, as shown in Figure 4.65, to examine any possible chemical change within the coating material due to the fuel cell electrochemical reaction. The EDX analysis of the cross section had shown that there was no chemical change in the material ten microns beneath the land and valley surfaces in comparison to the reference (control) area.

In summary, the SEM/EDX analysis of the active area of both the cathode and the anode sides of the bipolar plate shows that the coating material had insignificant chemical change. The aluminum oxides found on the active area was mainly due to the oxidation of the aluminum underneath the coating material caused by the coating imperfection. In addition, small amount of aluminum oxide was also believed to leach from the uncoated area such as inlet, outlet and manifold areas where there were no chromium carbide coating to protect the aluminum and acrylic conformal coating could have been missed during the manually application process.

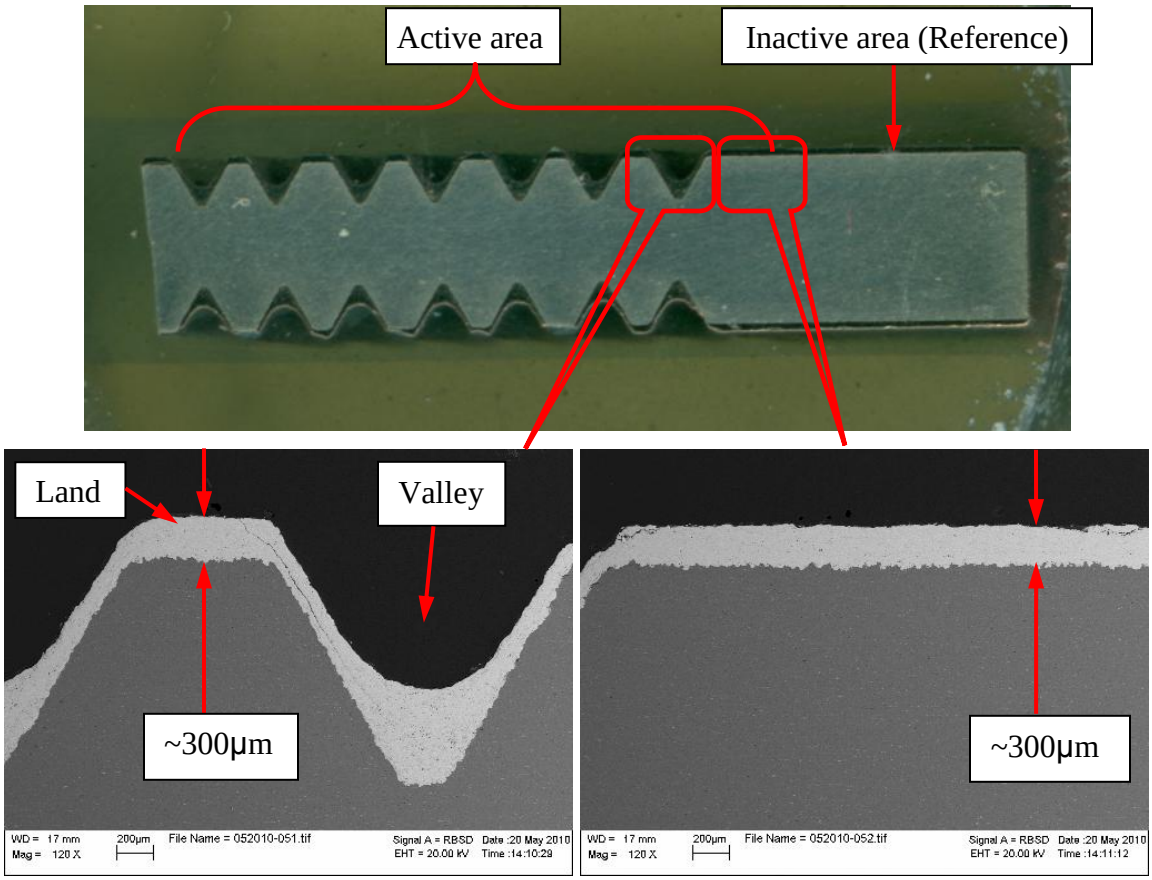

Figure 4.61: Cross section of active area and reference area of bipolar plate

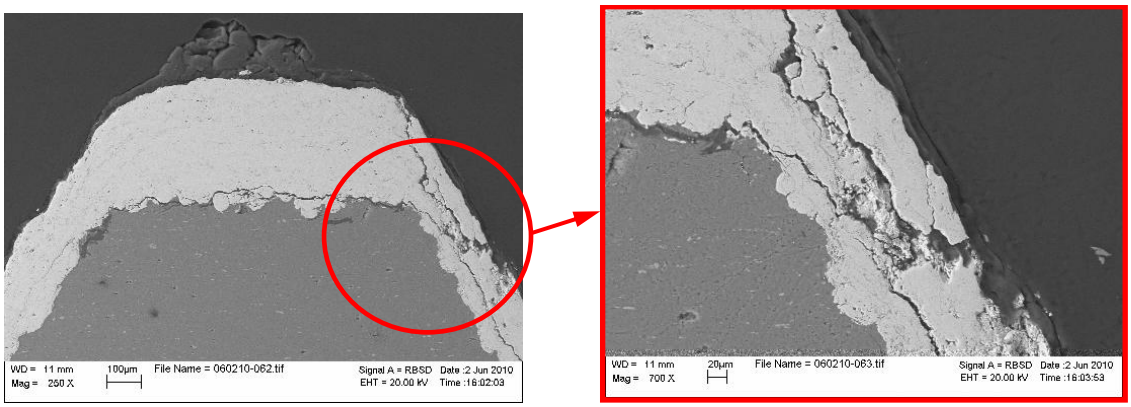

Figure 4.62: Cross section of a rib and coating defect

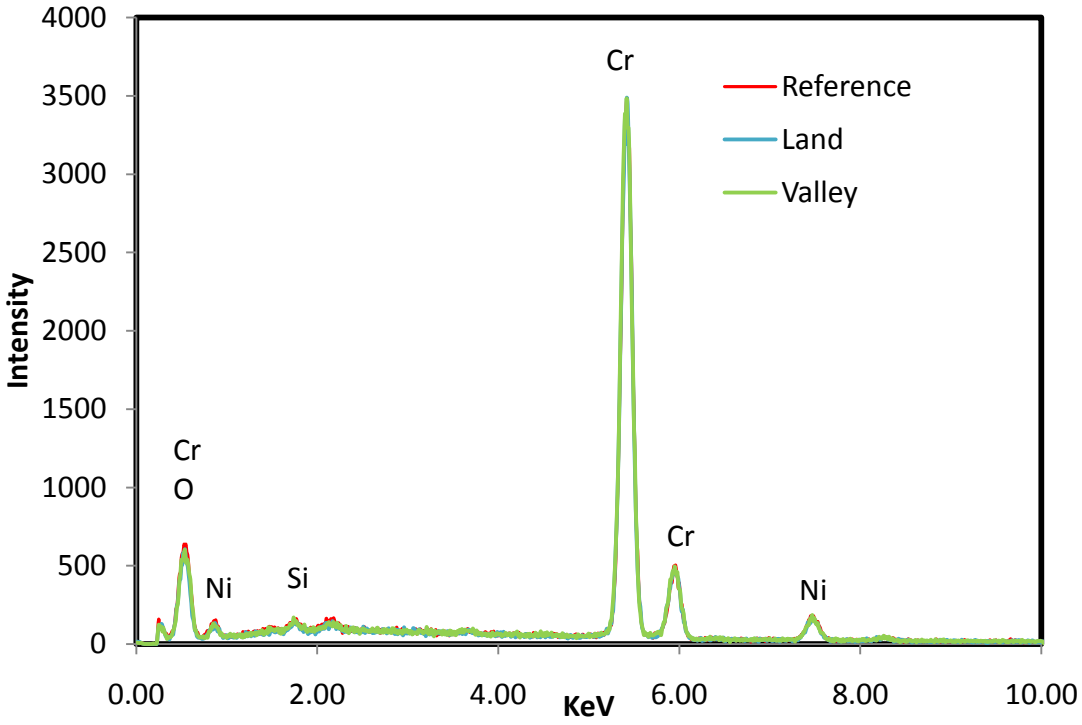

Figure 4.63: EDX spectrum of cross section of the anode side

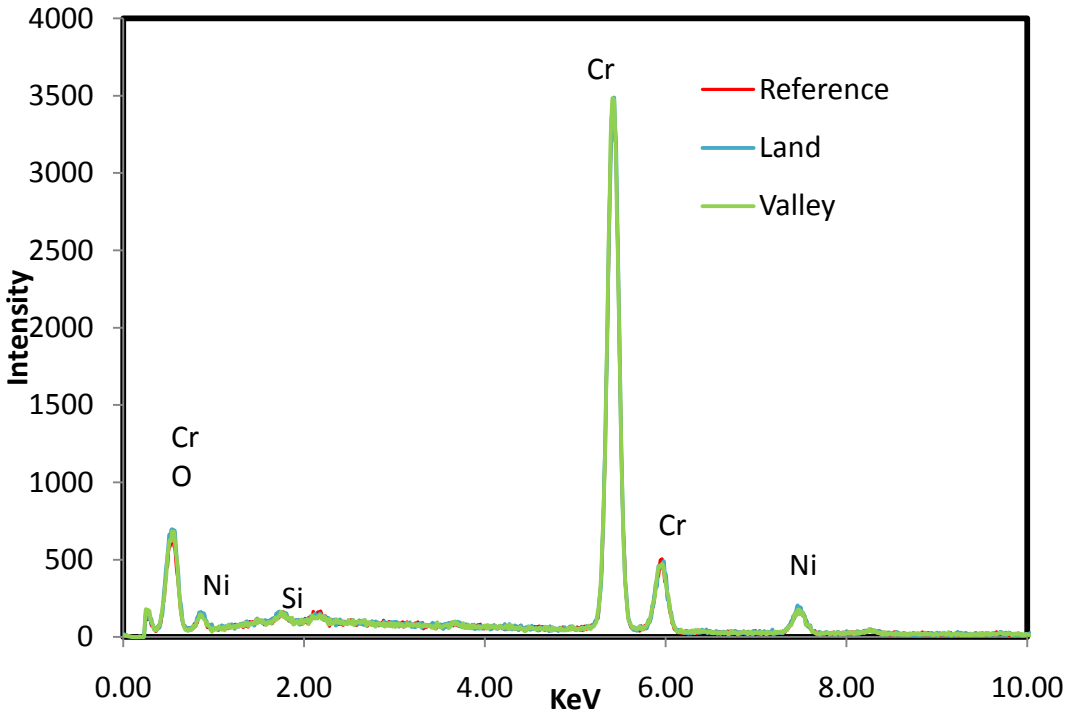

Figure 4.64: EDX spectrum of cross section of the cathode side

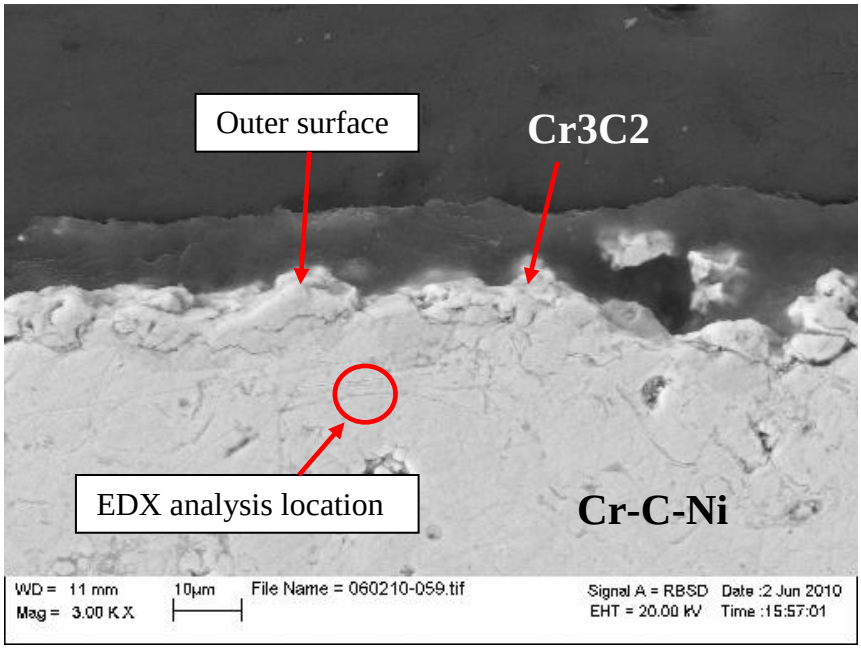

Figure 4.65: Electron beam location for EDX analysis (10µm below outer surface)

4.5.2 Inductively coupled plasma - optical emission spectroscopy (ICP-OES) analysis of the membrane electrode assembly (MEA) and collected water samples

The ICP analysis of the MEA and water samples from the three cell stack were collected during after the 750 hours of operation. Table 4.4 shows the weight of the MEA and water collected throughout the 750 hours of the three cell stack operation. The net weight of the MEA was 2.742g and the total amount of water was collected during two different fuel cell operating conditions. The amount of water collected during the first 250 hours of operation at 37°C and 0.4A/cm^2 without external humidification was approximately 5 liters (5kg) which agreed with the theoretical water weight value [21]. However, the amount of water collected during the additional 500 hours of operation at 80°C and 0.5A/cm^2 with external humidification was 25 liters (25kg) which was almost double the theoretical value. It was due to the combination of water generated during the electrochemical reaction and portion of the external humidification added to the air over the additional 500 hours.

Table 4.4 also shows the weight and percentage of each element occupied in the sample analyzed which were obtained from the ICP analysis. The analysis implied that a small amount of trace metals had leached from the bipolar plate onto the MEA during the 750 hours of operation. Knowing the metal used in MEA was only platinum (Anode: 0.2 mg/cm^2, Cathode: 0.5 mg/cm^2), platinum was opt out in the ICP analysis. As the composition of the bipolar plate's coating material was mainly chromium (>88%) and the double-layer coating material (Cr_3C_2 and Cr-C-Ni) was made of Cr, Ni and C mentioned in section 3.1, the dissolution of the coating material was relatively proportional and higher in chromium than other metals. The ICP analysis showed that chromium detected in the MEA was approximately 10 times more than nickel. It was believed that a small portion of the coating material was likely extracted from the bipolar plate and physically embedded to the MEA within the fuel cell stack due to higher compacting force and strongly adherence during 750 hours of operation. Therefore, chromium was the most noticeable trace metal in the MEA. The ICP analysis also agreed to the XRD analysis discussed in section 4.2.7 which indicated that chromium was found in the MEA after 1000 hours of fuel cell operation.

However, the ICP analysis of the water collected during the 750 hour operation showed almost undetectable trace of metal from the bipolar plates leached into the water because the concentrations of the expected metals in the water sample were 1ppm or less. It was also obvious that iron and copper found in the MEA and water samples were mainly obtained from fuel cell components other than the bipolar plates and MEAs, such as fittings, tubing, humidification system and air supply from the industrial air compressor. These metals did not come from the bipolar plates and/or MEAs because they did not contain iron and copper. In addition, a small amount of aluminum was found in the MEA and it most likely came from the aluminum under the coating due to the imperfection of the coating material as mentioned in the previous section.

In summary, the experiment of durability test and characterization study of a three-cell metallic fuel cell stack indicated the following:

- The three-cell metallic stack successfully operated for 750 hours at two different operating temperatures (37°C and 80°C), with the exception of two MEA physical

failures due to thermal and humidity cycling causing frequent expansion and contraction of the membrane.

- SEM and EDX analysis showed that the surface morphology, thickness and chemistry of the double-layer coating (Cr_3C_2 and Cr-C-Ni) remained unchanged after 750 hours of fuel cell operation and unaffected by the acidic environment inside the cell.
- The cross-section analysis shows that the coating may experience imperfection due to the complex and intricate flow-field geometry of the aluminum substrate.
- SEM and EDX analysis also showed a small amount of aluminum oxide sporadically found on the active area of the bipolar plate and ICP analysis indicated that 31ppm of Al was found in the MEA. It was attributed to localized coating imperfection and lack of protection in the uncoated area such as internal manifolds where manual application of sealant could have been missed.
- Traces of metal leached from the bipolar plate's coating onto the MEA were Al (31ppm), Cr (0.1%) and Ni (89ppm) that were likely extracted from the bipolar plate to the MEA within the fuel cell stack due to the high compacting force between the MEA and the bipolar plate.
- Fe (50ppm) and Cu (42ppm) found in the MEA samples were mainly obtained from components other than bipolar plates and from the industrial air compressor and pipelines that supplied air to the fuel cell.
- Negligible trace of metals (1ppm or less) from bipolar plates leached into the byproduct water of electrochemical reaction exited the fuel cell.

Table 4.5 shows the summary of bipolar plate requirements and comparison between DOE bipolar plate research target, current research status from other research institutes and the finding in this thesis. It is noted that more improvement of the coating material and bipolar plate design has to be done in the future to achieve lower ICR, lower corrosion current and lower cost. The suggested improvements are discussed in the section of future work.

Table 4.4: ICP analysis of MEA and water samples

	Al	Cr	Cu	Fe	Ni	Pt
MEA	31ppm	1000ppm (0.1%)	42ppm	50ppm	89ppm	N/A
Total weight (2.742g)	85μm	2.742mg	115μm	130μm	244μm	N/A
Water	<1ppm	<1ppm	<1ppm	1ppm	1ppm	<1ppm
Total weight (30kg)	-	-	-	30mg	30mg	-

Table 4.5: Bipolar plate requirement and summary of research status

	DOE2010 Target	Other current research status	Current research achievement
Interfacial contact resistance (milliohm.cm2)	10	10-15 (Brady et al.)	14
Corrosion current (Micro A/cm2)	1	1 (Brady et al.)	8 (SS316 substrate) 28 (Al substrate)
Durability (Hours)	>5000	>1000 hours (Brady et al.) 3500 hours (Treadstone Tech Inc.)	1000 hours
Cost/kW	$10	< $5 (Treadstone Tech Inc.)	$50.28

CHAPTER 5

Conclusions

5.1 Material evaluations and single cell testing

Phase I of this study showed that the chromium carbide corrosion-resistant coating, applied by the high velocity oxygen fuel (HVOF) thermal spray technique to the metallic bipolar plate as a substrate, demonstrated its potential for PEM fuel cell technology. The interfacial contact resistance (ICR) testing indicated that the Cr_3C_2-25NiCr coating with SS316 substrate had one of the lowest ICR values among the metallic candidate materials, including the graphite composite, the current industrial standard. The accelerated corrosion testing showed that using an aggressive acidic solution, such as 0.5M H_2SO_4 +200 ppm HF, caused etching of passive films and resulted in an impractical ICR value for fuel cell application. The pH3+0.1 ppm HF solution was used to simulate the acidic environment inside a fuel cell to obtain proper material behavior. The corrosion test with a pH3+0.1 ppm HF solution demonstrated that agglomerated Cr_3C_2-25%NiCr and activated Cr-C-Ni alloy feedstock powder produced a relatively dense coating in comparison to pure Cr_3C_2 and blended Cr_3C_2-7%NiCr feedstock powder. In addition, reducing Ni and increasing the Cr ratio in the coating enhanced the corrosion resistance of the coating. As a result, SS316 substrate with a pure Cr_3C_2 coating was found to have the lowest corrosion current among other coatings. Moreover, it was necessary for aluminum plates to use an intermediate layer of a dense Cr-C-Ni coating that contained only 4% of Ni to blanket and prevent corrosion on the aluminum substrate before applying the Cr_3C_2 coating. The results indicated that the low ICR of the coating was due to the stable Cr_3C_2 coating and the higher surface roughness caused by the thermal spray process.

Though the corrosion testing of the Cr_3C_2-25NiCr coating also showed that the corrosion current was higher than the DOE recommended value, single cells made of chromium carbide (Cr_3C_2-25NiCr) coated aluminum bipolar plates successfully performed for 1000 hrs at 70°C with minimal power degradation due to corrosion. This indicated the lack of development of a poor electrical conductor (passive layer) or the generation of any harmful substances that could have fouled the catalyst or poisoned the

electrolyte, which could reduce its ionic conductivity. Moreover, minimal power output degradation was an indication of the chemical stability of the chromium carbide coating under a corrosive environment inside the PEM fuel cell caused by its operating conditions such as high humidity, heat, and the acidic electrolyte.

The lifetime testing and SEM/EDX characterization indicated the existence of aluminum oxide (Al_2O_3) on the active area of the coated aluminum bipolar plates after one thousand hours of operation. The aluminum detected on the coating was believed to be coming from two different sources: 1). It was brought to the surface of the corrosion-resistant coating from the aluminum substrate through possible coating cracks or porosity and 2). It was mobilized by the reactant gases passing through the bare and uncoated back plates and the gas inlets because they were not covered by a sealant or any other type of corrosion protection coating. Excessive Al_2O_3 in the active flow field area can negatively affect the catalyst and the electrolyte and considerably degrade the cell's power output. Therefore, a corrosion-resistant coating material (either polymer or metal based) is recommended to be applied to the bipolar plates for blanketing the inside surface of the inlet and the outlet manifolds, where the Cr_3C_2-25NiCr coating cannot reach the internal area during spraying. The EDX analysis also showed possible chemistry changes of the coating surface due to dissociation of Ni from the NiCr binding material during the fuel cell operation.

Two improvements in the single cell performance were recognized as a result of the laboratory single cell testing. The new integrated terminal design in single cells showed an average of 18% savings in hydrogen consumption in comparison to the commonly used end plate terminal design. However, only metallic bipolar plates can benefit from the use of integrated terminal design due to their ductility, lack of brittleness and suitability for threading and anchoring the metal terminals directly to the plates forming a highly conductive terminal assembly. The graphite composite bipolar plates, on the other hand, are brittle. This can cause possible cracking and/or mechanical failure under the tightening force when the terminals are directly mounted to the bipolar plates. Thus, the graphite power stack fastening force should not exceed 140 N/m^2. Meanwhile, metallic stacks can achieve a much higher fastening force that considerably reduces the contact resistance between the plates and causes a sizable increase in the power output of the

stack. Accordingly, metallic plates are deemed safer, more robust and more reliable than the graphite composite plates. In addition, the results showed that a new humidity conservative flow field design, which was developed in the course of this work, demonstrated an average of 8% savings in hydrogen consumption compared to a standard PEM fuel cell triple serpentine design.

5.2 Fuel cell stack design and optimization of the fuel cell stack performance

During phase II of the study, the results of thermal and water management experimental work provided an understanding necessary for designing a PEM fuel cell power stack. Results of this study showed that when the 10 cell stack with graphite composite bipolar plates operated at a current density of 75mA/cm^2, the cells generated more heat than they could dissipate by natural convective and/or conductive heat transfer mechanisms. Therefore, both internal and external cooling systems were deemed necessary for the fuel cell stack to operate at higher power density while maintaining the stack temperature at an acceptable level of 80°C. Moreover, when the cell temperature reached 37°C or higher, the humidification of reactant gases was needed to enhance ion transport and prevent the loss of power caused by membrane dehydration.

The finite element analysis (FEA) model of a 50cm^2 active area bipolar plate showed that the aluminum cooling fin design was more favorable and effective in removing excess heat generated by the electrochemical reaction of the fuel cell due to its higher thermal conductivity in comparison to graphite composite plate. In addition, steady-state heat transfer analysis in a forced air design condition indicated that the temperature of a 50cm^2 active area graphite composite plate with a cooling fin feature was over 80°C. Therefore, an additional cooling system was needed if graphite composite bipolar plates were used in a forced air fuel cell stack. One the other hand, a forced convection fuel cell has an advantage of lower heat generation and lower temperature operation as well as a lower overall percentage of parasitic power. However, this design has low power density and therefore, requires more number of cells to achieve a certain required power, hence it is higher in capital cost and larger in size than the forced air system design. The current study shows almost no cost savings over a five-year period between the forced convection system and the forced air system. Therefore, the choice of using different air

supply systems depends on the application. The forced air fuel cell design is preferred in the automobile industry because the size and weight are critical issues. The forced convection fuel cell design can be used in residential power units, as size is not a critical issue in this application.

The above conclusions and findings directly contributed to the design and fabrication of a three-cell stack, based on the coated aluminum bipolar plates with the new double-layer coating, the integrated terminal design, the humidity conservative flow field design, the cooling fin design, and the forced air stack design. The stack successfully operated for 750 hours at two different operating temperatures (37°C and 80°C), with the exception of two MEA failures that were replaced to complete the lifetime testing. The membrane failures resulted primarily from the frequent expansion and contraction of the membrane caused by the thermal and humidity cyclic loading applied to the membrane while its dimensions were constrained.

The surface characterization of the bipolar plate showed that small amounts of aluminum oxide were found on the active area due to the imperfection in the coating, possibly caused by the intricate flow-field geometry, the internal stresses of the coating, and the coefficient of thermal expansion of different materials. However, the coating of the cathode and the anode active areas did not show any significant change in material chemistry, coating thickness, and surface morphology. Finally, the ICP analysis showed that a small amount of Cr, Ni, Al, Fe and Cu were found on the MEA. In which, Cr and Ni were believed to be coming from a small portion of the coating material that was likely extracted from the bipolar plate and physically embedded to the MEA because of a higher compacting force within the fuel cell stack during 750 hours of operation. On the other hand, Fe and Cu must have come from the external components other than the bipolar plates and MEAs. Moreover, the ICP analysis of the water sample collected during the 750 hour operation showed an almost undetectable trace of metal from the bipolar plates leached into the water.

In summary, the use of metallic bipolar plates to replace the commercial graphite composite plates demonstrated promising results. It improved the power output by using an integrated terminal design and reduced the capital cost by eliminating the need of terminal end plates. In addition, metallic bipolar plates are favorable for mass production

because of the lower manufacturing cost and the great manufacturability of metal. More importantly, metallic bipolar plates held their integrity for over 750 hours of lifetime testing.

5.3 Future work

The work presented in this thesis addresses some of the issues that could aid in making fuel cells a commercial reality. However, several tasks, listed below, are recommended for future work.

1. Evaluate SS316 single cell coated with pure Cr_3C_2 coating material

   The current research focused on coated aluminum bipolar plates. Single fuel cells made of coated SS316 bipolar plates need to be examined since a lower corrosion current in accelerated corrosion testing can be obtained by using coated SS316 substrate with pure Cr_3C_2 coating while maintaining low ICR. A longer lifetime performance will be expected and no additional electrochemically stable coating is needed on the internal manifold surface unlike the coated aluminum bipolar plate due to the stable chromium oxide formed naturally on the uncoated SS316 surfaces.

   In addition, although higher clamping pressure can enhance the ICR and resulting in higher cell performance, durability of the MEA can be an issue. Therefore optimizing the clamping pressure of metallic cells and different types of GDL can enhance the power density and durability of fuel cells. High frequency resistance measurement is recommended to be investigated as a part of the single cell testing setup.

2. Investigate suitable and cost effective manufacturing process for SS316 bipolar plate

   Though better performance can be expected of the coated SS316 single cell compared to that of a coated aluminum single cell, due to promising results obtained from the corrosion and ICR samples testing, more research on the coating improvement, the design and the manufacturing process of the coated SS316 bipolar plate is still needed to achieve low ICR (10 $m\Omega\ cm^2$), low corrosion current ($1\mu m/cm^2$) and low cost ($10/kW). Thinner bipolar plate is preferred and SS316 sheet

metal stock is ideal for bipolar plate fabrication and for low-cost mass production stamping process. However, Cr_3C_2 coating produced by thermal spray technology can cause deformation on the bipolar plate if the heat differential between the two sides of the plate is not lowered during the thermal spray process. New thermal spray application method and/or other new coating process need to be developed to reduce the high temperature differential on the bipolar plate while maintaining high bonding strength between the coating material and the bipolar plate. In addition, the basic bipolar plate features such as internal manifold, flow field pattern, cooling fin and integrated terminal designs must be modified to suit the low-cost mass production stamping process.

3. Design suitable balance of plant for 1kW fuel cell stack

   Thermal and water management is crucial in running fuel cell stacks at high temperature (80°C). As it was encountered during the present research work, fuel cell performance was very sensitive to the cell temperature and reactant gas humidity when operated at 80°C. The present work used a manually controlled humidification system which only allowed the fuel cell to operate efficiently at certain current density. In order for the fuel cell stacks to operate at various levels of power output while maintaining appropriate thermal and water management, automatic reactant gas humidification system and fuel cell temperature control system are needed to be developed. Therefore, the balance of plant is one of the important research fields in fuel cell technology.

4. Design, fabrication and performance evaluation of a 1kW fuel cell stack fitted with SS316 bipolar plates

   By combining all three above mentioned tasks, a 1kW fuel cell stack could be designed and fabricated. The stack performance should be evaluated through measurement of voltage, current, power, air/hydrogen consumption, efficiency and temperature.

References

[1] Energy Information Administration. (2009, May) International Energy Outlook 2009. [Online]. http://www.eia.doe.gov/oiaf/ieo/index.html

[2] Stacy C. Davis, Susan W. Diegel, Robert G. Boundy, *Transportation Energy Data Book*, 28th ed.: U.S. Department of Energy, Oak Ridge National Laboratory, 2009.

[3] Fuel Cells 2000. [Online]. www.fuelcells.org/basics/how.html

[4] Frano Barbir, *PEM Fuel Cells*., 2005, pp. 1-72.

[5] James Larmine, Andrew Dicks, *Fuel Cell Systems Explained*., 2000, pp. 1-36.

[6] S. Giddey, F.T. Ciacchi, S.P.S. Badwal, "Design, assembly and operation of polymer electrolyte membrane fuel cell stacks to 1 kWe capacity," *J. Power Sources*, vol. 125, pp. 155-165, 2004.

[7] Xianguo Li, Imran Sabir, "Review of bipolar plates in PEM fuel cells: Flow-field designs," *J. Power Sources*, vol. 30, pp. 359-371, 2005.

[8] James Larmine, Andrew Dicks, Fuel Cell Systems Explained., 2000, pp. 61-108.

[9] James Larmine, Andrew Dicks, Fuel Cell Systems Explained., 2000, pp. 109-122.

[10] U.S. Department of Energy. [Online]. http://www1.eere.energy.gov/hydrogenandfuelcells/fuelcells/fc_types.html

[11] Amir Faghri, Zhen Guo, "Challenges and opportunities of thermal management issues related to fuel cell technology and modeling," Int. J. Heat and Mass transfer, vol. 48, pp. 3891-3920, 2005.

[12] U.S. Department of Energy. [Online]. www1.eere.energy.gov/hydrogenandfuelcells/fuelcells/fc_challenges.html

[13] F. Barbir. Technical Challenges in PEM Fuel Cell Development. [Online]. http://www.powerpulse.net

[14] Haruki Tsuchiya, Osamu Kobayashi, "Mass production cost of PEM fuel cell by learning curve," Int. J. Hydrogen Energy, vol. 29, pp. 985-990, 2004.

[15] Isa Bar-On, Randy Kirchain, Richard Roth, "Technical cost analysis for PEM fuel cells," *J. Power Sources*, vol. 109, pp. 71-75, 2002.

[16] A. Heinzel, F. Mahlendorf, O. Niemzig, and C. Kreuz, "Injection moulded low cost bipolar plates for PEM fuel cells," *J. Power Sources*, vol. 131, pp. 35-40, 2004.

[17] D.P. Davies, P.L. Adcock, M. Turpin and S.J. Rowen, "Bipolar plate materials for solid polymer fuel cells," *J. Applied Electrochemistry*, vol. 30, pp. 101-105, 2000.

[18] J. Scholta, B. Rohland, V. Trapp and U. Focken, "Investigations on novel low-cost graphite composite bipolar plates," *J. Power Sources*, vol. 84, pp. 231-234, 1999.

[19] Zhigang Qi, Chunzhi He and Arthur Kaufman, "Effect of CO in the anode fuel on the performance of PEM fuel cell cathode," *J. Power Sources*, vol. 111, pp. 239-247, 2002.

[20] J.Y. Tilquin, R. Cote, D. Guay, J.P. Dodelet and G.Denes, "Carbon monoxide poisoning of platinum-graphite catalysts for polymer electrolyte fuel cells: comparison between platinum –supported on graphite and intercalated in graphite," *J. Power Sources*, vol. 61, pp. 193-200, 1996.

[21] Frano Barbir, *PEM Fuel Cells*., 2005, pp. 73-108.

[22] R. Eckl, W. Zehtner, C. Leu, U. Wagner, "Experimental analysis of water management in a self-humidifying polymer electrolyte fuel cell stack," *J. Power Sources*, vol. 138, pp. 137-144, 2004.

[23] [Online]. www.ewh.ieee.org/reg/7/millennium/ballard/ballard_info.html

[24] Richard Blunk, Mahmoud Hassan Abd Elhamid, Daniel Lisi, Youssef Mikhail, "Polymeric composite bipolar plates for vehicle applications," *J. Power Sources*, vol. 156 , pp. 151–157, 2006.

[25] Viral Mehta, Joyce Smith Cooper, "Review and analysis of PEM fuel cell design and manufacturing," *J. Power Sources*, vol. 114, pp. 32-53, 2003.

[26] Borup RL, Vanderborgh NE, "Design and testing criteria for bipolar plate material for PEM fuel cell application," *Mater Res SocSymp Proc 393* , pp. 151-155, 1995.

[27] Allen Hermann, Tapas Chaudhuri, Priscila Spagnol, "Bipolar plates for PEM fuel cells : A review," *Int. J. Hydrogen Energy*, vol. 30, pp. 1297-1302, 2005.

[28] Zhixiang Liu, Zongqiang Mao, Bing Wu, Lisheng Wang, Volkmar M. Schmidt, "Current density distribution in PEFC," *J. Power Sources*, vol. 141, pp. 205-210, 2004.

[29] Jeffrey Glandt, Sirivatch Shimpalee, Woo-kum Lee, John W. Van Zee, "Modeling the effect of flow field design on PEM fuel cell performance," in *2002 Spring National Meeting*, New Orleans, LA, March 2002.

[30] Srinivas C. Kosaraju, Juan C. Ordonez, "A numerical study of the effect of multiple flow channels with parallel and counterflow configurations on thermal and flow properties of PEM fuel cells," in *ASME The fifth International Conference on Fuel Cell Science, Engineering & Technology Conference*, 2007.

[31] Philip L. Hentall, J. Barry Lakeman, Gary O. Mepsted, Paul L. Adcock, Jon M. Moore, "New materials for polymer electrolyte membrane fuel cell current collectors," *J. Power Sources* , vol. 80, pp. 235-241, 1999.

[32] J. Wind, R. Spah, W. Kaiser, G. Bohm, "Metallic bipolar plates for PEM fuel cells," *J. Power Sources*, vol. 105, pp. 256-260, 2002.

[33] Heli Wang, Mary Ann Sweikart, John A. Turner, "Stainless steel as bipolar plate material for polymer electrolyte membrane fuel cells," *J. Power Sources*, vol. 115, pp. 243-251, 2003.

[34] Heli Wang, John A. Turner, "Ferritic stainless steels as bipolar plate material for polymer electrolyte membrane fuel cells," *J. Power Sources*, vol. 128, pp. 193-200, 2004.

[35] A.S. Woodman, E.B. Anderson, K.D. Jayne, and M.C. Kimble, "Development of Corrosion-Resistant Coatings for Fuel Cell Bipolar Plates," in *American Electroplaters and Surface Finishers Society 1999, AESF SUR/FIN '99 Proceedings*, June 1999.

[36] Michael C. Kimble, Alan S. Woodman, and Everett B. Anderson, "Characterization of Corrosion-Protective Methods for Electrically conductive coatings on Aluminum," in *American Electroplaters and Surface Finishers Society 1999, AESF SUR/FIN '99 Proceedings*, June 1999.

[37] H. Wang, M.P. Brady, G. Teeter, J.A. Turner, "Thermally nitrided stainless steels for polymer electrolyte membrane fuel cell bipolar plates Part 1: Model Ni–50Cr and austenitic 349TM alloys ," *J. Power Sources* , vol. 138, pp. 86–93, 2004.

[38] H. Wang, M.P. Brady, K.L. More, H.M. Meyer III, John A. Turner, "Thermally nitrided stainless steels for polymer electrolyte membrane fuel cell bipolar plates Part 2: Beneficial modification of passive layer on AISI446," *J. Power Sources*, vol. 138, pp. 79–85, 2004.

[39] M.P. Brady, K. Weisbrod, I. Paulauskas, R.A. Buchanan, K.L. More, H. Wang, M. Wilson, F. Garzon, L.R. Walker, "Preferential thermal nitridation to form pin-hole free Cr-nitrides to protect proton exchange membrane fuel cell metallic bipolar plates," *Scripta Materialia*, vol. 50, pp. 1017-1022, 2004.

[40] Shine Joseph, J.C. McClure, R. Chianelli, P. Pich, P.J. Sebastian, "Conducting polymer-coated stainless steel bipolar plates for proton exchange membrane fuel cells (PEMFC)," *Int. J. Hydrogen Energy*, vol. 30, pp. 1337-1344, 2005.

[41] Shuo-Jen Lee, Ching-Han Huang, Yu-Pang Chen, "Investigation of PVD coating on corrosion resistance of metallic bipolar plates in PEM fuel cell," *J. Materials Processing Technology*, vol. 140, pp. 688–693, 2003.

[42] I. Zafar, J. Guiheen, N. Dave, R. Timothy, World Patent WO00,128,019, April 19, 2001.

[43] T. Matsumoto, J. Niikura, H. Ohara, M. Uchida, H. Gyoten, K. Hatoh, E. Yasumoto, T. Kanbara, K. Nishida, Y. Sugawara, Europeon Patent EP1094535, April 25, 2001.

[44] Y. Li, W. Meng, S. Swathirajan, S. Harris, G. Doll, US patent 5,624,769, April 20, 1997.

[45] E.A. Cho, U.-S. Jeon, S.-A. Hong, I.-H. Oh, S.-G. Kang, "Performance of a 1kW-class PEMFC stack using TiN-coated 316 stainless steel bipolar plates," *J. Power Sources*, vol. 142, pp. 177-183, 2005.

[46] Moucheng Li, Suzhen Luo, Chaoliu Zeng, Jianian Shen, Haichao Lin, Chu'nan Cao, "Corrosion behavior of TiN coated type 316 stainless steel in simulated PEMFC environments," *Corrosion Science*, vol. 46, pp. 1369-1380, 2004.

[47] M.P. Brady, P.F. Tortorelli, K.L. More, H.M. Meyer III, Larry R. Walker,H. Wang, J.A. Turner, B. Yang and R.A. Buchanan, "Cost-Effective Surface Modification for Metallic Bipolar Plates," FY 2004 Progress Report 2004.

[48] K. Natesan, R. N. Johnson, "Corrosion resistance of chromium carbide coatings in oxygen-sulfur environments," *Surface and Coatings Technology*, vol. 33, pp. 341-351, 1987.

[49] J. Jayaraj, Y.C. Kim, K.B. Kim, H.K. Seok, E. Fleury, "Corrosion studies on Fe-based amorphous alloys in simulated PEM fuel cell environment," *Science and Technology of Advanced Materials* , vol. 6, pp. 282-289, 2005.

[50] Atul Kumara, Ramana G. Reddy, "Materials and design development for bipolar/end plates in fuel cells," *J. Power Sources*, vol. 129, pp. 62–67, 2004.

[51] Atul Kumara, Ramana G. Reddy, "PEM fuel cell bipolar plate material selection, design and integration," in *TMS*, Seatlle, WA, Feb 17-21, 2002, pp. 41-53.

[52] Mahlon S. Wilson, Christine Zawodzinski, Steffen Moller-Holst, Deanna N. Busick, Francisco A. Uribe and Thomas A. Zawodzinski, "PEMFC STACKS FOR POWER GENERATION," Proceedings of the 1999 U.S DOE Hydrogen Program Review.

[53] John A. Turner, Hei Wang, Michael P. Brady, "Corrosion Protection of Metallic Bipolar Plates for Fuel Cells," National Renewable Energy Laboratory, DOE Hydrogen Program Review 2005.

[54] Glyn M Griffths, Emma E Farndon, David R Hodgson, Ian M Long, "PEMcoat: A range of active coatings for metal bipolar plates," in *The Knowledge Foundation's 3rd Annual International Symposium*, Washington, D.C., April 22-24, 2001.

[55] D.P. Davies, P.L. Adcock, M. Turpin, S.J. Rowen, "Stainless steel as a bipolar plate material for solid polymer fuel cells," *J. Power Sources*, vol. 86, pp. 237–242, 2000.

[56] Shuo-Jen Lee , Jian-Jang Lai, Ching-Han Huang, "Stainless steel bipolar plates," *J. Power Sources* , vol. 145, pp. 362–368, 2005.

[57] Toyoaki Matsuura, Megumi Kato, Michio Hori, "Study on metallic bipolar plate for proton exchange membrane fuel cell," *J. Power Sources*, vol. 161, pp. 74–78, 2006.

[58] Dongming Zhang, Liangtao Duan, Lu Guo, Wei-Hsing Tuan, "Corrosion behavior of TiN-coated stainless steel as bipolar plate for proton exchange membrane fuel cell," *Int. J. Hydrogen Energy*, vol. 35, pp. 3721-3726, 2010.

[59] M.P. Brady, H.Wang, B.Yang, J.A. Turner, M. Bordignon, R. Molins, M. Abd Elhamid, L. Lipp, L.R.Walker, "Growth of Cr-Nitrides on commercial Ni–Cr and Fe–Cr base alloys to protect PEMFC bipolar plates," *Int. J. Hydrogen Energy*, vol. 32, pp. 3778–3788, 2007.

[60] Yu Fu, Guoqiang Lin, Ming Hou, Bo Wu, Hongkai Li, Lixing Hao, Zhigang Shao, Baolian Yi , "Optimized Cr-nitride film on 316L stainless steel as proton exchange membrane fuel cell bipolar plate," *Int. J. Hydrogen energy*, vol. 34, pp. 453–458, 2009.

[61] M.P. Brady, K.L. More, P.F. Tortorelli, L.R. Walke, K. Weisbrod, M. Wilson, F. Garzon, H. Wang, I. Paulauskas and R.A. Buchanan, "Cost-Effective Surface Modification for Metallic Bipolar Plates," FY 2003 Progress Report 2003.

[62] Shuo-Jen Lee, Ching-Han Huang, Jian-Jang Lai, Yu-Pang Chen, , "Corrosion-resistant component for PEM fuel cells," *J. Power Sources* , vol. 131, pp. 162–168, 2004.

[63] Ching-Yuan Bai, Ming-Der Ger, Min-Sheng Wu, "Corrosion behaviors and contact resistances of the low-carbon steel bipolar plate with a chromized coating containing carbides and nitrides," *Int. J. Hydrogen Energy* , vol. 34, pp. 6778-6789, 2009.

[64] M.C. Li, C.L. Zeng, S.Z. Luo, J.N. Shen, H.C. Lin, C.N. Cao , "Electrochemical corrosion characteristics of type 316 stainless steel in simulated anode environment for PEMFC," *Electrochimica Acta*, vol. 48, pp. 1735-1741, 2003.

[65] D.R. Hodgson, B. May, P.L. Adcock. D.P. Davies, "New lightweight bipolar plate system for polymer electrolyte membrane fuel cells," *J. Power Sources* , vol. 96, pp. 233-235, 2001.

[66] J. Jayaraj, Y.C. Kim, H.K. Seok, K.B. Kim, E. Fleury, "Development of metallic glasses for bipolar plate application," *Materials Science and Engineering A*, vol. 449–451, pp. 30–33, 2007.

[67] Y.J. Ren, C.L. Zeng, "Corrosion protection of 304 stainless steel bipolar plates using TiC films produced by high-energy micro-arc alloying process," *J. Power Sources*, vol. 171, pp. 778–782, 2007.

[68] Akira Taniguchi, Kazuaki Yasuda, "Highly water-proof coating of gas flow channels by plasma polymerization for PEM fuel cells," *J. Power Sources*, vol. 141, pp. 8–12, 2005.

[69] S. K. Chen, H. C. Lin, and C. Y. Chung, , "Corrosion resistance study of stainless-steel bipolar plates with NiAl coatings," Feng Chia University and National Science Council of Republic of China under the Grant Numbers FCU-93GB27 and NSC 93-2218-E-35-006,.

[70] J. S. Kim, W. H. A. Peelen, K. Hemmes, R. C. Makkus , "Effect of alloying elements on the contact resistance and the passivation behaviour of stainless steels," *Corrosion Science*, vol. 44, pp. 635-655, 2002.

[71] Scott Ehrenberg, Dirk Baars, Joe Kelly, Ian Kaye, "One piece bi-polar plate with cold plate cooling," Dais Analytic Corporation, Rogers Corporation, 2002.

[72] Sergei Gamburzev, A. John Appleby, "Recent progress in performance improvement of the proton exchange membrane fuel cell (PEMFC)," *J. Power Sources*, vol. 102, pp. 5–12, 2002.

[73] R. Hornung and G. Kappelt, "Bipolar plate materials development using Fe-based alloys for solid polymer fuel cells," *J. Power Sources*, vol. 72, pp. 20-21, 1998.

[74] C.E. Reid, W. R. Mérida, G. McLean, "Results and analysis of a PEMFC Stack using metallic bi-polar plates," in *Proceedings of 1998 Fuel Cell Seminar*, Palm Spring, 1998.

[75] A. M. Lafront, E. Ghali, A.T. Morales, , "Corrosion behavior of two bipolar plate materials in simulated PEMFC environment by electrochemical noise technique," *Electrochimica Acta 52*, vol. 52, pp. 5076-5085, 2007.

[76] Y. Hung, "Design and Fabrication of Metal Bipolar Plates Used in Proton Exchange Membrane (PEM) Fuel Cells," Stony Brook University, MS. Thesis December 2001.

[77] Renato A. Antunes, Mara Cristina L. Oliveira, Gerhard Ett, Volkmar Ett, "Corrosion of metal bipolar plates for PEM fuel cells: A review," *Int. J. Hydrogen Energy* , vol. 35, pp. 3632-3647, 2010.

[78] US Fuel Cell Council, Single Cell Test Protocol. [Online]. www.usfcc.com

[79] Frigus Primore. [Online]. www.frigprim.com/online/parallel_plates_coeff.html

[80] Lindon C. Thomas, Heat Transfer, 2nd ed., 2000, pp. 461-562.

[81] Frank P. Incropera, David P. DeWitt, Fundamentals of Heat and Mass Transfer, 4th ed., 1996, pp. 347-418.

[82] Matweb. [Online]. www.matweb.com

[83] (2005) The Engineering ToolBOX. [Online]. www.engineeringtoolbox.com/air-properties-d_156.html

[84] X Wang, J Rodriguez, J Hanson, D Gamarra, A Martinez-Arias, M Fernandez-Garcia, "Unusual Physical and Chemical Properties of Cu in Ce1-xCuxO2 Oxides," *J. Phys. Chem. B*, vol. 109, pp. 19595-19603 , 2005.

[85] X Wang, J.C. Hanson, A.I. Frenkel, J.-Y. Kim, and J.A. Rodriguez, "Time Resolved Studies for the Mechanism of Reduction of Copper Oxides with Carbon Monoxide: Complex Behavior of Lattice Oxygen and the Formation of Suboxides," *J. Phys. Chem. B.*, vol. 108, pp. 13667-13673, 2004.

[86] X Wang, J Rodriguez, J Hanson, D Gamarra, A Martinez-Arias, M Fernandez-Garcia. , "In Situ Studies of the Active Sites for the Water Gas Shift Reaction over Cu-CeO2 Catalysts: Complex Interaction Between Metallic Copper and Oxygen Vacancies of Ceria.," *J. Phys. Chem. B.*, vol. 110, pp. 428-434, 2006.

[87] Inc. Intertek USA. [Online]. http://www.qtionline.com/serviceOfferings/ElementalDivision/halogens/icp/sulfur/

[88] Gamry Instruments. [Online]. http://www.gamry.com/App_Notes/DC_Corrosion/GettingStartedWithEchemCorrMeasurements.htm

[89] Bharat Avasarala, Pradeep Haldar, "Effect of surface roughness of composite bipolar plates on the contact resistance of a proton exchange membrane fuel cell," *J. Power Sources* , vol. 188, pp. 225-229, 2009.

[90] A. Kraytsberg, M. Auinat, Y. Ein-Eli, "Reduced contact resistance of PEM fuel cell's bipolar plates via surface texturing," *J. Power Sources* , vol. 164 , pp. 697-703, 2007.

[91] W. R. Chang, J. J. Hwang, F. B Weng, S. H. Chan, "Effect of clamping pressure on the performance of a PEM fuel cell," *J. Power Sources* , vol. 166, pp. 149-154, 2007.

[92] Eric J. Carlson, "Cost Analyses of fuel cell stack/systems," FY2003 Progress Report 2003.

[93] K. L. More, "Microstructural characterization of PEM fuel cell membrane electrode assemblies," DOE FY 2004 Progress Report.

[94] K. L. More and K. S. Reeves, "Microstructural characterization of PEM fuel cell MEAs," Oak Ridge National Laboratory, Oak Ridge, TN, 2005.

[95] Wonseok Yoon, Xinyu Huang, Paul Fazzino, Kenneth L. Reifsnider, Michael A. Akkaoui, "Evaluation of coated metallic bipolar plates for polymer electrolyte membrane fuel cells," *J. Power Sources*, vol. 179, pp. 265–273, 2008.